UNIVERSITY OF THESSALY

SCHOOL OF ENGINEERING

DEPARTMENT OF MECHANICAL ENGINEERING

Doctor of Philosophy Dissertation

STRUCTURAL BEHAVIOR OF LIQUID STORAGE STEEL CONTAINERS UNDER STRONG DYNAMIC EXCITATION

by

MARIA VATHI

Diploma of Mechanical Engineering, University of Thessaly, 2008

M.Sc. in "Microsystems and Nanodevices", Dept. of Applied Mathematical and Physical Science, NTU Athens, 2010

M.Sc. in "Engineering - Economic Systems", Dept. of Electrical and Computer Engineering, NTU Athens, 2011

Supervisor: Dr. Spyros A. Karamanos, Professor

Submitted in partial fulfillment of

the requirements for the degree of

Doctor of Philosophy

2016

Approval of this doctoral thesis by the Department of Mechanical Engineering, School of Engineering, University of Thessaly, does not constitute in any way an acceptance of the views of the author by the said academic organization (L. 5343/32, art. 202, § 2).

Examination Committee:

Dr. Spyros A. Karamanos (Supervisor)
Professor, Department of Mechanical Engineering, University of Thessaly

Dr. J. Michael Rotter
Professor Emeritus, Department of Civil Engineering, University of Edinburgh

Dr. Euripides S. Mistakidis
Professor, Department of Civil Engineering, University of Thessaly

Dr. Alexis T. Kermanidis
Assistant Professor, Department of Mechanical Engineering, University of Thessaly

Dr. Philip C. Perdikaris
Professor, Department of Civil Engineering, University of Thessaly

Dr. Dimitrios S. Sophianopoulos
Associate Professor, Department of Civil Engineering, University of Thessaly

Dr. Charalampos J. Gantes
Professor, Department of Civil Engineering, National Technical University of Athens

iii

ACKNOWLEDGEMENTS

Firstly, I would like to express my sincere gratitude to my supervisor, Professor Spyros A. Karamanos, for the continuous support of my Ph.D study and related research. His guidance helped me in all the time of research and writing of this thesis. Also, I am grateful to the other members of the examining committee for their remarks and suggestions.

I would like to thank the Professors, the PhD students and the engineers with whom I have collaborated, for their help during my PhD research.

Moreover, I am grateful to my friends and colleagues for their friendship and encouragement.

Finally, I would like to express my very profound gratitude to my loved ones for providing me with support and continuous encouragement throughout my years of study and through the process of researching and writing this thesis. This accomplishment would not have been possible without them. Thank you.

STRUCTURAL BEHAVIOR OF LIQUID STORAGE STEEL CONTAINERS UNDER STRONG DYNAMIC EXCITATION

MARIA VATHI

University of Thessaly, Department of Mechanical Engineering, 2016

Supervisor: Dr. Spyros A. Karamanos, Professor

Abstract

Liquid containing tanks made of steel material are used in water storage and distribution systems, as well as in industrial plants for the storage and/or processing of a variety of liquids and liquid-like materials, including oil, liquefied natural gas, chemical fluids and wastes of various forms. The present research refers to ground-supported tanks and does not refer to underground or elevated tanks.

Tanks can be categorized as anchored and unanchored, if they are constructed with or without anchor bolts respectively. In the case of a strong seismic event unanchored tanks are likely to exhibit uplifting of their bottom plate, when the magnitude of the overturning moment exceeds a threshold value.

During a strong seismic event, liquid storage tanks may exhibit significant damages. Their structural response under strong seismic loading constitutes an important issue for safeguarding the structural integrity of industrial facilities. Typical steel tank damage can occur in the following forms: (a) buckling of the shell, because of excessive axial (meridional) compression due to overall bending of the structure under transverse seismic action, (b) damage of the roof and the top part, caused by sloshing of the upper part of the contained liquid when there is insufficient freeboard between the liquid surface and the roof, (c) base plate fatigue or/and fracture due to uplifting of the tank, (d) anchor bolt failure in the case of tanks anchored to the ground (e) shell damage at nozzle areas due to non-flexible connections with piping and other accessories, due to the inability of these elements to accommodate the deformations of the flexible shell. Shell buckling usually takes the form of "diamond shaped" or "elephant's

foot" buckling that appears at a short distance above the base and usually extends around most or of the entire circumference. In previous earthquake events, damages of various severity have been reported, e.g. from fracture of a pipe that created only slight leaks on minor repairs (damage to an overflow pipe) to complete loss of tank content.

Seismic analysis of liquid-containing tanks differs from typical civil engineering structures (i.e. buildings and bridges) mainly because of two reasons: first, during seismic excitation, liquid inside the tank exerts hydrodynamic force on tank walls and base, and second, tanks are generally less ductile and have significantly lower redundancy.

The present dissertation refers to the response of liquid storage tanks under strong dynamic excitation, with emphasis on seismic response. In particular, it emphasizes in two major phenomena which are examined extensively; (a) elephant's foot buckling and (b) base uplifting of unanchored tanks. The research is aimed at better understanding of tank mechanics and response, and defines a performance-based design framework that can be used for reliable development of vulnerability and assessment of seismic risk. The results of the present research can be also employed in possible future amendments and revisions in existing seismic design provisions. Modeling of tank structural behavior is performed using an efficient combination of detailed finite element models and simplified numerical techniques, which offer a simple and efficient tool for tank dynamic analysis.

Elephant's foot buckling is examined in Chapter 3 using three-dimensional and axisymmetric nonlinear finite element rigorous tools, in terms of buckling and post-buckling, considering material and geometric nonlinearities, accounting for initial imperfections for hydrostatic pressure and for internal pressure levels up to a significant percent of yield pressure. Two types of imperfections are considered: (a) imperfections from real measurements in an existing tank, which are of random shape and (b) axisymmetric imperfections in the form of an initial bulge at the bottom of the cylinder around the circumference of the cylinder. Special emphasis has been given on the development of local stresses and strains at the buckled area, in the pre-buckling and the post-buckling configuration. The numerical results have been compared with the predictions from the relevant provisions of EN 1993-1-6 and EN 1998-4. Lastly, the effectiveness of strengthening the tank with FRP wrapping against elephant's foot buckling failure is also examined.

A systematic two-step methodology for analyzing the seismic response of unanchored tanks that exhibit base uplifting has been developed and presented in Chapter 4, with emphasis on the failure of the welded connection between the base plate and the tank shell due to excessive local strain and fatigue. This methodology is applied on typical liquid storage tanks. The first step consists of a lateral-load analysis which determines the relationship between the overturning moment and the uplifting angle, as well as the relationship between the uplifting size and length. Based on those relationships, a nonlinear simplified model for the dynamic analysis of uplifted tanks is developed, calibrated and employed for the analysis of the tanks under seismic excitation. Upon calculating the global tank seismic response, the maximum bending strain at the plate-shell connection is calculated, and a low-cycle fatigue analysis of the connection is carried out considering the corresponding fatigue loading spectrum, an appropriate curve for low-cycle fatigue, and a fatigue damage accumulation factor. Subsequently, using a parametric study of 8 tanks with different aspect ratios, it is found that the stiffness of tank roof may have a significant influence on the uplifting mechanism and size.

In the last part of the dissertation, a framework for Performance-Based Design of liquid storage tanks under seismic loading conditions is defined (Chapter 5). The main failure modes are identified and quantified in terms of appropriate Engineering Demand Parameters (EDPs). In most of the cases, local strain has been considered as the principal EDP. Performance levels are defined for each mode of failure, considering an appropriate range of EDP values. The definition of performance level is based primarily on available experimental testing and numerical computations, as well as on engineering judgement. In addition, simple and efficient numerical models are proposed for the seismic analysis of tanks, so that reliable estimates of EDP are obtained. The above concepts are applied in typical tank case studies subjected to severe seismic actions. The proposed performance-based framework is aimed at increasing the safety of industrial facilities against strong seismic events.

ΔΟΜΙΚΗ ΣΥΜΠΕΡΙΦΟΡΑ ΧΑΛΥΒΔΙΝΩΝ ΔΟΧΕΙΩΝ ΑΠΟΘΗΚΕΥΣΗΣ ΥΓΡΟΥ ΥΠΟ ΙΣΧΥΡΗ ΔΥΝΑΜΙΚΗ ΦΟΡΤΙΣΗ

ΜΑΡΙΑ ΒΑΘΗ

Πανεπιστήμιο Θεσσαλίας, Τμήμα Μηχανολόγων Μηχανικών, 2016

Επιβλέπων: Δρ. Σπύρος Α. Καραμάνος, Καθηγητής

Περίληψη

Οι δεξαμενές αποθήκευσης υγρού χρησιμοποιούνται σε συστήματα διανομής νερού και σε βιομηχανικές εγκαταστάσεις για την αποθήκευση ή/και την επεξεργασία υγρών, όπως πετρελαίου, υγροποιημένου φυσικού αερίου, χημικών ρευστών και αποβλήτων διαφόρων μορφών. Η παρούσα μελέτη αναφέρεται σε δεξαμενές που στηρίζονται στο έδαφος (ground-supported tanks) και δεν περιέχει υπόγειες (underground tanks) ή ανυψωμένες δεξαμενές (elevated tanks).

Οι δεξαμενές επίσης διακρίνονται σε αγκυρωμένες και μη-αγκυρωμένες ανάλογα με το αν συγκρατούνται ή όχι σταθερά στο έδαφος με αγκύρια. Οι αστοχίες στις αγκυρωμένες δεξαμενές περιλαμβάνουν αστοχίες στη θεμελίωση, στις στηρίξεις και στο κέλυφος της δεξαμενής λόγω θλίψης. Σε αντίθεση με τις αγκυρωμένες δεξαμενές οι οποίες δεν επιτρέπουν το ανασήκωμά τους, οι δεξαμενές που δε φέρουν αγκυρώσεις είναι πιθανό να ανασηκωθούν λόγω της ροπής ανατροπής που δημιουργούν οι υδροδυναμικές πιέσεις που προκαλεί ο σεισμός.

Κατά τη διάρκεια ενός ισχυρού σεισμού, οι δεξαμενές αποθήκευσης υγρών μπορεί να παρουσιάσουν σημαντικές φθορές. Τυπικές αστοχίες δεξαμενών μπορεί να είναι των ακόλουθων μορφών: (α) λυγισμός του κελύφους που μπορεί να δημιουργηθεί λόγω υπερβολικής αξονικής συμπίεσης εξαιτίας ολικής κάμψης της κατασκευής, (β) ζημιά στην οροφή και στο ανώτερο κομμάτι της δεξαμενής λόγω του έντονου κυματισμού του ανώτερου τμήματος του περιεχόμενου υγρού στην περίπτωση που δεν υπάρχει μεγάλο κενό μεταξύ της επιφάνειας του υγρού και της οροφής, (γ) αστοχία λόγω κόπωσης ή/και θραύσης του πυθμένα

της δεξαμενής εξαιτίας του ανασηκώματος, (δ) αστοχία στα αγκύρια στην περίπτωση αγκυρωμένης δεξαμενής και, (ε) αστοχία των σωληνώσεων και άλλων εξαρτημάτων λόγω της αδυναμίας των στοιχείων αυτών να παραλάβουν τις παραμορφώσεις του εύκαμπτου κελύφους. Ο λυγισμός του κελύφους συνήθως είναι μορφής τύπου "diamond shape" ή τύπου "elephant's foot buckling" που εμφανίζεται σε μικρή απόσταση από την πλάκα έδρασης και συνήθως εκτείνεται σε μεγάλο τμήμα ή και ολόκληρη την περιφέρεια της δεξαμενής.

Η σεισμική ανάλυση των δεξαμενών διαφέρει από τις τυπικές κατασκευές πολιτικού μηχανικού (όπως κτίρια και γέφυρες) με δύο τρόπους: αρχικά, κατά τη διάρκεια της σεισμικής διέγερσης το υγρό μέσα στη δεξαμενή ασκεί υδροδυναμικές δυνάμεις στα τοιχώματα και στον πάτο. Κατά δεύτερον, οι δεξαμενές παρουσιάζουν απότομη κατάρρευση μετά το μέγιστο φορτίο.

Η παρούσα διδακτορική διατριβή αναφέρεται στην απόκριση δεξαμενών αποθήκευσης υγρών υπό ισχυρή δυναμική φόρτιση, επικεντρώνοντας στο πρόβλημα της σεισμικής απόκρισης. Στόχος είναι η αντιμετώπιση των παραπάνω ζητημάτων δομικής επάρκειας δεξαμενών, χρησιμοποιώντας κυρίως αριθμητικές προσομοιώσεις λαμβάνοντας υπόψη τις βασικές αρχές αντισεισμικού σχεδιασμού. Η έρευνα αποσκοπεί στην ανάπτυξη ενός ολοκληρωμένου πλαισίου για τον αντισεισμικό σχεδιασμό κατασκευών βιομηχανικών εγκαταστάσεων με βάση την επιτελεστικότητα. Για την προσομοίωση της δομικής συμπεριφοράς των δεξαμενών, χρησιμοποιείται το πρόγραμμα πεπερασμένων στοιχείων ABAQUS, ενώ για την εξέταση σεισμικών αποτελεσμάτων, αναπτύσσονται απλοποιημένα αριθμητικά μοντέλα. Τα αποτελέσματα αποσκοπούν στην καλύτερη κατανόηση της συμπεριφοράς ατμοσφαιρικών δεξαμενών αποθήκευσης υγρών υπό ισχυρό σεισμικό φορτίο.

Πιο αναλυτικά, η διατριβή απαρτίζεται από 7 κεφάλαια:

Στο 1ο Κεφάλαιο γίνεται μια σύντομη περιγραφή αστοχιών δεξαμενών αποθήκευσης υγρών σε συγκεκριμένους σεισμούς που έχουν καταγραφεί τα προηγούμενα χρόνια καθορίζοντας με αυτόν τον τρόπο την ανάγκη μελέτης της σεισμικής απόκρισης των δεξαμενών. Πραγματοποιείται επίσης βιβλιογραφική ανασκόπηση των εργασιών που αφορούν τη μελέτη της σεισμικής απόκρισης δεξαμενών αποθήκευσης υγρών.

Το 2ο Κεφάλαιο αφορά θέματα σχετικά με τη σεισμική ανάλυση και σχεδιασμό δεξαμενών αποθήκευσης υγρών. Αρχικά περιγράφονται τα πιο σημαντικά πρότυπα και κανονισμοί για τη σεισμική ανάλυση των δεξαμενών και στη συνέχεια παρουσιάζονται οι

σχετικές προδιαγραφές των προτύπων αυτών και οι συνήθεις αστοχίες που εμφανίζονται σε δεξαμενές αποθήκευσης υγρών.

Στο 3ο Κεφάλαιο γίνεται μελέτη του λυγισμού τύπου "elephant's foot" που αποτελεί και το πρώτο σημαντικό θέμα της διατριβής, και εξετάζεται η ευαισθησία των δεξαμενών αυτών σε δυο μορφές ατελειών. Διερευνάται επίσης η πιθανότητα ενίσχυσης δεξαμενών με περίσφυξη με φύλλα FRP για βελτίωση της αντοχής τους και αποφυγής αυτού του είδους λυγισμού.

Στο 4ο Κεφάλαιο μελετάται το δεύτερο σημαντικό θέμα της διδακτορικής διατριβής, το φαινόμενο του ανασηκώματος των μη αγκυρωμένων δεξαμενών υπό ισχυρή σεισμική φόρτιση. Η μέθοδος που χρησιμοποιείται αποτελείται από 2 βήματα: (α) μια ακριβή ανάλυση, μέσω μη-γραμμικής στατικής προσομοίωσης δεξαμενών με πεπερασμένα στοιχεία (β) ανάλυση που χρησιμοποιεί την προηγούμενη προσομοίωση για τη δημιουργία ενός απλοποιημένου μοντέλου για δυναμική ανάλυση των δεξαμενών σε σεισμική διέγερση. Πραγματοποιείται επίσης παραμετρική μελέτη της επίδρασης της οροφής στο ανασήκωμα της δεξαμενής. Για το σκοπό αυτό προσομοιώθηκαν οχτώ μη-αγκυρωμένες δεξαμενές με και χωρίς οροφή με πεπερασμένα στοιχεία.

Στο 5ο Κεφάλαιο διατυπώνεται ένα πλαίσιο για τον αντισεισμικό σχεδιασμό δεξαμενών με βάση την επιτελεστικότητα. Στόχος είναι η πρόταση ενός ολοκληρωμένου πλαισίου που θα περιλαμβάνει (α) τα επίπεδα επιτελεστικότητας, (β) τη συσχέτισή τους με τις πιθανές μορφές αστοχίας (γ) τη χρησιμοποίηση απλοποιητικών μοντέλων για τον καθορισμό των επιπέδων επιτελεστικότητας σε μία δεξαμενή για κάθε μορφή αστοχίας.

Τέλος, στο 6ο Κεφάλαιο συνοψίζονται τα σημαντικότερα συμπεράσματα της διδακτορικής διατριβής.

Table of Contents

xi

1. Introduction

Liquid containing tanks are used in water distribution systems and in industrial plants for the storage and/or processing of a variety of liquids and liquid-like materials, including oil, liquefied natural gas, chemical fluids and wastes of different forms.

There are many ways to classify a tank, and there is no universal method. The most fundamental classification of storage tanks is based upon whether they are aboveground or belowground (Myers 1997). Aboveground liquid storage tanks are called such because they have most of their structure aboveground. They are categorized into ground-supported and elevated tanks. Ground-supported tanks have their bottom usually placed directly on an earthen or concrete foundation and are generally made of reinforced concrete (RC), pre-stressed concrete (PSC), or steel. In elevated tanks, the container is supported on a structural tower, which could be in the form of a RC shaft or a steel frame. Underground tanks require special consideration for the earth loads to which they are subjected. Buoyancy must also be considered and they are often anchored into the ground, so that they do not pop out during periods when groundwater surrounds them. In addition, because they are underground, they are subjected to more severe corrosion.

Liquid storage tanks can be categorized as anchored and unanchored, if they are constructed with or without anchor bolts respectively. Unanchored tanks are likely to exhibit uplifting of their bottom plate, when the magnitude of the overturning moment exceeds a threshold value.

A classification commonly employed by many existing codes, standards and regulations refers to the internal pressure of the tank. In particular, tanks are classified as atmospheric tanks, low-pressure tanks and high-pressure tanks (often referred to as pressure vessels).

Most liquid storage tanks have a vertical cylindrical shape, because it is an economical, easily fabricated shape suitable for pressure containment. Vertical cylindrical tanks can be classified according to their roof type. Generally in refineries and especially for liquid fuels, there are fixed roof tanks, and floating roof tanks. Fixed roof tanks can be cone-roof, umbrella-roof or dome-roof tanks. On the other hand, floating roof tanks can be categorized into external (EFR) and internal floating roof tanks (IFR), depending on whether they are open on top or not, respectively.

1

In addition, tanks can be classified in terms of their bottom shape into flat-bottom, conical bottom, domed bottom or spheroid bottom tanks.

In the present work, ground-supported upright cylindrical steel tanks are examined in detail, mainly in terms of their seismic response. The present dissertation refers to the response of liquid storage tanks under strong dynamic excitation, focusing on two problems of their structural integrity; elephant's foot buckling and uplifting of their bottom plate.

1.1 Tank damages because of earthquakes

In the past, several major earthquakes have caused significant damage to industrial tanks in industrial facilities (Jennings 1971, Haroun 1983a, Manos and Clough 1985, Nielsen and Kiremidjian 1986, Cole et. al 1991, Iwatsubo 1998, Bendimerad et. al 1999, Steinberg et al. 1999, Johnson 2000, Eshghi and Razzaghi 2004, Suzuki 2006). A careful examination of their impact on these facilities will be valuable as one attempts to assess the seismic risks and damages to tanks and identify failure modes. In the following, some major earthquake events are briefly described in terms of their effects on industrial facilities with emphasis on liquid storage tanks:

•   Coalinga Earthquake, California U.S.A., May 2nd 1983, 6.5 Richter

•   Costa Rica Earthquake, Central America, April 22nd 1991, 7.5 Richter

•   Kobe Earthquake, Japan, January 17th 1995, 7.2 Richter

•   Kocaeli Earthquake, Turkey, August 17th 1999, 7.4 Richter

•   Bam Earthquake, Iran, December 26th 2003, 6.6 Richter

<u>Coalinga Earthquake</u>

Unanchored cylindrical ground supported tanks located at six sites within this oil producing area were damaged; damages included elephant's foot buckling at the base of three moderate sized tanks, joint rupture and top shell buckling in one large old riveted tank, bottom plate rupture of a relatively new welded tank and damage to the floating roofs of 11 tanks. Also

2

oil spilled over the top of many tanks and secondary damages occurred in pipe connections, ladders, etc.

Costa Rica Earthquake

In certain towns southward along the coast, and in the villages of Matina and Batan several examples of collapsed water tanks (steel vessels atop braced frames) were observed. The RECOPE refinery (the only one that serves Costa Rica) suffered a fire that burned a small portion of the refinery installation as well as two tanks. The fire was extinguished, however, the smaller oil tank exploded, throwing the tank wall and roof at approximately 30 meters away. Out of about 20 oil storage tanks (various sizes), one failed, apparently at the welded wall/base seam. There are several tank farms near the port of Moine, some with excellent examples of elephant's foot buckling.

Kobe earthquake

Damage was notable in boilers in power generation installations, and transformers and circuit breakers in substation installations. Oil storage tanks, piping, and expansion joints were damaged by ground liquefaction in gas turbine power stations. In thermal power stations, the fracture and deformation of the centers rest for large power generation boilers were notable. Steel beam support structures of boilers were deformed, and main steam tubes and water supply pumps were damaged. Petrochemical tanks and their piping were dynamically destroyed by ground liquefaction generated following the earthquake motion and large-scale ground movement, not by the earthquake motion itself, and subsequent differential settlement of ground, destruction, and lateral movement of shore protection. Tanks tipped due to ground variations. Also, many tanks were damaged by buckling and deformation of their lateral walls. The leakage of liquefied petroleum from a storage tank on the southern coast of Kobe was the most notable damage to HPG facilities, and it caused a large amount of LP-gas in the liquid phase, to leak from the inlet/outlet piping flange connection of an LP-gas storage system.

3

<u>Kocaeli Earthquake</u>

Some of the more prominent examples of hazardous materials releases triggered by the earthquake include: the intentional air release of 200 metric tons of hazardous anhydrous ammonia to avoid tank over-pressurization due to loss of refrigeration capabilities; the leakage of 6500 metric tons of toxic acrylonitrile (ACN) into air, soil and water from ruptured tanks; the spill of 50 metric tons of diesel fuel into Izmit Bay from a broken fuel loading arm; the release of 1200 metric tons of cryogenic liquid oxygen caused by structural failure of concrete support columns in two oxygen storage tanks; and the enormous fires, liquid petroleum gas leakages, and oil spills at the Tupras oil refinery. More particularly, the Tupras Refinery has a total of 45 storage tanks in three tank farm areas (for naphtha fuel, crude oil, and liquefied petroleum gas (LPG)). The most affected was the naphtha tank farm area where an enormous fire melted six steel storage tanks and consumed more than 18,000 m^3 of naphtha. It is believed that sparks, caused by metal-to-metal contact of the vibrating floating-roofs and the tank shells, ignited four tanks. Leaking naphtha from a damaged flange on one of the four tanks ignited and flowed downstream through the refinery's drainage system, spreading the fire to two additional naphtha tanks. Thirty of the forty-five tanks in the tank farms suffered damage. Typical damage to tanks included elephant's foot buckling of tank walls, bulging of tank tops due to sloshing of liquid, cracking of tank roof-shell wall joints, and damage to roof seals. A small amount of LPG leaked from a broken flange connection, but no ignition occurred.

<u>Bam Earthquake</u>

Several steel elevated water tanks experienced the strong ground motion, but most of them suffered no damage. Buckling of the slender bracing and rupture of poorly detailed bracing connection were common failure modes in damaged steel elevated tanks. The underground tanks at the Bam water treatment plant, which is 2 km southwest of the city, had no visible structural damage. On the other hand, two underground water tanks at the Baravat water treatment plant, which is constructed over the Bam fault, suffered major damage to tanks and annex structures during the earthquake and the plant was forced to shut down. Leakage from the tank wall and bottom occurred after the earthquake and cracks were also found at construction joints on the masonry retaining walls surrounding the tank. Three out of six on-grade cylindrical steel oil tanks at Roghan Jonub Company experienced leakage of liquid from

Institutional Repository - Library & Information Centre - University of Thessaly
20/04/2024 10:47:00 EEST - 3.139.101.198

roof-to-wall junctions from sloshing during the quake. Other damage modes such as elephant foot buckling, rupture of rigid piping, and tank were not observed in these tanks. A cylindrical on-grade gasoline tank next to Bam electrical power station, which was nearly empty, suffered heavy damage. Rigid piping connected to the tank ruptured, probably from the inaccurate erection of the pipes. The tank foundation was damaged due to tank uplift, but shell buckling did not occur.

1.2 Brief Literature Review on Seismic Response of Liquid Storage Tanks

The construction of liquid storage tanks has increased over the last years, mainly because of the need for continuous supply and storage of energy and water resources. In particular, the need to understand better their structural behavior and performance has become an important topic of structural mechanics. In particular, the analysis and design of liquid storage tanks against earthquake-induced actions has been recognized as a key issue towards safeguarding their structural integrity, and has been the subject of numerous analytical, numerical and experimental works. The pioneering works of Housner (1957, 1963), motivated by the need for accurate determination of seismic actions in tanks, presented a solution for the hydrodynamic effects in non-deformable vertical cylinders and rectangles. For the first time, the total seismic action was split in two parts, namely the "impulsive" part and the "convective" part. This concept constitutes the basis for the API 650 standard provisions (Appendix E) for vertical cylindrical tanks. Veletsos (1974), Veletsos and Yang (1977), Haroun and Housner (1981a), Haroun (1983b), have extended this formulation to include the effects of shell deformation, and its interaction with hydrodynamic effects. More recently, the case of uplifting of unanchored tanks as well as soil-structure interaction effects have been studied extensively, in the papers by Peek (1986), Natsiavas (1988), Veletsos and Tang (1990), Malhotra (1995). Notable contributions on the seismic response of anchored and unanchored liquid storage tanks have been presented by Fischer (1979), Rammerstorfer et al. (1988), Fischer et al. (1991), with particular emphasis on design implications. Apparently, those papers constitute the basis for the seismic design provisions concerning vertical cylindrical tanks in Eurocode 8 (EC8 – part 4.3 – Annex A). In addition to the numerous analytical/numerical works, notable experimental contributions on this subject have been reported (Haroun and Housner 1981b; Niwa and Clough 1982; Manos and Clough 1982). The reader is referred to the review paper of Rammerstorfer

5

et al. (1990) for a thorough presentation and a concise literature review of liquid storage tank response under seismic loads, including fluid-structure and soil-structure interaction effects. The reader is also referred to the paper by Ibrahim et al. (2001) who have reviewed a large number of publications on sloshing dynamics, addressing special issues such as nonlinear sloshing, equivalent mechanical models, stochastic excitation, deformable wall effects, hydrodynamic impact, or sloshing in low gravitation fields. Recently, a European research project has been completed (Pappa et. al. 2012) on the seismic analysis and design of industrial facilities, with particular emphasis on liquid storage tanks. The results from this study have been incorporated in specific design guidelines.

1.3   Scope and contribution of the present dissertation

The present dissertation focuses on the analysis and design of liquid storage tanks under dynamic excitation, motivated by their damage in severe seismic events towards safeguarding their structural integrity. The main purpose is the proposal of a simple and efficient methodology for the analysis and design of tanks which also constitutes an efficient tool for conducting a performance-based design.

The contribution of the present dissertation can be summarized in the following items:

- better understanding of the uplifting phenomenon during seismic excitation towards improvement of current design practice
- development of simplified and efficient methodologies for the analysis of anchored and unanchored tanks under lateral excitations with emphasis on the strength of the welded base plate-shell connection
- examination of elephant's foot buckling failure mode, its sensitivity on existing initial geometric imperfections, and tank strengthening with FRP wrapping.
- development of an efficient framework for the performance-based design of liquid storage tanks under seismic loading

6

1.4 Structure of the dissertation

The work in the present dissertation comprises the following chapters:

In Chapter 2, some important aspects of the seismic analysis behavior and design of tanks are presented. At first, the most important relevant Standards and Guidelines are described, with emphasis on EN 1998-4 Standard and API 650, followed by their relevant provisions on the seismic response of tanks. In addition, the failure modes of liquid storage tanks under seismic excitation are presented.

In Chapter 3, the elephant's foot buckling phenomenon is studied extensively and rigorously using three-dimensional nonlinear finite element tools, simulating buckling and post-buckling behavior, considering material and geometric nonlinearities and accounting for initial imperfections in the presence of hydrostatic pressure and high internal pressure level up to a significant percent of yield pressure. The effectiveness of strengthening the tank with FRP wrapping against elephant's foot buckling failure is also examined.

In Chapter 4, the uplifting phenomenon is examined extensively. A systematic two-step methodology for analyzing the seismic lateral and rocking response of unanchored tanks is developed, with emphasis on base plate uplifting and the fatigue of the welded connection between the base plate and the tank shell. Moreover, a parametric study of eight tanks with different aspect ratios is conducted in order to study how the existence of the tank roof affects the uplifting mechanism.

In Chapter 5, a Performance Based Design approach for liquid storage tanks design under seismic loading conditions is developed, with the purpose of proposing a methodology consisting of: (a) appropriate performance level definition, (b) correlation between the performance levels and the major failure modes of the tank, (c) simplified models for simple and efficient tank analysis.

In Chapter 6, the conclusions of the present dissertation are stated.

2. Overview of Seismic Analysis Behavior and Design of Tanks

2.1 Relevant Standards and Guidelines

There exist several relevant standards and guidelines for the seismic analysis of liquid storage tanks. In this paragraph, the most important European and American Standards as well as the New Zealand Recommendations (Priestly et al. 1986) are briefly presented.

A relatively new standard on tank seismic design is the 4th part of Eurocode 8 (EN 1998-4). It is a standard that concerns the seismic design of silos, tanks and pipelines for earthquake resistance, and is part of the CEN/TC250 standard group, often referred to as "Structural Eurocodes". It specifies principles and application rules for the seismic design of structural components including above-ground and buried pipeline systems, silos, storage tanks of different types and uses. This standard contains significant information on the calculation of seismic action based mainly on the work of Scharf (1990) as well as the work of Rotter (1990) for shell buckling under internal pressure (elephant's foot). EN 1998-4 rules are quite general and may refer to tanks of different material, i.e. steel, concrete, plastic. It should be noted that this standard should be used together with the other relevant Structural Eurocodes. More specifically, Eurocode 8 – Part 1 (EN 1998-1) should be used for the seismic input in terms of the design spectrum. In addition, Eurocode 3 Part 1-6 (EN 1993-1-6) gives basic design rules for the strength and structural stability of steel tanks, covering the basic failure modes of steel shells, namely plasticity, cyclic plasticity, buckling and fatigue, with emphasis on buckling. Finally, Part 4.2 of Eurocode 3 (EN 1993-4-2) provides principles and application rules for the general structural design of vertical cylindrical above-ground steel tanks for the storage of liquid products that should be taken into account.

API 650 is a standard dedicated to the general design of liquid storage tanks, developed by the American Petroleum Institute and widely used by the petrochemical industry for the design and construction of tanks in petrochemical facilities. In particular, Appendix E of API 650 refers exclusively to seismic design, contains provisions for both determining seismic actions on tanks, as well as calculating the strength of the tank. Appendix E of the new 11th edition of API 650 (2007) has significant revisions with respect to the previous 2003 edition and includes provisions for site-specific seismic input, calculation of hoop hydrodynamic stresses, distinction between ringwall and slab overturning moments, freeboard requirements, and consideration of vertical excitation effects. It should be noted that the seismic provisions

8

of the updated Appendix E are in accordance with the provisions of ASCE 7 Standard, which refers to structural loading.

EN 14015 is a European standard outside the Structural Eurocode framework, i.e. independent of EN 199x Standards, which specifies the requirements for the materials, design, fabrication, erection, testing and inspection of site built, vertical, cylindrical, flat bottomed, above-ground, welded, steel tanks for the storage of liquids at ambient temperatures and above. It constitutes an updated version of the classical British Standard BS 2654, which is a specification for the manufacture of vertical steel welded non-refrigerated storage tanks with butt-welded shells for the petroleum industry. It is a complete standard for tank design analogous to API 650. Recommendations for seismic design and analysis of storage tanks are stated in Annex G of EN 14015, which are quite similar with the requirements of Annex E of API 650 (2003).

The New Zealand Seismic Tank Design Recommendations is a document that, when published in 1986, contained pioneering recommendations for the seismic design of storage tanks, developed by a Study Group of the New Zealand National Society for Earthquake Engineering. The intention of this study group was to collate existing information, available in research papers and codes, and to produce uniform recommendations that would cover a wide range of tank configurations and contained materials. These recommendations attempted to produce a unified approach for the seismic design of storage tanks, regardless of material or function, and to provide additional information to that already available in alternative sources. Several decades after their publication, these recommendations have been widely referenced and adopted internationally, including EN 1998-4. It remains one of the most comprehensive guidelines available for the seismic design of storage tanks. The NZSEE study group has recently been working to revise the 1986 document to bring the recommended seismic design loads in line with the latest NZ Loading Code NZS 1170. The completed revision of the document is soon to be published (Whittaker and Saunders 2008).

9

2.2 Seismic Loading on Liquid Storage Tanks

2.2.1 Lateral Seismic Action

2.2.1.1 General

A cylindrical coordinate system is usually used to describe the tank geometry with orthogonal coordinates: r, φ, z where the origin at the centre of the tank bottom and the z axis is vertical (Figure 1). The height of the tank to the original of the free surface of the fluid and its radius are denoted by H and R, respectively, ρ is the mass density of the fluid, while the non-dimensional coordinates $\xi = r/R$ and $\zeta = z/H$ in the radial direction and along the height of the tank respectively are usually considered.
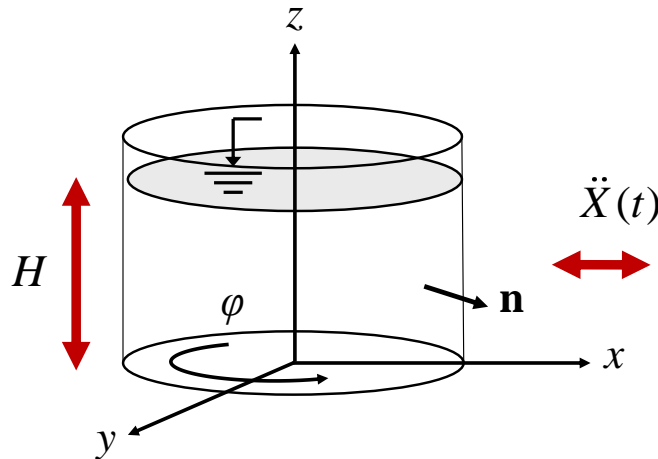
Figure 1: Cylindrical coordinate system describing tank geometry.

The liquid contained in an upright cylinder subjected to horizontal seismic excitation $\ddot{X}_g(t)$ may be considered as ideal fluid (potential flow) resulting in a hydrodynamic problem (Ibrahim 2005) associated with the motion of the liquid free surface and the development of standing waves. The solution of the hydrodynamic problem shows that the liquid motion can be expressed as the sum of two separate contributions, called impulsive and convective, respectively. The impulsive component of the motion satisfies exactly the boundary conditions at the tank wall and the bottom of the tank and corresponds to zero pressure at the free surface of the fluid. It represents the motion of the fluid part that "follows" the motion of the container.

10

The convective term is associated with liquid sloshing of its free surface, and satisfies the kinematic and dynamic conditions at the free surface.

As a result, the hydrodynamic pressure is decomposed into an impulsive part and a convective part. In an analogous manner, the total mass of the liquid, m_L, can be considered as the sum of two parts, an impulsive part, m_I, and a convective part, m_C so that $m_L = m_I + m_C$.

The convective motion is associated with an infinite number of modes and the corresponding masses are computed as follows:

$$\frac{m_{Cn}}{m_L} = \frac{2\tanh\left(k_n R\,\gamma\right)}{k_n R\,\gamma\left(k_n^2 R^2 - 1\right)}, \quad n = 1, 2, 3, \dots \tag{1}$$

where n is the number of sloshing mode, R is the radius of the tank, γ is the tank aspect ratio defined as the ratio of the liquid height over the tank radius ($= H / R$) and $k_n R = \lambda_n$ are the roots of equation $J_1'(\cdot) = 0$. More specifically the first three roots are $k_1 R = \lambda_1 = 1.841$, $k_2 R = \lambda_2 = 5.331$, $k_3 R = \lambda_3 = 8.536$ corresponding to the first 3 sloshing modes. Note that the total convective mass is the sum of the individual convective masses, $m_C = \sum_{n=1}^{\infty} m_{Cn}$. Usually, consideration of only the first one ($n = 1$), or the first two mode ($n = 1, 2$) in some special cases, is adequate for design purposes.

Masses m_I and m_{Cn} for $n = 1, 2$ are plotted in Figure 2 as functions of the tank aspect ratio $\gamma = H / R$. The impulsive mass is expressed as the ratio m_I / m_L of the impulsive mass over the total liquid mass. This ration increases with increasing values of γ, tending asymptotically to unity. On the other hand, the convective mass, expressed in normalized form as m_{C1} / m_L, decreases with increasing values of γ. The value of m_{C2} is quite small, but may have some effect on the dynamic response in broad tanks where $\gamma \to 0$.

In the course of a design procedure, the impulsive mass m_I should consist of the above impulsive mass of the liquid, plus the mass of the moving tank wall, m_{SH}, and the mass of the tank roof, m_R.
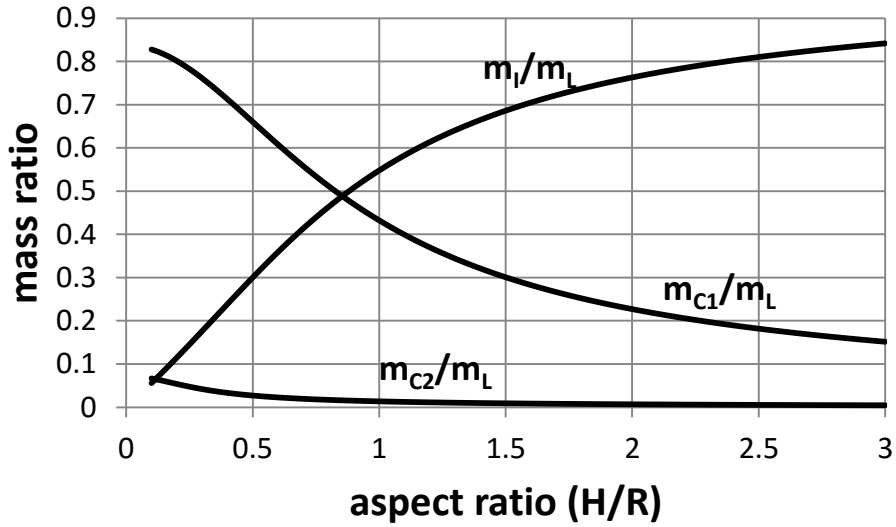
Figure 2: Mass ratio as a function of the aspect ratio.

In case of rigid (non-deformable) tank walls, the impulsive motion follows exactly the ground motion. In such a case the impulsive circular frequency has an infinite value ($\omega_I \to \infty$) and the impulsive period is zero ($T_I = 0$). This is not applicable in the case of flexible (deformable) tank walls. To simplify the analysis it is reasonable to assume that the flexibility of tank wall affects almost exclusively the impulsive component of the response and therefore the impulsive hydrodynamic effects for flexible tanks are generally significantly larger than those for rigid tanks. On the other hand, the convective components of the response can be considered insensitive to variations in wall flexibility, because they are associated with natural periods of vibration that are significantly longer than the dominant periods of the ground motion or pipe wall vibration motion. Therefore, the convective components of seismic action for tank proportions normally encountered in practice can be considered the same as those obtained for rigid tanks.

Analytical expressions are available for the impulsive vibration period and frequency accounting for tank flexibility. From hydrodynamics, the natural circular frequency and natural period of the impulsive response of flexible tanks are calculated by the expressions:

$$\omega_I = \frac{2\pi}{Y_I H \sqrt{\dfrac{\rho R}{t_{eq} E}}} \tag{2}$$

12

$$T_I = Y_I H \sqrt{\frac{\rho R}{t_{eq} E}} \qquad (3)$$

where ρ is the mass density of the fluid, E is Young's modulus, t_{eq} is the equivalent uniform thickness of the tank wall (can be taken as the weighted average over the wetted height of the tank wall, the weight may be taken proportional to the strain in the wall of the tank, which is maximum at the base of the tank) and coefficient Y_I is given in Table 1 for specific values of the aspect ratio γ of the tank ($\gamma = H / R$). For intermediate values of γ, a simple interpolation may be used.

Table 1: Coefficient Y_I in terms of the aspect ratio.

H/R	0.3	0.5	0.7	1.0	1.5	2.0	2.5	3.0
Y_I	9.28	7.74	6.97	6.36	6.06	6.21	6.56	7.03

Furthermore, the circular frequency and natural period of the convective response, denoted as ω_{Cn} and T_{Cn} respectively, for the n-th sloshing mode can be calculated by the following expressions:

$$\omega_{Cn} = \sqrt{g \frac{\lambda_n}{R} \tanh(\lambda_n \gamma)}, \; n = 1, 2, 3, ... \qquad (4)$$

$$T_{Cn} = \frac{2\pi}{\omega_{Cn}}, \; n = 1, 2, 3, ... \qquad (5)$$

where λ_n are the roots of $J_1'(\cdot) = 0$ ($\lambda_1 = 1.841$, $\lambda_2 = 5.331$ and $\lambda_3 = 8.536$ for the first 3 sloshing modes).

The impulsive and convective damping coefficients can be taken equal to $\xi_I = 5\%$ and $\xi_C = 0.5\%$ for the impulsive and the convective motion respectively.

13

2.2.1.2 Impulsive motion and pressure

The impulsive motion can be expressed in terms of the impulsive acceleration of the liquid storage tank, $\ddot{u}_I(t)$, which can be calculated from the following linear oscillator equation:

$$\ddot{u}_I + 2\xi_I \omega_I(\dot{u}_I - \dot{X}) + \omega_I^2(u_I - X) = 0 \tag{6}$$

where $u_I(t)$ is the generalized coordinate representing the total impulsive displacement motion of the tank, ξ_I the viscous damping ratio of the impulsive motion and ω_I the impulsive frequency defined in Eq. (2). Setting

$$a_I(t) = u_I(t) - X \tag{7}$$

one can obtain

$$\ddot{a}_I + 2\xi_I \omega_I \dot{a}_I + \omega_I^2 a_I = -\ddot{X}(t) \tag{8}$$

In the above expressions, function $a_I(t)$ can be considered as the generalized coordinate representing the relative impulsive displacement of the tank with respect to its base. The spatial-time variation of the "*impulsive*" component of hydrodynamic pressure within the liquid domain is given by the following expression:

$$p_I(\xi,\zeta,\varphi,t) = C_I(\xi,\zeta)\rho H \cos\varphi \, \ddot{u}_I(t) \tag{9}$$

where the spatial coefficient C_I is defined:

$$C_I(\xi,\zeta) = 2\sum_{n=0}^{\infty} \frac{(-1)^n}{I_1'(\nu_n/\gamma)\nu_n^2} \cos(\nu_n\zeta) I_1\left(\frac{\nu_n}{\gamma}\xi\right) \tag{10}$$

in which $\nu_n = \dfrac{2n+1}{2}\pi$, $\gamma = H/R$ is the aspect ratio of the tank, whereas $I_1(\cdot)$ and $I_1'(\cdot)$ denote the modified Bessel function of order 1 and its derivative respectively.

For seismic design purposes, the distribution of the impulsive hydrodynamic pressure on the pipe walls is assumed as follows:

$$p_I(\xi,\zeta,\varphi) = C_I(\xi,\zeta)\rho H \cos\varphi \, S_a(T_I) \tag{11}$$

14

where ξ is taken equal to 1 for computing the pressure on the lateral surface of tank shell, whereas ζ should be considered equal to zero for calculating the pressure on the tank bottom plate.
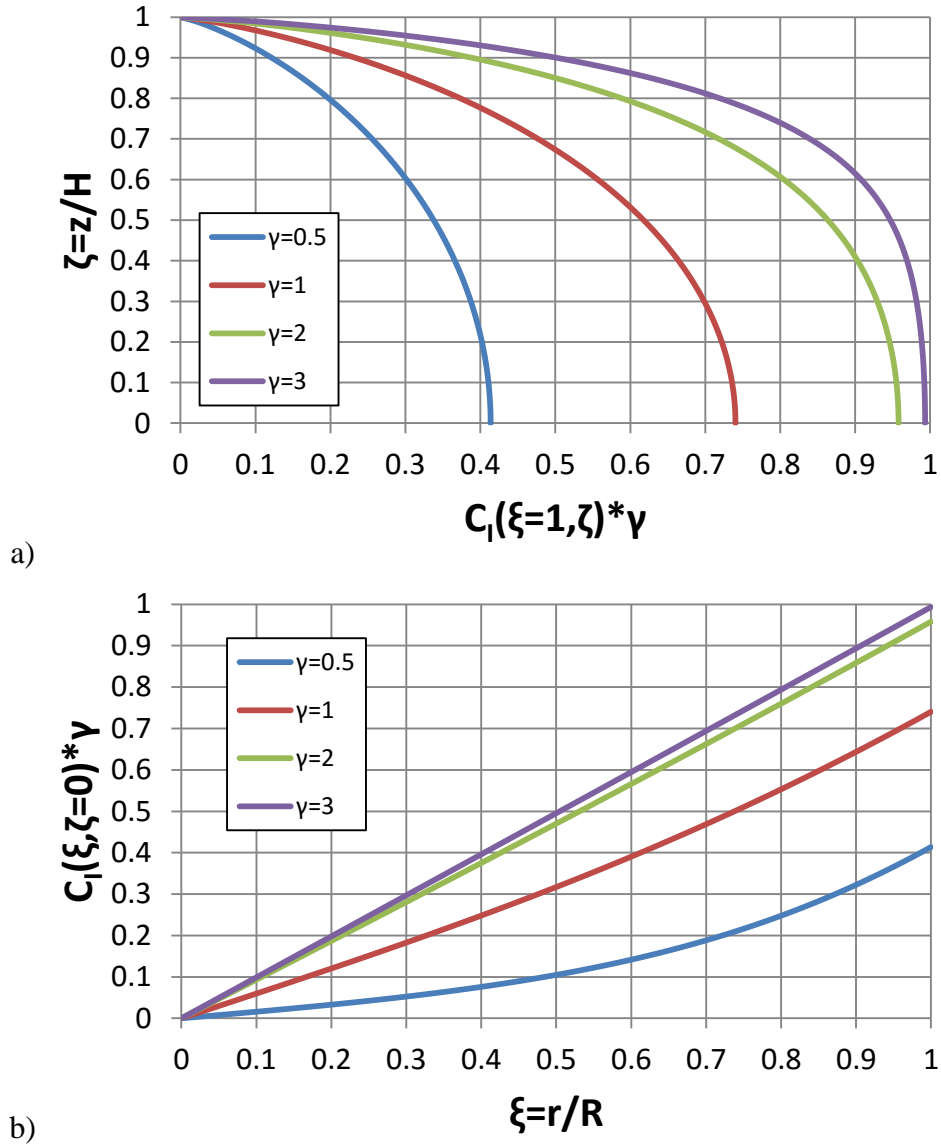

a)

b)

Figure 3: Variation of the impulsive pressure (normalized to $\rho R a_g$) for four values of $\gamma = H / R$; a) variation along the height; b) radial variation on the tank bottom. a_g is the maximum ground acceleration.

15

2.2.1.3 Convective motion and pressure

The convective acceleration, $\ddot{u}_{Cn}(t)$, is calculated from the following linear oscillator equation:

$$\ddot{u}_{Cn} + 2\xi_{Cn}\omega_{Cn}(\dot{u}_{Cn} - \dot{X}) + \omega_{Cn}^2(u_{Cn} - X) = 0 \tag{12}$$

where $u_{Cn}(t)$ is the generalized coordinate representing the total convective motion of the liquid associated with the n-th mode, ξ_{Cn} the viscous damping ratio of the convective motion for the n-th sloshing mode and ω_I the convective frequency. Setting:

$$a_{Cn}(t) = u_{Cn}(t) - X \tag{13}$$

one can write

$$\ddot{a}_{Cn} + 2\xi_{Cn}\omega_{Cn}\dot{a}_{Cn} + \omega_{Cn}^2 a_{Cn} = -\ddot{X}(t) \tag{14}$$

where $a_{Cn}(t)$ is the generalized coordinate representing the relative convective motion of the liquid associated with the n-th sloshing mode.

The spatial distribution within the liquid domain and time variation of the "convective" component of hydrodynamic pressure associated with the n-th convective mode is given by the following expression:

$$p_{Cn}(\xi,\zeta,\varphi,t) = \rho\psi_n \cosh(\lambda_n\gamma\zeta) J_1(\lambda_n\xi)\cos\varphi\, \ddot{u}_{Cn}(t) \tag{15}$$

where:

$$\psi_n = \frac{2R}{(\lambda_n^2 - 1)J_1(\lambda_n)\cosh(\lambda_n\gamma)} \tag{16}$$

J_1 is the Bessel function of the first order and $\lambda_1 = 1.841$, $\lambda_2 = 5.331$, $\lambda_3 = 8.536$ are the roots of $J_1'(\lambda) = 0$. In Eq. (15), r is taken equal to R ($\xi = 1$) for the pressure on the lateral surface, whereas z is taken equal to zero ($\zeta = 0$) for the pressure on the bottom plate. In the majority of practical applications, only the first convective mode ($n = 1$) of the fluid is necessary (Pappa et al. 2011) and the distribution of the pressure is as follows:

16

$$p_C\left(\xi,\zeta,\varphi\right)=1.146R\rho\,\frac{\cosh(1.841\gamma\zeta)J_1(1.841\xi)}{\cosh(1.841\gamma)}\cos\varphi\,S_a(T_{C1}) \tag{17}$$

where J_1 is the Bessel function of first order. In the above expressions, r is taken equal to R ($\xi=1$) for determining the hydrodynamic pressure on the lateral tank (shell) surface, whereas z is taken equal to zero ($\zeta=0$) for the hydrodynamic pressure on the bottom plate. In addition, 1.841 is the first root of $J_1'(0)=0$.
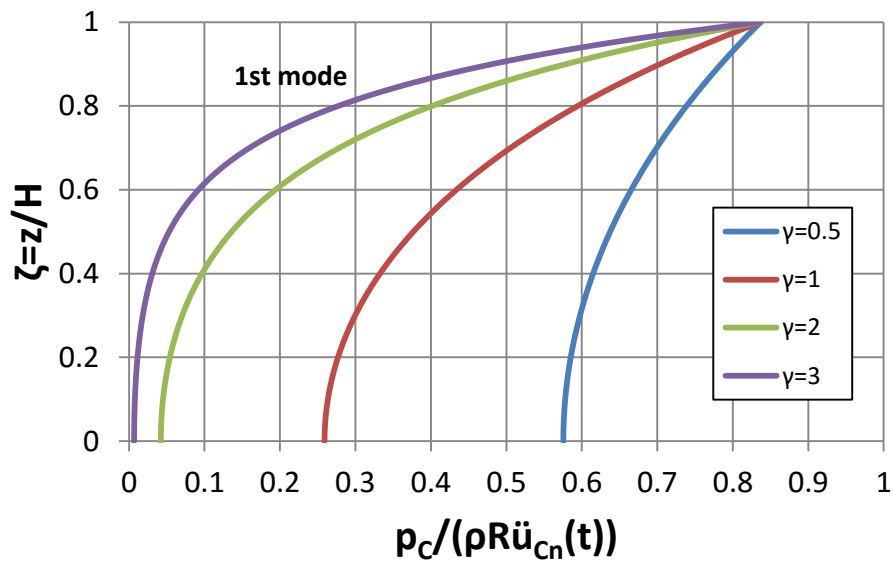

Figure 4: Variation of first mode sloshing pressures on tank wall along the tank height.
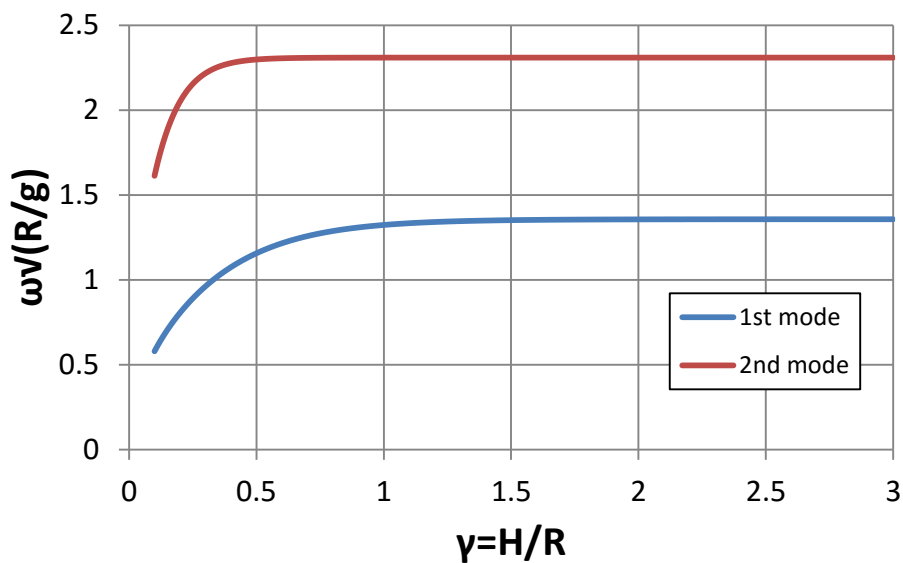
Figure 5: Values of the first two sloshing frequencies as functions of γ.

17

In broad tanks (i.e. tanks with large values of H/R ratio) the sloshing pressures may be significant near the bottom, while in slender (tall) tanks the sloshing effect is limited to the vicinity of liquid surface.

2.2.1.4 Horizontal seismic forces

Integrating the pressure distribution on the tank wall, the impulsive base shear force at the base of the wall can be calculated as follows:

$$Q_I(t) = \int_{B_q} p_I(\mathbf{n} \cdot \mathbf{e}_x) dB_q \tag{18}$$

where $\mathbf{e}_x$ is the unit vector in the direction of the earthquake, $\mathbf{n}$ is the unit normal vector to the liquid surface and B_q the boundary surface of the liquid.

The result of this integration can be readily written as follows:

$$Q_I(t) = m_I \ddot{u}_I(t) \tag{19}$$

where m_I is the impulsive mass defined in Figure 2 and $\ddot{u}_I(t)$ is the impulsive acceleration parameter, defined in Eq. (6).

The convective base shear can be obtained by integrating the convective pressure (p_C) components on the lateral shell of the tank:

$$Q_C(t) = \int_{B_q} p_C(\mathbf{n} \cdot \mathbf{e}_x) dB_q \tag{20}$$

The result of this integration can be readily written as follows:

$$Q_C(t) = \sum_{n=1}^{\infty} m_{Cn} \ddot{u}_{Cn}(t) \tag{21}$$

where m_{Cn} is the convective mass for the n-th mode defined in Figure 2 and $\ddot{u}_{Cn}(t)$ is the convective acceleration parameter for the n-th sloshing mode, defined in Eq. (12).

18

In the course of a spectral seismic analysis of the tank, the impulsive base shear Q_I and convective base shear Q_{Cn} for the n-th mode at the base of the wall can be computed in terms of the corresponding spectral acceleration as follows:

$$Q_I = m_I S_a(T_I) \tag{22}$$

$$Q_{Cn} = m_{Cn} S_a(T_{Cn}), \ n = 1, 2, 3, ... \tag{23}$$

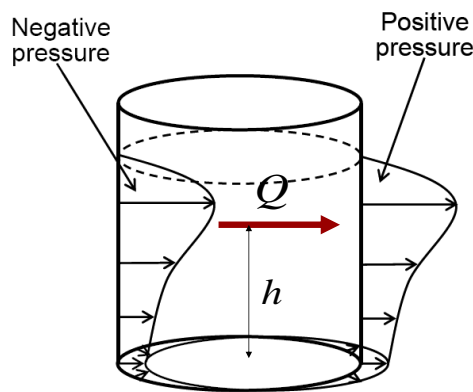**Figure 6:** Horizontal seismic force Q acting at a height h.

2.2.1.5 *Ringwall and slab overturning moment / heights*

The ringwall moment, M, is the overturning moment that acts immediately above the bottom plate of the tank. It includes only the contribution of pressure on the wall and should be used for the calculation of stresses and stress resultants in the tank wall and at its connection to the base, for tank structural verification. On the other hand, the slab moment, M', is the overturning moment that acts immediately below the bottom plate of the tank. It includes the contribution of pressure on the wall together with the pressure on the tank bottom and should be used for the verification of its support structure, base anchors or foundation.

The impulsive ringwall base moment is calculated through the following integration:

$$M_I(t) = \int_{B_q} p_I z (\mathbf{n} \cdot \mathbf{e}_x) dB_q \tag{24}$$

The result of this integration can be readily written as follows:

19

$$M_I(t) = m_I h_I \ddot{u}_I(t) \tag{25}$$

or

$$M_I(t) = Q_I(t) h_I \tag{26}$$

where m_I is the impulsive mass defined in Figure 2, h_I is the height at which acts the horizontal seismic force, $Q_I(t)$, and $\ddot{u}_I(t)$ is the impulsive acceleration parameter, defined in Eq. (6).

The convective ringwall base moment is calculated in an analogous manner:

$$M_C(t) = \int\limits_{B_q} p_C z(\mathbf{n} \cdot \mathbf{e}_x) dB_q \tag{27}$$

The result of this integration can be readily written as follows:

$$M_C(t) = \sum_{n=1}^{\infty} m_{Cn} h_{Cn} \ddot{u}_{Cn}(t) = \sum_{n=1}^{\infty} Q_{Cn}(t) h_{Cn} \tag{28}$$

where m_{Cn} is the convective mass for the n-th mode defined in Figure 2, h_{Cn} is the height at which acts the horizontal seismic force for the n-th sloshing mode, $Q_{Cn}(t)$, and $\ddot{u}_{Cn}(t)$ is the convective acceleration parameter for the n-th sloshing mode, defined in Eq. (12).

Analytical expressions for the heights at which impulsive and convective forces are acting are available from hydrodynamics, represented also in graphical form in Figure 7. For the impulsive moment:

$$h_I = H \frac{\displaystyle\sum_{n=0}^{\infty} \frac{(-1)^n}{v_n^4} \frac{I_1(v_n/\gamma)}{I_1'(v_n/\gamma)} \left(v_n(-1)^n - 1\right)}{\displaystyle\sum_{n=0}^{\infty} \frac{I_1(v_n/\gamma)}{v_n^3 I_1'(v_n/\gamma)}} \tag{29}$$

$$h_I' = H \frac{\dfrac{1}{2} + 2\gamma \displaystyle\sum_{n=0}^{\infty} \frac{v_n + 2(-1)^{n+1} I_1(v_n/\gamma)}{v_n^4 I_1'(v_n/\gamma)}}{2\gamma \displaystyle\sum_{n=0}^{\infty} \frac{I_1(v_n/\gamma)}{v_n^3 I_1'(v_n/\gamma)}} \tag{30}$$

For the convective moment:

$$h_{Cn} = H\left(1 + \frac{1 - \cosh(\lambda_n \gamma)}{\lambda_n \gamma \sinh(\lambda_n \gamma)}\right) \qquad (31)$$

$$h'_{Cn} = H\left(1 + \frac{2 - \cosh(\lambda_n \gamma)}{\lambda_n \gamma \sinh(\lambda_n \gamma)}\right) \qquad (32)$$
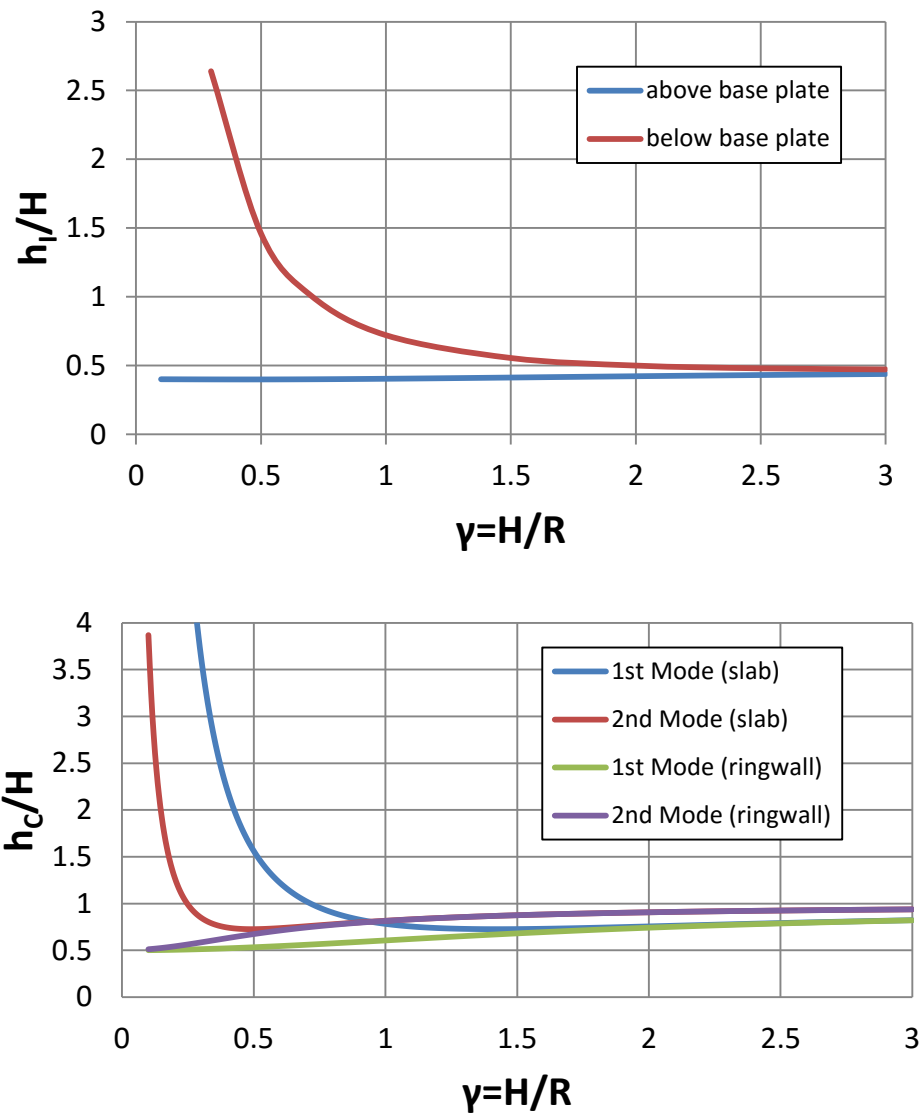

Figure 7: Ratios h_I / H , h'_I / H , h_C / H and h'_C / H as functions of the aspect ratio.

21

In the course of a spectral design and analysis procedure, the impulsive and convective ringwall moments are given by the following expressions:

$$M_I = m_I h_I S_a(T_I) \tag{33}$$

$$M_C = m_{Cn} h_C S_a(T_{Cn}) \tag{34}$$

Furthermore, simplified equations for the height h_I are stated in Section 6.1.2 of API 650 (American Petroleum Institute 2007) as alternative to Eq. (29):

when $D/H \geq 1.333$:

$$h_I = 0.375H \tag{35}$$

when $D/H < 1.333$:

$$h_I = \left[0.5 - 0.094 \frac{D}{H} \right] H \tag{36}$$

and

$$h_C = \left[1 - \frac{\cosh\left(\frac{3.67H}{D} \right) - 1}{\frac{3.67H}{D} \sinh\left(\frac{3.67H}{D} \right)} \right] H \tag{37}$$

Similarly, the impulsive and convective slab moments are given by the following expressions:

$$M_I' = m_I h_I' S_a(T_I) \tag{38}$$

$$M_C' = m_{Cn} h_C' S_a(T_{Cn}) \tag{39}$$

and an alternative equation for the height h_I' can be found in Section 6.1.2 of API 650 (American Petroleum Institute 2007):

when $D/H \geq 1.333$:

$$h_I' = 0.375 \left[1 + 1.333 \left(\frac{0.866 \frac{D}{H}}{\tanh\left(0.866 \frac{D}{H} \right)} - 1 \right) \right] H \tag{40}$$

22

when $D/H < 1.333$:

$$h_I' = \left[0.5 - 0.06 \frac{D}{H} \right] H \tag{41}$$

2.2.1.6 Combination of impulsive/convective action

In the course of a spectral analysis and design procedure, the impulsive and convective action should be combined in order to compute the total horizontal hydrodynamic force. In particular it is necessary to combine (a) the sloshing modes to obtain the resultant convective action and (b) the impulsive and convective actions for the total seismic force.

Both combinations should be conducted according to the SRSS rule, rather than the addition of the maximum convective and maximum impulsive forces as noted in a recent publication (Pappa et al. 2011).

More specifically, the total horizontal seismic force is:

$$Q_T = \sqrt{\left[m_I S_a(T_I) \right]^2 + \sum_{n=1}^{N_1} \left[m_{Cn} S_a(T_{Cn}) \right]^2} \tag{42}$$

where N_1 is the number of sloshing modes considered.

The above SRSS combination rule applies also to the total "ringwall" and "slab" moments:

$$M_T = \sqrt{\left[m_I h_I S_a(T_I) \right]^2 + \sum_{n=1}^{\infty} \left[m_{Cn} h_C S_a(T_{Cn}) \right]^2} \tag{43}$$

$$M_T' = \sqrt{\left[m_I h_I' S_a(T_I) \right]^2 + \sum_{n=1}^{\infty} \left[m_{Cn} h_C' S_a(T_{Cn}) \right]^2} \tag{44}$$

One should note that the impulsive force is significantly higher than the convective force. Therefore, in most of the cases, refinements on the value of the convective force and the combination of the corresponding modes are of little importance on the calculation of the total seismic force (Pappa et al. 2011).

23

2.2.1.7 Meridional Stresses

The meridional stress, σ_z, in mechanically anchored tanks is related to meridional membrane force, N, per unit circumferential length:

$$\sigma_z = N / t_i \tag{45}$$

where t_i is the thickness of the tank shell course under consideration and the axial force N per unit circumferential length is given by the following equations:

- On the compression side of the tank (Figure 8 - location 1):

$$N = -1.273 \frac{M_T}{D^2} - w_t \left(1 + cA_v\right) \tag{46}$$

- On the tension side of the tank (Figure 8 - location 2):

$$N = 1.273 \frac{M_T}{D^2} - w_t \left(1 - cA_v\right) \tag{47}$$

where A_v is the spectral acceleration coefficient for the vertical motion in $[\% g]$ ($A_v = 100 a_{gv} / g$), w_t is the load per unit circumferential length because of shell and roof weight acting at the base of shell [N/m] calculated by:

$$w_t = \frac{W_s}{\pi D} + w_{rs} \tag{48}$$

and c is a factor that reflects the contribution of the vertical component. In Eq. (48) W_s is the total weight of the tank shell and appurtenances and w_{rs} is the load acting on the shell roof. Note that the first term in Eq. (46) and (47) is directly obtained from simple mechanics of materials considering bending stresses of a beam of circular cross-section.
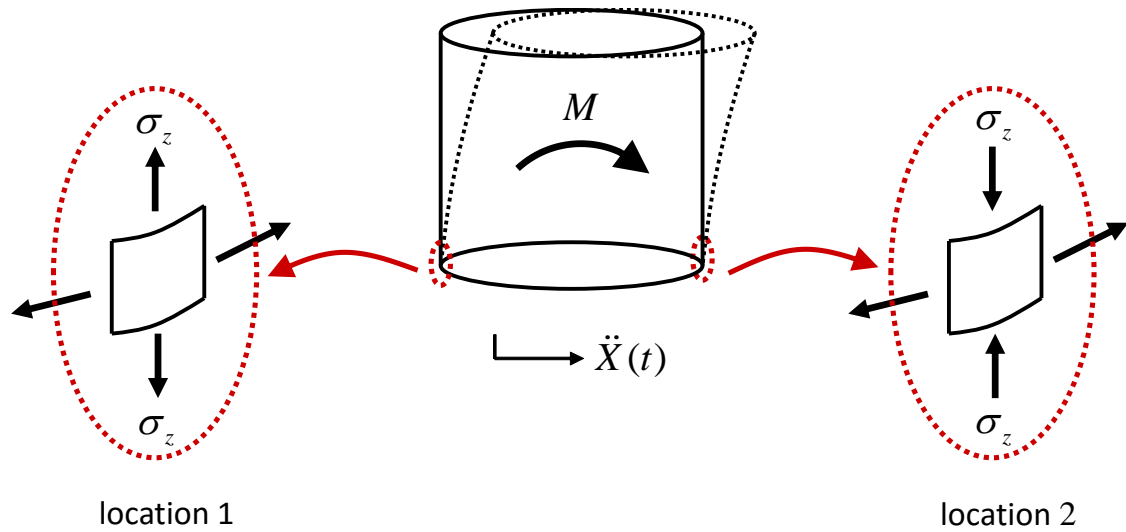
Figure 8: Meridional stresses σ_z on the tension side (location 1) and the compression side (location 2) of the tank under seismic loading.

In API 650 (2007) the value of c is taken equal to 0.40, whereas EN 1998-4 does not give an explicit expression for the effect of the vertical ground acceleration component on the meridional stresses.

2.2.1.8 Hoop Hydrodynamic Stresses

In the course of seismic loading, the hydrodynamic pressure loading on the tank wall, apart from the development of significant meridional stresses, results also in the development of additional stresses in the circumferential direction, denoted as σ_h, called hoop hydrodynamic stresses.

25
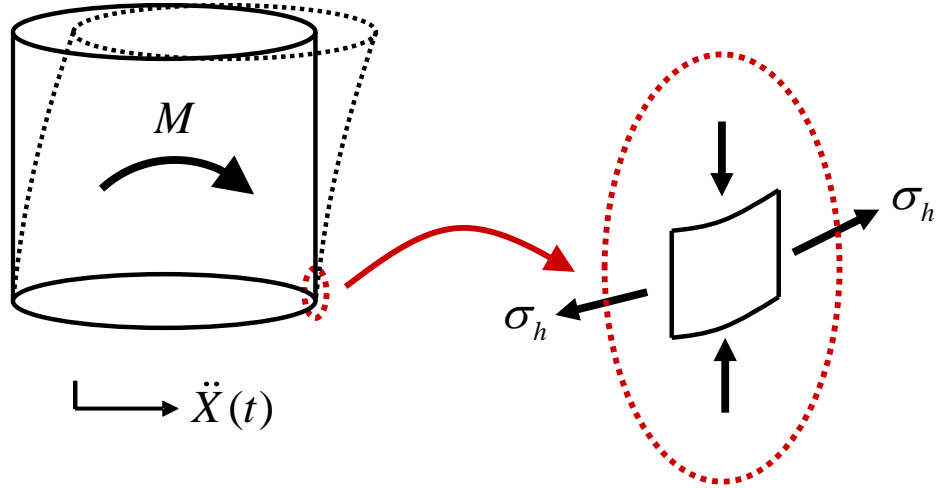
Figure 9: Hoop hydrodynamic stresses σ_h.

Explicit equations for computing hoop hydrodynamic stresses for the convective and impulsive component of liquid motion (denoted as σ_{hC} and σ_{hI} respectively), in terms of the z coordinate of the tank and the D/H (aspect) ratio of the tank, are reported by Wozniak and Mitchell (1978), also adopted by API 650 (American Petroleum Institute 2007), Appendix E, Section E.6.1.4, as follows:

For tanks with $D/H \geq 1.333$:

$$\sigma_{hI} = \frac{8.48 A_I GDH}{t_i}\left[\frac{z_1}{H} - 0.5\left(\frac{z_1}{H}\right)^2\right]\tanh\left(0.866\frac{D}{H}\right) \tag{49}$$

For tanks with $D/H < 1.33$ and $z_1 < 0.75D$:

$$\sigma_{hI} = \frac{5.22 A_I GD^2}{t_i}\left[\frac{z_1}{0.75D} - 0.5\left(\frac{z_1}{0.75D}\right)^2\right] \tag{50}$$

For tanks with $D/H < 1.33$ and $z_1 \geq 0.75D$:

$$\sigma_{hI} = \frac{2.6 A_I GD^2}{t_i} \tag{51}$$

For all proportions of D/H:

26

$$\sigma_{hC} = \frac{1.85 A_C G D^2 \cosh\left[\dfrac{3.68(H - z_1)}{D}\right]}{t_i \cosh\left[\dfrac{3.68H}{D}\right]} \tag{52}$$

In the above equations, stresses are expressed in [MPa], D is the nominal tank diameter in [m], H is the maximum design product level in [m], t_i is the thickness of the shell ring under consideration in [mm], $z_1 = H - z$ is the distance from the liquid surface in [m], G the specific gravity of tank contents and A_I and A_C are the impulsive and convective spectral acceleration coefficients in [$\%g$] defined as: $A_I = 100 S_a(T_I)/g$ and $A_C = 100 S_a(T_C)/g$.

The hoop stresses due to impulsive and convective motion should be combined, using the SRSS rule, and superimposed to the hydrostatic stress σ_{hs} to obtain the total hoop stress as follows:

$$\sigma_h = \sigma_{hs} + \sqrt{\sigma_{hI}^2 + \sigma_{hC}^2} \tag{53}$$

where σ_h is the total hoop stress in the shell, to be used for hoop strength design.

When vertical acceleration is taken into account, the above equation is written as follows:

$$\sigma_h = \sigma_{hs} + \sqrt{\sigma_{hI}^2 + \sigma_{hC}^2 + (A_v \sigma_{hs})^2} \tag{54}$$

where A_v is the spectral acceleration coefficient for the vertical motion in [$\%g$].

2.2.1.9 Sloshing wave height

From hydrodynamics, the elevation of the liquid free surface (sloshing wave height) is given by the following expression,

$$\eta(r, \theta, t) = \sum_{n=1,2,3...}^{\infty} \frac{2\lambda_n R J_1(\lambda_n \xi) \tanh(\lambda_n \gamma) \cos\theta \; a_{Cn}}{J_1(\lambda_n)(\lambda_n^2 - 1)} \tag{55}$$

In this expression, $\lambda_1 = 1.841$, $\lambda_2 = 5.331$, $\lambda_3 = 8.536$ are the roots of $J_1'(\lambda) = 0$, and a_{Cn} are the generalized coordinates of the convective motion with respect to the tank base given by Eq.

27

(14). Considering only 1 term ($n = 1$), $r = R$, one obtains Eq. (56) for the maximum elevation $\eta_{\max}$:

$$\eta_{\max} = 0.84 R S_a (T_C) / g \tag{56}$$

that can be used for design purposes.

2.2.2 Vertical seismic action

The hydrodynamic pressure on the walls of a rigid tank due to vertical ground acceleration $A_v(t)$ can be computed by the following equation:

$$p_v(\zeta, t) = \rho H (1 - \zeta) \ddot{X}_v(t) \tag{57}$$

where $\ddot{X}_v(t)$ is the vertical ground acceleration input.

The corresponding hydrodynamic pressure distribution is axisymmetric and does not produce a shear force or moment resultant at any horizontal level of the tank, or immediately above or below the base.

In the course of a spectral dynamic analysis, the peak vertical ground acceleration a_{gv} can be used for the calculation of p_v in the above equation replacing $\ddot{X}_v(t)$.

If one assumes that the tank is not moving rigidly with vertical acceleration $\ddot{X}_v(t)$, it may be reasonable to assume a contribution to the hydrodynamic pressure, $p_{vf}(\zeta, t)$, due to the deformability (radial "breathing") of the shell as suggested by Fischer and Seeber (1988). This additional term may be calculated as:

$$p_{vf}(\zeta, t) = 0.815 f(\gamma) \rho H \cos\left(\frac{\pi}{2} \zeta\right) a_{vf}(t) \tag{58}$$

where:

$$f(\gamma) = 1.078 + 0.274 \ln \gamma \qquad \text{for } 0.8 \leq \gamma < 4 \tag{59}$$

$$f(\gamma) = 1.0 \qquad\qquad\qquad \text{for } \gamma < 0.8 \tag{60}$$

28

and $a_{vf}(t)$ is the acceleration response of a simple oscillator having a frequency equal to the fundamental frequency ω_{vd} of the axisymmetric vibration of the tank containing with the liquid. This fundamental frequency ω_{vd} can be calculated by the corresponding fundamental period, estimated by the expression:

$$T_{vd} = 4R \left[\frac{\pi \rho H (1-v^2) I_0(\gamma_1)}{2EI_1(\gamma_1)t_{eq}} \right]^{1/2} \qquad \text{(for } \zeta = 1/3) \tag{61}$$

where $\gamma_1 = \dfrac{\pi}{2\gamma}$ and $I_0(\cdot)$, $I_1(\cdot)$ denote the modified Bessel function of order 0 and 1, respectively. In the course of a spectral dynamic analysis, the maximum value of $a_{vf}(t)$ is obtained from the vertical acceleration response spectrum for the appropriate values of period and damping. If soil flexibility is neglected, the applicable damping values are those of the material of the shell. Furthermore, the behavior factor value, q, adopted for the response due to the impulsive component of the pressure and the tank wall inertia may be used for the response to the vertical component of the seismic action. The maximum value of the pressure due to the combined effect of p_v and p_{vf} may be obtained by applying the SRSS combination rule to the individual maxima.

2.2.3 Rocking Seismic Action

2.2.3.1 General

In reality, apart from the horizontal movement of the tank base plate during horizontal ground shaking, there is also a rocking component of motion. Accordingly, a thorough examination and understanding of the rocking response of liquid storage tanks is fundamental to the evaluation of the response of flexibly supported tanks. Veletsos and Tang (1987) have made a comprehensive analysis of the dynamic response of liquid containing, upright cylindrical tanks to a rocking base motion of arbitrary temporal variation.

The model used is shown in Figure 10. It is an upright, circular cylindrical tank of radius R which is filled with liquid to a height H and is excited by an angular or rocking base motion

about a horizontal axis. The angular acceleration of the base or ground at any time, t, is denoted by $\ddot{\theta}_g(t)$, and the associated velocity and displacement are denoted by $\dot{\theta}_g(t)$ and $\theta_g(t)$, respectively.
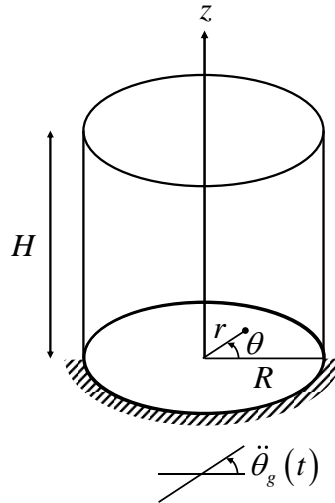
Figure 10: The model of Veletsos and Tang (1987).

The height of the tank to the original of the free surface of the fluid and its radius are denoted by H and R, respectively, ρ is the mass density of the fluid, while the non-dimensional coordinates $\xi = r / R$ and $\zeta = z / H$ in the radial direction and along the height of the tank respectively are usually considered.

The impulsive and convective rocking masses can be calculated as follows:

$$m_I^r = m_I \frac{h_I'}{H} \tag{62}$$

$$m_{Cn}^r = m_{Cn} \frac{h_{Cn}'}{H} \tag{63}$$

Analytical expressions are also available for the impulsive and convective frequencies accounting for tank flexibility. The natural circular frequencies of the impulsive and convective response are calculated by the expressions:

$$\omega_I^r = \frac{Y_I}{2\pi} \frac{1}{H} \sqrt{\frac{E}{\rho}} \tag{64}$$

30

$$\omega_{Cn}^r = \omega_{Cn} = \sqrt{g \frac{\lambda_n}{R} \tanh(\lambda_n \gamma)} \, , \; n = 1, 2, 3, \ldots \tag{65}$$

where ρ is the mass density of the fluid, E is Young's modulus, coefficient Y_I is given in Table 1 for specific values of the aspect ratio γ of the tank ($\gamma = H / R$) and λ_n are the roots of $J_1'(\cdot) = 0$ ($\lambda_1 = 1.841$, $\lambda_2 = 5.331$ and $\lambda_3 = 8.536$ for the first 3 sloshing modes).

The impulsive and convective damping coefficients can be taken equal to $\xi_I^r = 5\%$ and $\xi_C^r = 0.5\%$ for the impulsive and the convective motion respectively, as in lateral loading.

2.2.3.2 Impulsive motion and pressure

The impulsive motion can be expressed by the following linear oscillator equation:

$$\ddot{a}_I^r + 2\xi_I^r \omega_I^r \dot{a}_I^r + \omega_I^{r2} a_I^r = -H\ddot{\theta}_g \tag{66}$$

where $a_I^r(t)$ is the generalized coordinate representing the relative impulsive displacement of the tank with respect to its base, ξ_I^r the viscous damping ratio of the impulsive motion and ω_I^r the impulsive frequency defined in Eq. (64).

The spatial-time variation of the "*impulsive*" component of hydrodynamic pressure within the liquid domain is given by the following expression:

$$p_I(z, \theta, t) = C_I^r(r, z) H\ddot{\theta}_g(t) \rho R \cos\theta \tag{67}$$

where the spatial coefficient C_I^r is defined:

$$C_I^r(r, z) = 2\gamma \sum_{n=1}^{\infty} \frac{1}{v_n^2} \left[(-1)^{n+1} - \frac{2}{v_n} \right] \frac{I_1\left(\dfrac{v_n \xi}{\gamma}\right)}{I_1'\left(\dfrac{v_n}{\gamma}\right)} \cos(v_n \zeta) + \xi(1 - \zeta) \tag{68}$$

in which $v_n = \dfrac{2n+1}{2}\pi$, $\gamma = H / R$ is the aspect ratio of the tank, whereas $I_1(\cdot)$ and $I_1'(\cdot)$ denote the modified Bessel function of order 1 and its derivative respectively.

31

2.2.3.3 Convective motion and pressure

The convective motion can be expressed by the following linear oscillator equation:

$$\ddot{a}_{Cn}^{r} + 2\xi_{Cn}^{r}\omega_{Cn}^{r}\dot{a}_{Cn}^{r} + \omega_{Cn}^{r2}a_{Cn}^{r} = -H\ddot{\theta}_{g} \tag{69}$$

where $a_{Cn}^{r}(t)$ is the generalized coordinate representing the relative convective motion of the liquid associated with the n-th sloshing mode, ξ_{Cn}^{r} the viscous damping ratio of the convective motion for the n-th sloshing mode and ω_{I}^{r} the convective frequency.

The spatial distribution within the liquid domain and time variation of the "convective" component of hydrodynamic pressure associated with the n-th convective mode is given by the following expression:

$$p_{Cn} = \sum_{n=1}^{\infty}\psi_{n}^{r}(r,z)\ddot{u}_{Cn}^{r}(t)\rho R\cos\theta \tag{70}$$

where:

$$\psi_{n}^{r}(r,z) = \psi_{n}(r,z)\frac{h_{Cn}'}{H} \tag{71}$$

2.2.3.4 Hydrodynamic Base Shear

The impulsive base shear $Q_{I}^{r}(t)$ and convective base shear $Q_{Cn}^{r}(t)$ for the n-th mode at the base of the wall can be computed as follows:

$$Q_{I}^{r}(t) = m_{I}^{r}\left(\ddot{a}_{I}^{r} + H\ddot{\theta}_{g}(t)\right) \tag{72}$$

$$Q_{Cn}^{r}(t) = m_{Cn}^{r}\left(\ddot{a}_{Cn}^{r} + H\ddot{\theta}_{g}(t)\right) \tag{73}$$

32

2.2.3.5 Ringwall overturning moments

The impulsive and convective ringwall base moments are calculated through the following equations:

$$M_I^r(t) = i_o m_I^r H \left(\ddot{a}_I^r + H \ddot{\theta}_g(t) \right) \tag{74}$$

$$M_{Cn}^r(t) = m_{Cn}^r h_{Cn} \left(\ddot{a}_{Cn}^r + H \ddot{\theta}_g(t) \right) \tag{75}$$

where i_o is a dimensionless coefficient computed by the following expression:

$$i_o = \frac{1}{6} + 2\gamma \sum_{n=1}^{\infty} \frac{1}{v_n^3} \left[(-1)^{n+1} - \frac{2}{v_n} \right] \frac{I_2\left(\dfrac{v_n}{\gamma}\right)}{I_1'\left(\dfrac{v_n}{\gamma}\right)} \tag{76}$$

in which I_2 is the modified Bessel function of the second order.

2.2.3.6 Sloshing wave height

The maximum elevation of the liquid free surface (sloshing wave height) of the tank under rocking excitation is given by the following expression:

$$\eta_{\max} = 0.837 R \frac{h_{C1}'}{H} \frac{A_1^r}{g} \tag{77}$$

2.2.3.7 Effects of Tank Inertia

The instantaneous value of the base shear due to the tank inertia because of the shell and roof weight is given by:

$$Q_s^r(t) = \left(\frac{1}{2} m_{SH} + m_R \right) H_T \ddot{\theta}_g(t) \tag{78}$$

and the corresponding bending moment is given by:

33

$$M_s^r(t) = \left(\frac{1}{3}m_{SH} + m_R\right)H_T^2\ddot{\theta}_g(t) \tag{79}$$

in which m_{SH} and m_R are the total masses of the tank wall and roof, respectively, and H_T is the total height of the tank.

2.3   Failure modes of liquid storage tanks

Liquid storage tanks, subjected to strong seismic loading, may exhibit the one or more of the following failure modes, which are analyzed in more detail in the following paragraphs:

- Elephant's foot buckling

- Roof damage

- Failure of base plate

- Anchor bolt failure

- Nozzle (attached piping) failure

2.3.1   Elephant's foot buckling

Under earthquake loading, overturning is resisted by axial compressive stresses in the wall. The governing failure mode is usually buckling under axial compression in the presence of internal pressure. The internal pressure exerted by the stored liquid can significantly enhance the buckling strength, but high internal pressures lead to severe local bending near the base. Local yielding then precipitates an elastic-plastic buckling failure. This failure mode is commonly known as "elephant's foot buckling" and governs the design of many bin, silo and tank structures. It usually occurs in tanks with low height-to-radius (aspect) ratio (H/R). Buckling of the lower courses has occasionally resulted in the loss of tank contents due to weld or piping fracture and, in some cases, total collapse of the tank. Elephant's foot is considered as the major source of liquid storage tank failure under seismic action (O'Rourke and So 2000).

34

Figure 11: Elephant's foot buckling caused by strong earthquake action.

The most interesting issue refers to post-buckling response, meaning additional strength of the tank shell after the formation of elephant foot. Post-buckling has been studied by Peek and El-Bkaily (1991). For this purpose they used a 100-ft diameter and 40-ft high tank. Their results show that the ultimate seismic overturning moment that can be withstood by the tank is 31 percent higher than the overturning moment at which elephant's foot bulging begins. The reason for this is redistribution of vertical compressive stresses in the tank wall: initially these vertical compressive stresses are concentrated over a small contact length. However, as the elephant's foot bulge develops, the size of the contact length increases, resulting in a more favorable distribution of stresses.

2.3.2 Roof Damage (sloshing buckling)

Apart from elephant's foot buckling at the tank bottom, previous experience from real earthquakes has indicated that fixed roof liquid storage tanks may exhibit roof damage due to excessive sloshing. This is called "sloshing buckling" (Figure 12).

Figure 12: Tank roof damage due to sloshing; Kocaeli, Turkey earthquake 1999.

35

2.3.3 Failure of base plate

This mode may occur in unanchored (self-anchored) tanks, which exhibit base uplifting (Peek 1988, Natsiavas and Babcock 1988, Malhotra and Veletsos 1994c, Vathi and Karamanos 2013, 2014a, 2014b). Due to uplifting, significant inelastic deformation occurs at the shell-plate welded connection, leading to either rupture because of excessive tensile strain or low-cycle fatigue damage due to repeated loading (Prinz and Nussbaumer 2012, Vathi and Karamanos 2015), as shown in Figure 13.
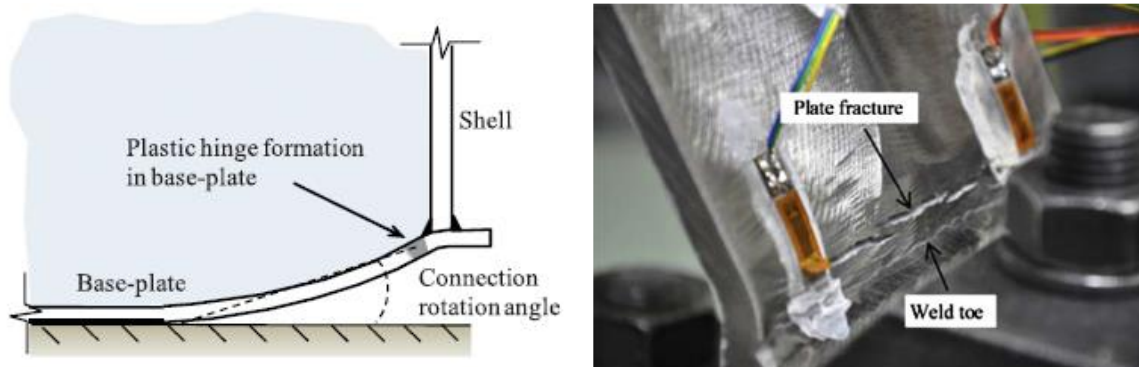
Figure 13: Schematic representation of fatigue failure of the tank-shell connection; low-cycle fatigue test verification (Prinz and Nussbaumer 2012).

2.3.4 Anchor bolt failure

In case self-anchoring is not adequate, tanks are anchored with bolts. However, the anchor system may fail because of excessive tension, as shown in Figure 14, which may occur in several forms:

• anchor bolt yielding

• anchor bolt fracture

• "prying" or shear failure of welded plates

• concrete punching shear

• anchor bolt "pull-out"

It is customary to overdesign the anchor system in terms of the last 2 modes (punching shear and pull-out), so that the failure modes of bolt or steel plate are critical.

36

Figure 14: Anchor bolt failure in seismically-loaded tanks.

2.3.5 Nozzle (attached piping) failure

Nozzles are locations that may trigger a catastrophic failure of the liquid storage tank. The nozzle acts as an end-support for the attached pipe, and the corresponding seismic reaction forces and moments may cause significant local tank shell distortion, leading to fracture or low-cycle fatigue damage.

Figure 15: Nozzle (attached piping) failure due to elephant's foot buckling.

2.3.6 Other failure modes

The above failure modes are not the only ones that may occur in a liquid storage tank under seismic loading. In several instances, buckling at the top course of the tank may also occur due to "negative pressure" because of liquid oscillations; the thin-walled shell is locally subjected to external pressure and may buckle. It is important to note that, at the top of the tank, hydrostatic pressure is small, so that this overtaking is quite likely to occur, depending on the magnitude of the seismic action. The first attempt to explain this phenomenon was reported in

37

the paper by Natsiavas and Babcock (1987). Moreover, top shell buckling may be "assisted" by the impact of sloshing waves on the roof, as described before.

Furthermore, tanks with floating roofs and inflammable containment may exhibit catastrophic failure because of seal destruction and the friction of roof edge with the tank shell (Figure 16), which may trigger fire (De Angelis et al. 2010).

Figure 16: Failure of floating roof.

In the present dissertation, special emphasis is given on elephant's foot buckling of liquid storage tanks and the uplifting phenomenon of the base plate during strong seismic motion.

38

3. Analysis of Local Buckling in Liquid Steel Tanks under Lateral Loading

Upright cylindrical steel storage tanks, subjected to lateral loading, may fail in the form of local buckling, usually near their bottom, because of the simultaneous action of excessive axial compression in the presence of internal pressure, a failure mode known as "elephant's foot buckling". However, buckling of the tank may occur in another location, depending on the type of initial imperfections. The present chapter is aimed at examining this failure mode rigorously, considering material and geometric nonlinearities, accounting for initial imperfections. In addition, the response and buckling of liquid storage tanks with wrinkling imperfections from real imperfection measurements is studied. Finally, the strengthening of liquid storage tanks tanks with CFRP wrapping against elephant's foot buckling failure is examined.

3.1 Introduction

Thin-walled bottom-supported steel shells of upright cylindrical shape are subject to internal pressure from stored materials. When subjected to severe lateral loading (e.g. seismic loading), overturning is resisted by axial compressive stresses in the wall. Under this combined loading condition, the shell may exhibit local buckling in the form of a localized outward bulge near its bottom (Figure 17), which is associated with loss of lateral resistance and shell failure. The biaxial stress state at the critical area of buckling formation (axial compression and circumferential tension) is the key issue for understanding the buckling mechanism. In particular, the presence of internal pressure has a significant effect on the buckling strength. Low values of pressure may have a beneficial effect on shell capacity, whereas high pressure values may result in early local yielding near the shell bottom, and precipitate the formation of an elastic-plastic buckling failure (Malhotra 2000). This buckling failure mode is commonly known as "elephant's foot buckling" and has been observed in quite a few post-earthquake inspections of liquid storage tanks. It has been also recognized as a major design issue for storage shells, such as bins, silos and tanks.

39

Figure 17: Elephant's foot buckling in liquid storage tanks (a) existing tank (Malhotra 2000), (b) buckling shape from present finite element analysis.

Despite several early works on buckling of internally pressurized cylinders (Harris et al. 1957, Weingarten et al. 1965, Hutchinson 1965), "elephant's foot buckling" has received relatively little attention. The first systematic study on this subject has been reported in the paper by Rotter (1990), using finite element axisymmetric models. This work resulted in the proposal of a semi-empirical equation, which has been adopted by several design standards and recommendations such as the New Zealand Seismic Tank Design Recommendations and Earthquake Standard NZS6254. Furthermore, this equation has been the basis for the recent European standard EN 1993-1-6 for shell design, and the Seismic Eurocode for tanks EN 1998-4. A recent experimental study on buckling of internally-pressurized cylinders has been reported in the paper by Mathon and Limam (2006), whereas for a thorough presentation of this subject, in relation with the provisions of EN 1993-1-6, the reader is referred to the paper by Rotter (2006). In a more recent paper, Rotter (2009) presented some of the most critical aspects of extreme loading on silos and tanks, together with their structural behaviour and failure modes, pointing out the need for additional research on the structural performance of those structures.

The present chapter focuses on the analysis and design of liquid storage tanks under lateral loading, motivated by their damage in severe seismic events. A typical steel shell is considered with height-to-diameter ratio equal to about 1. The shell is considered fixed at its base against displacement and rotation, and subjected to lateral load at a certain height. More specifically, the loading set-up employed is inspired from the one in the experiments of Mathon

40

and Limam (2006). Different levels of internal pressure are considered, particularly hydrostatic pressure and constant pressure at levels up to 80% of nominal yield pressure.

3.2 Description of Tank Case Study

A fixed bottom cylindrical shell, with diameter, D, equal to 6.3 meters, and constant thickness equal to 6 mm is considered and simulated numerically. The shell height, H_T, is 7.4 meters, with liquid fill height, H, equal to 6.9 meters. The contained liquid is water ($\rho = 1000$ kg/m^3) and the shell material is mild steel with yield stress 235 MPa. For the purposes of the present study the tank is simulated as anchored, so the tank shell is simulated completely fixed at its bottom (clamped at its base). The tank geometry is depicted in Figure 18.
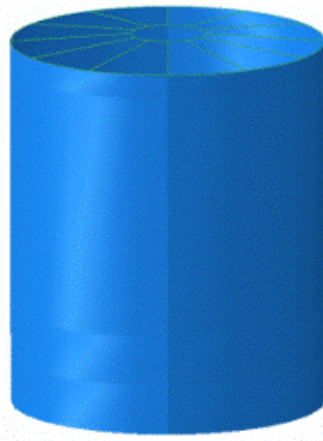
Figure 18: Tank used for the parametric study.

The contained liquid is water ($\rho = 1000$ kg/m^3) and the material of the tank shell, and the roof is structural steel S235 (equivalent to A36 steel) with yield stress $\sigma_y = 235$ MPa. For the purposes of the present study, the tank is simulated as anchored.

3.3 Model Description

The model is developed in ABAQUS/Standard and employs shell elements for the fixed-bottom cylindrical shell. The shell is discretized with four-node reduced-integration shell

41

finite elements, which account for geometric and material nonlinearities. The element size at the critical location in the longitudinal direction of the cylinder is chosen 0.8% of the tank radius (Figure 19), to simulate accurately the elephant's foot buckling formation. From shell buckling theory, the buckling wavelength has a length equal to $\dfrac{2\pi}{\sqrt[4]{12\left(1-v^2\right)}}\sqrt{Rt} \cong 475.2$ mm, which corresponds to 18-19 elements.

The model is inspired by the experimental set-up described in the paper by Mathon and Limam (2006), shown in Figure 20(a) and Figure 20(b); the cylinder is bottom-fixed, capped at its top, using a "kinematic coupling" constraint at the top nodes considering a central "reference point". Lateral loading is applied at the top of a fictitious rigid member, connected with the "reference point" of the top cross-section [Figure 20(c)]. Inelastic deformation of the steel material is taken into account through a J_2 flow plasticity constitutive model.

The analysis is conducted in two steps. In the first step, internal pressure is raised up to a certain prescribed level [Figure 20(a) and Figure 20(b)]. Subsequently, keeping the pressure constant, the lateral load is gradually increased until shell buckling occurs. The latter step is performed through a Riks continuation algorithm, to trace all snap-back and snap-through features of the equilibrium path.

(a)   (b)
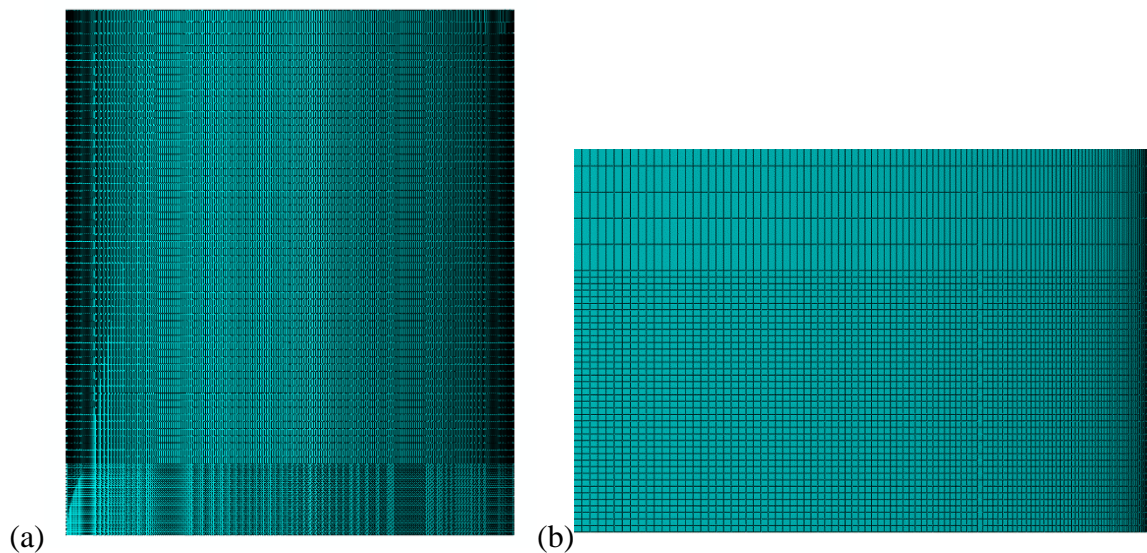
Figure 19: Finite element modelling of the tank under consideration; (a) entire tank, (b) critical location of the cylinder.

42
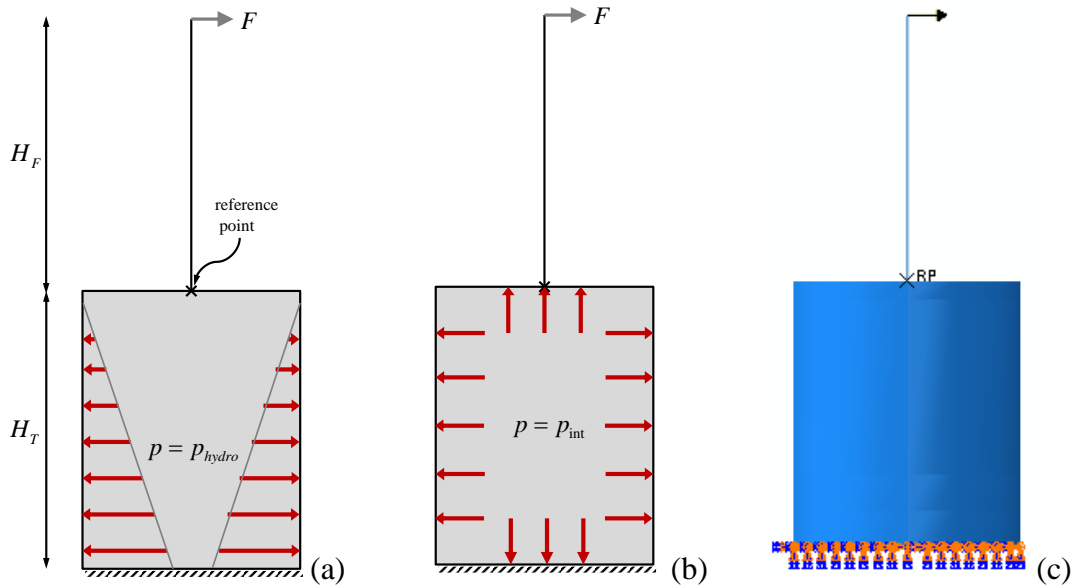
Figure 20: Schematic representation of shell tank loading under lateral load; (a) with hydrostatic pressure, (b) with internal constant pressure, (c) finite element model in ABAQUS used for both cases of internal pressure.

3.4 Types of imperfection used in the analysis

Two types of imperfections are considered for the study of the sensitivity of the liquid storage tank: (a) imperfections from real measurements in an existing tank, which are of random shape and (b) axisymmetric imperfections in the form of an initial bulge at the bottom of the cylinder around the circumference of the cylinder. For the sake of simplicity, these imperfections are referred to as "Type SI1" and "Type SI2" imperfections and are described in more detail in the following.

Type SI1 – asymmetric   Type SI2 - axisymmetric
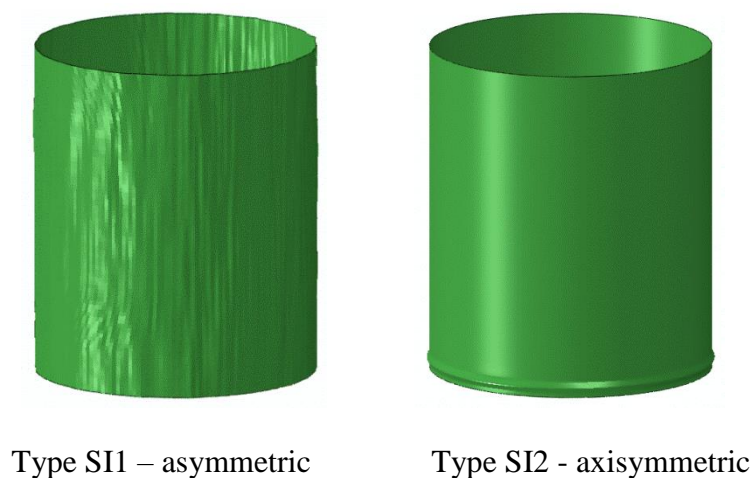
Figure 21: Type SI1 and Type SI2 imperfections.

43

(a) <u>Type SI1 imperfections from real measurements</u>

Recently, in order to assess the structural integrity of a specific liquid storage tank located in Greece, a study on the local distortions of this tank has been made. The tank can be seen in Figure 22. It is a 27.8-meter-diameter tank with a total height of 16.5 meters. The filling height of the tank H is equal to 15.7, and its thickness varies from 6.4 mm at its top course to 17.7 mm at its bottom course. It has a 6-mm-thick bottom plate with an 8-mm-thick annular plate. This tank is described in more detail in paragraph 4.3 as it is used in the next paragraphs for the numerical analyses and is named as "Tank I".

The tank surface was scanned with ultrasonic and laser scanners to determine the thickness variation along the tank height and circumference and to determine the shell distortions. From digital mapping of the tank and appropriate post-processing of the scanned data a uniform grid of points/nodes was obtained with a grid of 10 cm x 10 cm, which corresponds to 137104 points. This grid represents adequately the geometry of the imperfect cylinder (Figure 23).

Subsequently, this information has been processed by our research partners in the National Technical University of Athens using the spectral representation method for the simulation of non-homogeneous random fields to generate random imperfect shapes of this tank (Papadopoulos et al. 2015). The random imperfect shapes of this tank are adjusted to the tank under consideration.

Figure 22: The tank used for the measurements.

44
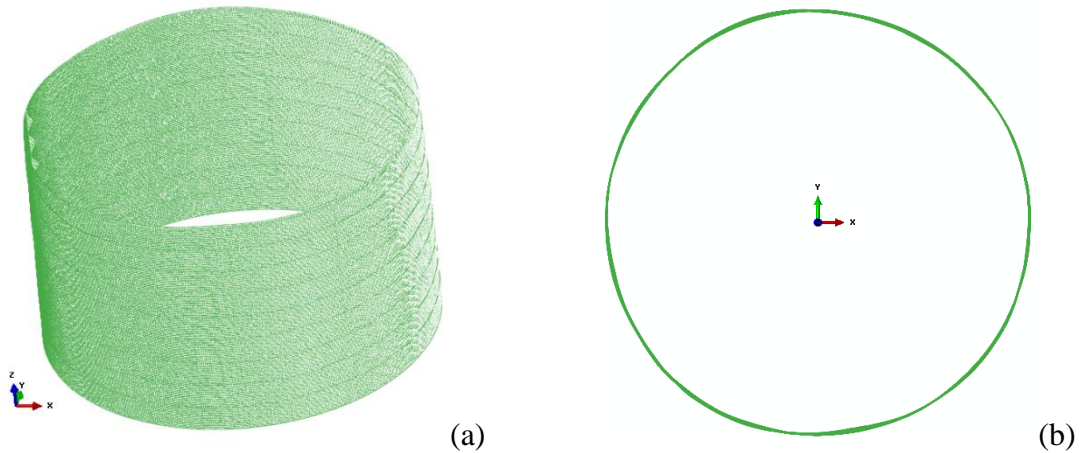
Figure 23: Cloud of points (nodes) of the tank that were extracted from the measurements (a) side view of the tank, (b) top view of the tank.

(b) <u>Type SI2 imperfection: axisymmetric imperfections</u>

Initial imperfections are also considered in the form of an initial "bulge" for the analysis of imperfect shells. These initial imperfect shapes are obtained from the post-buckling shape of the perfect cylinder, they have the shape of elephant's foot buckle and they are scaled appropriately to obtain the desired imperfection amplitude.

3.5 Numerical results

Results are presented for the tank under consideration. The center of the top section of the shell is connected to a fictitious "stiff rod" where lateral loading is applied. Three different rod lengths are chosen; $H_F = 0$, $H_F = H_T$ and $H_F = 5H_T$. For convenience, we define a new non-dimensional parameter $e = H_F / H_T$ such that the three rod lengths are represented by $e = 0$, $e = 1$ and $e = 5$. This parameter expresses the gradient of the bending moment along the tank; as it becomes larger, the moment diagram becomes more uniform.

In the following, the maximum imperfection amplitude w_0 is expressed in terms of shell thickness t. In the case of Type SI1 imperfection, w_0 is the maximum imperfection amplitude all over the shell surface, and may appear at any point of the tank, whereas in the case of Type

SI2 imperfection, w_0 appears at the lower part of the tank at a particular height above the tank bottom.

3.5.1 Type SI1 imperfection

Results are presented for the tank under consideration for 10 random imperfection shapes (namely imp1, imp2, etc.), shown in Figure 24 for $w_0/t = 10$. For this type of imperfection, the internal pressure is considered as hydrostatic pressure (Figure 20a), with a maximum value of 0.0677 MPa at the bottom of the tank (filling height equal to 6.9 m).

The sensitivity of the maximum moment (calculated at the tank bottom) sustained by the cylinder in terms of the imperfection amplitude for each of the 10 imperfection shapes is shown from Figure 25 to Figure 34. Apparently, the tank is sensitive to this type of imperfection, but the sensitivity is rather moderate. Furthermore the height of lateral load may not be a critical factor for the value of maximum moment. This can be also concluded from the results in Figure 35, Figure 36 and Figure 37 where the maximum moment in terms of the imperfection amplitude is shown for each value of the dimensionless parameter ℓ. The lower bound curve of the results shows the small sensitivity of the tank to this type of imperfection. The consecutive stages of buckling of the tank under consideration for imperfection shape #1, $e = 5$ and $w_0/t = 0.63$, are shown in Figure 38.

46
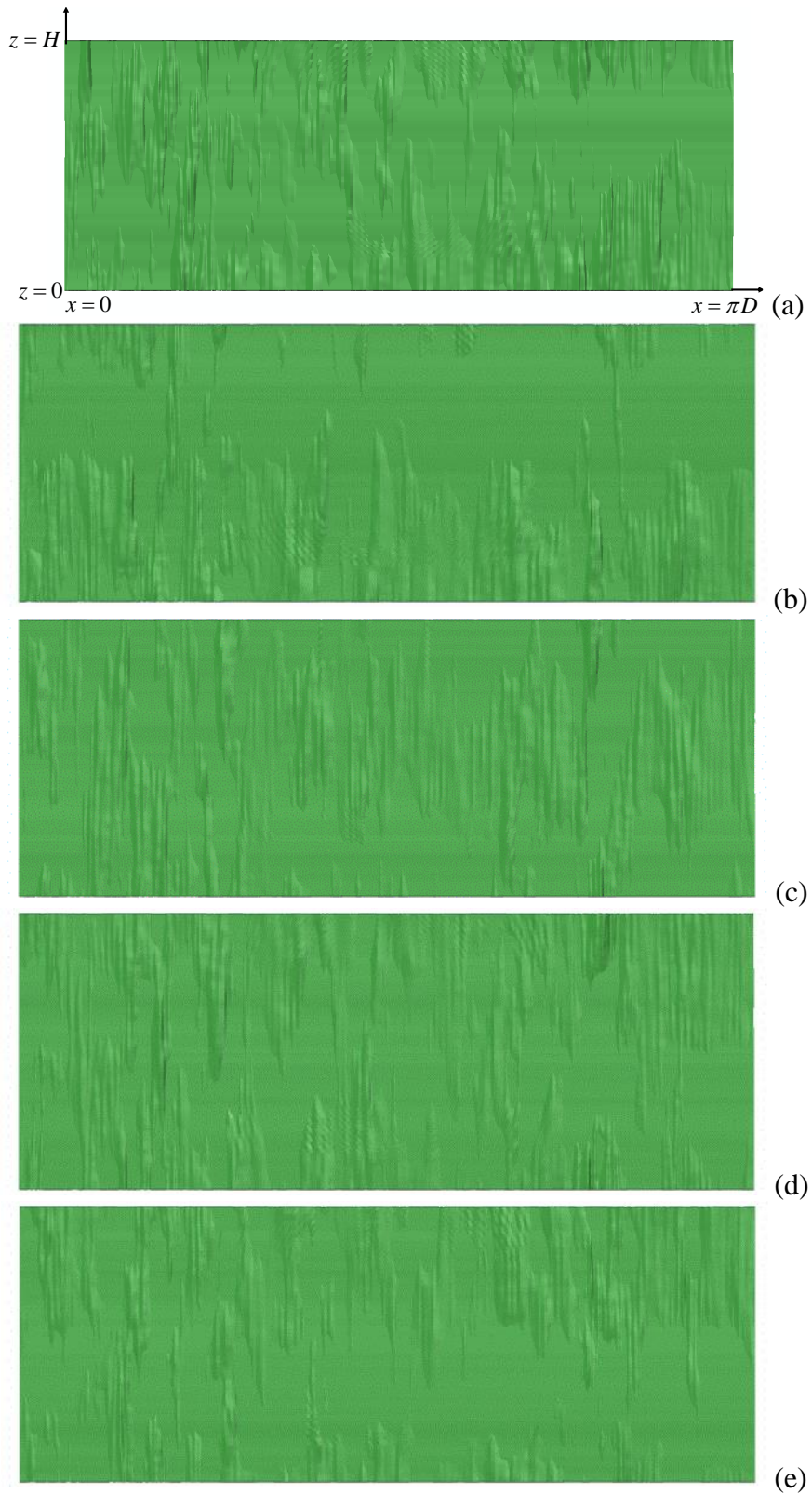
Figure 24: The 10 imperfection shapes used in the analyses, for $w_0/t = 10$; (a) imp1, (b) imp2, (c) imp3, (d) imp4, (e) imp5, (f) imp6, (g) imp7, (h) imp8, (i) imp9, (j) imp10.

47

(f)

(g)

(h)

(i)

(j)
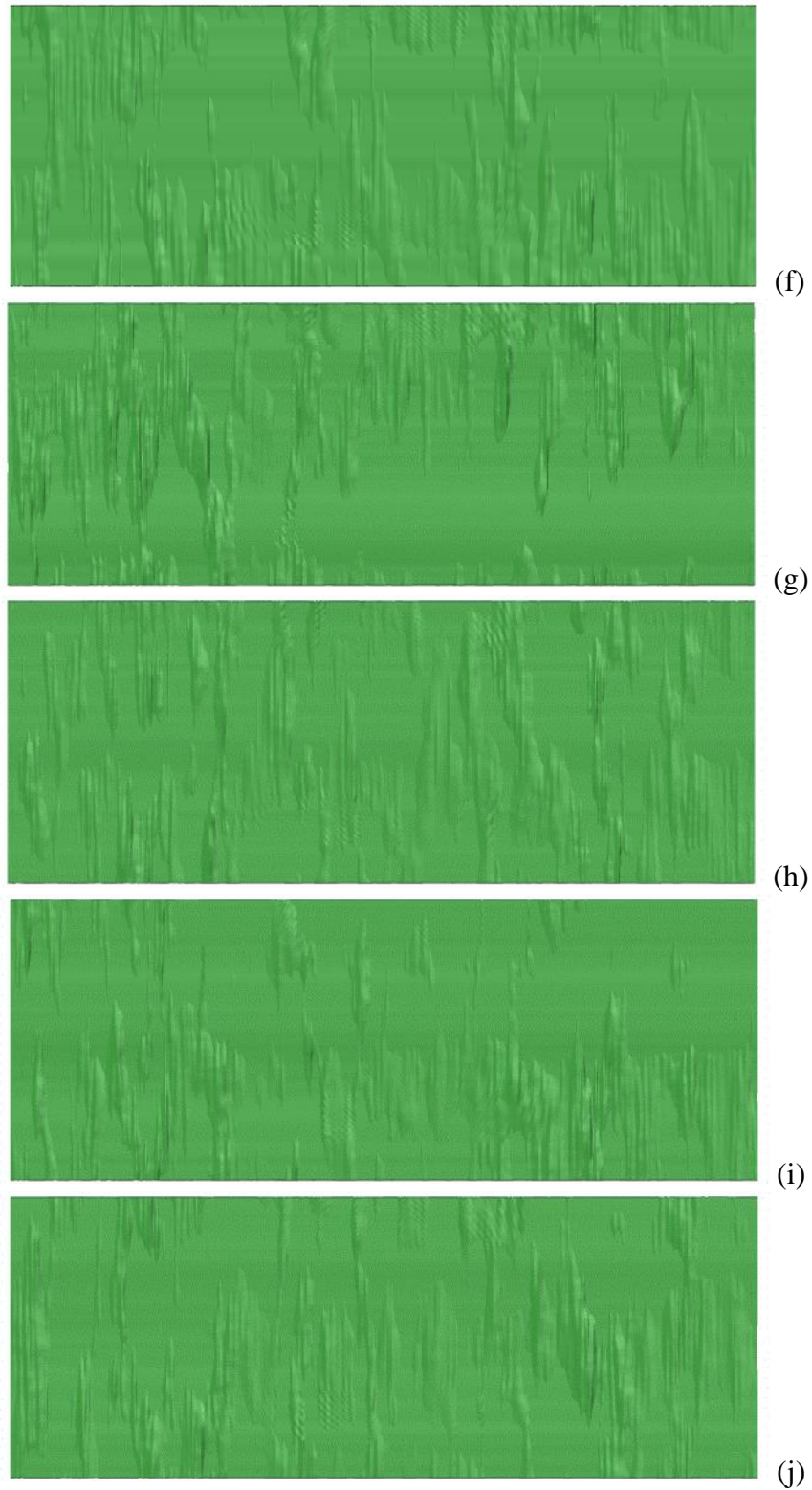
Figure 24 (cont'd): The 10 imperfection shapes used in the analyses, for $w_0 / t = 10$; (a) imp1, (b) imp2, (c) imp3, (d) imp4, (e) imp5, (f) imp6, (g) imp7, (h) imp8, (i) imp9, (j) imp10.

48
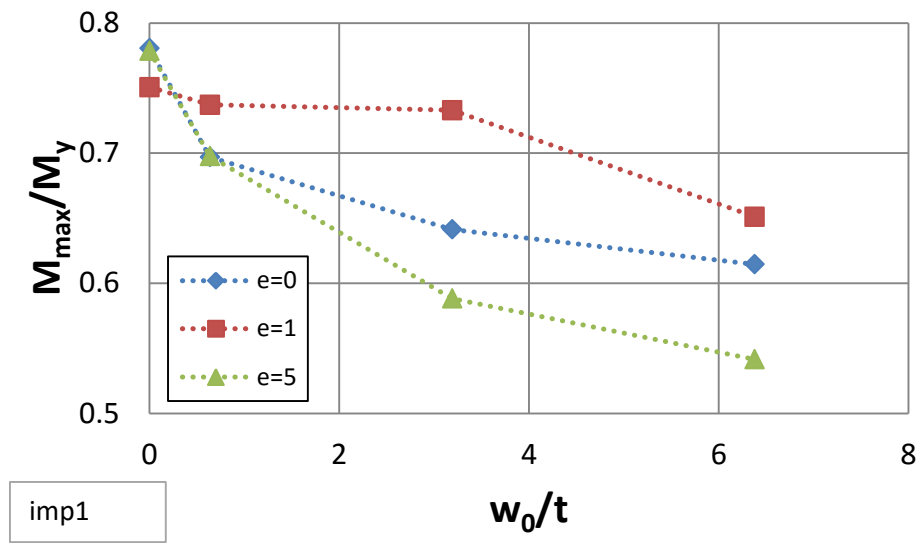
Figure 25: Normalized maximum moment-imperfection curves for the case of hydrostatic pressure for different lengths of the rigid rod for imperfection shape #1.
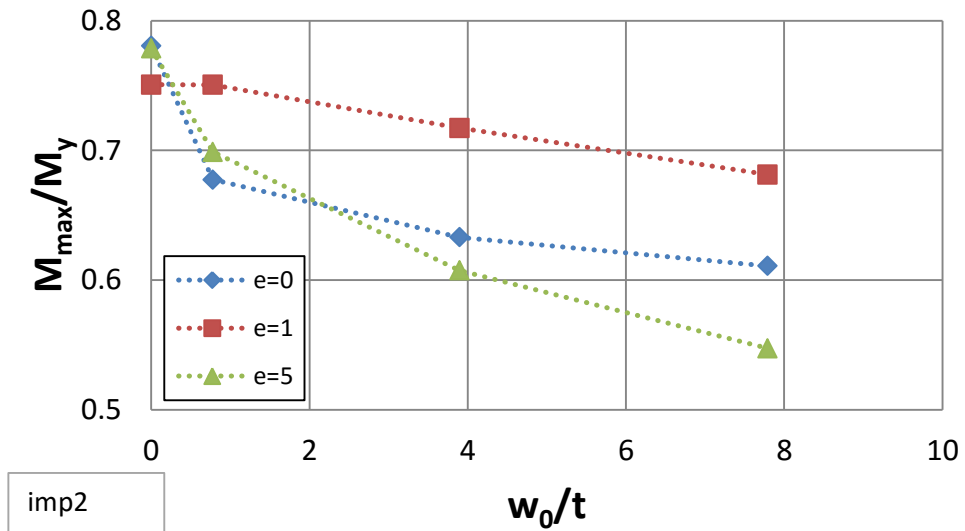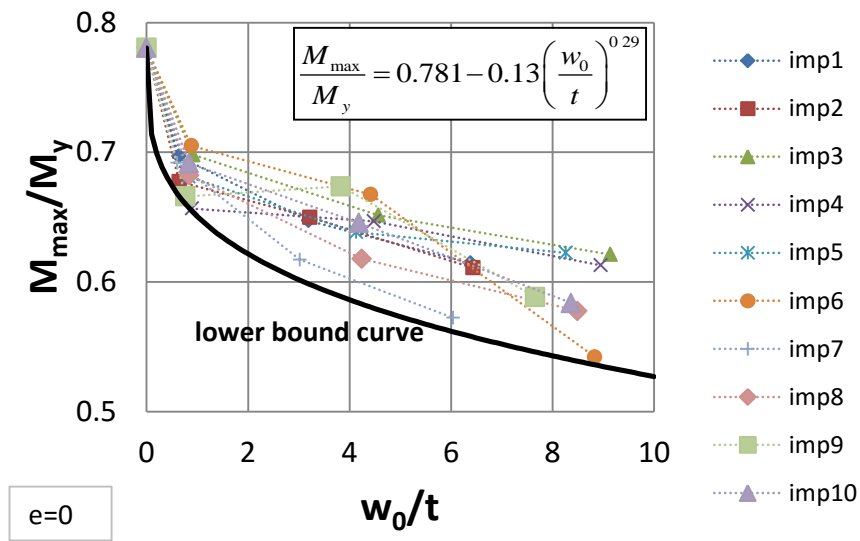

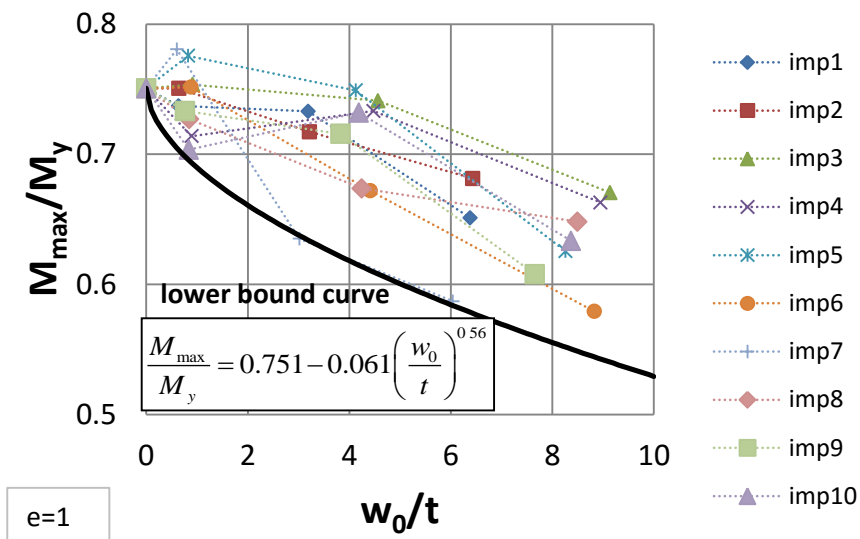**Figure 26:** Normalized maximum moment-imperfection curves for the case of hydrostatic pressure for different lengths of the rigid rod for imperfection shape #2.

49
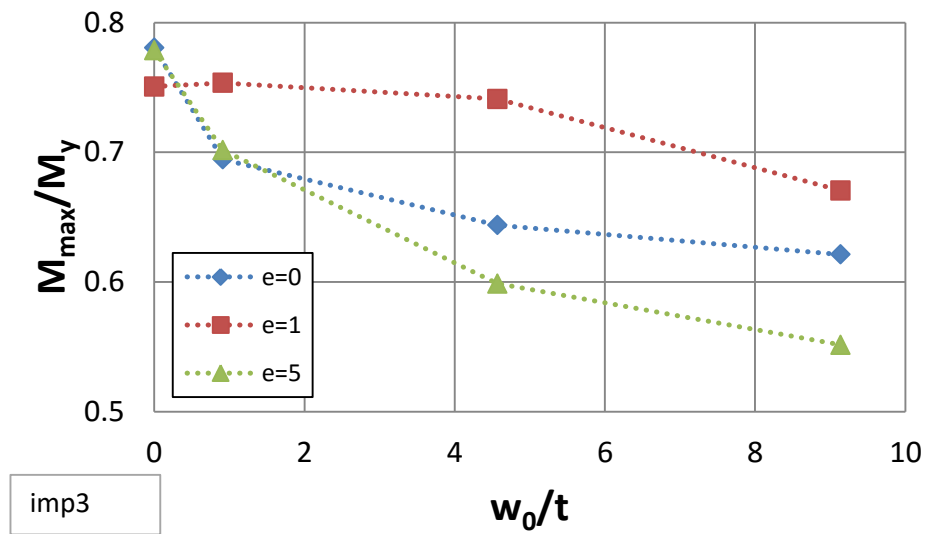
Figure 27: Normalized maximum moment-imperfection curves for the case of hydrostatic pressure for different lengths of the rigid rod for imperfection shape #3.
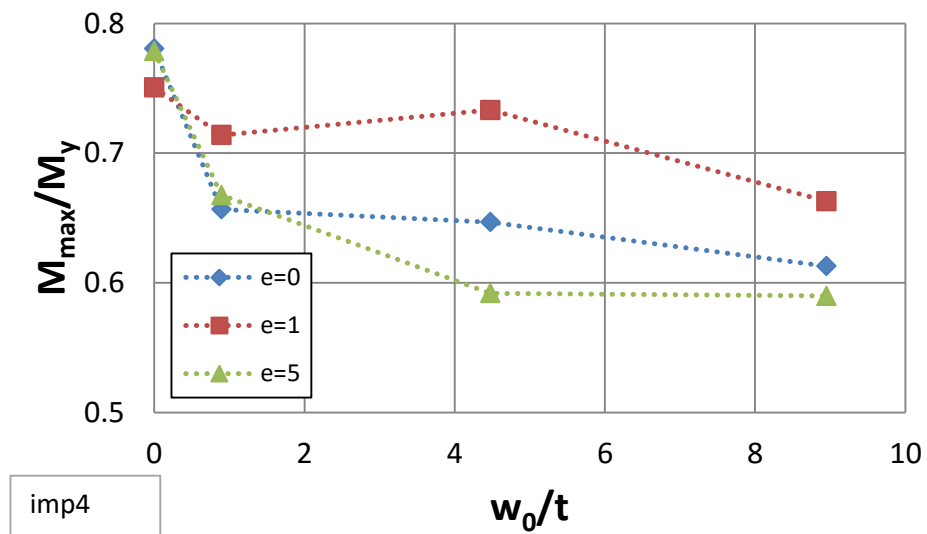
Figure 28: Normalized maximum moment-imperfection curves for the case of hydrostatic pressure for different lengths of the rigid rod for imperfection shape #4.

50
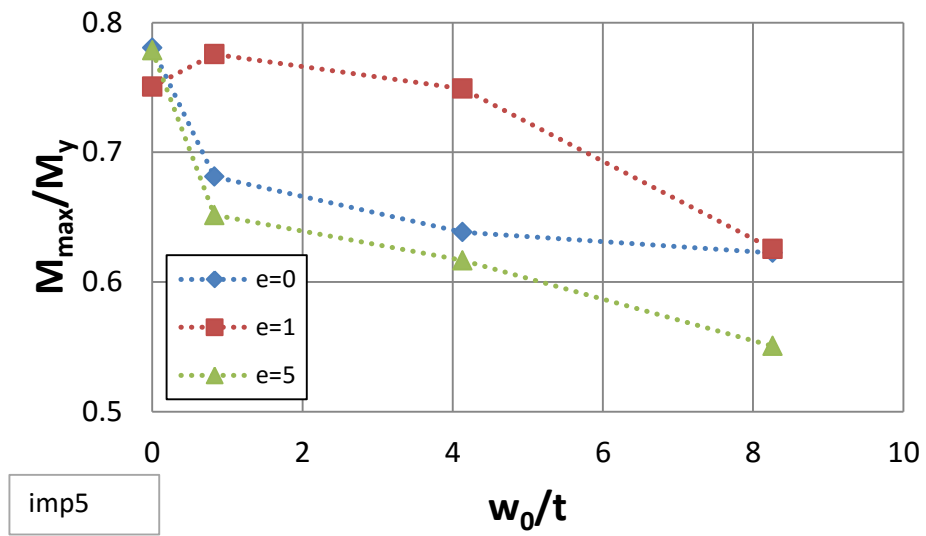
Figure 29: Normalized maximum moment-imperfection curves for the case of hydrostatic pressure for different lengths of the rigid rod for imperfection shape #5.
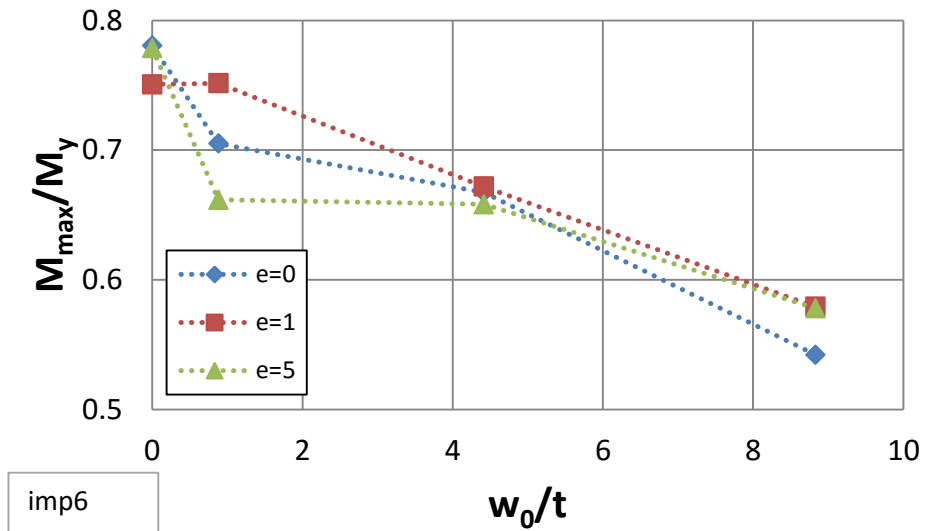
Figure 30: Normalized maximum moment-imperfection curves for the case of hydrostatic pressure for different lengths of the rigid rod for imperfection shape #6.
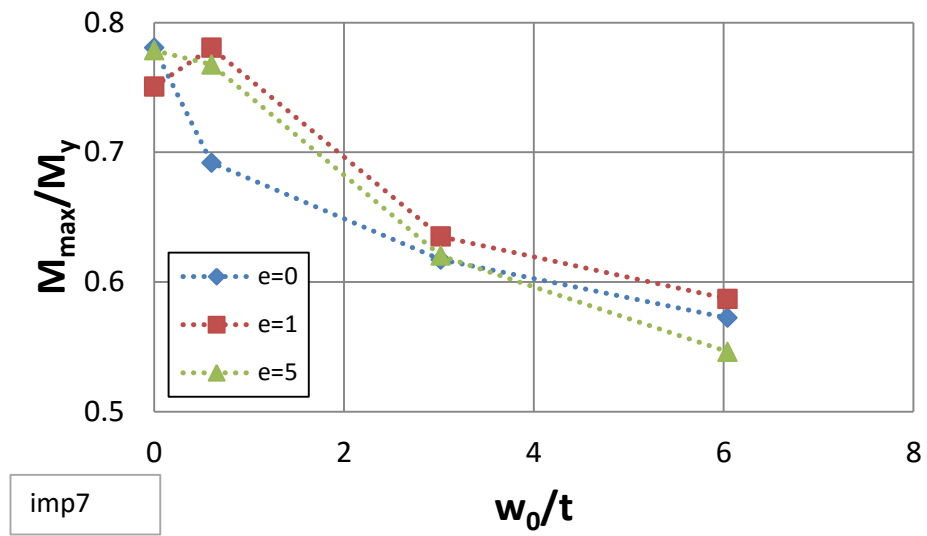
Figure 31: Normalized maximum moment-imperfection curves for the case of hydrostatic pressure for different lengths of the rigid rod for imperfection shape #7.
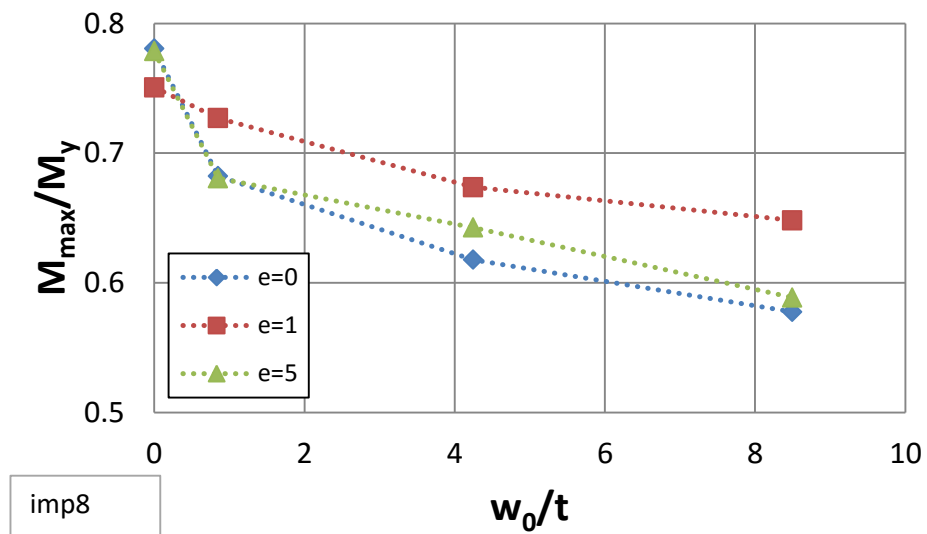
Figure 32: Normalized maximum moment-imperfection curves for the case of hydrostatic pressure for different lengths of the rigid rod for imperfection shape #8.

52
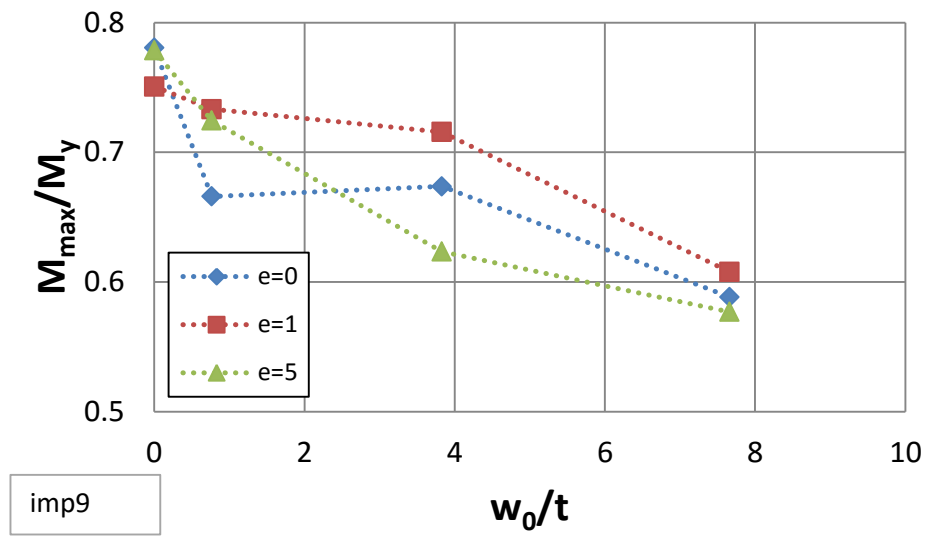
Figure 33: Normalized maximum moment-imperfection curves for the case of hydrostatic pressure for different lengths of the rigid rod for imperfection shape #9.
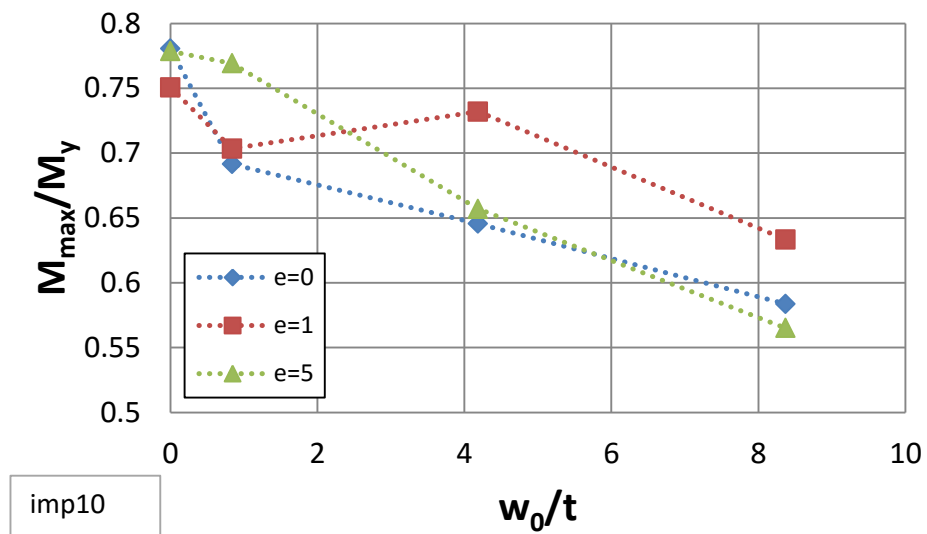
Figure 34: Normalized maximum moment-imperfection curves for the case of hydrostatic pressure for different lengths of the rigid rod for imperfection shape #10.

53

Figure 35: Normalized maximum moment-imperfection curves for the case of hydrostatic pressure for $e=0$.

Figure 36: Normalized maximum moment-imperfection curves for the case of hydrostatic pressure for $e=1$.

54

$$\frac{M_{max}}{M_y} = 0.779 - 0.14 \left(\frac{w_0}{t}\right)^{0.29}$$

e=5
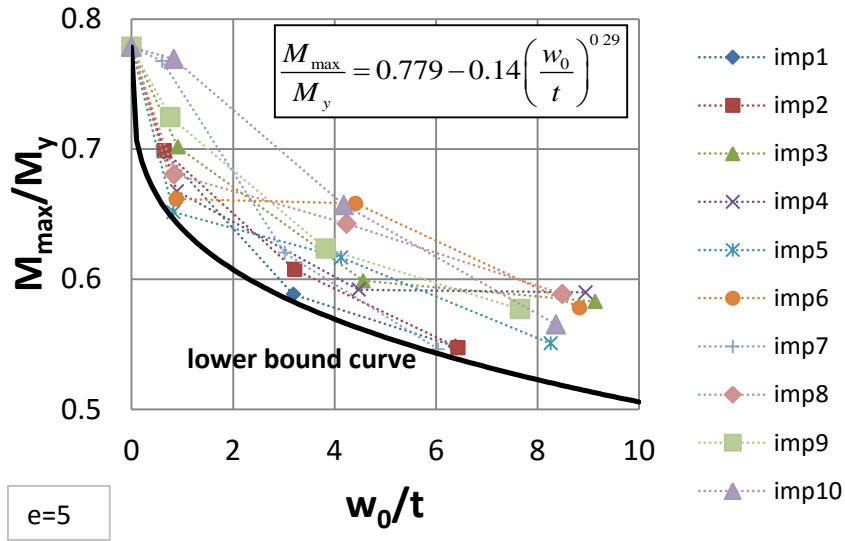
Figure 37: Normalized maximum moment-imperfection curves for the case of hydrostatic pressure for $e = 1$.
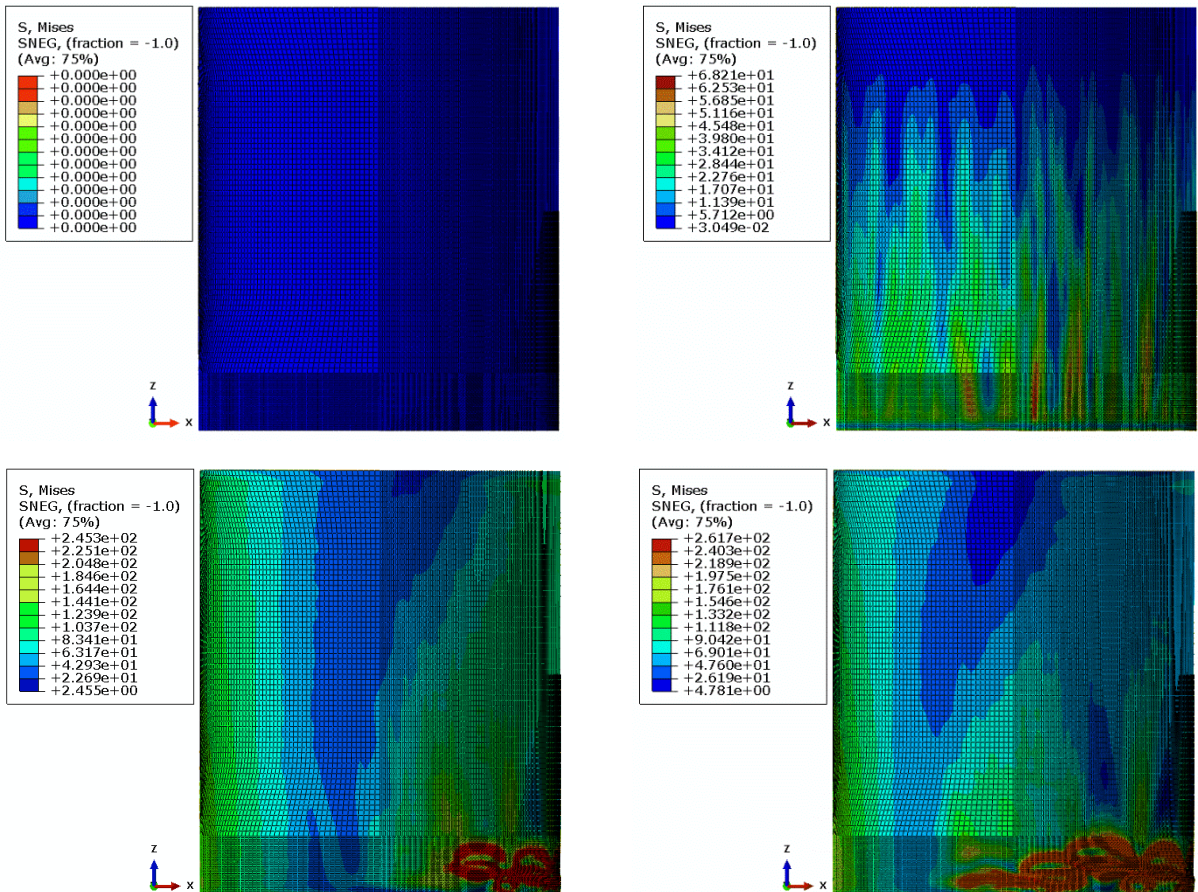
Figure 38: Consecutive stages of buckling of the tank under consideration for imperfection shape #1, $e = 5$ and $w_0 / t = 0.63$. The first stage corresponds to the undeformed state and the second stage to the end of the acting of the hydrostatic pressure.

55
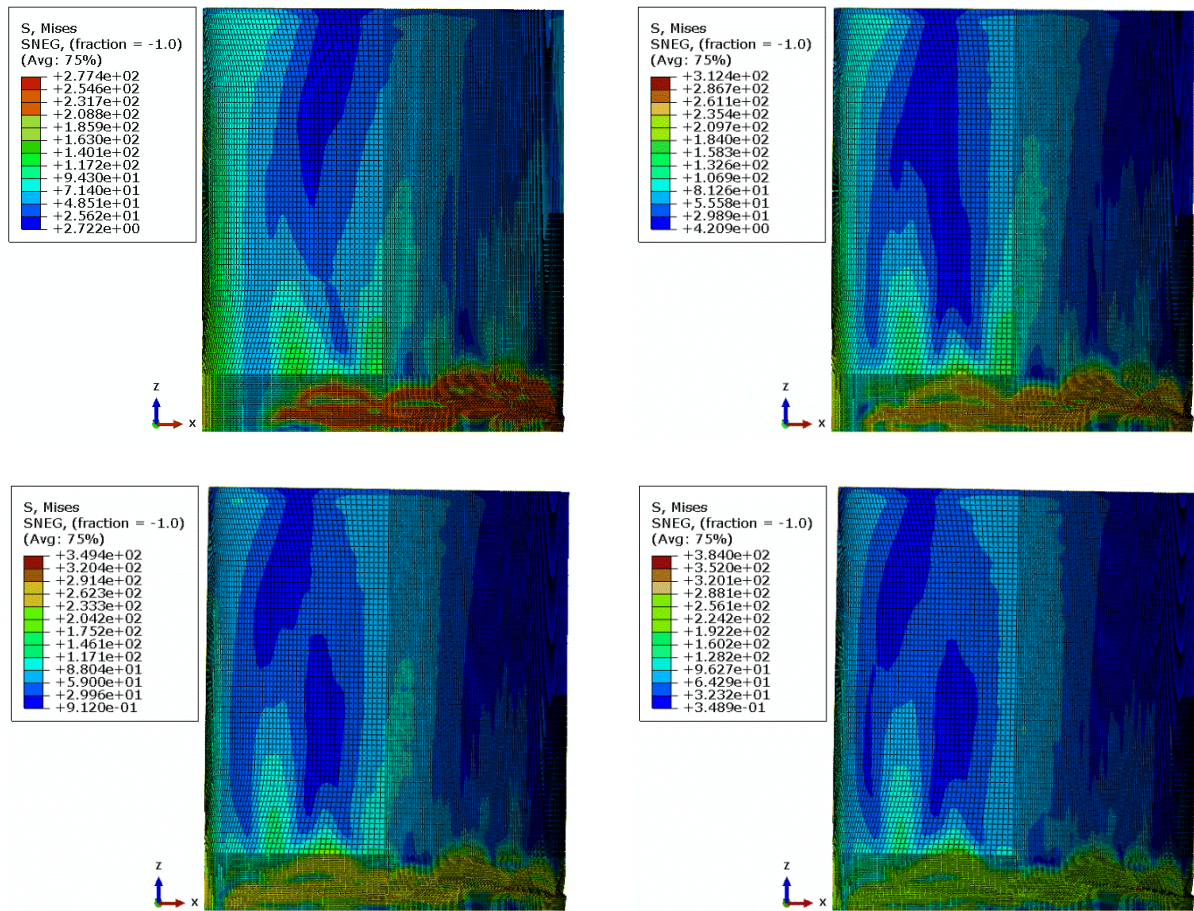
Figure 38 (cont'd): Consecutive stages of buckling of the tank under consideration for imperfection shape #1, $e=5$ and $w_0/t = 0.63$. The first stage corresponds to the undeformed state and the second stage to the end of the acting of the hydrostatic pressure.

3.5.2 Type SI2 imperfection

Results are presented for the tank under consideration with initial imperfections of type B, which has a shape similar to elephant's foot buckling. The finite element model is similar to the one used for type SI1 imperfection. However, in this case both hydrostatic pressure and constant internal pressure up to 80% of the nominal yield pressure are considered. In the latter case, the tank is closed on its top (capped) and pressure on the top section results in an upward capped force which is taken into account in the analysis.

The buckling shape is shown in Figure 39 and the consecutive stages of elephant's foot buckling gradual formation in the finite element model (for $e=5$ and $w_0/t = 0.45$) are depicted in Figure 40. The moment-displacement curves for the case of hydrostatic pressure are shown

56

in Figure 41 for different values of initial imperfection amplitude. The moment reported in those graphs corresponds to its value at the tank bottom, whereas the corresponding displacement is the horizontal displacement of the "reference point" at the top of the tank. The sensitivity of the maximum moment sustained by the cylinder on the value of the imperfection amplitude is shown in Figure 42, showing that the height of lateral load may not be an important factor for the value of maximum moment capacity. The mean curve and its equation are also depicted on this graph.
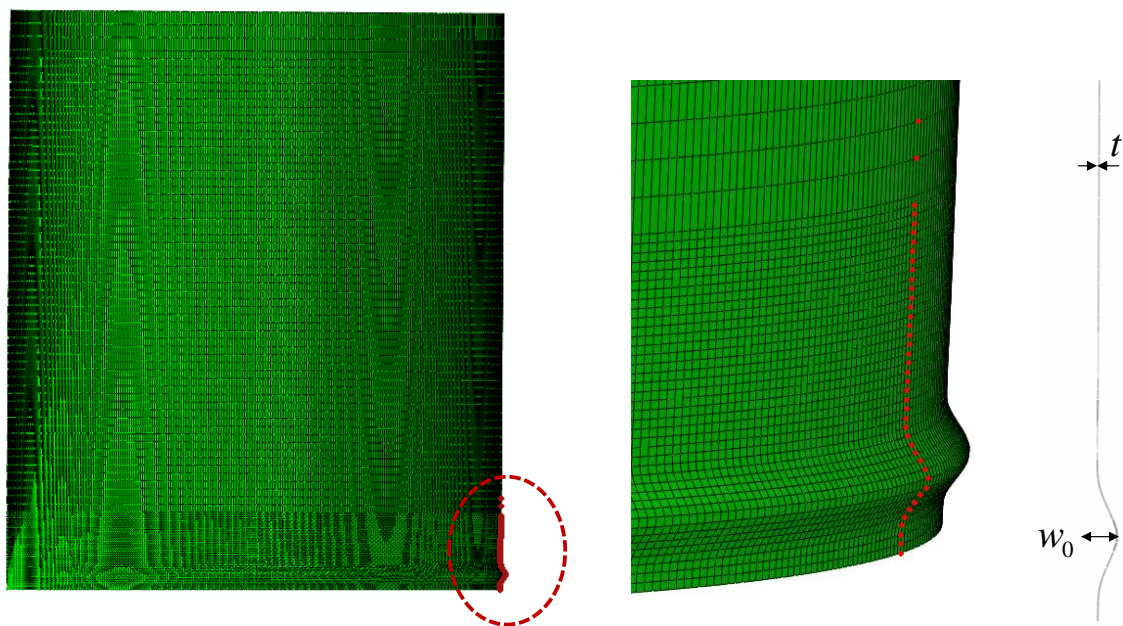
Figure 39: Initial bulge taken from the post-buckling shape of the perfect cylinder to be used for the analysis of imperfect shells after appropriate scaling.

The previous results represent the global behavior of the tank. In order to examine the local behavior of the tank, the stresses and strains at the critical location of the tank are computed. The evolution of longitudinal (axial) and hoop stresses and strains at the critical location of the buckled area are shown in Figure 43, Figure 44, Figure 45 and Figure 46, in terms of the maximum bulging (outward) displacement of the buckled area, for the case of the initially imperfect cylinder with $e = 5$ and $w_0/t = 0.45$. The values of stress in Figure 43 and Figure 44 show that the membrane stresses are quite low with respect to the stresses developed

57

at the inner and outer surface of the shell. The results show that the stresses and strains are larger on the outer surface of the buckled area.

The cylindrical shell under consideration is also analyzed under lateral load, in the presence of internal pressure value of 40% of yield pressure including capped effects on the top. The base moment-lateral displacement diagram is shown in Figure 47, whereas the maximum moment is plotted in terms of the imperfection amplitude in Figure 48.
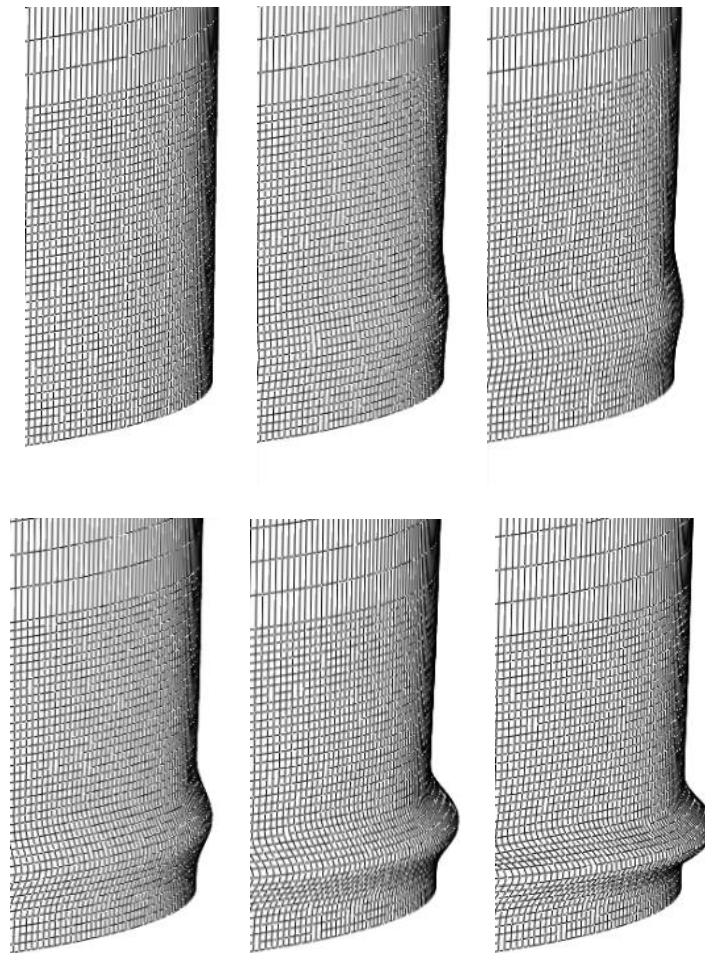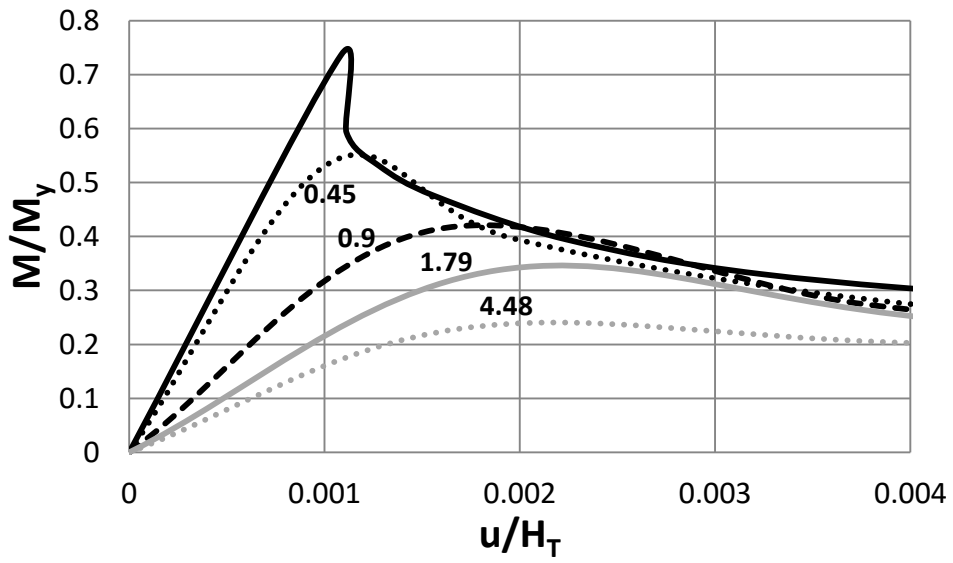

Figure 40: Consecutive stages of elephant's foot buckling formation in the finite element simulation (for $e = 5$ and $w_0 / t = 0.45$).

Figure 41: Normalized moment-displacement curves for $e=5$ and hydrostatic pressure.

$$\frac{M_{max}}{M_y} = 0.735 - 0.311\left(\frac{w_0}{t}\right)^{0.322}$$
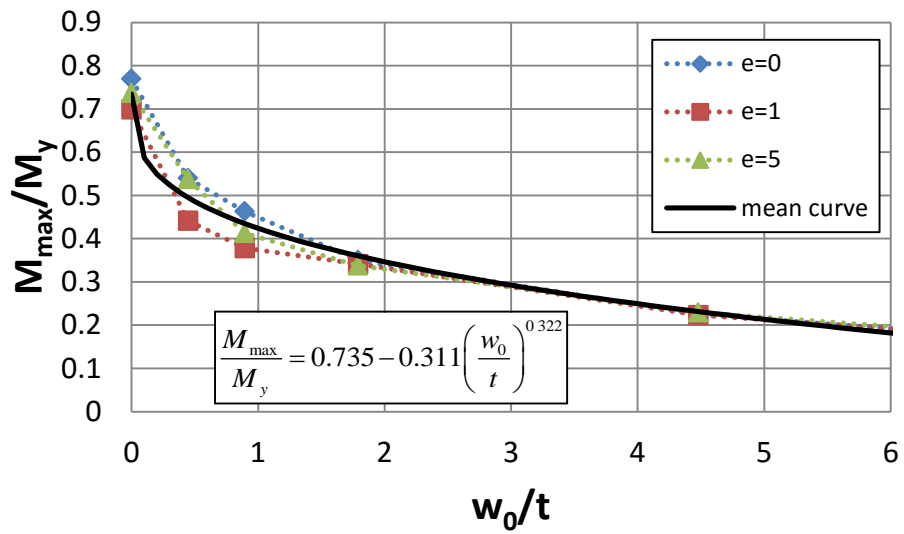
Figure 42: Normalized maximum moment-imperfection curves for the case of hydrostatic pressure for different lengths of the rigid rod. The equation of the mean curve is also depicted on the graph.
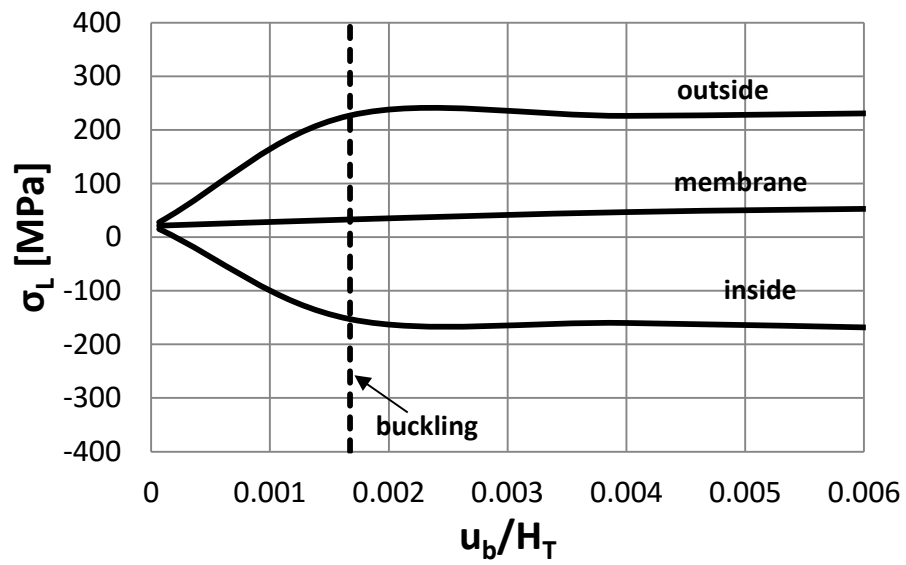
59

Figure 43: Longitudinal stresses at the critical location of the buckled area in terms of the normalised maximum bulging (outward) displacement of the buckled area.
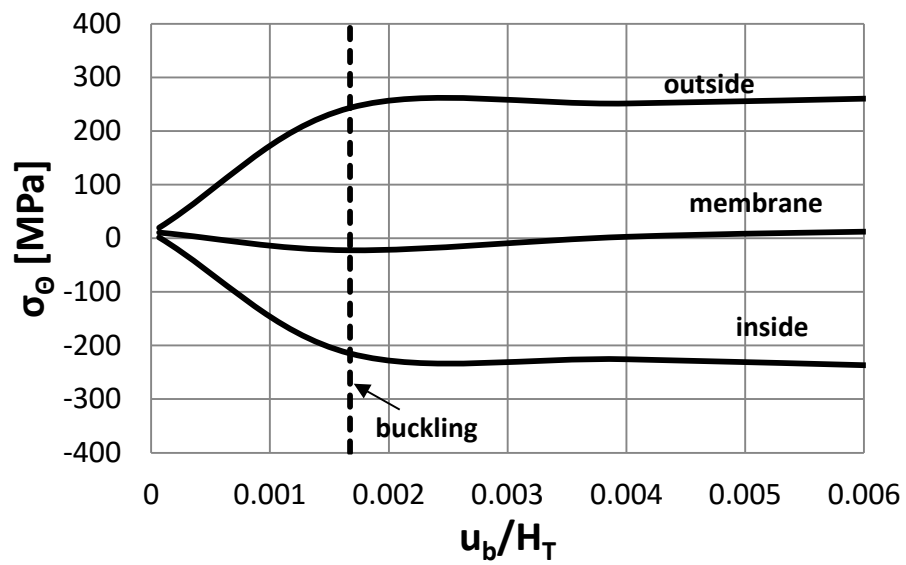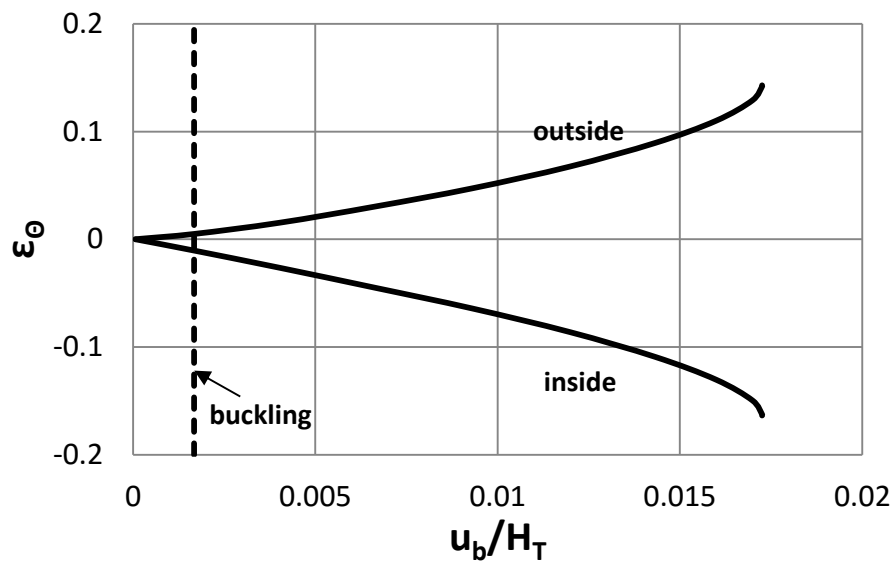

Figure 44: Hoop stresses at the critical location of the buckled area in terms of the normalised maximum bulging (outward) displacement of the buckled area.
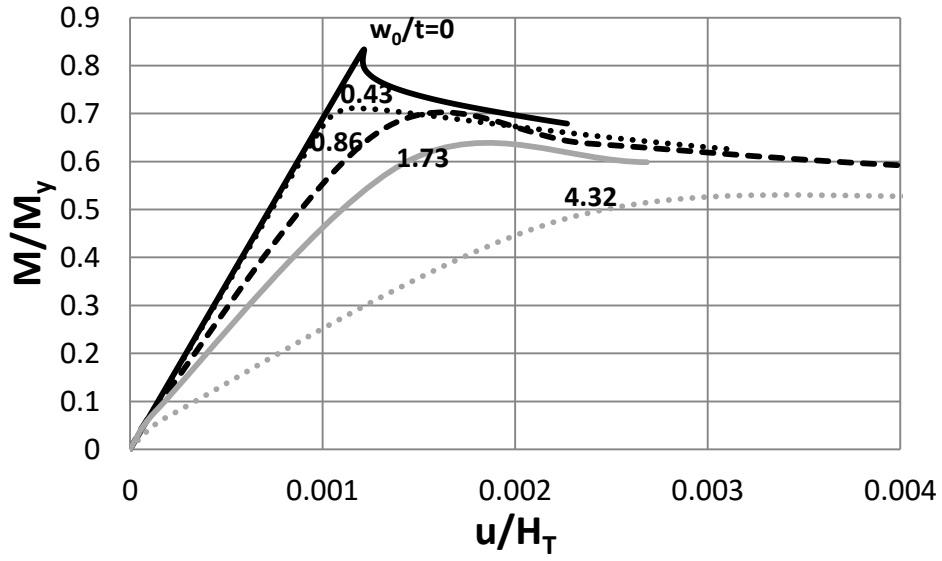
60
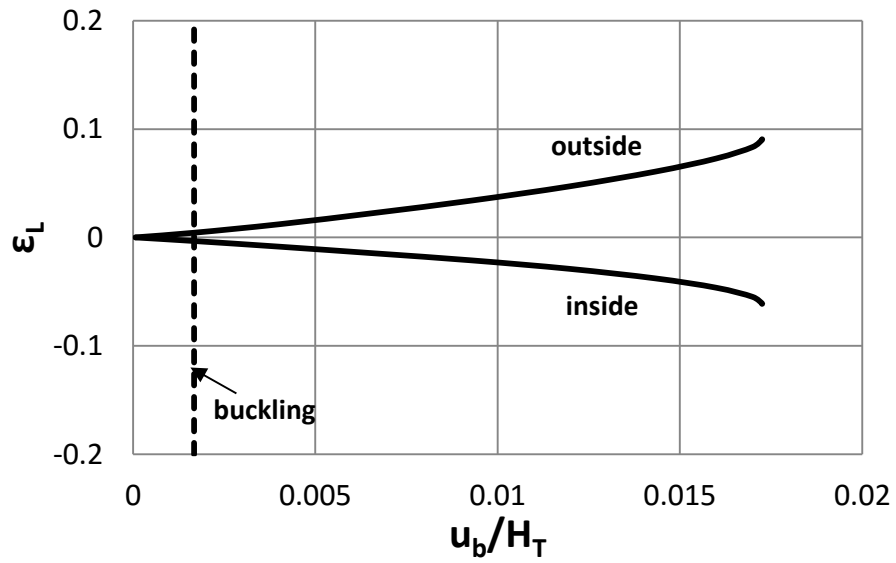
Figure 45: Longitudinal strains at the critical location of the buckled area in terms of the normalised maximum bulging (outward) displacement of the buckled area.

Figure 46: Hoop strains at the critical location of the buckled area in terms of the normalised maximum bulging (outward) displacement of the buckled area.

61

Figure 47: Normalized moment-displacement curves for $e = 5$ and pressure value equal to 40% of yield pressure.
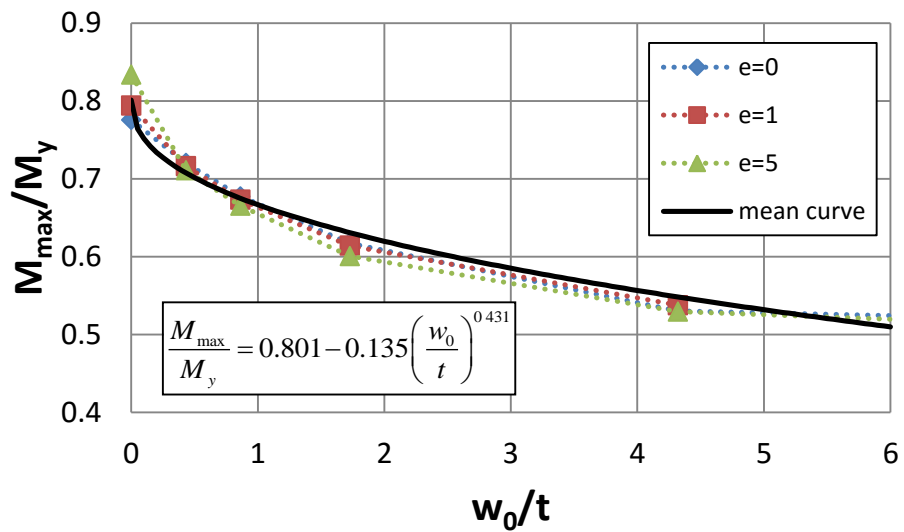

Figure 48: Normalized maximum moment-imperfection curves for the case of internal pressure value of 40% of yield pressure for different lengths of the rigid rod. The equation of the mean curve is also depicted on the graph.

62

The tank has been analyzed under lateral loading ($e = 5$) for different levels of internal pressure. The results show that the presence of pressure at a level up to 80% may have a certain effect on the lateral resistance of the cylindrical shell. In particular, in Figure 49 for $w_0/t = 0$ (perfect geometry) the maximum overturning moment sustained by the tank drops from 85.4% to 76.5% of the yield moment for pressure range from 1% to 80% of the yield pressure. For $w_0/t = 0.45$ the maximum overturning moment sustained by the tank increases from 59.7% to 76.2% of the yield moment for pressure range from 1% to 70% of the yield pressure and drops to 75.5% for pressure equal to 80% of the yield pressure. Figure 50 and Figure 51 show the base moment-displacement curves for some of the pressures. The above observations are in good correlation with the experimental results presented by Mathon and Limam (2006).
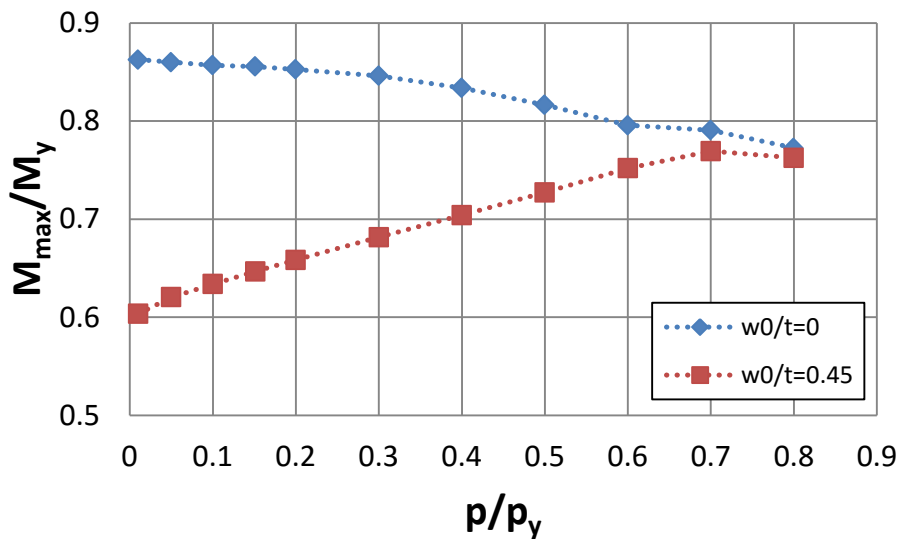

Figure 49: Normalized maximum moment in terms of the internal pressure for $e = 5$ and $w_0/t = 0$.
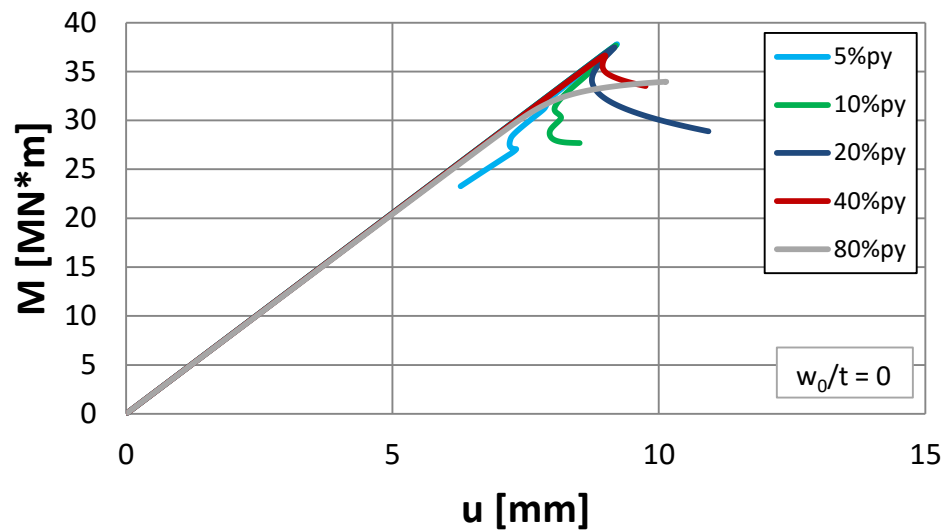
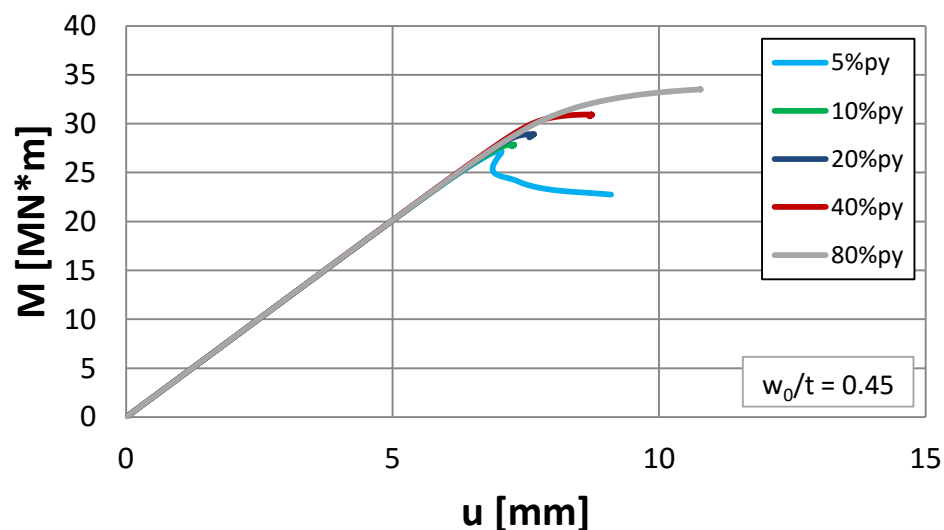**Figure 50:** Base moment - displacement curves for $e = 5$ and $w_0 / t = 0$.

Figure 51: Base moment - displacement curves for $e = 5$ and $w_0 / t = 0.45$.

3.5.2.1 On the use of axisymmetric shell models for elephant's foot buckling

In addition to the three-dimensional models described above, the possibility of using axisymmetric models for buckling analysis of pressurized cylinders under lateral loading is also examined. The shape of the elephant's foot buckle extends over a significant circumferential sector of the cylinder on either side of the most-stressed generator (Figure 52), so that the assumption of axisymmetric conditions for the elephant's foot pattern seems quite reasonable.

64

The axisymmetric model employed is shown in Figure 53. The length of the axisymmetric strip, H_{ax}, is chosen significantly larger than the length over which the elephant's foot buckling pattern extends, obtained in the 3D analyses, and it is smaller than the total height of the tank for simplification. The bottom end of the model is fixed (clamped), whereas the top end is pinned.
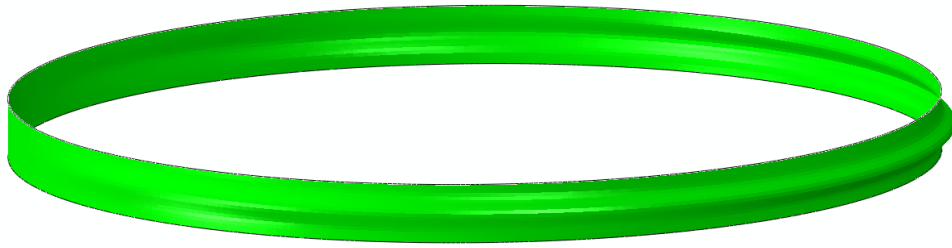

Figure 52: Lower section of the buckled tank for $e=5$ and $w_0/t=0$. The shape of the elephant's foot buckle extends over a significant circumferential sector of the cylinder.
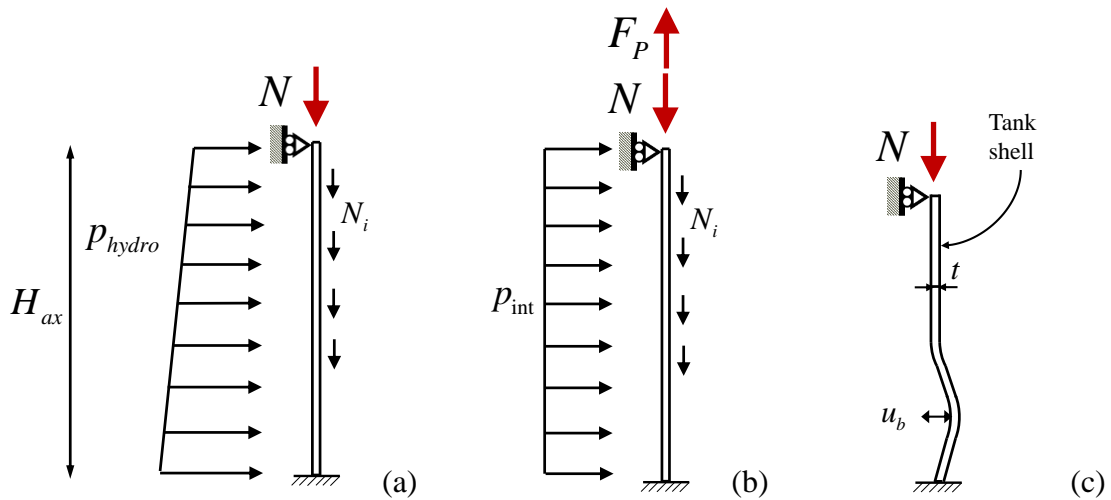

Figure 53: Schematic representation of the axisymmetric model: (a) buckling analysis under hydrostatic pressure, (b) buckling analysis under internal constant pressure, (c) deformed shape.

Pressure is applied on the inner surface. It is raised first up to the desired level and then kept constant, whereas axial loading is distributed in several nodes along the model height, according to the distribution of membrane forces along the shell generator calculated in the 3D

65

analyses, so that a representative distribution of axial compression along the shell generator exists.

The results from the axisymmetric model are shown in Figure 54 and Figure 55, in terms of the moment-displacement curve. The value of moment is computed by multiplying the membrane force with the bending resistance of the horizontal circular section of the tank (equal to πR^2, where R is the radius of the tank).

The results of the axisymmetric model are compared with the results of the three-dimensional model in Figure 56 and Figure 57. The comparison shows that there exists a fairly good correlation between the two models for small imperfection amplitudes, despite the fact that the axisymmetric analysis results are rather conservative. It is the author's opinion that axisymmetric models can be used for a simplified model analysis, since they provide a reasonable level of accuracy.
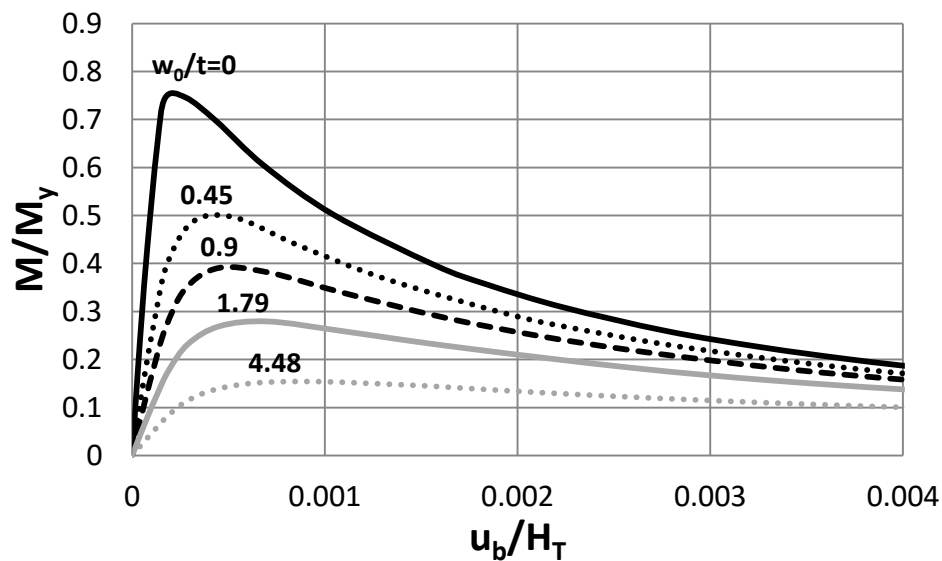

Figure 54: Normalized moment-displacement curves obtained from the axisymmetric model for different imperfection amplitudes in the case of the hydrostatic pressure.
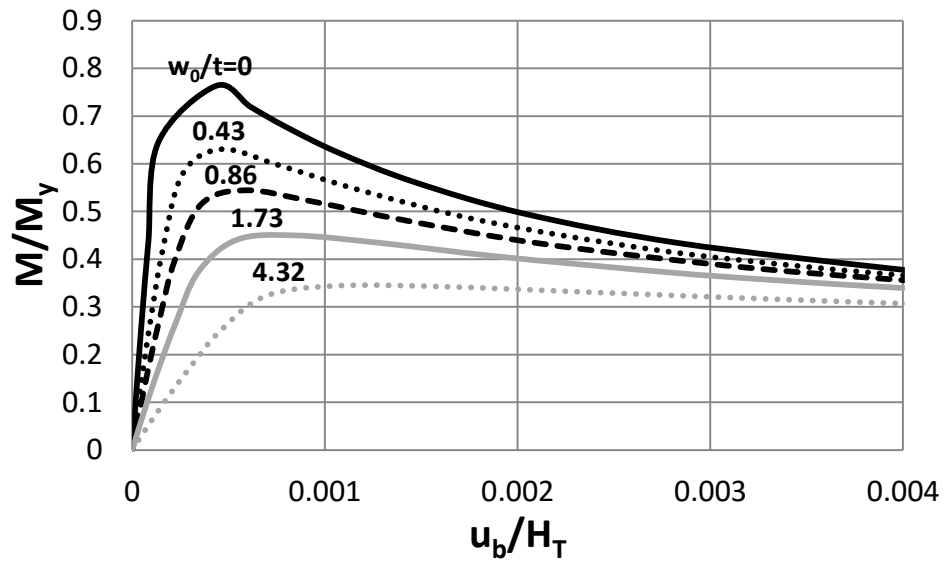
66

Figure 55: Normalized moment-displacement curves obtained from the axisymmetric model for different imperfection amplitudes in the case of internal pressure equal to 40% of the yield pressure.
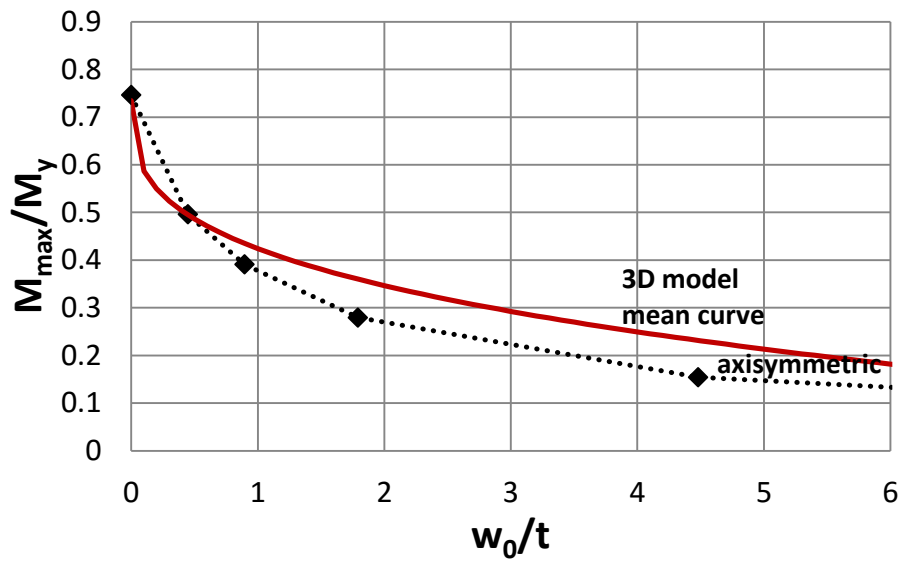

Figure 56: Normalized maximum moment in terms of imperfection for the three-dimensional and the axisymmetric model in the case of hydrostatic pressure.
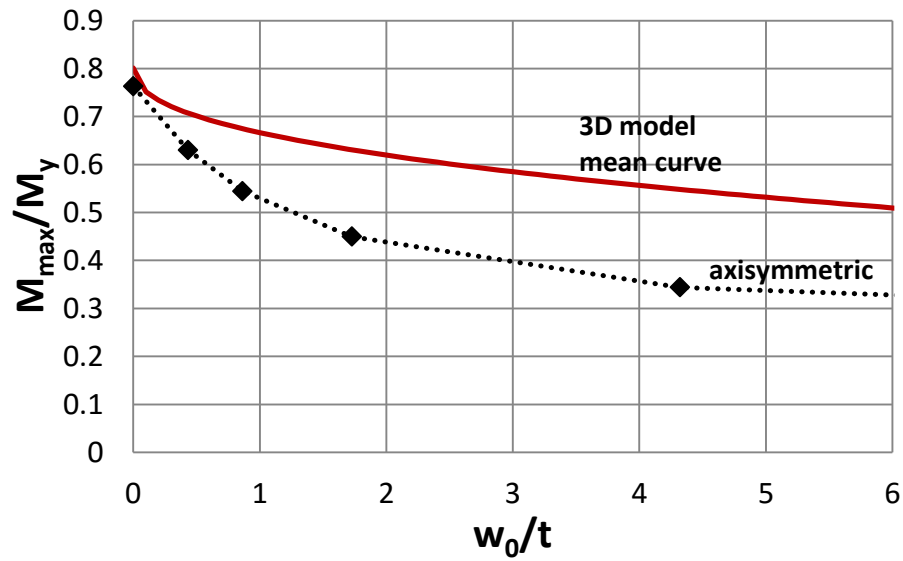
67

Figure 57: Normalized maximum moment in terms of imperfection for the three-dimensional and the axisymmetric model in the case of internal pressure equal to 40% of yield pressure.

3.5.2.2 Comparison with EN design provisions for steel shell design

The results obtained numerically with the three-dimensional model are also compared with the provisions of EN 1993-1-6, paragraph 8.5.2 and Annex D (D.1.5) and those of EN 1998-4, paragraph A.10.3, in Figure 58 and Figure 59, which are summarized in the following. The maximum moments predicted by both standards can be computed by multiplying the meridional buckling stress, σ_b, with $\pi R^2 t$.

- EN 1993-1-6 provisions (Paragraph 8.5.2 and D.1.5)

The characteristic buckling stress should be obtained by multiplying the yield strength σ_y by the buckling reduction factor χ_x:

$$\sigma_b = \chi_x \sigma_y \tag{80}$$

The buckling reduction factor χ_x is a function of the relative slenderness of the shell, (denoted as $\overline{\lambda}$):

$$\chi_x = 1 \quad \text{when} \quad \overline{\lambda_x} \le \overline{\lambda_0} \tag{81}$$

68

$$\chi_x = 1 - \beta_{xp} \left(\frac{\overline{\lambda_x} - \overline{\lambda_0}}{\overline{\lambda_p} - \overline{\lambda_0}} \right)^{\overline{\eta}} \quad \text{when} \quad \overline{\lambda_0} < \overline{\lambda_x} < \overline{\lambda_p} \tag{82}$$

$$\chi_x = \frac{\alpha_{xp}}{\overline{\lambda_x}^2} \quad \text{when} \quad \overline{\lambda_p} \leq \overline{\lambda_x} \tag{83}$$

where $\overline{\lambda_0} = 0.20$ is the squash limit relative slenderness, α_{xp} is the elastic imperfection reduction factor to be defined below, $\beta_{xp} = 0.60$ is the plastic range factor and $\overline{\eta} = 1.0$ is the interaction exponent. The relative slenderness of the shell is defined as follows:

$$\overline{\lambda_x} = \sqrt{\sigma_y / \sigma_e} \tag{84}$$

where σ_e is given by:

$$\sigma_e = 0.6 E C_x \frac{t_s}{R} \tag{85}$$

and C_x is a parameter depending on the boundary conditions and t_s is the thickness of the bottom shell course less corrosion allowance. The value of the plastic limit relative slenderness $\overline{\lambda_p}$ should be determined from:

$$\overline{\lambda_p} = \sqrt{\frac{\alpha_{xp}}{1 - \beta_{xp}}} \tag{86}$$

The elastic imperfection reduction factor accounts for the effects of geometric imperfections on the elastic buckling stress σ_e. For the case of internally-pressurized cylinders under axial compression: $\alpha_{xp} = \min(\alpha_{xpe}, \alpha_{xpp})$, where the factors α_{xpe} and α_{xpp} are calculated as follows:

$$\alpha_{xpe} = \alpha_x + (1 - \alpha_x) \left| \frac{\overline{p}_{\min}}{\overline{p}_{\min} + \frac{0.3}{\alpha_x^{0.5}}} \right| \tag{87}$$

$$\overline{p}_{\min} = \left(\frac{p_{\min}}{\sigma_e} \right) \left(\frac{\overline{r}}{t_s} \right) \tag{88}$$

$$\alpha_x = \frac{0.62}{1 + 1.91(\Delta w_k / t_s)^{1.44}} \tag{89}$$

69

$$\frac{\Delta w_k}{t_{eq}} = \frac{1}{Q}\sqrt{\frac{\overline{r}}{t_s}}$$

(90)

and:

$$\alpha_{xpp} = \left\{1 - \left(\frac{\overline{p}_{max}}{\overline{\lambda}_x^2}\right)^2\right\}\left[1 - \frac{1}{1.12 + s^{1.5}}\right]\left[\frac{s^2 + 1.21\overline{\lambda}_x^2}{s(s+1)}\right]$$

(91)

$$\overline{p}_{max} = \left(\frac{p_{max}}{\sigma_e}\right)\left(\frac{\overline{r}}{t_s}\right)$$

(92)

In the above expressions, $s = \frac{1}{400}\cdot\left(\frac{\overline{r}}{t_s}\right)$, Δw_k is the characteristic imperfection amplitude, t_{eq} is the equivalent uniform thickness of the tank wall, $\overline{r}$ is the radius of the cylinder middle surface, α_x is the unpressurised meridional elastic imperfection reduction factor, Q is the meridional compression fabrication quality parameter ranging from 40 (excellent quality) to 16 (poor quality), p_{min} is the smallest design value of local internal pressure at the location of the point being assessed, guaranteed to coexist with the meridional compression and p_{max} is the largest design value of local internal pressure at the location of the point being assessed that can coexist with the meridional compression.

- EN 1998-4 provisions (Paragraph A.10.3)

The buckling stress can be calculated by the following equation:

$$\sigma_b = \sigma_e\left[1 - \left(\frac{p_{max}R}{t\sigma_y}\right)^2\right]\left(1 - \frac{1}{1.12 + r^{1.5}}\right)\left[\frac{r + \sigma_y/250}{r+1}\right]$$

(93)

where:

$$r = \frac{R}{400t}$$

(94)

To achieve a fair comparison, the imperfection amplitude of Eq. (90) is taken equal to the value considered in the numerical analyses. The comparison in Figure 58 and Figure 59 shows good correlation for small imperfection amplitudes. However, this comparison is out of the imperfection range specified by EN 1993-1-6 (larger than the specified "poor fabrication

70

quality" value, shown in Figure 59 as EN 1993-1-6 limit). This may explain the difference between numerical results and EN 1993-1-6 predictions. This behavior is also shown in Figure 60 and Figure 61 where the buckling stress is given in terms of the relative slenderness of the shell [Eq. (84)] for "medium fabrication quality". The value of the relative slenderness for the tank under consideration is equal to 0.989. Furthermore, the value of the buckling stress of the finite element analysis in the case of hydrostatic pressure and internal pressure equal to 40% of yield pressure is calculated using the equation of the mean curves depicted on Figure 42 and Figure 48 respectively assuming that $Q = 25$.

Furthermore, the provisions of EN 1998-4 appear to be somewhat conservative for small values of imperfection amplitude, but may not provide reliable predictions for imperfection amplitudes of moderate and large values.
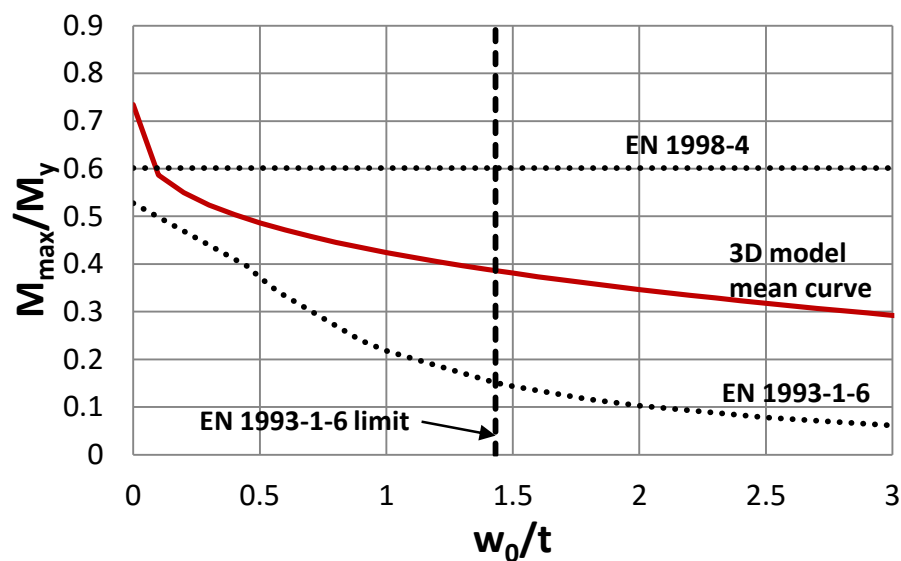

Figure 58: Normalized maximum moment in terms of imperfection for three-dimensional analysis and the relevant provisions of EN 1993-1-6 and EN 1998-4 in the case of hydrostatic pressure.
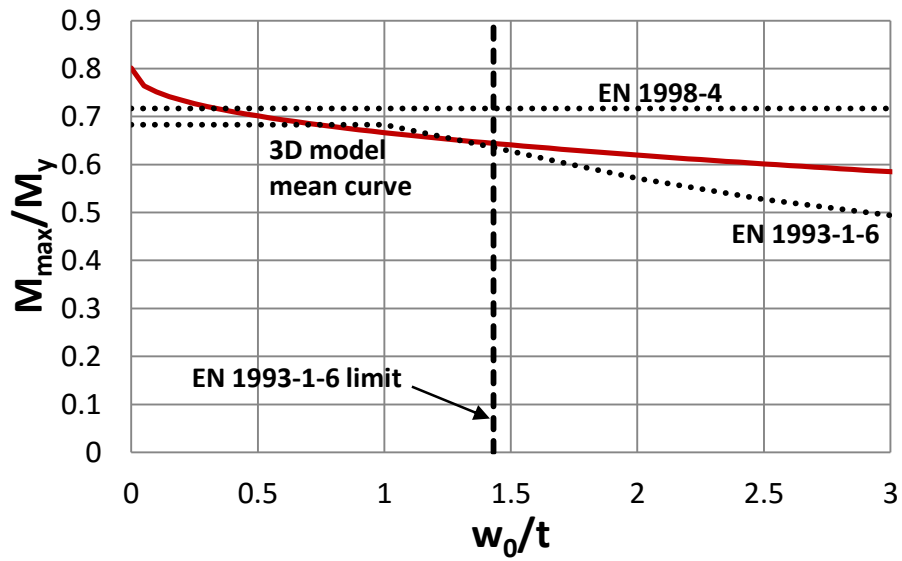
71

Figure 59: Normalized maximum moment in terms of imperfection for three-dimensional analysis and the relevant provisions of EN 1993-1-6 and EN 1998-4 in the case of internal pressure equal to 40% of yield pressure.

Figure 60: Normalized buckling stress in terms of the relative slenderness of the shell for three-dimensional analysis and the relevant provisions of EN 1993-1-6 for "medium fabrication quality" ($Q = 25$) in the case of hydrostatic pressure.
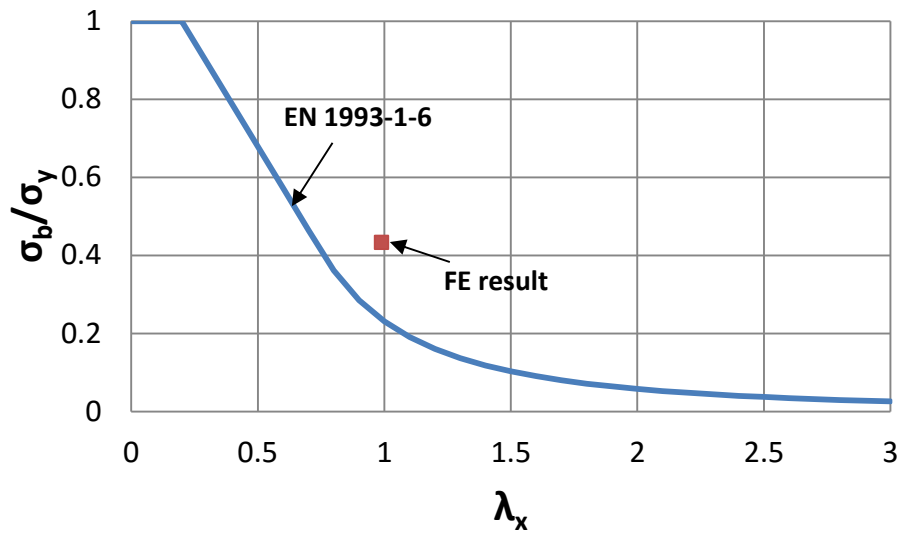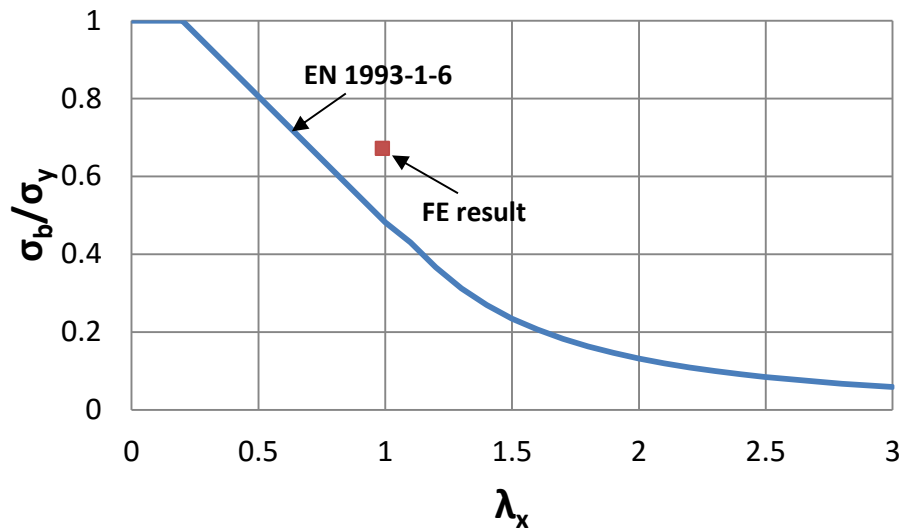
72

Figure 61: Normalized buckling stress in terms of the relative slenderness of the shell for three-dimensional analysis and the relevant provisions of EN 1993-1-6 for "medium fabrication quality" ($Q = 25$) in the case of internal pressure equal to 40% of yield pressure.

3.6   Strengthening liquid storage tanks against elephant's foot buckling with FRP

There exist several methods for mitigating the effects of elephant's foot buckling in liquid storage tanks. Current international standards for both static design and earthquake design imply an increase of the wall thickness of the bottom course. Alternatively, Chen et al. (2005, 2006) proposed an alternative way to strengthen the shell against elephant's foot buckling using a ring stiffener at a critical location, around the tank.

The use of fibre reinforced polymer (FRP) composites for strengthening steel structures has emerged in recent years as an efficient and promising strengthening technique against local buckling of shell-like structures. Batikha et al. (2009) studied the effects of strengthening cylindrical shells under internal pressure against elephant's foot buckling by using externally-bonded FRPs. They used the linear elastic bending axisymmetric equations for the strengthened cylindrical shell (without consideration of second-order effects) and illustrated these techniques through exploratory examples.

The contents of the present section are part of national project UPGRADE (Gazetas et al. 2015), aimed at developing efficient methodologies for evaluating seismic vulnerability and

73

upgrading of port facilities. Particularly, the improvement of strength of liquid storage tanks against elephant's foot buckling failure by using sheets of Carbon FRP (CFRP) at critical locations is examined with finite element modelling, and a brief description of this analysis is offered below.

Description of the numerical model

Numerical results are presented for the tank under consideration with 6.3 meters diameter and 7.4 meters height, described previously in section 3.5. The numerical model is similar to the model used in the previous sections of the present Chapter. The amendment of the model consists of the addition of a CFRP wrap as a new part near the bottom of the tank. The tank is anchored, so the tank shell is considered completely fixed (clamped) at its bottom. The center of the top section of the shell is connected to a fictitious "stiff rod", and lateral loading is applied at the top of the rod. Hydrostatic pressure inside the shell is considered with a maximum value of 0.0677 MPa for a filling height of 6.9 m.

The CFRP part is also modelled with four-node reduced-integration shell elements (S4R) and the material properties shown in Figure 62.

According to the previous section of the present Chapter, the height of lateral load may not be a critical factor for the value of maximum moment, so the analysis can be conducted with only one value of rod length. Herein the value of e is equal to 5. The height of the CFRP is chosen according to the results of section 3.5 so that elephant's foot buckling is prevented. Herein, it is chosen equal to 0.5 m, somewhat larger than the length of the elephant's foot buckling pattern. The geometric characteristics of the tank model used in the analysis are shown in Figure 63.

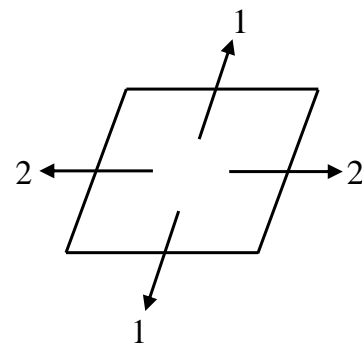| Material Characteristics of CFRP – C322U	
E_1 = 135000 MPa	G_{12} = 5000 MPa
E_2 = 10000 MPa	G_{13} = 5000 MPa
v_{12} = 0.3	G_{23} = 2500 MPa

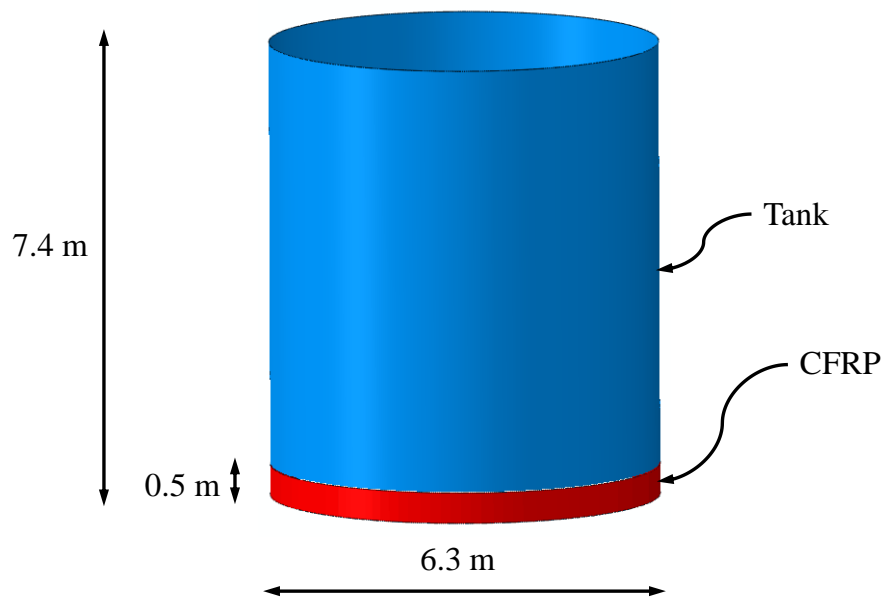**Figure 62:** Material Characteristics of CFRP –C322U.

74

Figure 63: Geometric characteristics of the tank used in the analysis.

The following cases are examined:

- Effect of CFRP on the strength of the tank for perfect and imperfect tank geometry
- Effect of CFRP thickness on the strength of the tank for perfect tank geometry

(a) Effect of CFRP on the strength of the tank for perfect and imperfect tank geometry

In this case, the effect of FRP wrapping on tank strength is examined, for perfect and imperfect tank geometries. More specifically, the imperfection amplitude is chosen equal to $w_0 / t =$ 0 (perfect), 0.45 and 0.9, where t is the shell thickness. In Table 2, the maximum normalized moments are presented for each type of strengthening in terms of the imperfection amplitude and the respective buckled tank shapes are shown in Figure 64. It is shown that the presence of FRP wrapping increases the strength of the tank and prevents elephant's foot formation. In addition, the orientation of the FRP fibers has a certain effect on the strength of the tank. For tanks without imperfections, the use of FRP with fibers oriented in the axial direction improves the strength of a tank by a significant amount, more than the use of FRP with fibers oriented in the hoop direction. This can be attributed to the fact that in this case the "acting mechanism" is the axial compression of the tank. On the other hand, for tanks with initial imperfections the prevailing mechanism is the motion in the hoop direction due to the

75

internal pressure which tends to increase the elephant's foot bulge, so the use of FRP with fibers oriented in the hoop direction appears to be more suitable for this case.

(b) Effect of CFRP thickness on the strength of the tank for perfect tank geometry

In this case, the effect of the thickness of FRP on tank strength is examined, for perfect tank geometry. In Table 3, the maximum normalized moments are presented for each type of strengthening with 2 plies of CFRP. It is shown that increasing the number of FRP plies, the tank strength increases even more.

The main conclusion from the analyses is that the use of FRP is a simple and economic way of improving tank strength against elephant's foot buckling.

Table 2: Maximum normalized moments for different types of strengthening, for perfect and imperfect tank geometry.

Type of strengthening	M_{max} / M_y for $w_0 / t = 0$	M_{max} / M_y for $w_0 / t = 0.45$	M_{max} / M_y for $w_0 / t = 0.9$
No CFRP	0.736	0.537	0.412
CFRP with fibers in the hoop direction	0.803	0.748	0.666
CFRP with fibers in the axial direction	0.879	0.702	0.620

Table 3: Maximum normalized moments for strengthening with 2 plies of CFRP.

Type of strengthening	M / M_y
(a) 2 plies of CFRP, 1st hoop, 2nd axial	0.845
(b) 2 plies of CFRP, 1st axial, 2nd hoop	0.824
(c) 2 plies of CFRP with fibers in the hoop direction	0.812
(d) 2 plies of CFRP with fibers in the axial direction	0.861

76
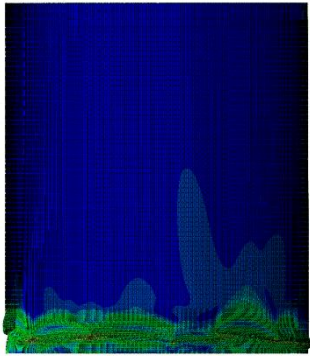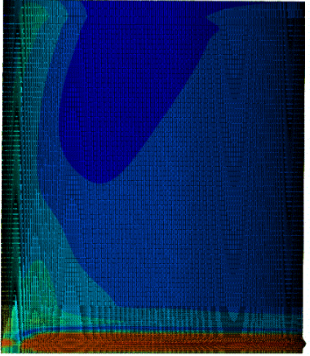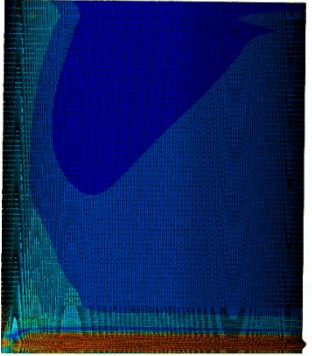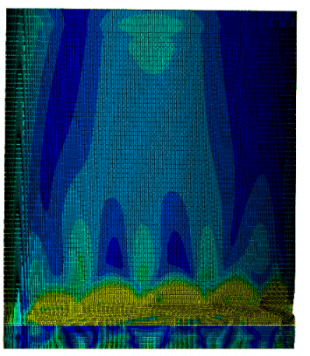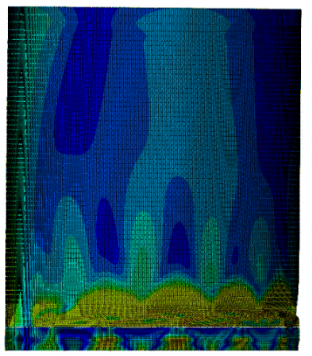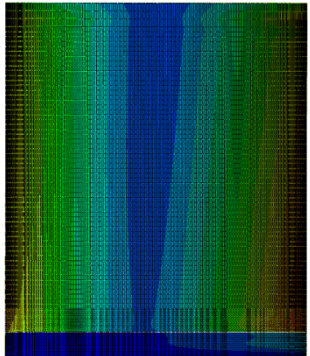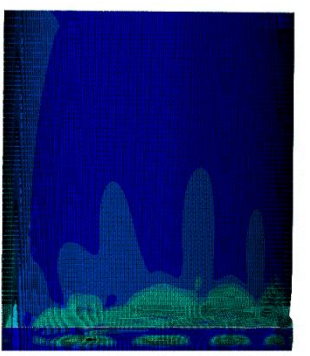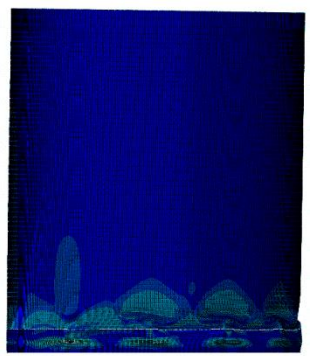
Type of strengthening	$w_0/t = 0$	$w_0/t = 0.45$	$w_0/t = 0.9$
No CFRP			
CFRP with fibers in the hoop direction			
CFRP with fibers in the axial direction			

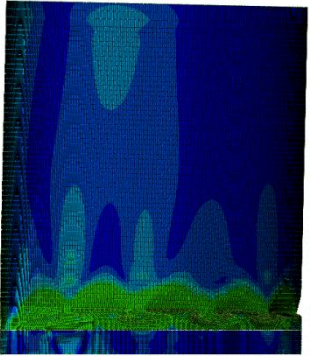**Figure 64:** Buckled tank shapes for each type of strengthening of Table 2.

77

4. Structural Response of Unanchored Liquid Storage Tanks

4.1 Introduction

In numerous practical applications, relatively broad aboveground liquid storage tanks are constructed unanchored, in the sense that their bottom plate is in simple contact with the ground, without anchor bolts. In such a case, under strong lateral dynamic loading (e.g. seismic), the tank may exhibit uplifting of its bottom plate, when the magnitude of the overturning moment exceeds a threshold value. Although uplift does not necessarily result in tank failure, its consequences may lead to serious damage of any attached piping connections of the uplifted bottom plate, and possible failure of the connection between the tank shell and the bottom plate. Furthermore, it may result in an increase of the axial stress acting on the tank wall which may lead to a precipitation of "elephant's foot" buckling. This behaviour is shown schematically in Figure 65; the critical locations are locations 1 and 2. Location 1 is the area where uplifting of the tank occurs and location 2 is the area where elephant's foot buckling takes place.
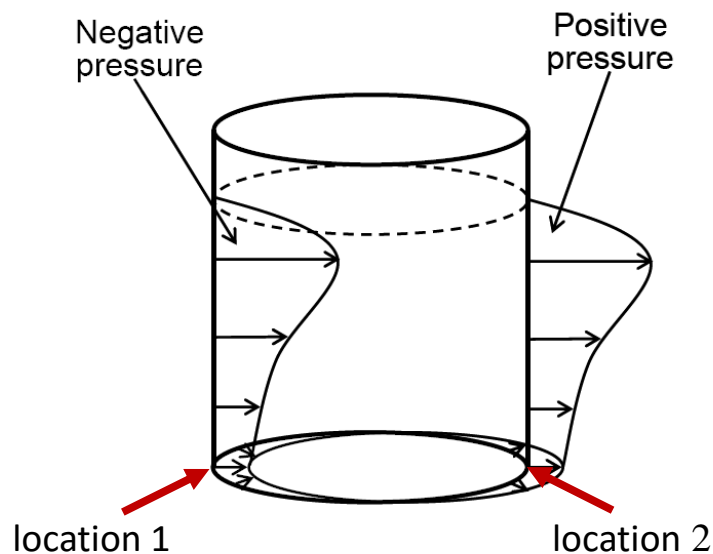

Figure 65: Locations affected by uplifting during seismic action in an unanchored tank.

Valuable insight into the uplifting resistance of a plate may be obtained from the solution of the simple problem of a prismatic beam uplifted at one end. Several solutions of the beam problem have been attempted in the past. Ignoring the effect of membrane forces

78

(Wozniak and Mitchell 1978, Leon and Kausel 1986), the maximum load capacity for the beam is reached as soon as two plastic hinges develop: one at the uplifted end (i.e. at the shell-plate connection), and the second at the section where the moment takes a maximum value within the beam. An approximate solution that incorporates the effects of the membrane forces was proposed by Cambra (1982) using, on the basis of experimental data, simplifying assumptions regarding the magnitude of the axial and shearing forces in the beam. A second-order beam theory that accounts for membrane forces more accurately was used by Auli et al. (1985), but did not account for the effects of flexible end constraints and of plastic yielding within the beam. Ishida and Kobayashi (1988) used the finite element method to solve the beam problem; in their analysis they made a series of simplifying assumptions regarding the distribution of forces in the base plate and the foundation in order to analyze the rocking response of tanks. Malhotra and Veletsos (1994a) studied extensively uplifting behavior, idealizing the base plate as a uniformly loaded semi-infinite, prismatic beam that rests on a rigid foundation. The effect of elastic end constraints, the influence of the axial force on bending and the effect of plastic yielding in the beam were considered. In a recent publication, Ahari et al. (2009) used a tapered beam to model base uplift of unanchored tanks.

The aforementioned beam models did not take into account the effect of hoop stresses, which develop in the base plate close to the junction with the shell wall. A fundamental step forward in the uplifting analysis of liquid storage tanks is the consideration of a partially uplifted base plate. More recent studies on plate uplifting were carried out by a combination of finite-difference and energy technique (Peek and Jennings 1988, Peek 1988) and by the Ritz energy method (Haroun et al. 1987, Haroun and Badawi 1988, Lau and Clough 1989). Both axisymmetric and asymmetric solutions have been presented in these studies and the results compared with those obtained from experiments. A significant contribution of these studies has been the demonstration of the importance of membrane action on the load-carrying mechanism. The reported methods are generally rather complex and non-efficient for dynamic response analyses of uplifting tanks, in which the solution of the plate problem must be obtained at numerous integration steps. The complex nature of these analyses has not been favorable for an in-depth parametric study of the numerous factors involved and a simple interpretation of the results. Additionally, those studies did not consider the effects of load reversals and of the associated energy dissipation due to yielding; these effects may be important in dynamic response analyses. Malhotra and Veletsos (1994b) attempted to improve this approach by

79

computing the vertical and rocking resistances of a uniformly loaded circular plate to forces that are distributed along its boundary. They described an exact method for axisymmetric vertical uplifting and an approximate method for asymmetric rocking uplifting. The latter was modeled by a series of semi-infinite prismatic beams. The two analyses were compared for evaluating the accuracy of the approximate method.

The response of the partially uplifted base plate of these tanks is highly complex and non-linear due to continuous variation of the base contact area, plastic yielding of the plate material, and the effects of membrane forces associated with large displacements in the plate. Most previous studies on base uplifting dealt with the response of tanks, supported on rigid foundations (Haroun et al. 1987). Studies on the dynamic response of unanchored tanks supported on rigid foundations have shown that base uplifting influences significantly the dynamic behavior of tanks, leading to axial compressive stresses in their walls that are substantially higher than those in similarly excited fixed-base systems, as noted by Peek (1986). In practice many unanchored tanks are supported either directly on a flexible soil foundation or on a rigid ring foundation at the perimeter and a flexible soil foundation inside. There are relatively fewer studies on the uplifting response of such tanks. The first studies on the behavior of unanchored fluid-filled tanks were experimental. During the period 1977-1982, Clough and his associates at UC Berkeley reported results from shaking table and static tilt tests (Clough 1977; Niwa 1978; Clough and Niwa 1979; Manos and Clough 1982). Furthermore, Shih performed scale model tests in an effort to gain a better understanding of the response and the failure mechanism of the tanks (1981). The results of these experiments showed that the response of the unanchored tank is quite different than that predicted by current seismic codes and is highly influenced by the uplift mechanism. Natsiavas (1987, 1988, 1990) and Natsiavas and Babcock (1988) presented analytical models for determining the dynamic response and the hydrodynamic loads developed on unanchored liquid-filled tanks under horizontal base excitation. Malhotra and Veletsos (1994c, 1995), based on their previous works (1994a, 1994b), thoroughly investigated the effects of uplifting of the bottom plate of the tank on the entire tank-liquid system, for a rigid foundation. In subsequent publications, Malhotra (1995, 1997) revisited the uplifting problem for a flexible foundation.

In the present chapter, the uplifting mechanism of the tank bottom is examined using numerical simulation tools. For this purpose, two typical liquid storage tanks are modeled using finite elements, both anchored and unanchored, and their behavior is discussed with respect to

80

the seismic provisions of API 650 in Appendix E and the relevant provisions of EN 1998-4 in Annex A. The main purpose of the present chapter is the proposal of a simple and efficient methodology for the analysis and design of the shell-bottom plate connection where fracture may occur due to excessive tensile loading or low-cycle fatigue, associated with loss of containment (Prinz and Nussbaumer 2012). Towards this purpose, a hybrid approach is followed: (a) a non-linear static detailed analysis is conducted first, applying the distribution of hydrodynamic pressure due to impulsive and convective motion through an incremental static analysis and subsequently (b) the results are used in a nonlinear dynamic analysis of the tanks. Towards conducting this dynamic analysis, a simplified model is developed, accounting for uplifting, and adopting an efficient methodology for calculating the local strain at the welded connection and assessing its fatigue strength. The proposed simplified methodology constitutes an efficient tool for conducting a performance-based design, as described in Chapter 5.

4.2 Methods of Analysis

Three methodologies of unanchored tank analysis can be used for simulating base plate uplifting. The first methodology consists of a nonlinear static analysis that determines the basic uplifting mechanics. The second methodology consists of a simplified, yet calibrated and efficient model, for dynamic analysis. The third methodology consists of a rigorous finite element simulation of the entire tank-liquid system for dynamic analysis. In the present work, a combination of the first two methodologies is adopted and a brief description is offered below. The third methodology is not examined, and could be the subject of a future research effort.

(1) <u>Nonlinear Static Analysis of Base Plate Uplifting</u>

Three types of nonlinear static analysis have been proposed:

a) Modelling of the tank base plate using a uniformly loaded prismatic beam which uplifts at one end (Malhotra and Veletsos 1994a).

b) Modelling of the partially uplifted base plate using axisymmetric and/or asymmetric solutions (Malhotra and Veletsos 1994b).

81

c) Finite element modeling of the tank using an incremental nonlinear static analysis, sometimes referred to as "pushover analysis" (such a term will not be employed in the present dissertation). Hydrodynamic pressure distribution on the tank is applied gradually (statically) on the inner surface of the tank shell and the bottom plate and tank deformation is monitored during the uplifting process.

(2) <u>Nonlinear Dynamic Analysis</u>

Modeling of the tank as an equivalent spring-mass mechanical model, using the results from the nonlinear static analysis (1), described above, so that the dynamic response under seismic excitation is obtained.

In the present dissertation we use a combination of methodologies (1c) and (2).

4.3   Description of Tank Case Studies

Two typical fixed-roof liquid storage tanks are considered and simulated numerically. They represent real cases, i.e. tanks constructed in areas of seismic activity. The tanks have been designed using the relevant API 650 rules, before the issue of the new version of Appendix E, launched in 2007.

The first tank is a moderately-broad tank, referred to as Tank I. It is a 27.8-meter-diameter tank with a total height of 16.5 meters. The tank is unanchored. The filling height of the tank H is equal to 15.7, which corresponds to an aspect ratio of the tank, $\gamma(=H/R)$, equal to 1.131. The tank thickness varies from 6.4 mm at its top course to 17.7 mm at its bottom course and the bottom plate is 6 mm thick with an 8-mm-thick annular plate. It has an L120x120x12 stiffening ring at the top (wind stiffener) and the mass of the roof and the shell are 35000 kg and 118100 kg respectively.

The second tank considered, referred to as Tank II, is a broad 46.9-meter-diameter tank with a total height of 19.95 meters. The filling height of the tank H is equal to 18.37 resulting to an aspect ratio, $\gamma(=H/R)$, equal to 0.783. The tank thickness varies from 8 mm at its top

82

course to 22.23 mm at its bottom course. It has an L76x76x10 stiffening ring and the mass of the roof and shell are 45863.5 kg and 301549 kg respectively.

In both tanks, the contained liquid is water ($\rho = 1000$ kg/m^3) and the material of the tank shell, the bottom plate and the roof is structural steel S235 (equivalent to A36 steel) with yield stress $\sigma_y = 235$ MPa. For the purposes of the present study, the tanks are simulated as both anchored and unanchored. Both tanks have truss roofs with L- and UPN beams of different shapes. The tank geometries are depicted in Figure 66.
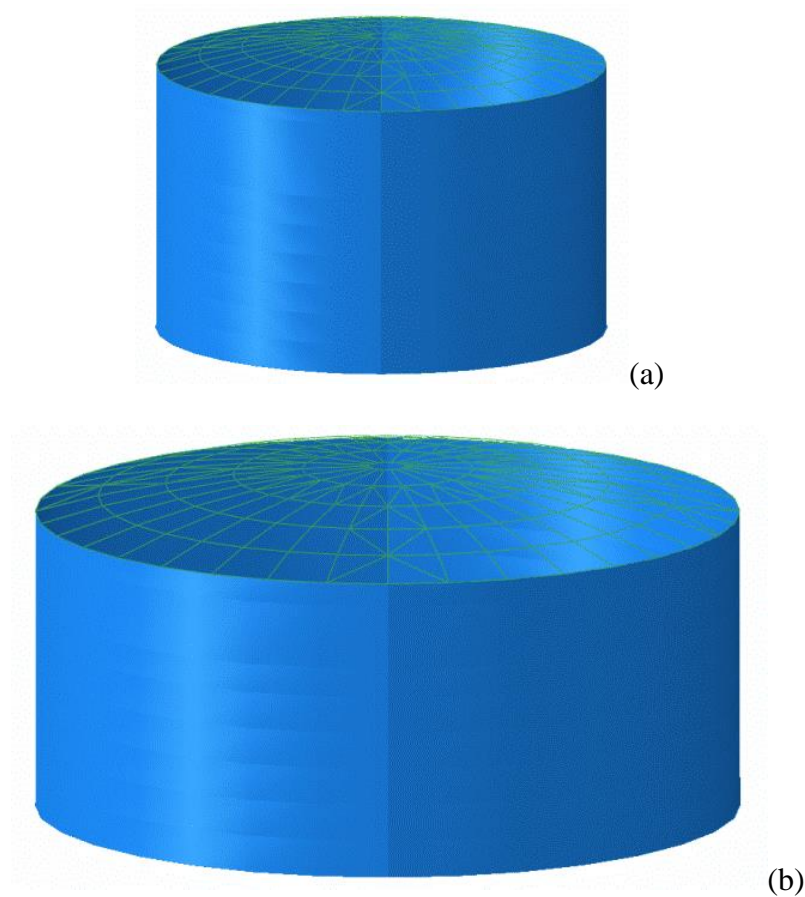

(a)

(b)

Figure 66: Tanks used for the parametric study; (a) Tank I, (b) Tank II.

83

4.4 Nonlinear static analysis of tanks under lateral loading

4.4.1 Model Description

General-purpose finite element program ABAQUS is used for the simulation of the structural behaviour of the tank under static loading, assuming both anchored and unanchored conditions (Figure 67). In the case of unanchored tanks, the tank shell and the bottom plate are modelled with shell finite elements, with special attention on the annular base plate of the tank. More specifically, the tank and the bottom plate are modeled with four-node reduced-integration shell elements (S4R). In such a case, the effects of uplifting of the unanchored tank are simulated with the use of appropriate contact conditions between the bottom plate of the tank and the ground. The type of contact used is "hard" contact and the two surfaces can be separated after contact at the beginning of the analysis to allow later uplifting of the bottom plate (Figure 68). The friction coefficient between the tank base plate and the ground is assumed to be 0.3. The material of the ground is considered to be a material with density $7500\,\text{kg/m}^3$, Young's modulus equal to 110000 MPa and Poisson's ratio equal to 0.3. The ground is simulated using solid eight-node reduced-integration elements (C3D8R). Lastly, the tank roof is modelled with the use of two-node (linear) beam-type finite elements (B31) (Figure 69).

When modelling the tank as anchored, the tank shell is simulated completely fixed (clamped) at its bottom.
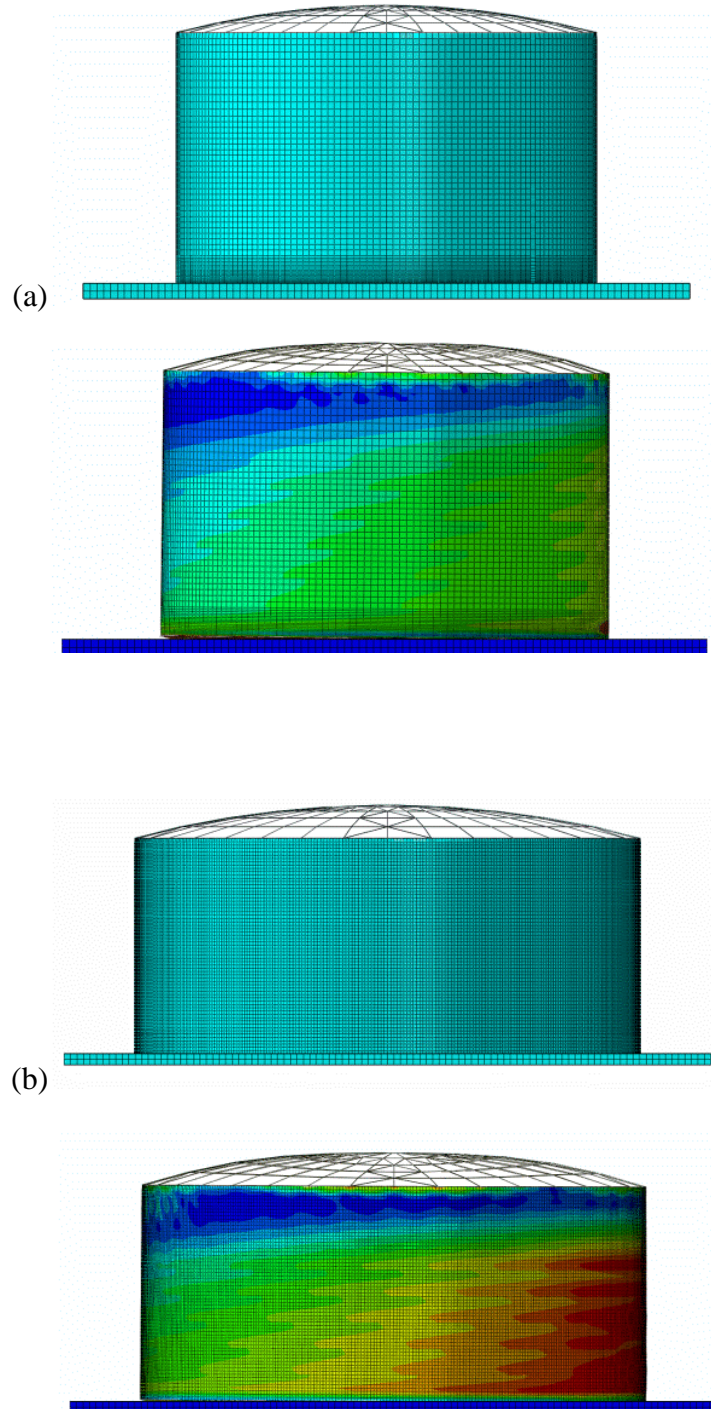
84

Figure 67: Finite element modelling of the tanks under consideration, undeformed and at the end of the analysis where uplifting occurs; (a) Tank I, (b) Tank II.

85
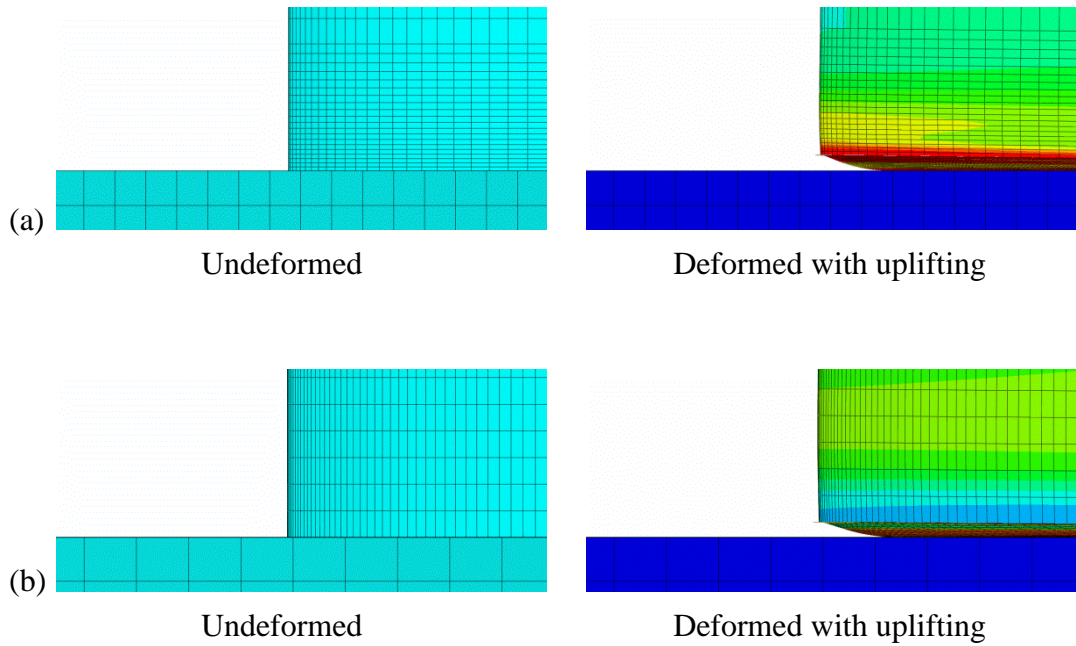
Figure 68: Uplifting of the bottom plate for (a) Tank I and (b) Tank II.
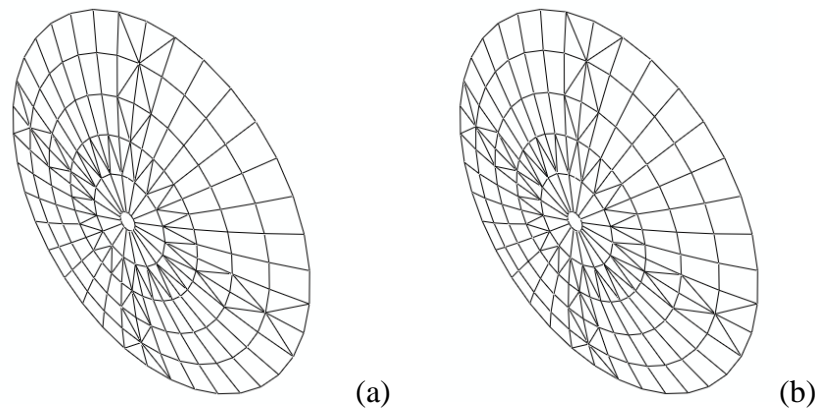
Figure 69: Tank roofs for the two tanks under consideration; (a) Tank I, (b) Tank II.

The material of the tanks is described through a von Mises (J_2) plasticity model, with isotropic hardening. The yield stress of tank and base-plate material is equal to 235 MPa, the Young's modulus is $E = 210,000$ MPa, and the hardening modulus is assumed equal to 210 MPa which corresponds to 1/1000 of Young's modulus. For the ground, an elastic material has been used with Young's modulus equal to half the modulus of steel, implying a practically non-deformable ground.

An incremental non-linear static analysis is conducted in three steps. In the first step, gravity of the tank is applied, whereas in the second step, hydrostatic pressure of the liquid is

86

activated. Finally, in the third step, horizontal hydrodynamic loading is applied, through an incremental elastic-plastic analysis with large displacements. The distribution of hydrodynamic pressures on the tank wall follows the corresponding solution of the hydrodynamic problem (e.g. Ibrahim 2005), for both the impulsive and convective component of liquid motion. More specifically, the distribution of hydrodynamic pressure is assumed for the impulsive motion:

$$P_I(\xi,\zeta,\theta,t) = C_I(\xi,\zeta)\rho H S_I \cos\varphi \tag{95}$$

where C_I is a spatial function of the non-dimensional coordinates of the tank which depends on the tank aspect ratio (Figure 3), ρ is the liquid density, H is the liquid height, R is the tank radius, S_I is the impulsive acceleration, $\xi = r/R$ and $\zeta = z/H$ are the non-dimensional coordinates assuming a cylindrical coordinate system, r, φ, z, with origin at the center of the tank bottom and the vertical z axis. For the convective motion, only the first mode is considered.

$$P_C = 1.146R\rho \frac{\cosh(1.841\gamma\zeta)}{\cosh(1.841\gamma)} J_1(1.841\xi) S_C \cos\varphi \tag{96}$$

where J_1 is the Bessel function of first order and S_C is the convective acceleration. In the above expressions, r is taken equal to R ($\xi = 1$) for determining the pressure on the lateral surface, whereas z is taken equal to zero ($\zeta = 0$) for the pressure on the bottom plate. The variation of the first mode sloshing pressures on the tank wall along the tank height for four aspect ratios can be seen in Figure 4.

The hydrodynamic pressure distribution is applied on the inner surface of the tank shell and the bottom plate through a special-purpose load-user subroutine in the ABAQUS model. The Bessel functions are approximated by appropriate polynomials.

4.4.2 Numerical Results for Tank I and Tank II

Representative results of the behavior of the two tanks are reported in the present section. Numerical results for the unanchored tank are examined and subsequently they are compared with results from the anchored tank. The general configuration of the deformed unanchored tank is shown schematically in Figure 70.
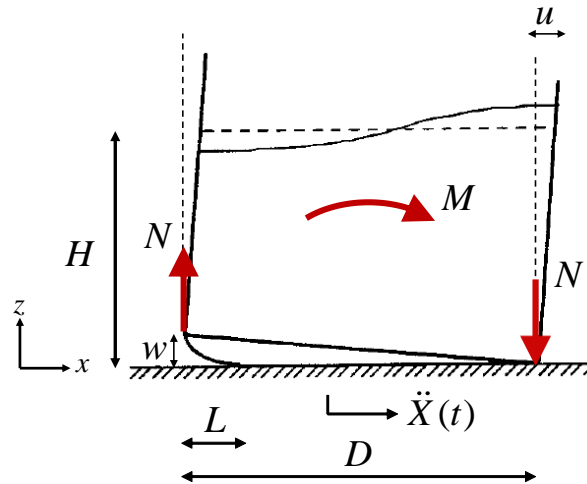
Figure 70: Uplifting parameters of an unanchored tank.

The evolution of top horizontal displacement of the two tanks is shown in Figure 71, in terms of the overturning moment M due to hydrodynamic loading. The maximum overturning moment is computed as the sum of the ringwall impulsive and convective moments of Eq. (33) and Eq. (34), scaled appropriately for each time increment of the analysis. The value of u is normalized by the liquid height H and the value of M is normalized by WH, where W is the total weight of the contained liquid, a normalization suggested in EN 1998-4. At the level of normalized overturning moment equal to 0.03 the slope of the curve significantly changes, indicating the beginning of the uplifting of the tanks and the occurrence of inelastic deformation. Furthermore, the results indicate a smaller sensitivity of the uplifting on the value of tank aspect ratio, than the one suggested by EN 1998-4.

The global behaviour of the tanks is also represented in Figure 72, which shows the maximum vertical uplift of the simulated unanchored tanks in terms of the normalized overturning moment at the tank base. The curves for aspect ratio $\gamma = H / R =$ 0.8, 1.0, 2.0 are from the work of Scharf (1990), also adopted by EN 1998-4. The comparison between the finite element results and those in EN 1998-4 also shows that the EN 1998-4 curves are non-conservative, predicting smaller uplift than one obtained by the present finite element analysis.

88
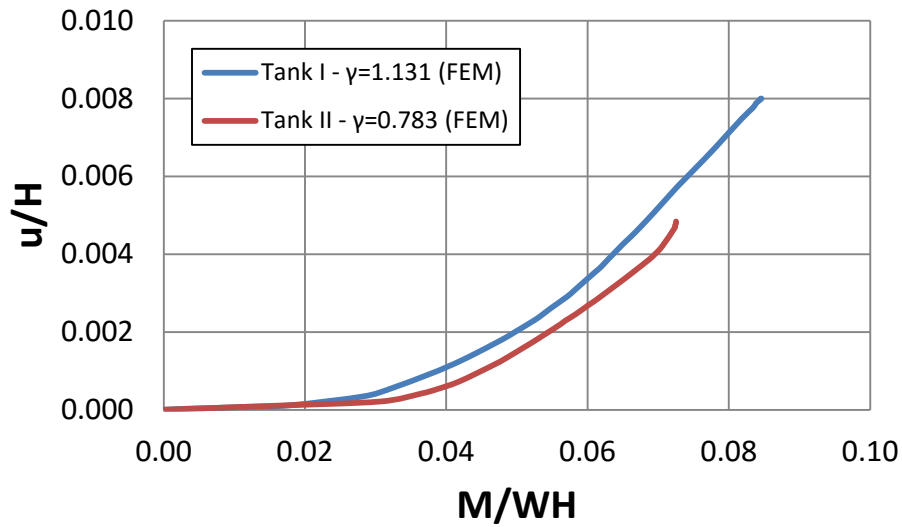
Figure 71: Overturning moment M versus top horizontal displacement u, subjected to finite element static analysis.
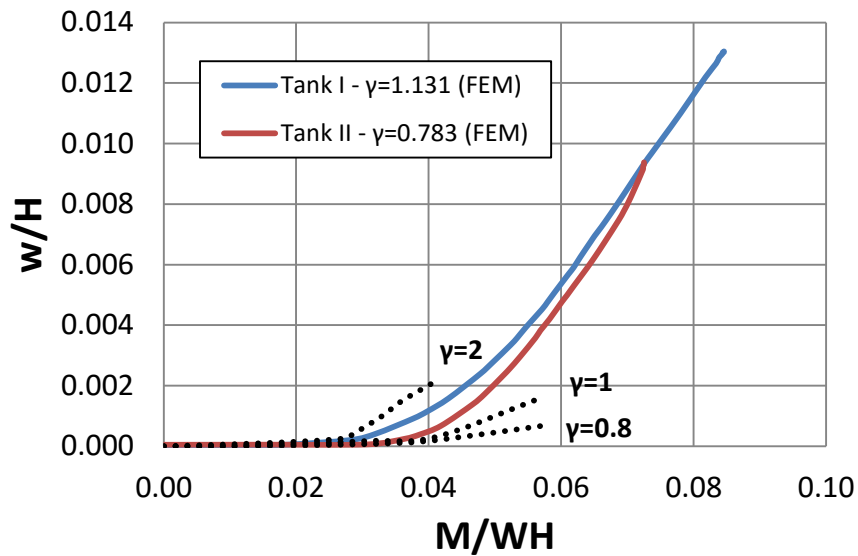
Figure 72: Maximum vertical uplift of the tank w versus overturning moment M; the present finite element results are compared with the curves for $\gamma = H / R = 0.8, 1.0, 2.0$ (Scharf 1990), adopted by EN 1998-4.

For estimating the radial membrane stresses in the plate, the calculation of length L of the uplifted part of the tank bottom is necessary. The relationship between the length of the uplifted part of the base (normalized by R, the radius of the tank) and the overturning moment (normalized by WH) is shown in Figure 73. The results indicate that the increase of the value

89

of the overturning moment causes an increase of the value of the length of the uplifted base plate, as expected.

Combining the results from Figure 72 and Figure 73 one can develop the graph of Figure 74. It is interesting to note that once uplift occurs, the dependence of L on the vertical uplift w is quasi linear. Comparing the present numerical results with those in A.9 of EN 1998-4, it is shown that the EN 1998-4 curves indicate a similar trend in their behaviour but they are somewhat conservative. With the normalization of the parameters in Figure 74 one may easily produce Figure 75, which gives the relationship between the vertical uplift and uplifted length of the tank in a more universal manner.

Figure 76 shows the increase of the compressive membrane force in the case of the unanchored tanks compared to the one of the anchored tanks. For Tank II, the effect of uplifting is small, so the ratio of the membrane forces is close to unity. Moreover, in Figure 77 the most compressed area of Tank I can be seen, for both the anchored and unanchored case.

Figure 78 to Figure 81 depict the compressive membrane forces N_a and N_u along the height for the two tanks, for anchored and unanchored conditions. It can be seen clearly that the compressive force in the case of the unanchored tanks is larger than the one in the case of the anchored tanks after uplifting occurs.
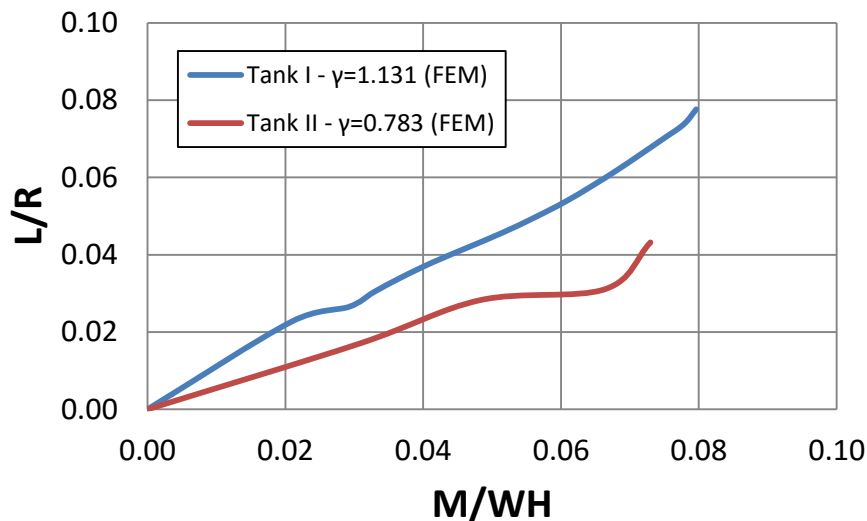
Figure 73: Normalized length of uplifted part of the base plate L versus overturning moment.

90
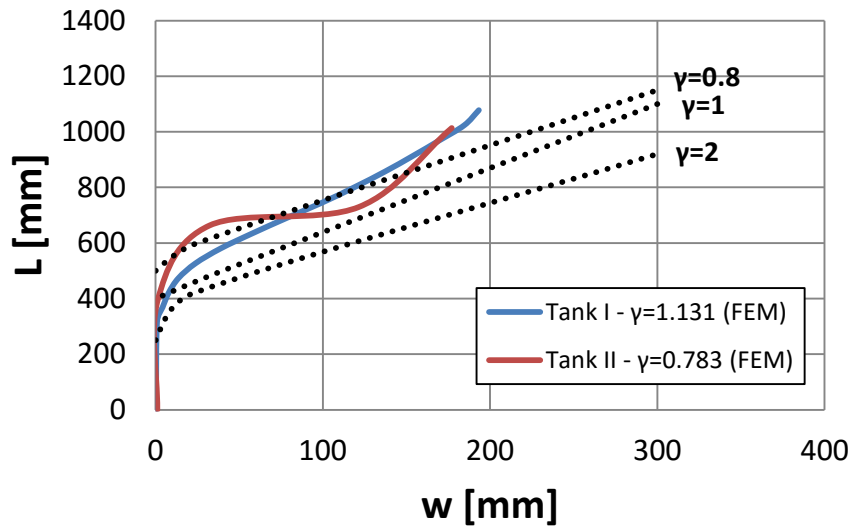
Figure 74: Length of uplifted part of the base as a function of the vertical uplift at the edge; the present finite element results are compared with the curves for $\gamma = H / R = 0.8$, 1.0, 2.0 (Scharf 1990), adopted by EN 1998-4.
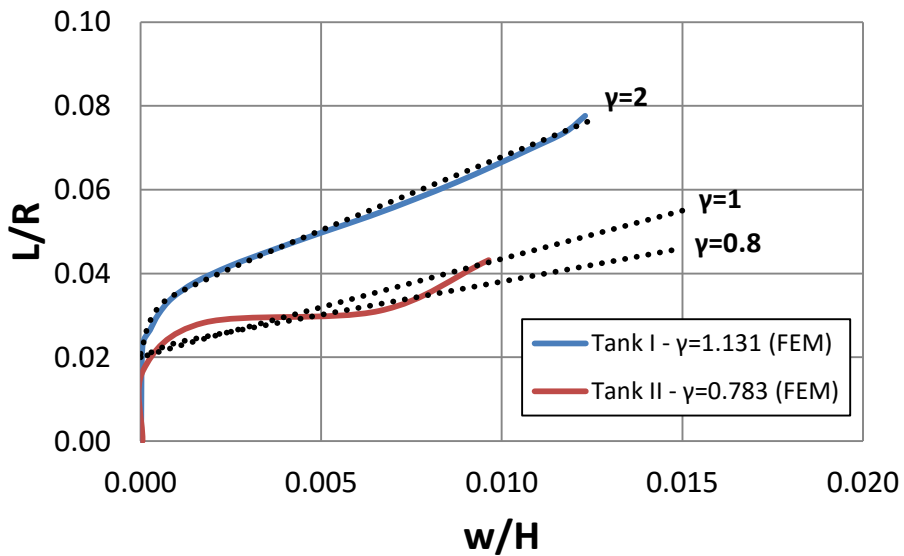
Figure 75: Normalized length of uplifted part of the base as a function of the normalized vertical uplift at the edge; the present finite element results are compared with the curves for $\gamma = H / R = 0.8$, 1.0, 2.0 (Scharf 1990), adopted by EN 1998-4.
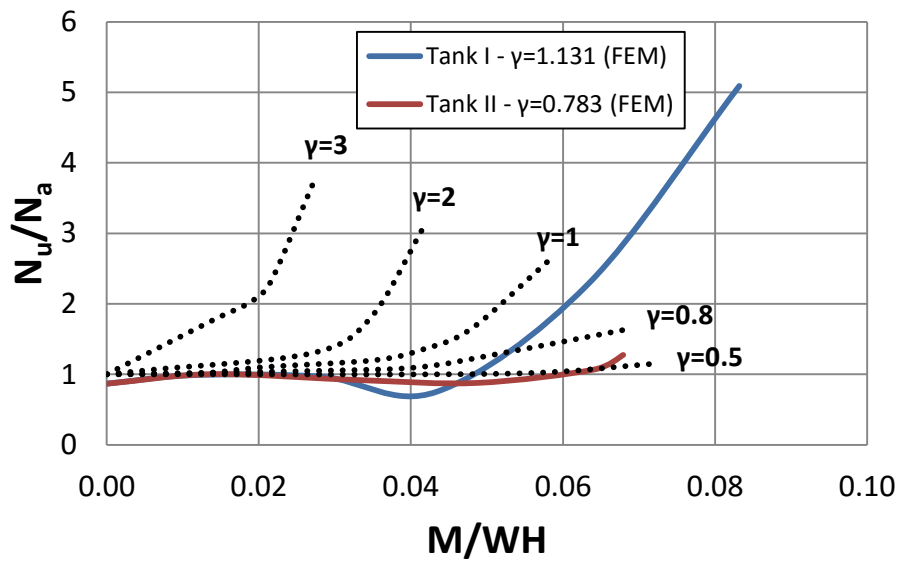
Figure 76: Ratio of maximum compressive axial membrane forces for the unanchored over the anchored tank versus the overturning moment; the present finite element results are compared with the curves for $\gamma = H / R =$ 0.8, 1.0, 2.0 (Scharf 1990), adopted by EN 1998-4.
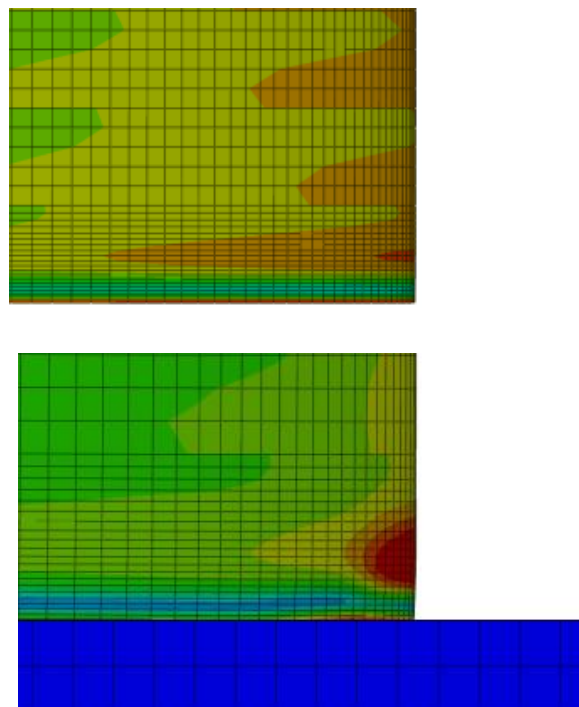
Figure 77: The compressed area of Tank I for the (a) anchored case and (b) unanchored case.

92
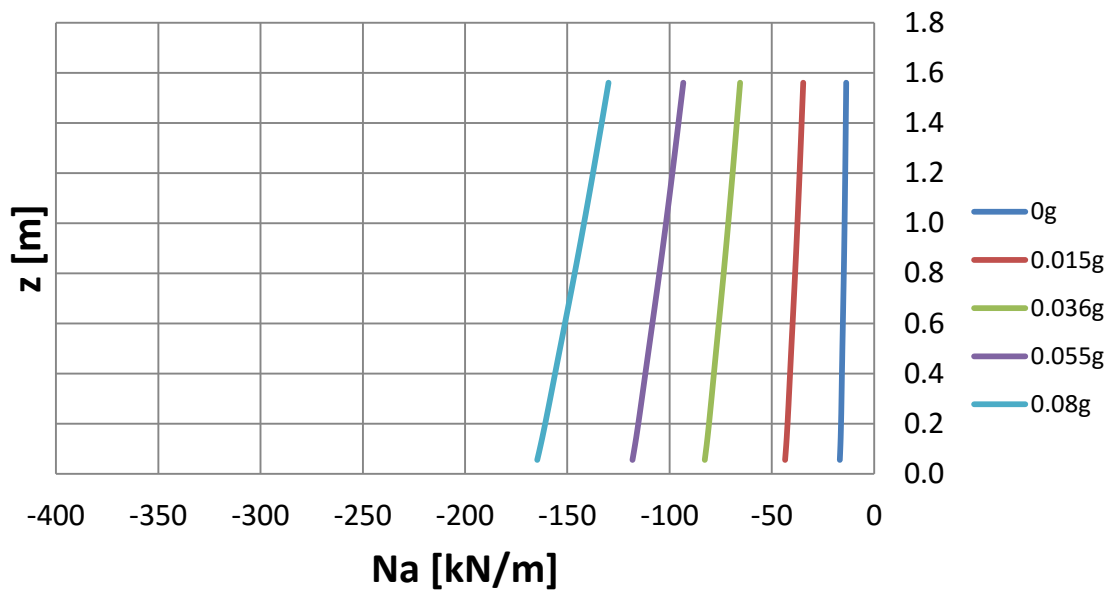
Figure 78: Compressive membrane forces in the meridional direction of anchored Tank I.
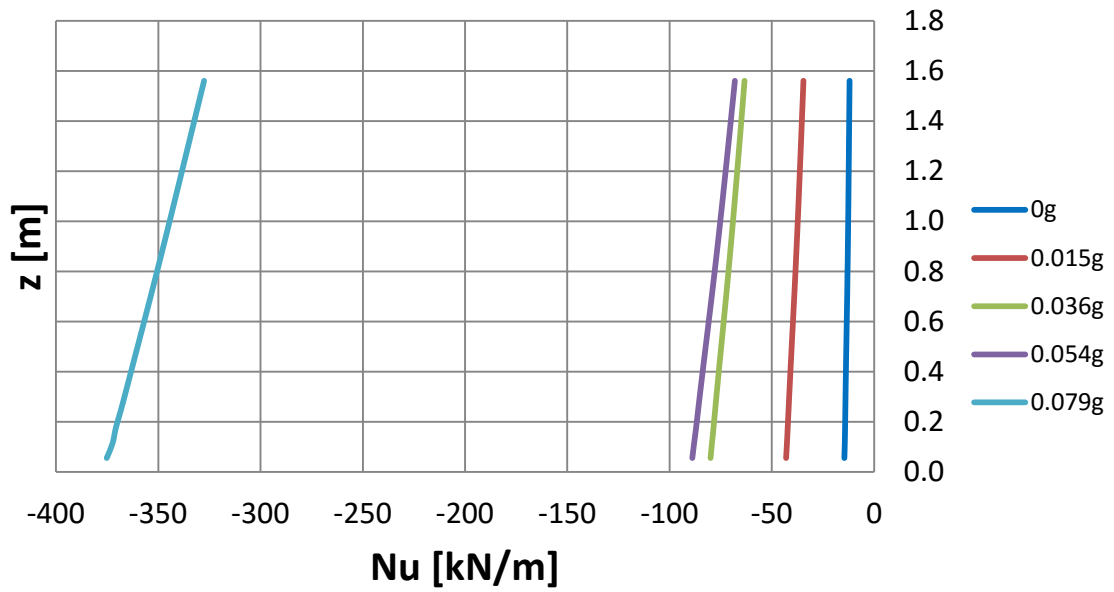
Figure 79: Compressive membrane forces in the meridional direction of unanchored Tank I.

93
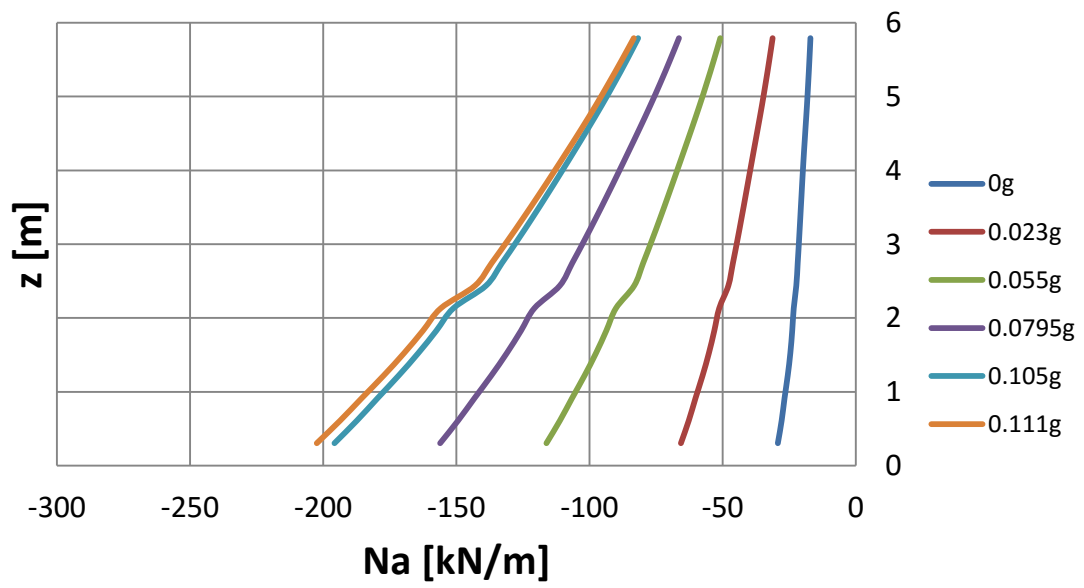
Figure 80: Compressive membrane forces in the meridional direction of anchored Tank II.
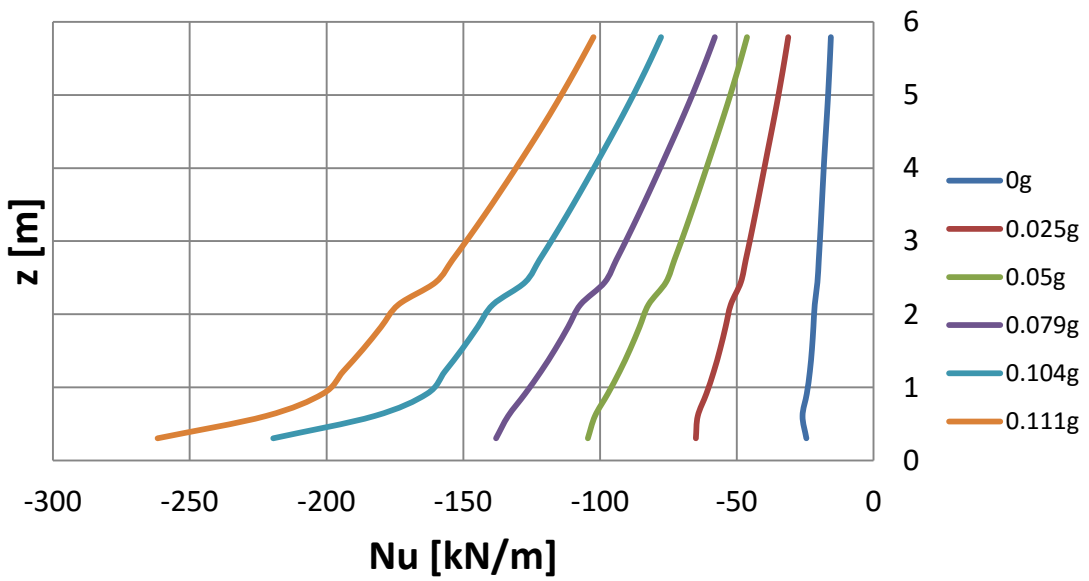
Figure 81: Compressive membrane forces in the meridional direction of unanchored Tank II.

94

The relationship between the membrane forces, at the uplifting and compression side of the anchored and unanchored tanks, is depicted in Figure 83 and Figure 84. These forces are also compared with the analytical formula of Eq. (97):

$$N = \pm \frac{M}{\pi R^2} - w_t \tag{97}$$

where M is the ringwall moment (i.e. the overturning moment due to hydrodynamic loading just above the base plate), R is the radius of the tank and w_t is the load per unit circumferential length because of shell and roof weight acting at the base of shell. The positive sign, "+", is used for the calculation of the uplifting membrane force and the negative sign, "-", for the compressive membrane force. Here, for the sake of uniformity, the compressive membrane forces are given in absolute values. Figure 82 and Figure 83 show that compressive membrane forces are the same for the anchored and unanchored tank for small values of overturning moment. At the level of normalized overturning moment equal to 0.03 the slope of N_u significantly increases due to the beginning of the uplifting of the tank. Moreover, the simple analytical formula gives good predictions with respect to finite element results for the case of the anchored tank.

The comparison of the uplifting membrane forces and the simple analytical formula (Figure 84, Figure 85) shows that there is good agreement between the three lines when there is no uplift of the tank. However, when uplifting occurs, the analytical formula may not describe the uplifting behavior of the tanks.

Figure 86 and Figure 87 show the relationship between the membrane uplifting axial force versus the vertical uplift of the tank. When the tank starts to uplift, there is a significant increase in the value of the uplifting force N_u.

95
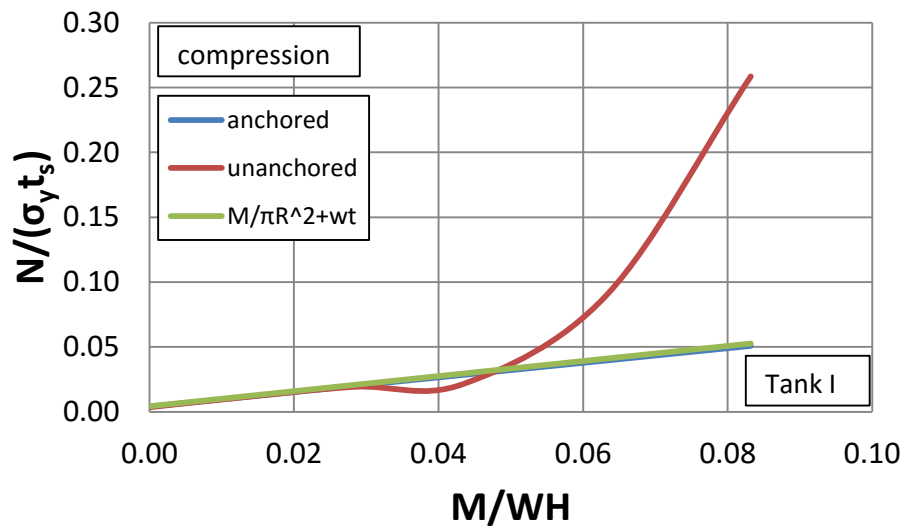
Figure 82: Absolute value of membrane compressive axial forces in the case of the anchored and unanchored simulated tanks and the corresponding analytical formula in terms of the overturning moment for Tank I.
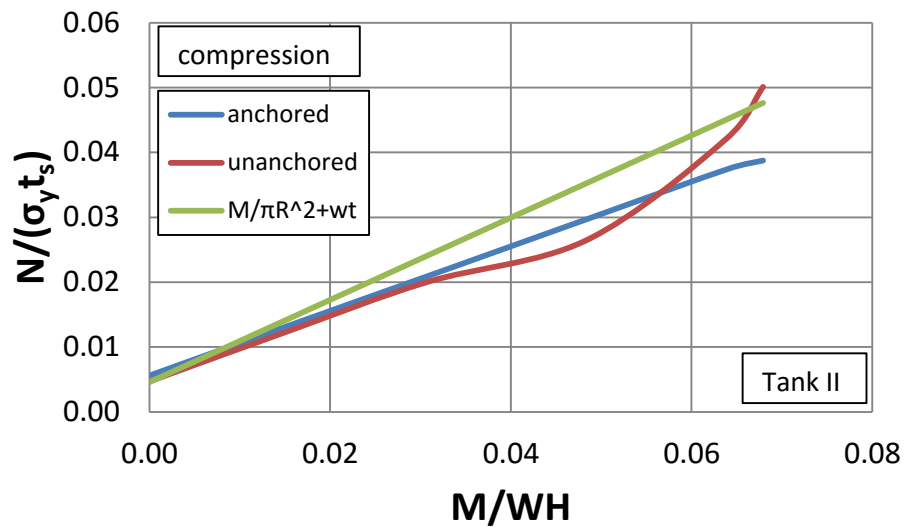
Figure 83: Absolute value of membrane compressive axial forces in the case of the anchored and unanchored simulated tanks and the corresponding analytical formula in terms of the overturning moment for Tank II.
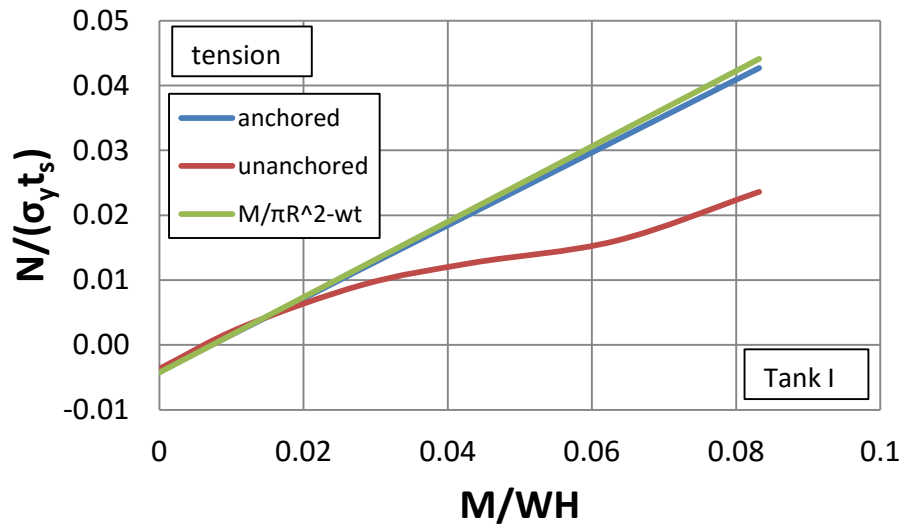
Figure 84: Membrane uplifting forces in the case of the anchored and unanchored simulated tanks and the corresponding analytical formula in terms of the overturning moment for Tank I.
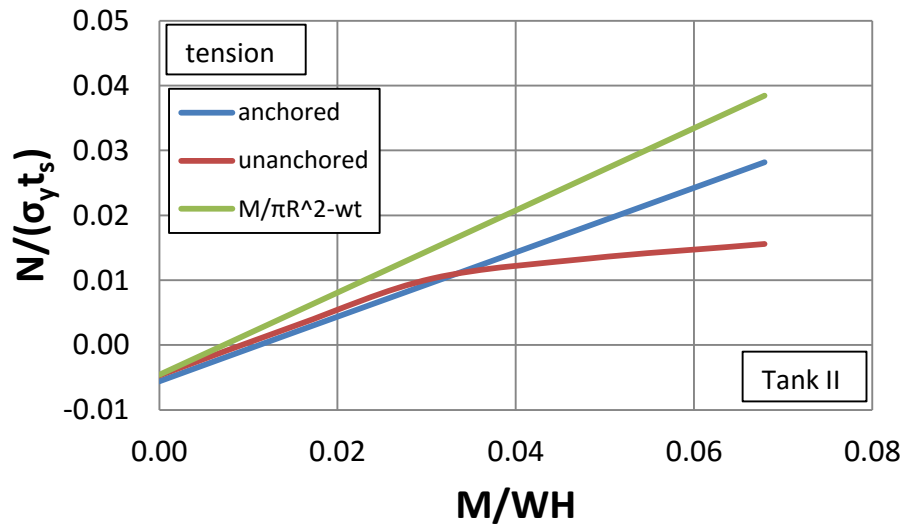
Figure 85: Membrane uplifting forces in the case of the anchored and unanchored simulated tanks and the corresponding analytical formula in terms of the overturning moment for Tank II.

97
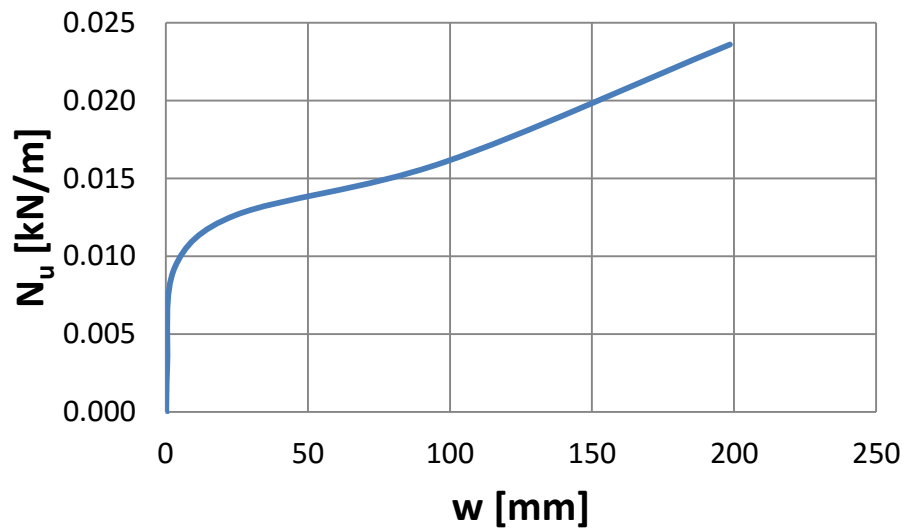
Figure 86: Membrane uplifting axial force versus vertical uplift size of Tank I.
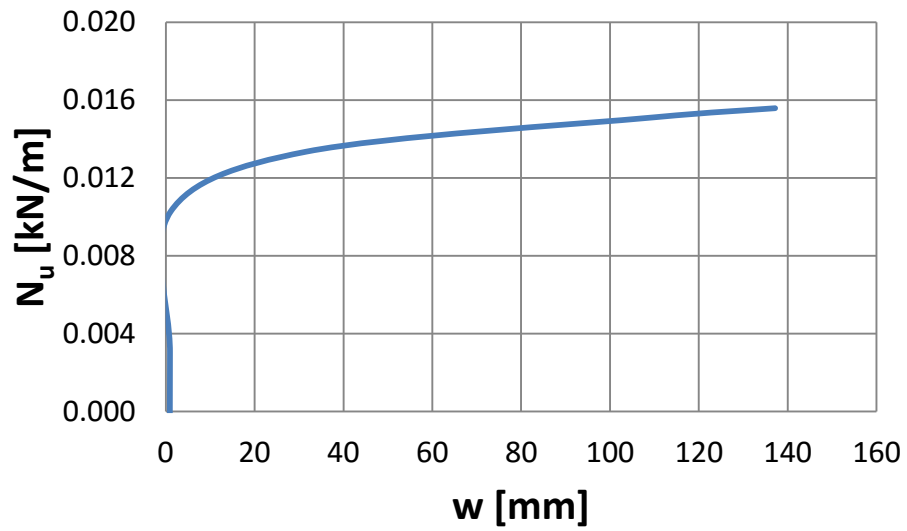
Figure 87: Membrane uplifting axial force versus vertical uplift size of Tank II.

This relationship can be shown alternatively in the diagrams of Figure 88 and Figure 89. In these graphs, ψ is the average rotation of the tank base due to uplifting (rocking angle), calculated as follows:

$$\psi = \frac{w}{D} \tag{98}$$

The results show that the $M - \psi$ relationship can be approximated with a bilinear expression also depicted in the same graphs. The expressions in the graphs are used in the dynamic analysis.

The equivalent plastic strain of the tank base plate is shown in Figure 90 and Figure 91 for Tank I and II respectively, in terms of the horizontal coordinate x, shown in Figure 92. The equivalent plastic strain becomes maximum at two locations of the base plate, (a) at the junction of the tank wall and the base plate and (b) at a small distance from the weld. At these two locations significant plastic yielding develops. The same behavior applies for the logarithmic strain, shown in Figure 93 and Figure 94 for Tank I and II respectively, in terms of the horizontal coordinate x. These locations are depicted in Figure 95 and Figure 96, for Tank I and II respectively, at various uplifting configurations.
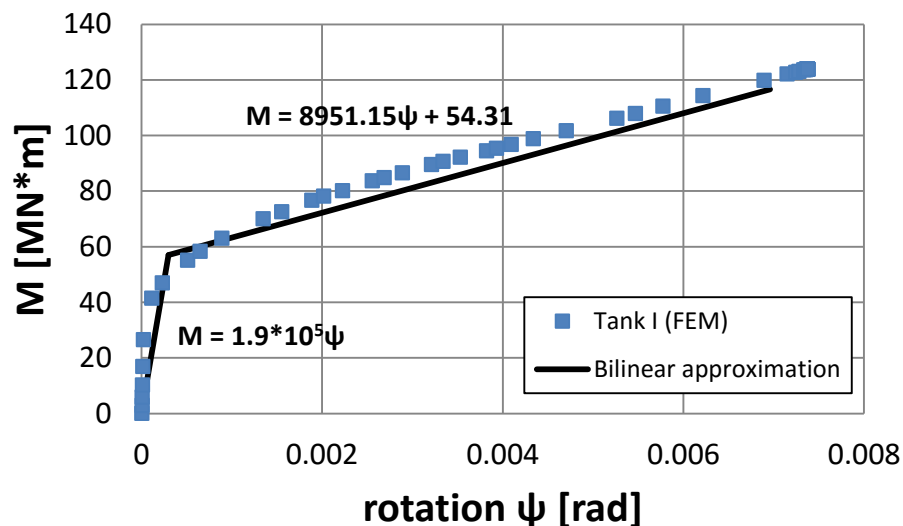
Figure 88: Overturning moment versus rotation subjected to finite element static analysis for Tank I.

99
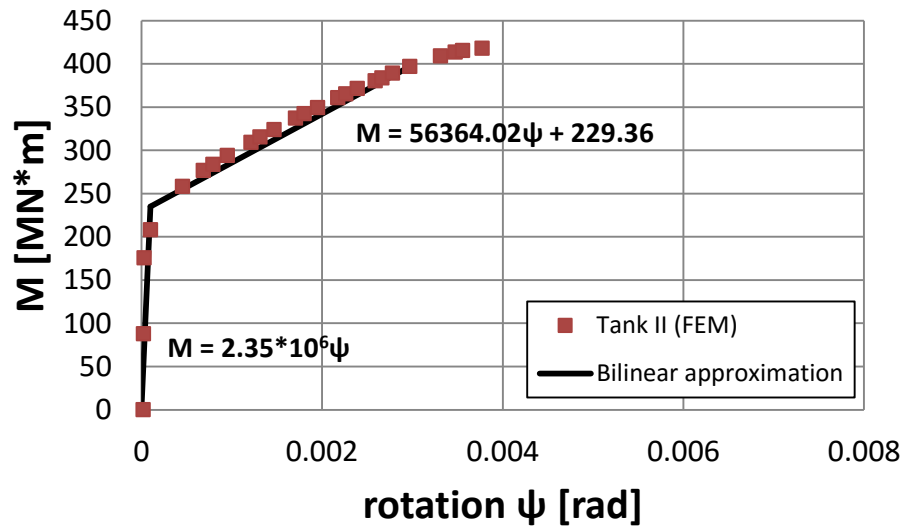
Figure 89: Overturning moment versus rotation subjected to finite element static analysis for Tank II.
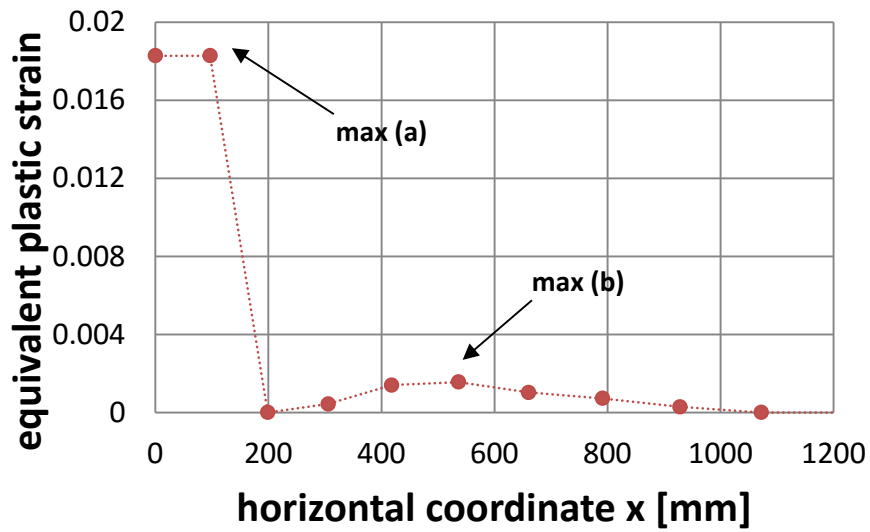
Figure 90: Equivalent plastic strain at the nodes of the tank base plate in terms of the horizontal coordinate x for Tank I, on the inner surface of the base plate at 0.106g.

100
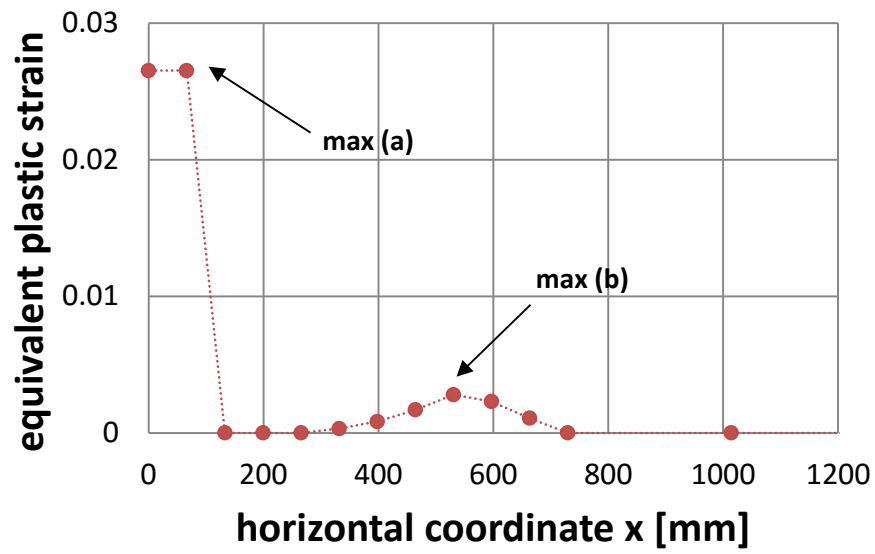
Figure 91: Equivalent plastic strain at the nodes of the tank base plate in terms of the horizontal coordinate x for Tank II, on the inner surface of the base plate at 0.119g.
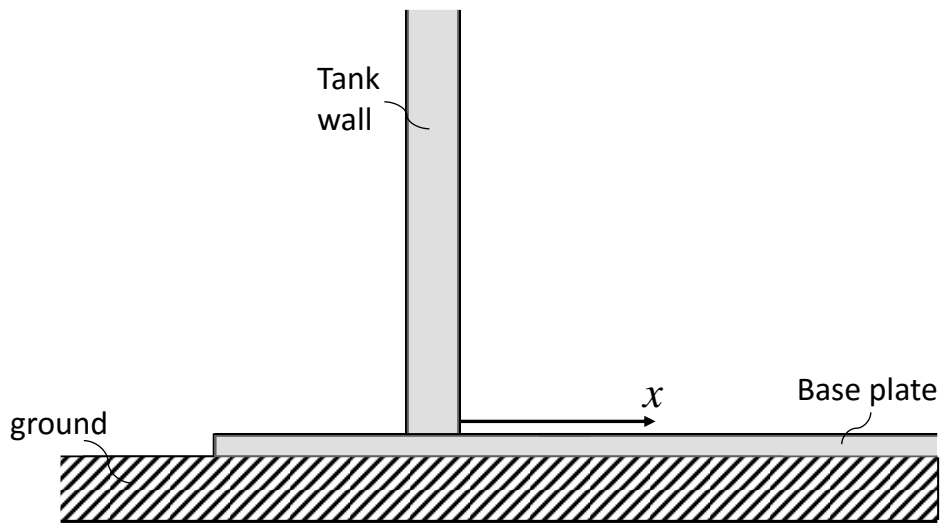
Figure 92: Horizontal Coordinate x .
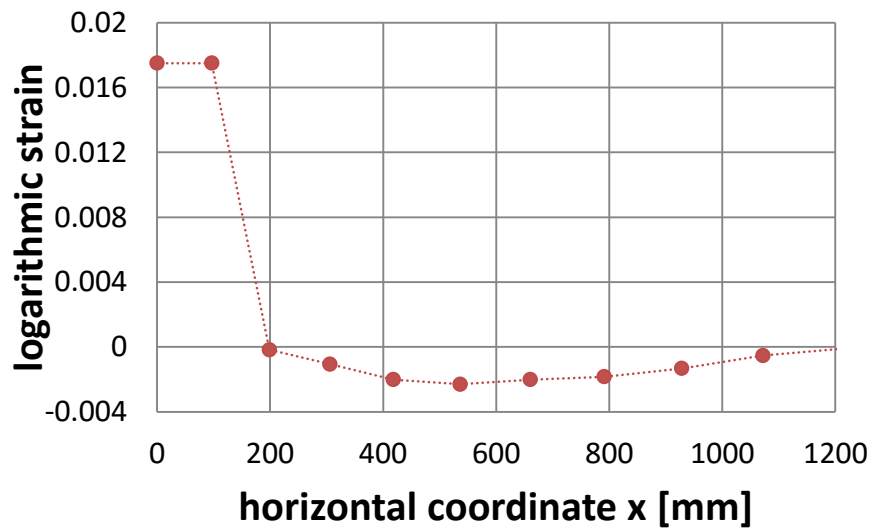
Figure 93: Logarithmic strain at the nodes of the tank base plate in terms of the horizontal coordinate x for Tank I, on the inner surface of the base plate at 0.106g.
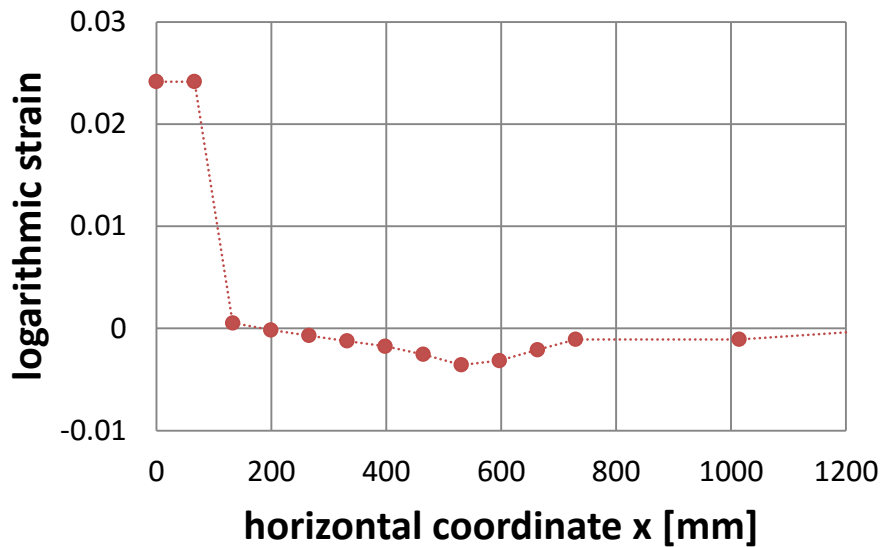
Figure 94: Logarithmic strain at the nodes of the tank base plate in terms of the horizontal coordinate x for Tank II, on the inner surface of the base plate at 0.119g.

102
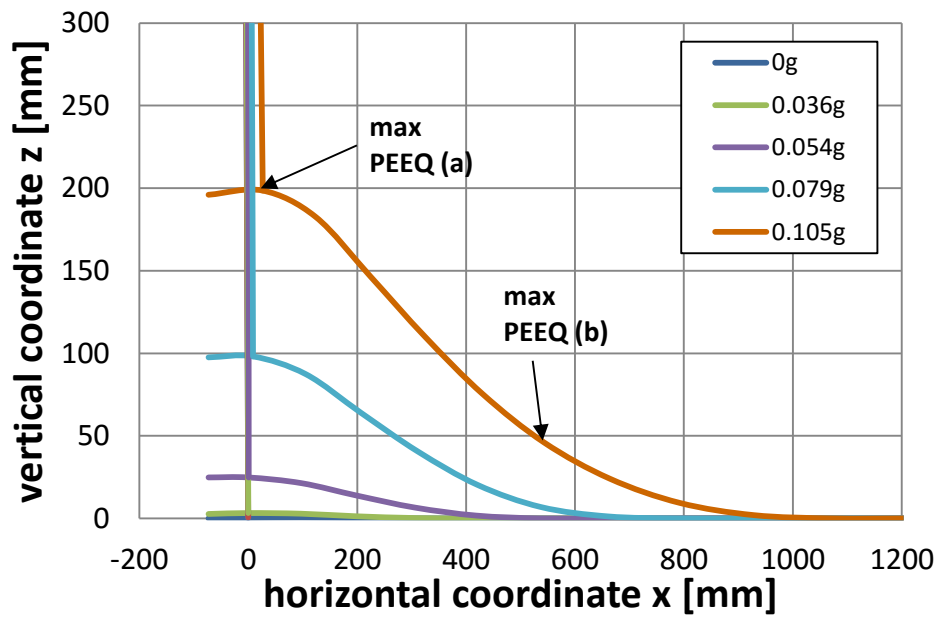
Figure 95: Deformed bottom plate of Tank I showing the two points of maximum equivalent plastic strain.
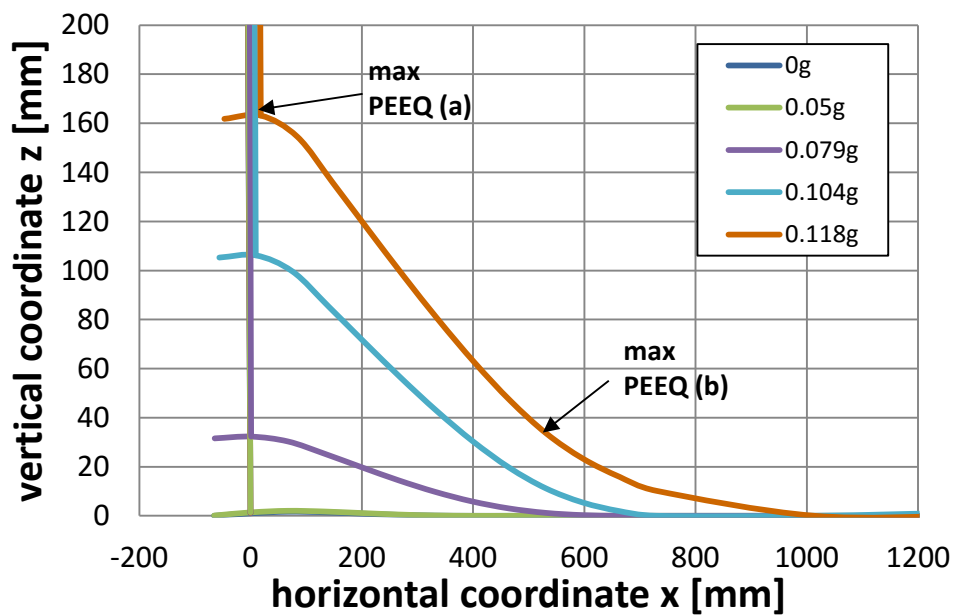
Figure 96: Deformed bottom plate of Tank II showing the two points of maximum equivalent plastic strain.

103

4.5 Nonlinear dynamic analysis of tanks

4.5.1 Lateral Seismic Action

4.5.1.1 Model description

The tank-liquid system is simulated with a simplified model that accounts for the hydrodynamic response of the liquid. The tank is excited by a horizontal base-ground seismic acceleration motion, $\ddot{X}_g$. From basic hydrodynamics, the motion of the fluid in a liquid storage tank can be decomposed in: (a) the impulsive motion which corresponds to the motion of the fluid that follows the motion of the container and (b) the convective motion which represents liquid sloshing. For the sake of completeness, anchored tank modeling is described first. Subsequently, the case of unanchored tanks is presented. The ultimate purpose of this analysis is the calculation of local strain at the shell-bottom plate connection, towards fatigue assessment. Previous experimental works indicated that this is a possible failure mode in unanchored tanks (Prinz and Nussbaumer 2012).

4.5.1.2 Anchored tanks

In anchored tanks, due to the fact that sloshing natural frequencies are substantially lower than the natural frequencies of the impulsive motion, the two motions can be considered independently, performing an "uncoupled" analysis (Veletsos and Yang 1977).

The convective motion is modeled through an appropriate linear oscillator at an appropriate height (h_C), which represents the first sloshing mode (Figure 97). Consideration of additional sloshing modes is possible; introducing additional linear oscillators, but their effects on the total seismic response is not significant and may be omitted for the purposes of the present analysis (Pappa et al. 2011). The values of sloshing frequency ω_C , mass m_C and height h_C depend on the tank aspect ratio (Ibrahim 2005), whereas for oil and water tanks, a value of 0.5% can be considered for the damping ratio of the sloshing motion ξ_C .

The impulsive motion includes the effects of tank shell deformation, and can be also expressed in terms of a linear oscillator at a certain height. The impulsive frequency ω_I , mass

<center>104</center>

m_I and height h_I depend on the aspect ratio of the tank and the tank shell thickness. The damping ratio of the impulsive motion ξ_I can be taken equal to 5%. More details on the above model for deformable steel tanks under lateral seismic loading can be found in the papers by Veletsos and Yang (1977) and Ibrahim (2005).
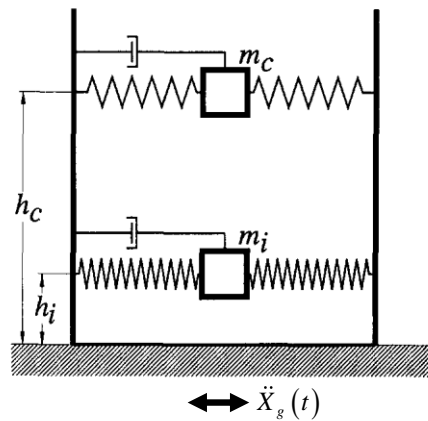
Figure 97: Simplified model for anchored liquid storage tank (Malhotra 2000).

Equations of motion

The impulsive motion is described by the equation:

$$\ddot{a}_I(t) + 2\xi_I \omega_I \dot{a}_I(t) + \omega_I^2 a_I(t) = -\ddot{X}_g(t) \tag{99}$$

and the convective motion:

$$\ddot{a}_C(t) + 2\xi_C \omega_C \dot{a}_C(t) + \omega_C^2 a_C(t) = -\ddot{X}_g(t) \tag{100}$$

where a_I and a_C are the impulsive and convective generalized coordinates, $\ddot{a}_I$ and $\ddot{a}_C$ are the corresponding accelerations and ω_I and ω_C are the impulsive and convective frequencies. The method of solution is described in the Annex.

The total impulsive and convective accelerations of the system are calculated considering the following change of variables:

$$\ddot{u}_I(t) = \ddot{a}_I(t) + \ddot{X}_g(t) \tag{101}$$

$$\ddot{u}_C(t) = \ddot{a}_C(t) + \ddot{X}_g(t) \tag{102}$$

105

so that the overturning moment is calculated as follows:

$$M(t) = m_I \ddot{u}_I(t) h_I + m_C \ddot{u}_C(t) h_C \tag{103}$$

and the maximum compressive-tensile force per unit circumferential length:

$$N = \sigma t = \frac{M}{I} R t = \frac{1.273 M}{D^2} \tag{104}$$

The above equation refers to meridional force due to hydrodynamic loading only. Hydrostatic and dead load contributions to this compressive force should be considered in the course of design practice.

4.5.1.3 Unanchored tanks

The major feature of unanchored tank seismic response is base uplifting. The basic features of the model described above for anchored liquid storage tanks are also applicable in the present case. The impulsive motion should include tank rotation due to uplifting, using an appropriate rotational spring at the tank base, as shown in Figure 98. A first attempt to model this "spring" has been reported by Malhotra and Veletsos (1994c). A recent effort has been reported by Vathi and Karamanos (2014a), Vathi and Karamanos (2014b), Vathi and Karamanos (2015) and it is described in detail in the present dissertation. The key modelling issue for accurate modeling is the $M - \psi$ relationship (Figure 88) obtained in the static analysis described previously.
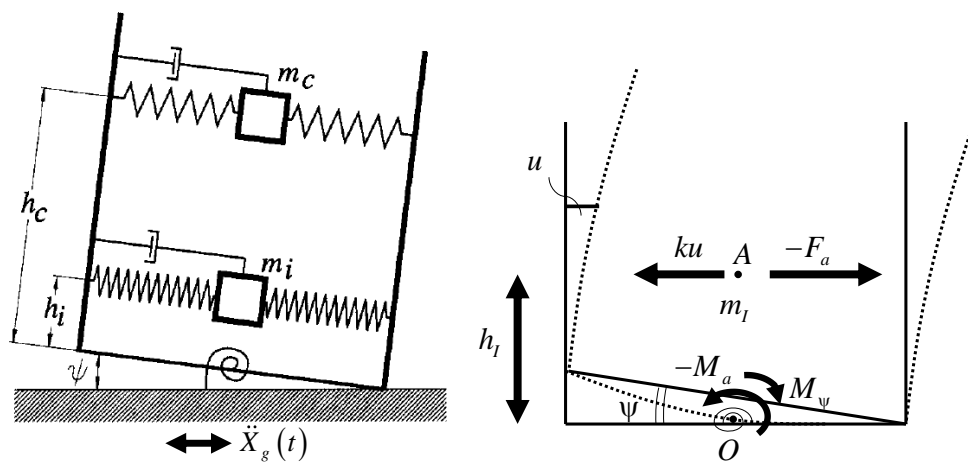
Figure 98: Simplified model for unanchored liquid storage tank; point O is the tank base center and point A is the "impulsive" center.

Equations of motion

Because of uplift, the equations of motion are more complex than those used in the anchored case containing two degrees of freedom. For simplicity, it is assumed that the convective component of response is negligible on the overturning moment. Considering a mass-spring model for the impulsive motion, equilibrium of inertia and "elastic" forces in the horizontal direction requires:

$$F_a + ku = 0 \tag{105}$$

or

$$m_I\left(\ddot{u} + \ddot{X}_g + \ddot{\psi}h_I\right) + ku = 0 \tag{106}$$

and setting $k = \omega_I^2 m_I$ one obtains:

$$m_I\ddot{u} + m_I h_I \ddot{\psi} + m_I \omega_I^2 u = -m_I \ddot{X}_g \tag{107}$$

The equilibrium of moments with respect to point O results in:

$$M_a + M_\psi + m_I h_I\left(\ddot{u} + \ddot{X}_g\right) = 0 \tag{108}$$

and for $M_a = I_O\ddot{\psi}$:

$$m_I h_I \ddot{u} + I_O \ddot{\psi} + M_\psi\left(\psi\right) = -m_I h_I \ddot{X}_g \tag{109}$$

where I_O is the rotational moment of inertia of the impulsive part of the liquid, with respect to point A. Setting $\delta = h_I\psi$, the above equations become:

$$m_I\ddot{u} + m_I\ddot{\delta} + m_I\omega_I^2 u = -m_I\ddot{X}_g \tag{110}$$

$$m_I\ddot{u} + \left(\frac{I_O}{h_I^2}\right)\ddot{\delta} + \frac{1}{h_I}M_\psi\left(\psi\right) = -m_I\ddot{X}_g \tag{111}$$

The equations are nonlinear because of the nonlinear spring law $M_\psi\left(\psi\right)$ and can be written in incremental form as follows, where appropriate damping terms are added:

$$m_I\Delta\ddot{u} + m_I\Delta\ddot{\delta} + + c_1\Delta\dot{u} + m_I\omega_I^2\Delta u = -m_I\Delta\ddot{X}_g \tag{112}$$

107

$$m_I \Delta \ddot{u} + \left(\frac{I_O}{h_I^2} \right) \Delta \ddot{\delta} + c_2 \Delta \dot{\delta} + \frac{1}{h_I^2} K_\psi \Delta \delta = -m_I \Delta \ddot{X}_g \tag{113}$$

noting that $\Delta M_\psi(\psi) = K_\psi \Delta \psi$. The first equation expresses the dynamic equilibrium in the horizontal direction due to impulsive motion of the tank, and the second equation is the dynamic equilibrium of the tank against overturning.

In equations (112) and (113), $c_1 = c_I = 2\xi_I m_I \omega_I$ is the damping coefficient for impulsive motion, with a damping ratio $\xi_I = 5\%$, whereas $c_2 = 2\xi_O \sqrt{K_\psi I_O / h_I^4}$ is the damping coefficient for the rotational movement of the tank, where a damping ratio ξ_O of the uplifting (rocking) motion equal to 10% is considered.

The system of equations (112) and (113) is solved using Newmark's method (Bathe 1996) considering the $M - \psi$ relationship, shown in Figure 88 to obtain the values of lateral and rotational accelerations, velocities and displacements at each time increment, as outlined in the Annex.

It is interesting to note that the equations of motion proposed in the paper by Malhotra and Veletsos are the following, neglecting damping terms:

$$m_I \ddot{u}_0 + k(u_0 - \psi h_I) = -m_I \ddot{X}_g \tag{114}$$

$$k(u_0 - \psi h_I) h_I = M_\psi(\psi) \tag{115}$$

Setting $u = u_0 - \psi h_I$, the above equations become:

$$m_I(\ddot{u} + \ddot{\psi} h_I) + ku = -m_I \ddot{X}_g \tag{116}$$

$$kuh_I = M_\psi(\psi) \tag{117}$$

By solving Eq.(116) for ku and substituting into Eq.(117), the second equation becomes:

$$m_I(\ddot{u} + \ddot{\psi} h_I) h_I + m_I \ddot{X}_g h_I + M_\psi(\psi) = 0 \tag{118}$$

Setting $\delta = h_I \psi$, Eq.(116) and Eq. (118) become:

$$m_I \ddot{u} + m_I \ddot{\delta} + m_I \omega_I^2 u = -m_I \ddot{X}_g \tag{119}$$

108

$$m_I \ddot{u} + m_I \ddot{\delta} + \frac{1}{h_I} M_\psi (\psi) = -m_I \ddot{X}_g \qquad (120)$$

Eq. (119) is identical to Eq. (110), but Eq. (120) is similar but not identical to Eq. (111). They become identical if one assumes that $I_O = m_I h_I^2$. In the present study, in order to account for the rotational motion of the tank, the rotational moment of inertia of the impulsive part of the liquid, I_O, has been computed with respect to the tank base plate according to Steiner's theorem as follows:

$$I_O = m_I \left(\frac{R^2}{4} + \frac{H^2}{3} \right) \qquad (121)$$

Calculation of local strain at the base plate connection

Upon calculation of the uplifting angle $\psi(t)$ and the overturning moment $M(t)$, the uplifting size (i.e. the uplifting displacement at the tank edge) is $w(t) = D\psi(t)$ and the membrane meridional compression can be calculated from Eq. (104). Furthermore, the maximum strain at the shell-plate connection can be estimated using an assumed-shape cosine function for the deformation of the base plate. Based on the numerical results shown in Figure 95 and Figure 96, it is reasonable to assume that the plate deflects along the radial direction in the following shape with displacement w_1:

$$w_1(x) = \frac{w}{2} \left(\cos \frac{\pi x}{L} + 1 \right) - \frac{\Delta}{2} \left(1 - \cos \frac{2\pi x}{L} \right) \qquad (122)$$

In Eq.(122), x is the coordinate along the radial direction of the base plate, with origin ($x = 0$) at the tank edge (i.e. at the wall-base plate junction) and w is the uplift height (at $x = 0$). In addition, the second term in the right-hand side refers to the deflection of a fixed-fixed beam of height $h = t_b$, width b, length L fixed to both of its ends subjected to uniform distributed load q (due to hydrostatic pressure p) along its length, where Δ is the maximum value at mid-span. The value of Δ can be calculated from the hydrostatic pressure p using simple Mechanics of Materials as follows:

$$\Delta = \frac{1}{384}\frac{qL^4}{EI} = \frac{1}{384}\frac{p\cancel{b}L^4}{\dfrac{E\cancel{b}t_a^3}{12(1-v^2)}} = \left(\frac{pL^3}{Et_a^3}\right)\frac{(1-v^2)L}{32} \simeq \frac{L}{35}\left(\frac{p}{E}\right)\left(\frac{L}{t_a}\right)^3 \tag{123}$$

where t_a is the thickness of the annular plate. The two terms of Eq. (122) are also depicted in Figure 99. The validity of this equation is shown in Figure 100 and Figure 101, where it is compared with the finite element results of Figure 95 and Figure 96, for Tank I and Tank II respectively. It is shown that this equation provides good results, especially for small uplift sizes. The reason is the tank bottom plate consists of a base plate and annular plate with different thicknesses. For larger uplift values, part of the base plate may participate in the uplifting process, apart from the annular plate of the tank, so the thickness of the uplifted part of the tank won't be uniform. In this case, the value of the thickness of the annular plate in the denominator of Eq. (123) may need to be corrected to take into account this change of thickness.

$$w_1(x) = \frac{w}{2}\left(\cos\frac{\pi x}{L}+1\right) - \frac{\Delta}{2}\left(1-\cos\frac{2\pi x}{L}\right)$$
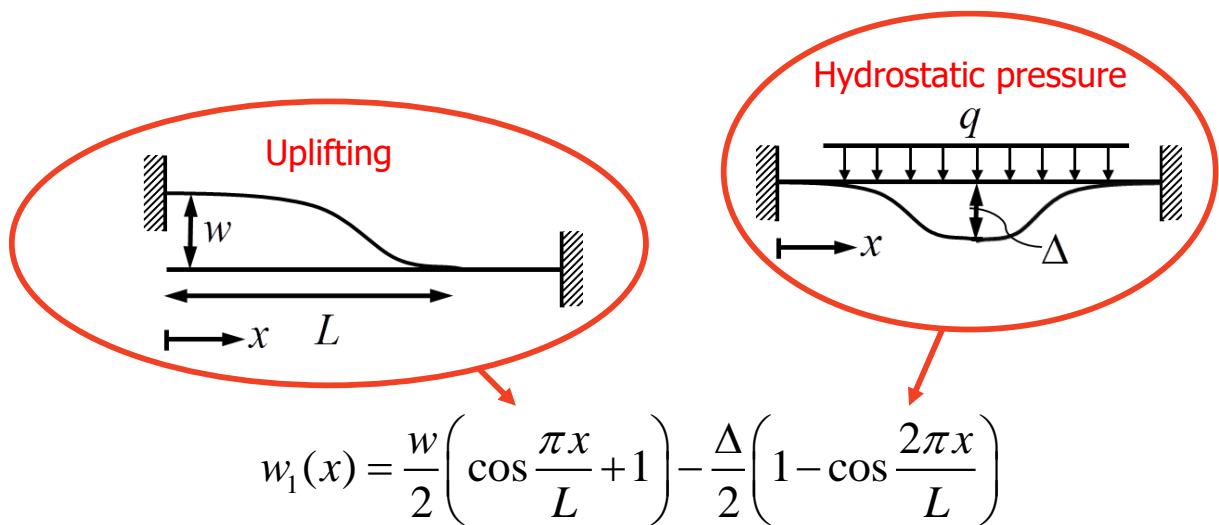
Figure 99: Schematic representation of the two terms of the assumed shape function of base plate deflection [Eq. (122)].

110
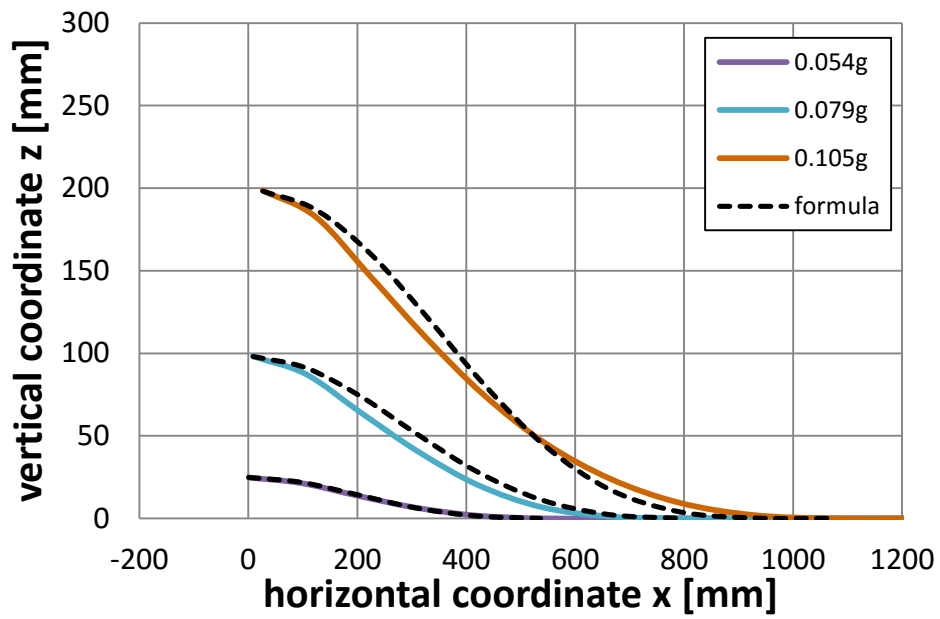
Figure 100: Deformed bottom plate of Tank I; the finite element results of Figure 95 are compared with Eq. (122)

.
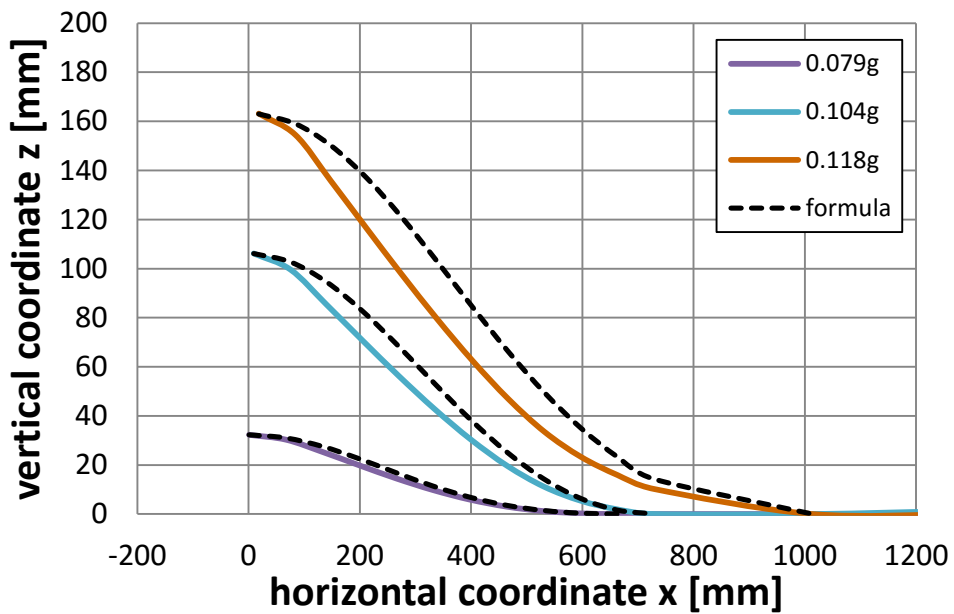
Figure 101: Deformed bottom plate of Tank II; the finite element results of Figure 96 are compared with Eq. (122)

111

Subsequently, the corresponding bending strain at the plate can be estimated as:

$$\varepsilon(x) = \frac{t}{2} \frac{d^2 w_1(x)}{dx^2} \tag{124}$$

Inserting Eq. (122) into Eq. (124) one obtains the following expression for the bending strain:

$$\varepsilon(x) = -\frac{\pi^2 t}{4L^2} \left(w \cos \frac{\pi x}{L} + 4\Delta \cos \frac{2\pi x}{L} \right) \tag{125}$$

where the maximum strain is located at $x = 0$ and is equal to:

$$\varepsilon_{max} = \varepsilon(0) = \frac{\pi^2 t}{4L^2} (w + 4\Delta) \tag{126}$$

Furthermore, in the above equations, the uplifting length L should be considered as a function of uplifting size w, as indicated in Figure 74. Assuming the following expression of the uplifting length:

$$w = \beta L^4 \tag{127}$$

where β is a constant, one obtains:

$$\varepsilon(x) = \frac{\pi^2 L^2 t}{4} \left(\beta \cos \frac{\pi x}{L} + \frac{4p}{35Et^3} \cos \frac{2\pi x}{L} \right) \tag{128}$$

and the maximum strain is

$$\varepsilon_{max} = \frac{\pi^2 t L^2}{4} \left(\beta + \frac{4p}{35Et^3} \right) \tag{129}$$

Fatigue analysis

The time history of bending strains to calculate the loading spectrum is an irregular function. Therefore, the "rainflow cycle counting" method is employed. With this method, the strain ranges $\Delta \varepsilon_i$ and the corresponding numbers of cycles for each range, n_i are calculated. In order to determine tank failure due to fatigue subjected to a specific seismic input, this spectrum should be combined with an appropriate fatigue curve. In the present study, the linear $\log \Delta \varepsilon - \log N$ fatigue curve shown in Figure 102 is used. Values of $N > 10^5$ cycles ($\log N >$

112

5) correspond to high-cycle fatigue and are taken from the provisions of BS 7608, for T-joint plated welded detail of Class F2 (Table 8 of BS 7608). For smaller numbers of cycles, the log-log line is extended linearly into the low-cycle fatigue regime. It should be noted that the left end of the curve ($N=1$) indicates $\Delta\varepsilon=5\%$ which corresponds to static loading, a reasonable value for strain limit. Using this fatigue curve, the number of cycles to failure N_i for each strain range $\Delta\varepsilon_i$ is obtained. Finally, using Miner's rule, a fatigue damage parameter D is calculated:

$$D = \sum_i \frac{n_i}{N_i} \tag{130}$$

where fatigue fracture corresponds to a unit value.
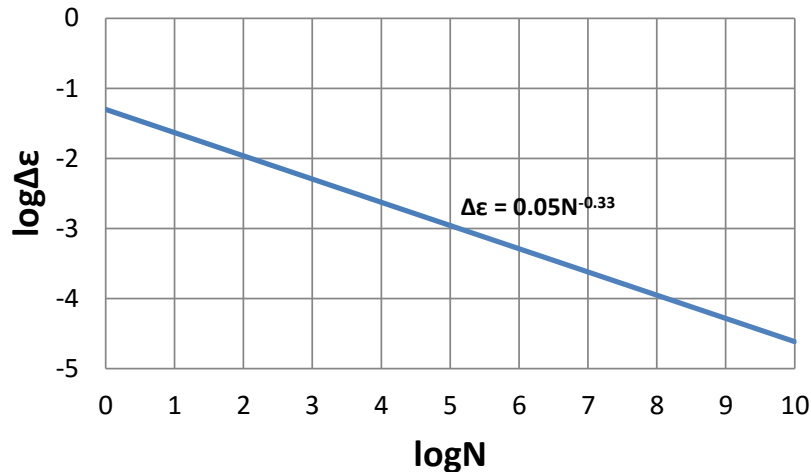
Figure 102: Strain amplitude fatigue curve.

Stress and strain concentration at weld toe

The calculation of the fatigue loading spectrum refers to local strain ranges $\Delta\varepsilon_i$ obtained from the methodology outlined from equations (122)-(129). However, these equations do not account for the local effects on the stress and strain field due to weld discontinuity, sometimes referred to as "hot spot effects" or "geometric effects". Those effects should be considered through an appropriate strain concentration factor *SNCF* that multiplies the $\Delta\varepsilon_i$ values and provides a reliable estimate of local strain at the vicinity of the welded connection to be used for fatigue analysis.

113

For calculating the value of $SNCF$, Neuber's method can be employed, as described in various textbooks (Dowling 1993), where the local (hot spot) stress and strain, denoted as $\bar{\sigma}$ and $\bar{\varepsilon}$, are related to the corresponding nominal values σ and ε through the following equation:

$$\bar{\sigma} \cdot \bar{\varepsilon} = SCF^2 \sigma \cdot \varepsilon \tag{131}$$

where SCF is the elastic stress concentration factor.
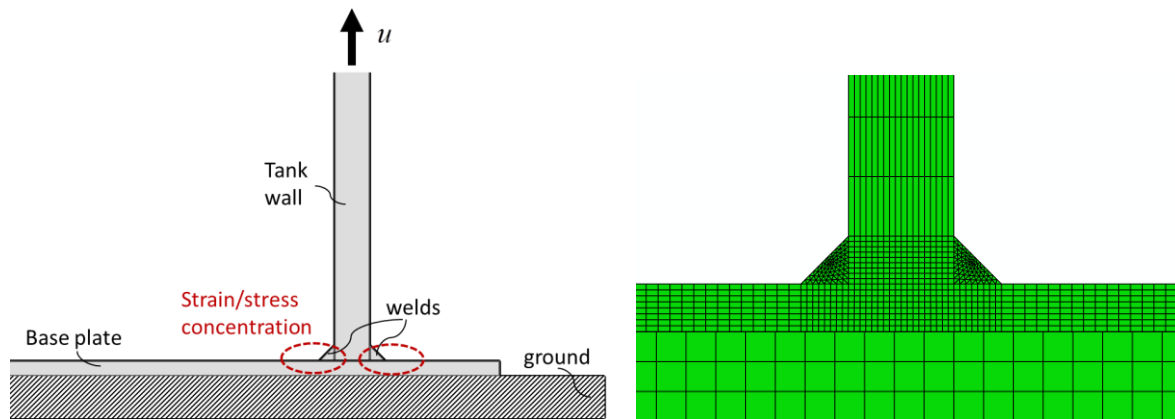
Figure 103: Calculation of elastic SCF using a finite element model.

To calculate the SCF value, a special numerical procedure is necessary. Direct measurement of stress at the (Gauss) point nearest to the weld from the finite element analysis may not provide a reliable estimate of stress concentration, due to sharp discontinuity of the stress/strain field at the weld toe. Therefore, an extrapolation of stresses to the weld toe from a defined region near the weld should be used (Karamanos et al. 2000), as shown schematically in Figure 104. The SCF value can be calculated as the ratio of the extrapolated stress at the weld toe with the nominal one.

114
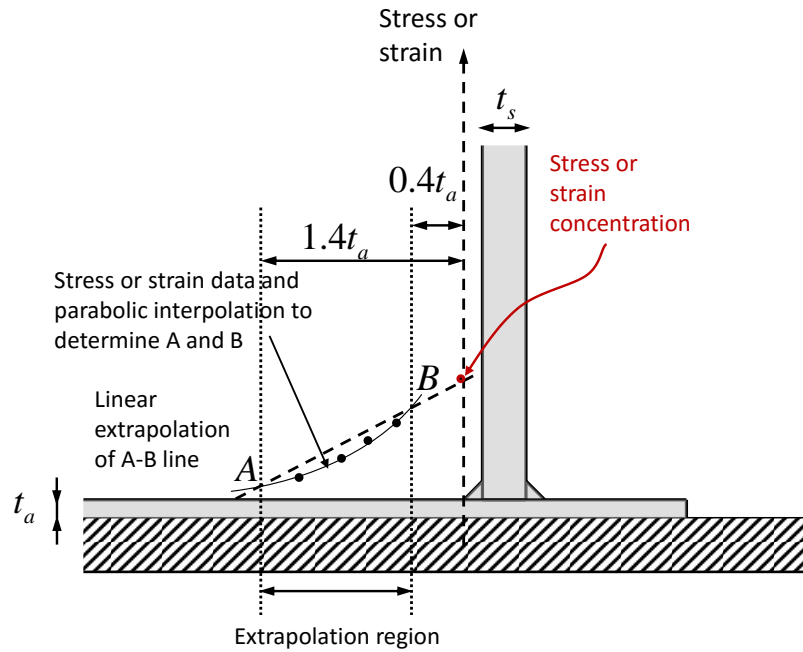
Figure 104: Schematic representation of the extrapolation method to calculate the elastic stress concentration factor.

Furthermore, a power-law constitutive equation is adopted for the steel material:

$$\sigma = K\varepsilon^n \tag{132}$$

It is assumed that this law relates both the nominal stress and strain σ and ε, as well as the local stress and strain $\bar{\sigma}$ and $\bar{\varepsilon}$, so that

$$\bar{\sigma} = K\bar{\varepsilon}^n \tag{133}$$

Given the nominal values σ and ε, and the value of elastic SCF, the system of equations (131) and (133) can be solved for the two unknowns $\bar{\sigma}$ and $\bar{\varepsilon}$, so that the $SNCF$ value is

$$SNCF = \bar{\varepsilon}/\varepsilon \tag{134}$$

Upon calculation of the $SNCF$ value, this is multiplied with the corresponding strains ε (computed from Eq.(129)) in order to obtain the local strains $\bar{\varepsilon}$, to be used in the "rainflow" cycle counting analysis.

115

Low-cycle fatigue tests of welded connections in unanchored steel liquid storage tanks

The choice of an appropriate low-cycle fatigue curve and the determination of local strain at the weld toe for evaluating the strength of the tank-plate connection, may not be a trivial task. Towards this purpose, a dedicated research effort, which combines experimental and numerical work, is planned within the INDUSE-2-SAFETY project (Bursi et al. 2015a). Monotonic and cyclic loading tests will be performed on a series of welded base-tank connections. In particular eight T-joint plated connections are considered corresponding to the connection of a 54.864 meter-diameter-tank with a maximum design product level equal to 14.3 meters (aspect ratio $\gamma = H / R = 0.521$). The proposed experimental set-up is shown in Figure 105 (to be further developed by the Structural Laboratory in Civil Engineering of University of Thessaly) and the geometric characteristics of the specimens are shown in Figure 107. The specimens have been manufactured (Figure 108) and experiments are expected to be completed by the end of the year 2016.
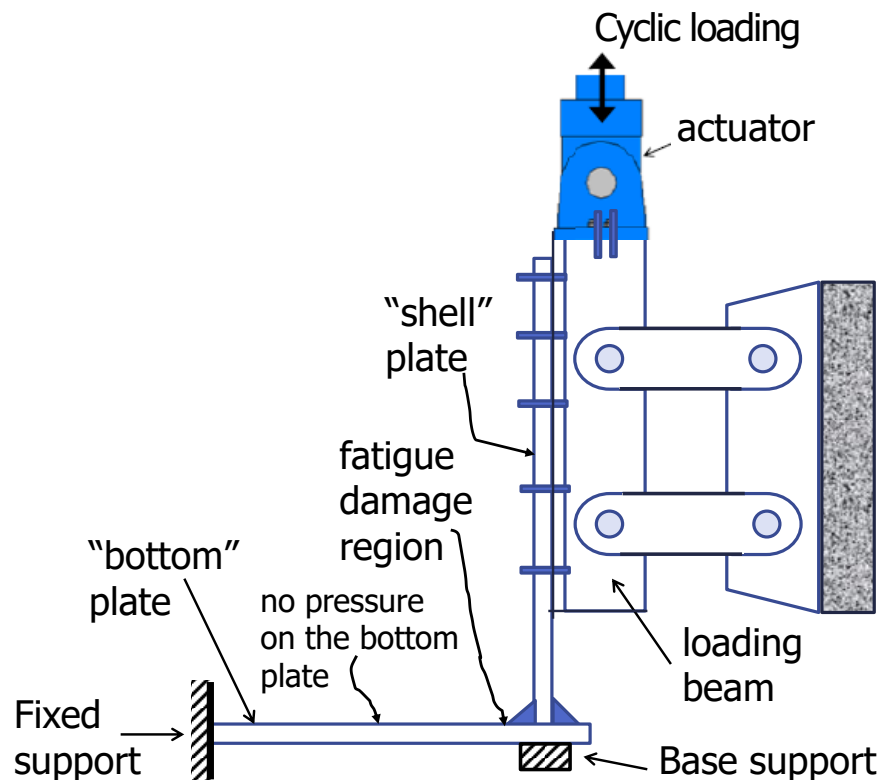
Figure 105: Experimental set-up.

116

Figure 106: Structural Laboratory in Civil Engineering of University of Thessaly.

plan view   side view   front view

weld detail

w.1   w.2

fillet weld 8mm   fillet weld 11mm
6 specimens   6 specimens
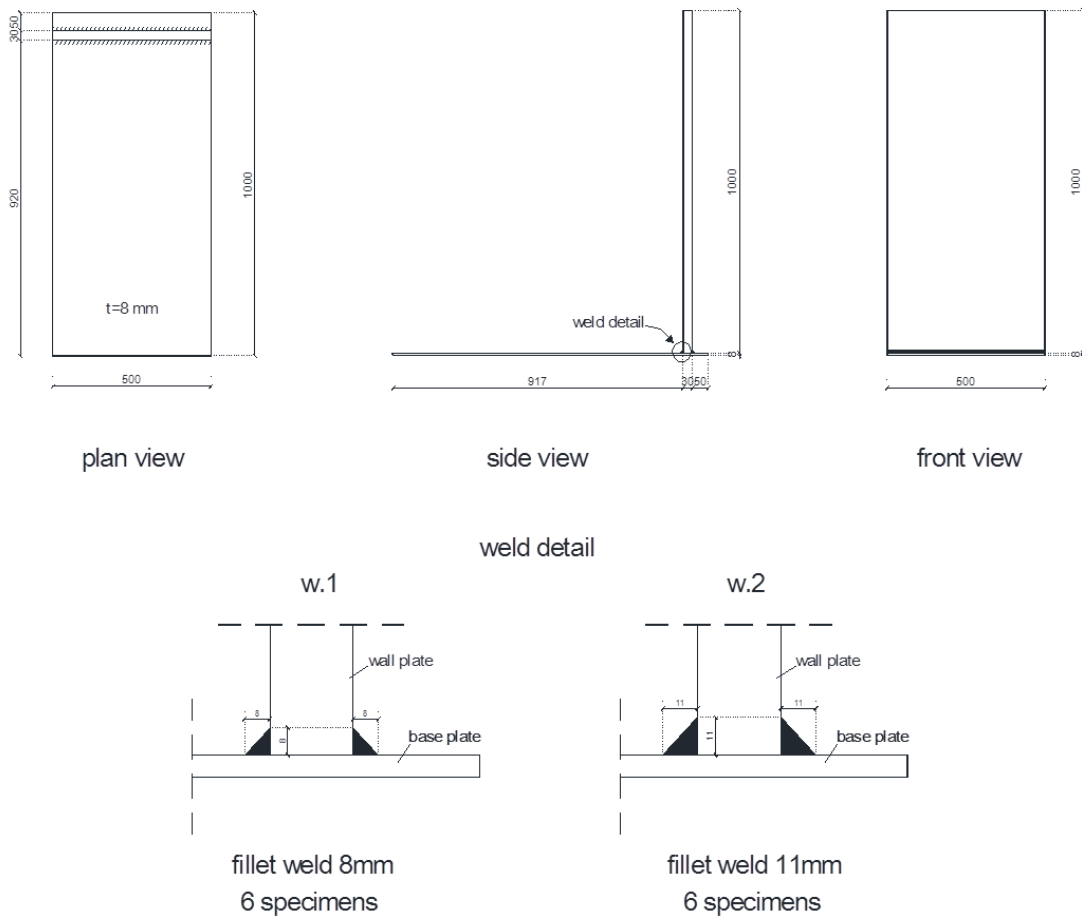
Figure 107: Geometric characteristics of the specimens.

117

Figure 108: The manufactured specimens.

4.5.2 Rocking Seismic Action

4.5.2.1 Model Description

The tank-liquid system is simulated with a simplified model that accounts for the hydrodynamic response of the liquid. The tank is excited by an angular or rocking base motion about a horizontal axis. The motion of the fluid is also decomposed in an impulsive and convective part. In the following, the model described in paragraph 2.2.3 is adjusted appropriately to be used for the simplified analysis of anchored and unanchored tanks. The analysis for anchored tanks follows the analysis of Veletsos and Tang (1987) and it is extended herein for unanchored tanks.

4.5.2.2 Anchored Tanks

The tank-liquid system investigated is shown in Figure 109.

118
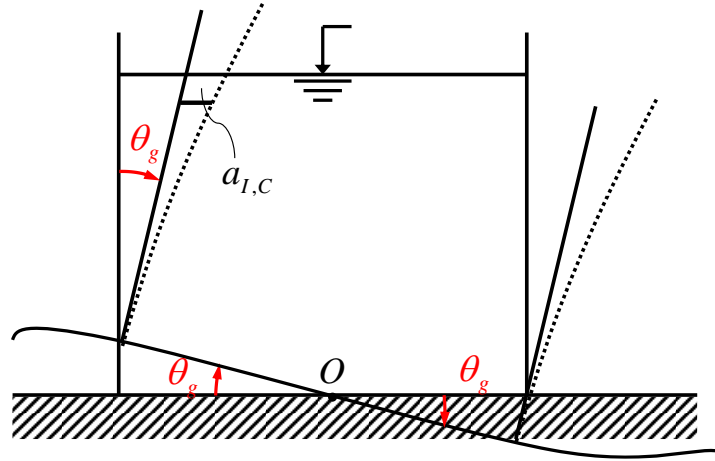
Figure 109: Simplified model for anchored liquid storage tanks under rocking seismic action.

Equations of motion

Equilibrium of forces in the horizontal direction requires:

$$m_{I,C}^r \left(\ddot{a}_{I,C}^r + H\ddot{\theta}_g \right) + ka_{I,C}^r = 0 \tag{135}$$

or with damping:

$$m_{I,C}^r \ddot{a}_{I,C}^r + c_{I,C}^r \dot{a}_{I,C}^r + ka_{I,C}^r = -m_{I,C}^r H\ddot{\theta}_g \tag{136}$$

or dividing with the rocking mass $m_{I,C}^r$:

$$\ddot{a}_{I,C}^r + 2\xi_{I,C}^r \omega_{I,C}^r \dot{a}_{I,C}^r + \omega_{I,C}^{r2} a_{I,C}^r = -\ddot{X}_g \tag{137}$$

where $a_{I,C}^r(t)$ is the generalized coordinate representing the relative impulsive or convective displacement of the tank with respect to its base, $\xi_{I,C}^r$ the viscous damping ratio of the impulsive or convective motion, ω_I^r the impulsive or convective frequency and:

$$\ddot{X}_g = H\ddot{\theta}_g . \tag{138}$$

where $\ddot{\theta}_g$ is the angular acceleration. The method of solution is the same with the one for anchored tanks under lateral seismic action, outlined in the Annex.

119

The tank-liquid system investigated is shown in Figure 110.
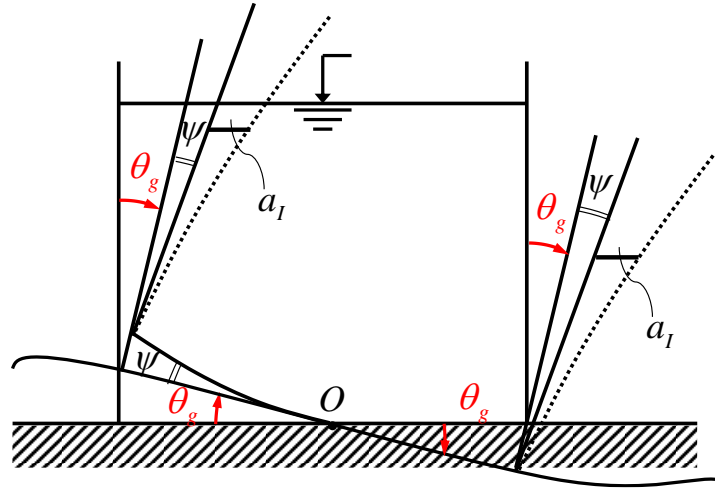
Figure 110: Simplified model for unanchored liquid storage tanks under rocking seismic action.

Equations of motion

For simplicity, it is assumed that the convective component of response is negligible on the overturning moment. Equilibrium of forces in the horizontal direction requires:

$$m_I^r \ddot{a}_I^r + k^r a_I^r + m_I^r h_I^r \ddot{\psi}^r = -m_I^r H \ddot{\theta}_g \tag{139}$$

And the equilibrium of moments gives:

$$I_O^r \ddot{\psi}^r + M_\psi^r \left(\psi^r \right) + i_o m_I^r \left(\ddot{a}_I^r + H \ddot{\theta}_g \right) H = 0 \tag{140}$$

where I_O^r is the rotational moment of inertia of the impulsive part of the liquid. By setting $k^r = \omega_I^{r2} m_I^r$, Eq.(139) becomes:

$$m_I^r \ddot{a}_I^r + m_I^r \omega_I^{r2} a_I^r + m_I^r h_I^r \ddot{\psi}^r = -m_I^r H \ddot{\theta}_g \tag{141}$$

Setting $\delta^r = h_I^r \psi^r$, the above equations become:

$$m_I^r \ddot{a}_I^r + m_I^r \ddot{\delta}^r + m_I^r \omega_I^{r2} a_I^r = -m_I^r H \ddot{\theta}_g \tag{142}$$

120

$$m_I^r \ddot{a}_I^r + \frac{I_O^r}{i_o H h_I^r} \ddot{\delta}^r + \frac{1}{i_o H} M_\psi^r \left(\psi^r \right) = -m_I^r H \ddot{\theta}_g \tag{143}$$

The above equations are nonlinear because of the nonlinear spring law $M_\psi \left(\psi \right)$ and can be written in incremental form as follows, where appropriate damping terms are added:

$$m_I^r \Delta \ddot{u}_I^r + m_I^r \Delta \ddot{\delta}^r + c_1^r \Delta \dot{u}_I^r + m_I^r \omega_I^{r2} \Delta u_I^r = -m_I^r H \Delta \ddot{\theta}_g \tag{144}$$

$$m_I^r \Delta \ddot{u}_I^r + \frac{I_O^r}{i_o H h_I^r} \Delta \ddot{\delta}^r + c_2^r \Delta \dot{\delta}^r + \frac{K_\psi^r}{i_o H h_I^r} \Delta \delta^r = -m_I^r H \Delta \ddot{\theta}_g \tag{145}$$

noting that $\Delta M_\psi^r = K_\psi^r \Delta \psi^r$.

In equations (143) and (144), $c_1^r = c_I^r = 2 \xi_I^r m_I^r \omega_I^r$ is the damping coefficient for impulsive motion, with a damping ratio $\xi_I^r = 5\%$, whereas $c_2^r = 2 \xi_O^r \sqrt{K_\psi^r I_O^r / h_I^{r4}}$ is the damping coefficient for the rotational movement of the tank, where a damping ratio ξ_O^r of the uplifting (rocking) motion equal to 10% is considered.

The system of equations (143) and (144) is solved using Newmark's method (Bathe 1996) outlined in the Annex.

4.6 Numerical results

4.6.1 Results for Lateral Seismic Action

Using the simplified dynamic model described in the previous section, Tank I and II have been analyzed dynamically using a series of seismic accelerograms of increasing amplitude. The Duzce earthquake (Duzce, Turkey, 1999) with maximum PGA equal to 0.36 g is considered as a basis, multiplied by a factor λ, which controls the amplitude of the seismic input. The accelerogram for $\lambda = 1$ is shown in Figure 111. The two tanks have been analyzed under both anchored and unanchored conditions.

In Figure 112 and Figure 113 the time history of the base moment, M, is shown for Tank I ($\lambda = 0.5$) and Tank II ($\lambda = 0.4$) respectively, under anchored conditions. Figure 114 and Figure 115 refer to the time history of the vertical uplift, W, for Tank I ($\lambda = 0.5$) and Tank II (

121

$\lambda = 0.4$) respectively, under unanchored conditions. The time history of the base moment, M, for the two tanks under unanchored conditions is also shown in Figure 116 and Figure 117.
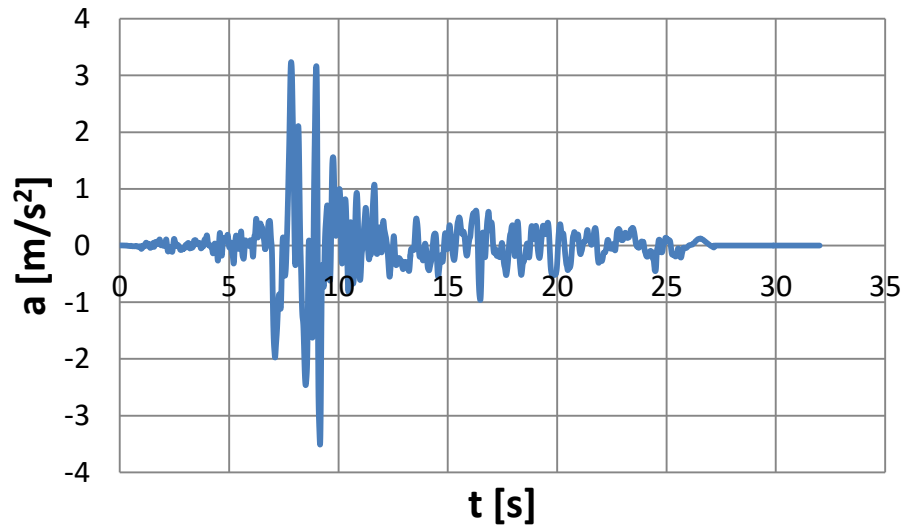
Figure 111: Accelerogram of the Duzce earthquake, Turkey (1999).
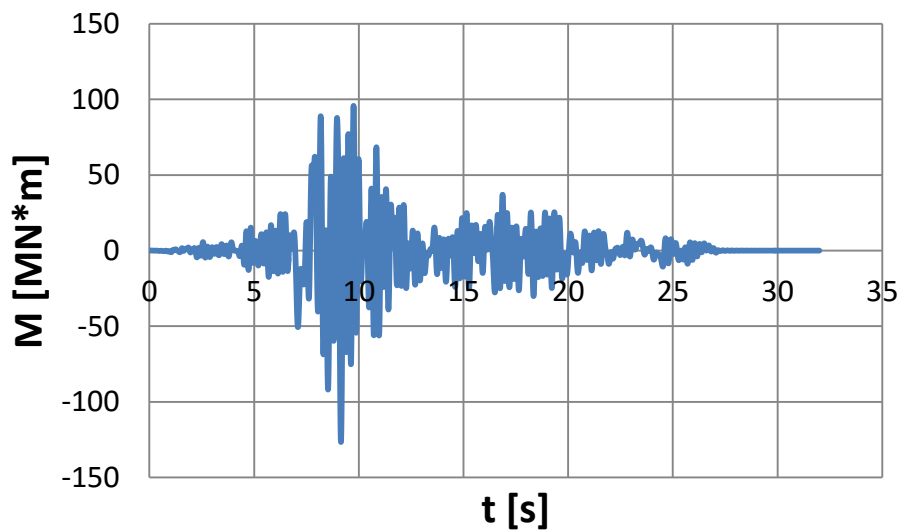
Figure 112: Time history of the base moment, M, for Tank I ($\lambda = 0.5$), under anchored conditions.

122
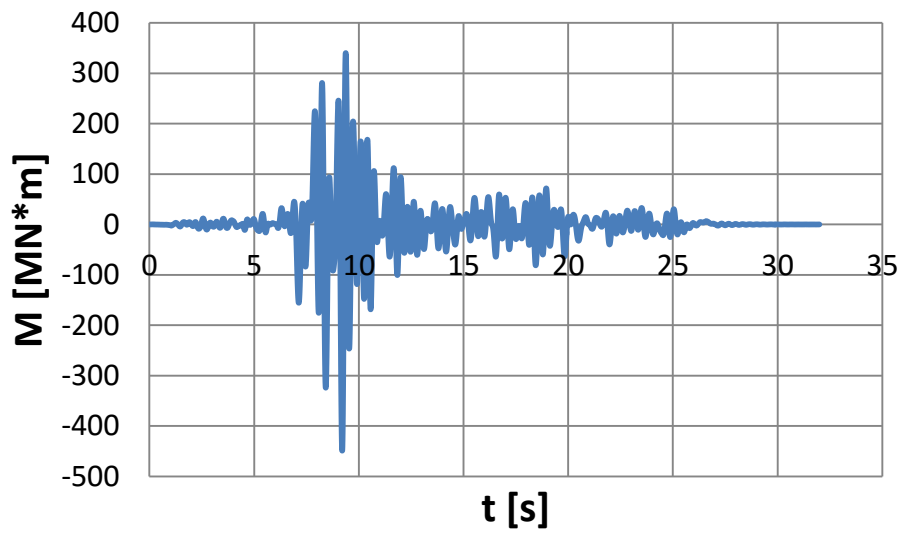
Figure 113: Time history of the base moment, M , for Tank II ($\lambda = 0.4$), under anchored conditions.
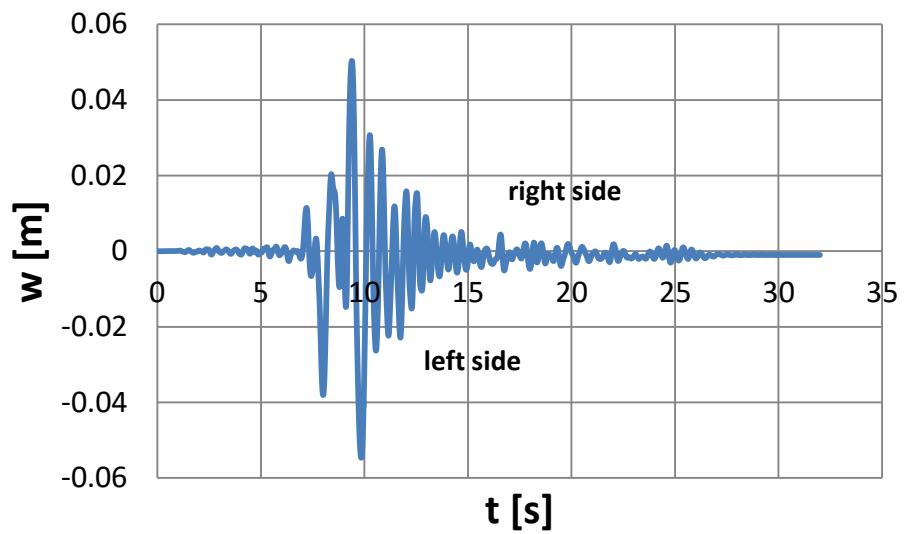
Figure 114: Time history of the vertical uplift, w , for Tank I ($\lambda = 0.5$), under unanchored conditions.

123
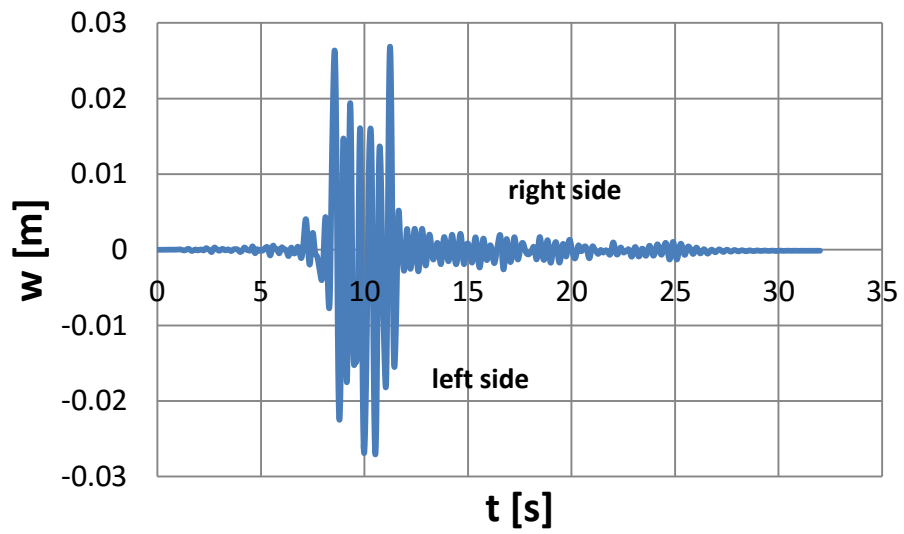
Figure 115: Time history of the vertical uplift, w, for Tank II ($\lambda = 0.4$), under unanchored conditions.
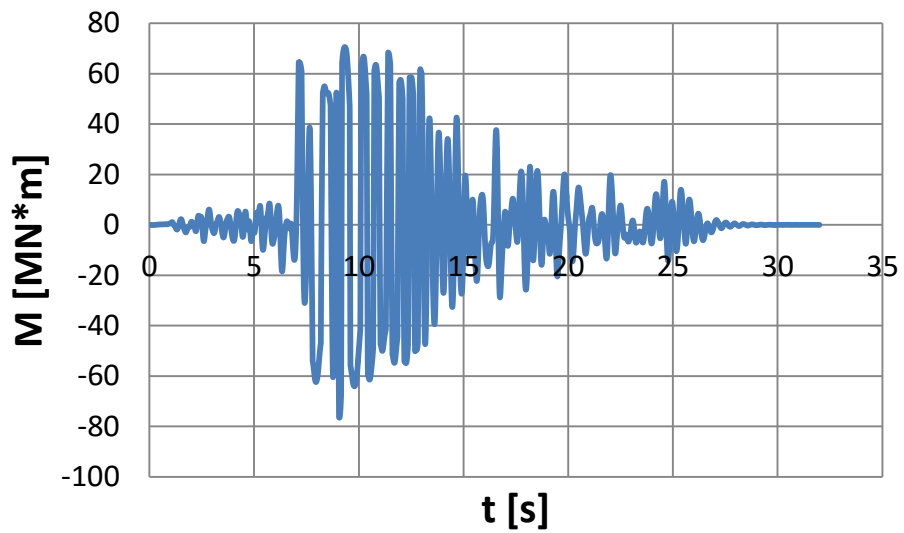
Figure 116: Time history of the base moment, M, for Tank I ($\lambda = 0.5$), under unanchored conditions.

124
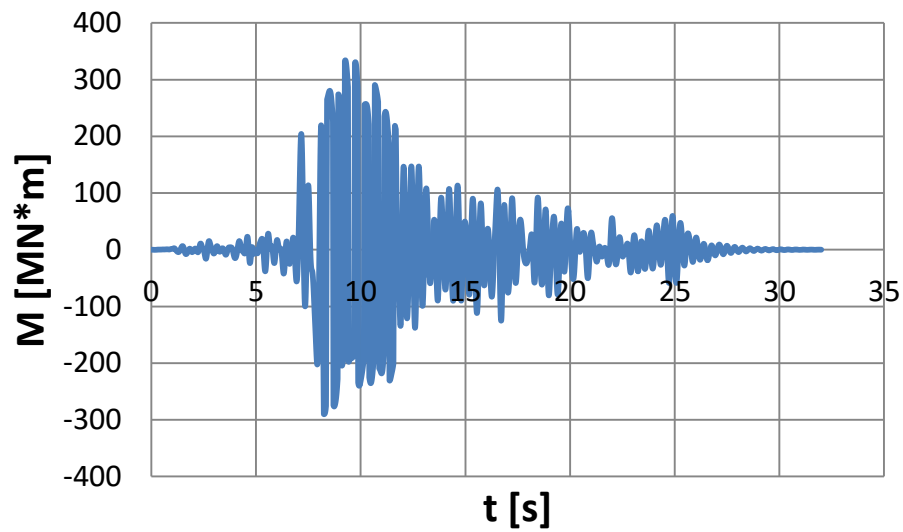
Figure 117: Time history of the base moment, M, for Tank II ($\lambda = 0.4$), under unanchored conditions.

Using the relation between the uplifting length L and the uplifting displacement w in equation (127), with β equal to 0.238 m^{-3} for Tank I and 0.231 m^{-3} for Tank II, the strain histories at the right and left side of the tank are computed for the earthquake under consideration, as shown in Figure 118, Figure 119, Figure 120 and Figure 121.

To conduct a fatigue analysis, the $SNCF$ value is calculated through the elastic SCF and Neuber's method. Considering an axisymmetric finite element model of the welded connection area, as described in the previous section, and using the extrapolation method of the paper by Karamanos et al. (2000), the SCF value is found equal to 1.32 for Tank I and 1.23 for Tank II. In addition, the parameters of power-law stress-strain equation for S235 Steel (equivalent to A36) are taken equal to $K = 98.4$ ksi and $n = 0.15$ (Kaufmann et al. 2001), and the $SNCF$ values for the two tanks, according to Eq.(134), are 8.55 and 7.72 respectively.

The strain ranges $\Delta\varepsilon_i$, the corresponding number of acting cycles n_i as obtained from the rainflow counting method, the number of cycles to failure N_i obtained from the fatigue curve of Figure 102 and the results for the fatigue damage factor, as obtained from Miner's rule, are shown in Table 4 and Table 5, for the two tanks under consideration. For the level of seismic input considered, the connections appear to be safe against fatigue fracture. On the other hand, repeating the above analysis for seismic level $\lambda = 1$, it can be shown that both tanks are not safe against fracture of the shell-bottom plate connection, because the value of damage parameter exceeds unity.

125
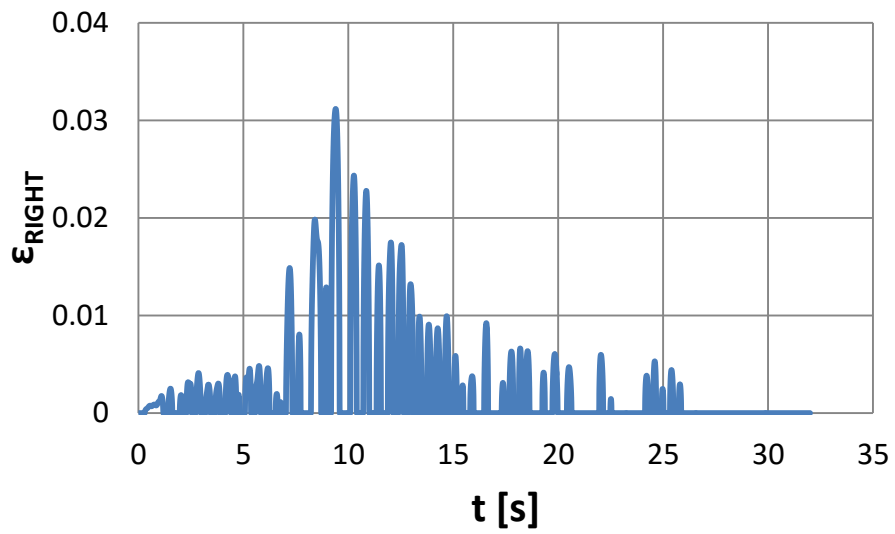
Figure 118: Time history of the local bending strains at the plate-shell connection at the right side of Tank I for the seismic input of Figure 111 ($\lambda = 0.5$).
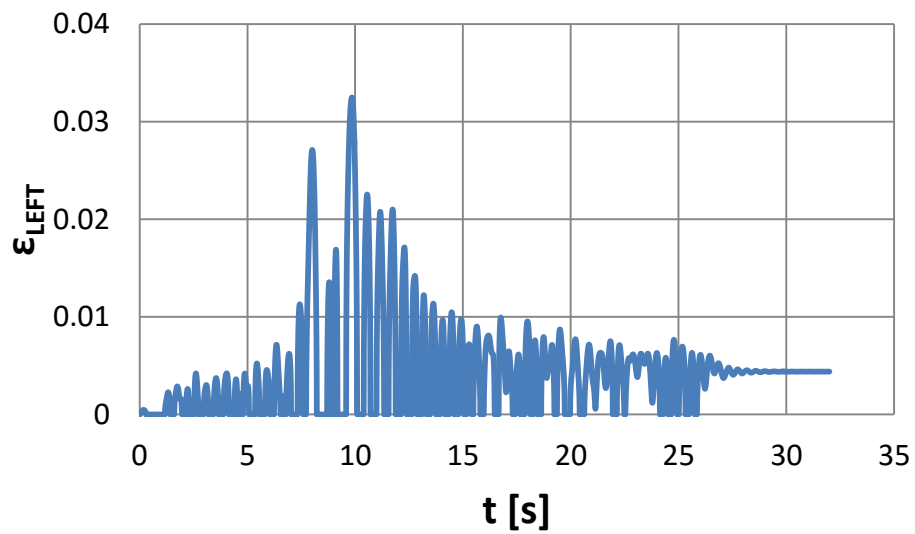
Figure 119: Time history of the local bending strains at the plate-shell connection at the left side of Tank I for the seismic input of Figure 111 ($\lambda = 0.5$).

126
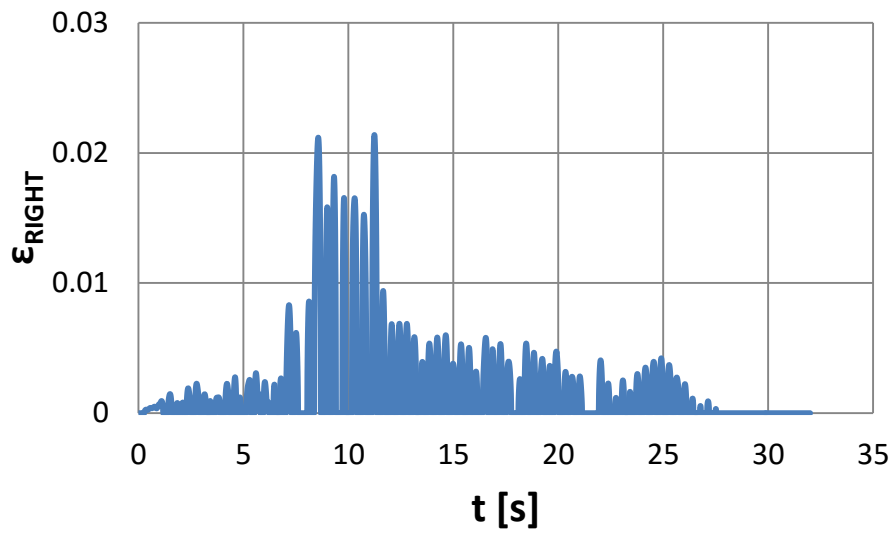
Figure 120: Time history of the local bending strains at the plate-shell connection at the right side of Tank II for the seismic input of Figure 111 ($\lambda = 0.4$).
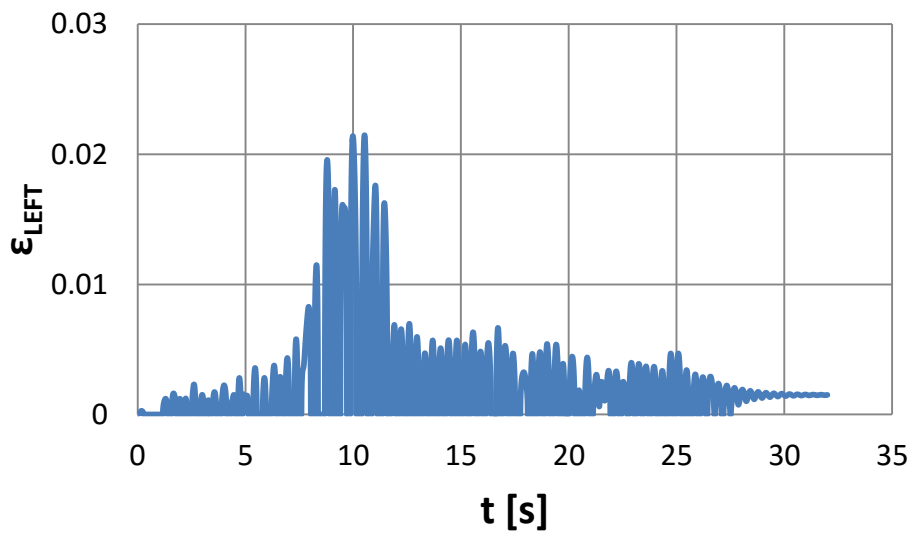
Figure 121: Time history of the local bending strains at the plate-shell connection at the left side of Tank II for the seismic input of Figure 111 ($\lambda = 0.7$).

127

Table 4: Fatigue analysis of Tank I using rainflow cycle counting method ($\lambda = 0.5$).

Right Side of Tank I				Left Side of Tank I			
$\Delta\varepsilon$	$\Delta\bar{\varepsilon}$	n_I	N_I	$\Delta\varepsilon$	$\Delta\bar{\varepsilon}$	n_I	N_I
0.0002	0.0014	12	52782	0.0002	0.0014	23	53033
0.0005	0.0040	17	2109	0.0005	0.0041	14	1938
0.0008	0.0065	7	461	0.0008	0.0068	17	416
0.0011	0.0091	6	169	0.0011	0.0095	7	151
0.0014	0.0117	1	80	0.0014	0.0122	3	71
0.0017	0.0143	3	44	0.0017	0.0149	2	39
0.0020	0.0169	2	27	0.0021	0.0176	2	24
0.0023	0.0195	1	18	0.0024	0.0203	2	16
0.0026	0.0221	1	12	0.0027	0.0230	1	11
0.0029	0.0247	1	9	0.0030	0.0257	0	8
0.0032	0.0273	0	7	0.0033	0.0284	1	6
0.0035	0.0299	1	5	0.0036	0.0312	1	5
$D = 0.664$				$D = 0.854$			

Table 5: Fatigue analysis of Tank II using rainflow cycle counting method ($\lambda = 0.4$).

Right Side of Tank II				Left Side of Tank II			
$\Delta\varepsilon$	$\Delta\bar{\varepsilon}$	n_I	N_I	$\Delta\varepsilon$	$\Delta\bar{\varepsilon}$	n_I	N_I
0.0001	0.0009	20	183752	0.0001	0.0009	25	173881
0.0003	0.0027	20	6809	0.0003	0.0027	20	6641
0.0006	0.0045	15	1464	0.0006	0.0045	19	1436
0.0008	0.0062	10	532	0.0008	0.0063	13	523
0.0010	0.0080	2	250	0.0010	0.0081	1	246
0.0013	0.0098	1	137	0.0013	0.0099	0	135
0.0015	0.0116	0	83	0.0015	0.0116	1	82
0.0017	0.0134	0	54	0.0017	0.0134	0	53
0.0020	0.0152	2	37	0.0020	0.0152	0	37
0.0022	0.0169	2	27	0.0022	0.0170	4	26
0.0024	0.0187	1	20	0.0024	0.0188	1	20
0.0027	0.0205	2	15	0.0027	0.0206	2	15
$D = 0.359$				$D = 0.395$			

Effect of rotational spring on base moment

Comparison of time histories of base moment for the two tanks under anchored conditions with the corresponding time histories for the tanks under unanchored conditions (Figure 112, Figure 113, Figure 116 and Figure 117) shows that the base moment is smaller for the unanchored tanks. In order to examine this result, a parametric study of different shapes of the bilinear spring is conducted. Particularly, two cases are considered:

128

(a) The slope of the second part of the bilinear spring is considered as a parameter, and analyses are conducted so that the effects of this slope on the base moment are obtained.

(b) The spring is considered to be linear, and analyses are conducted so that the effects of their slope on the base moment are obtained.

In these analyses Tank I is considered.

The analytical expressions of the rotational spring in this parametric study are stated below in Table 6, and their graphical representation is shown in Figure 122 and Figure 123.

Table 6: Analytical expressions of the rotational spring of the parametric study.

Shape	Case	Type	Equation of first line	Equation of second line
(1)		Bilinear	$M = 190000\psi$	$M = 190000\psi$
(2)		Bilinear	$M = 190000\psi$	$M = 62105.26\psi + 38.37$
(3)	(a)	Bilinear	$M = 190000\psi$	$M = 31891.89\psi + 47.43$
(4)		Bilinear	$M = 190000\psi$	$M = 17659.57\psi + 51.70$
(5)		Bilinear	$M = 190000\psi$	$M = 8951.15\psi + 54.31$
(6)		Linear	$M = 79545.45\psi$	
(7)	(b)	Linear	$M = 380000\psi$	
(8)		Linear	$M = 1.9\times10^{100}\psi$	

In the above expressions, (5) is the bilinear spring used previously.

Using the simplified dynamic model described in the previous section for Tank I ($\lambda = 0.5$) for the different shapes of the rotational spring, the new time histories of the base moment can be derived. The time histories of the base moment for each of the shapes of the spring are shown in Figure 124 through Figure 131. The results are summarized in Table 7 for case (a) and Table 8 for case (b). For case (a), it is shown that when the slope of the second line of the bilinear approximation of the rotational spring decreases, the base moment also decreases. Moreover, for large inclination angles, the base moment of the unanchored tank is larger than the base moment of the anchored tank (Table 7 and Table 8). Therefore, it is concluded that the change of slope of the base moment due to uplifting leads to the smaller values of the base moment in the unanchored case. It should be noted that for very large inclination angles [shape (8), Table 8] assuming a stiff spring, the base moment of the unanchored tank becomes almost

129

equal to the base moment of the anchored tank, which shows that the simplified model for unanchored tanks works well.
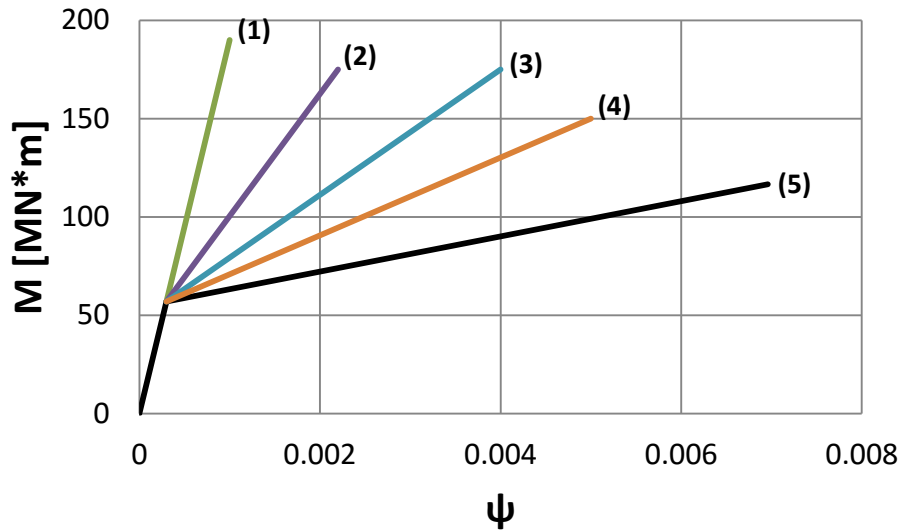
Figure 122: Approximation of the overturning moment versus rotation for Tank I; parametric study of different shapes of the rotational spring [case (a)].
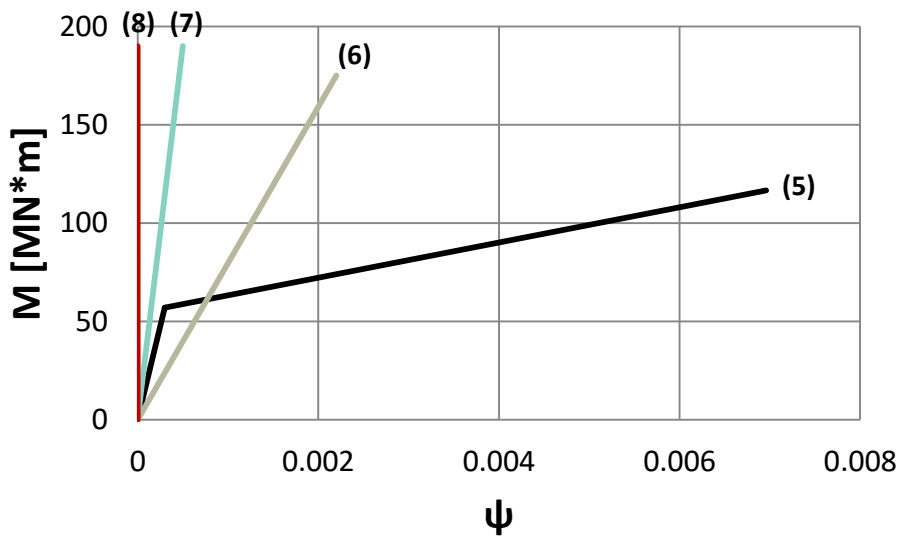
Figure 123: Approximation of the overturning moment versus rotation for Tank I; parametric study of different shapes of the rotational spring [case (b)].

130

(1)
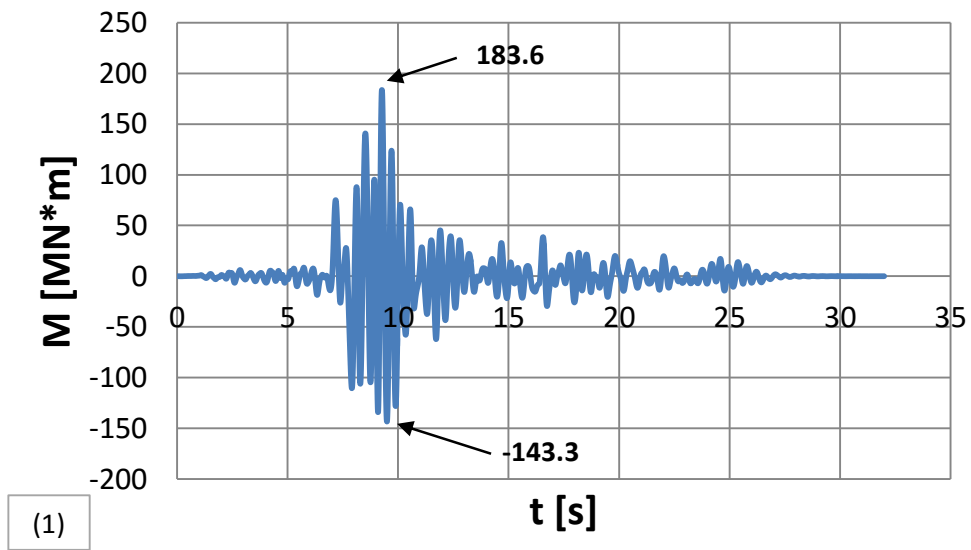
Figure 124: Time history of the base moment, M, for Tank I ($\lambda = 0.5$), under unanchored conditions for shape (1).

(2)
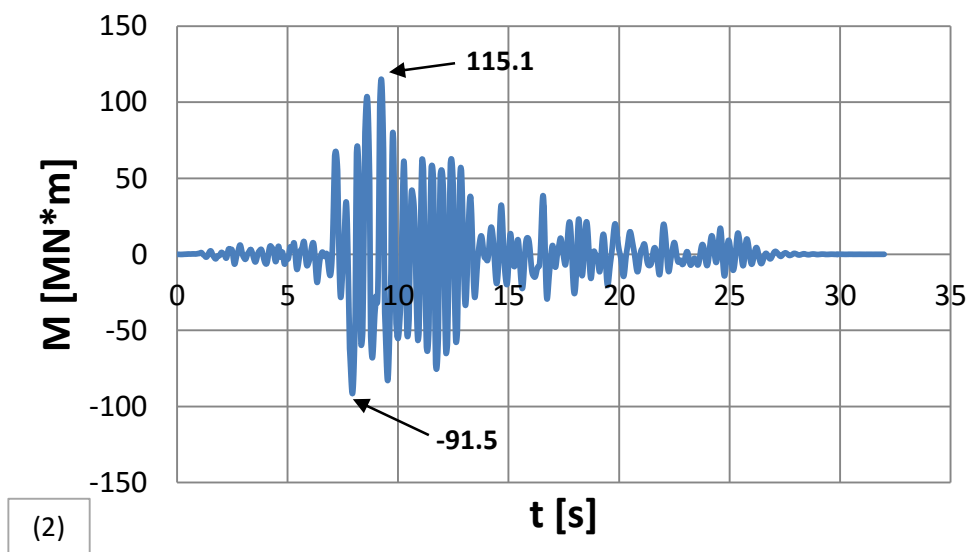
Figure 125: Time history of the base moment, M, for Tank I ($\lambda = 0.5$), under unanchored conditions for shape (2).

131
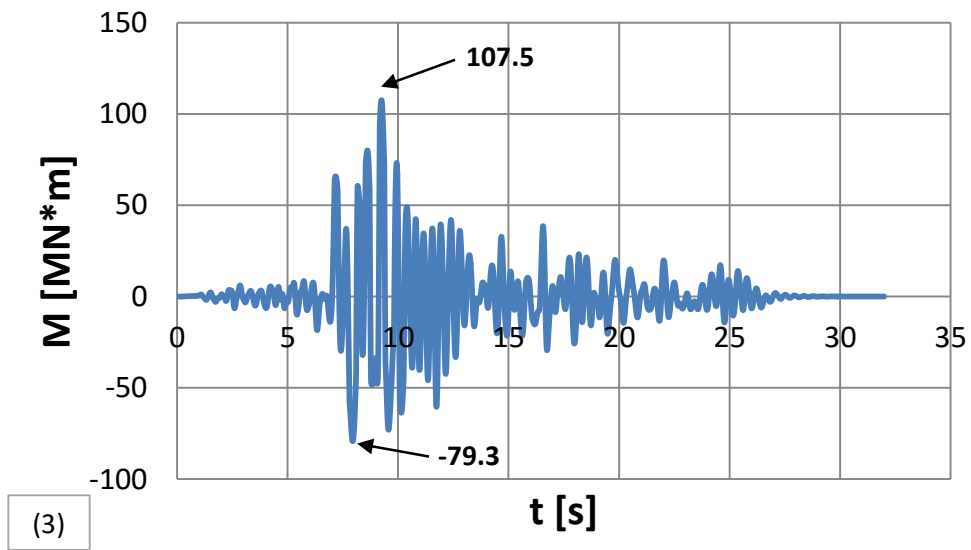
Figure 126: Time history of the base moment, M, for Tank I ($\lambda = 0.5$), under unanchored conditions for shape (3).
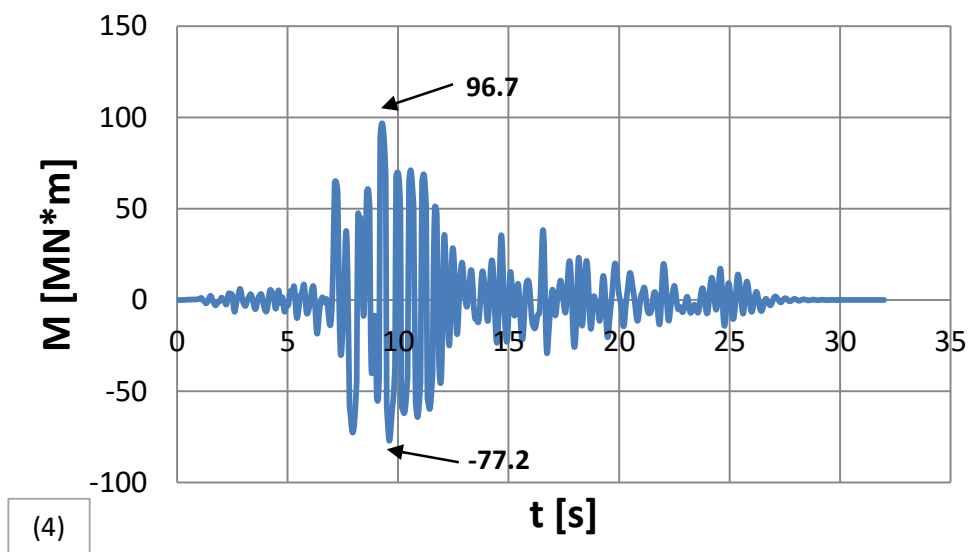
Figure 127: Time history of the base moment, M, for Tank I ($\lambda = 0.5$), under unanchored conditions for shape (4).

132
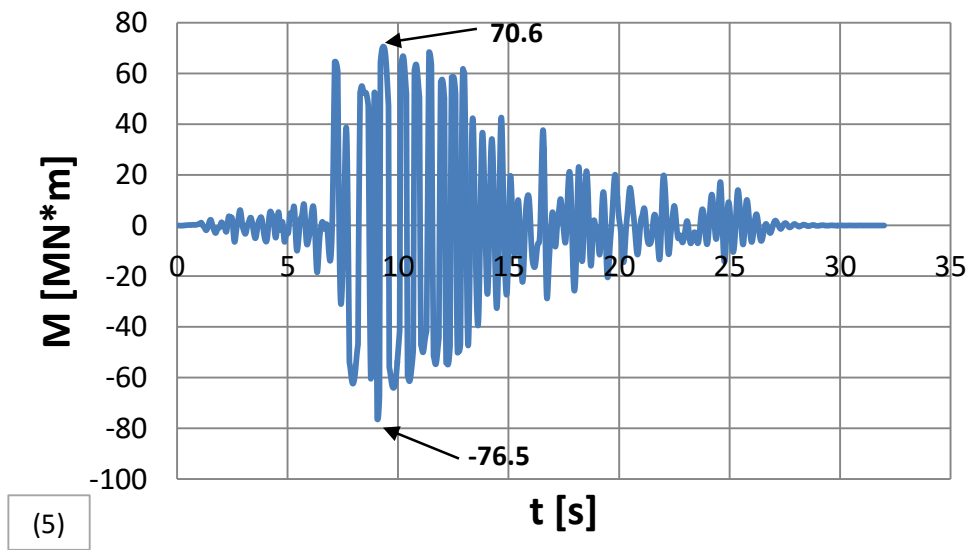
Figure 128: Time history of the base moment, M, for Tank I ($\lambda = 0.5$), under unanchored conditions for shape (5) (original).
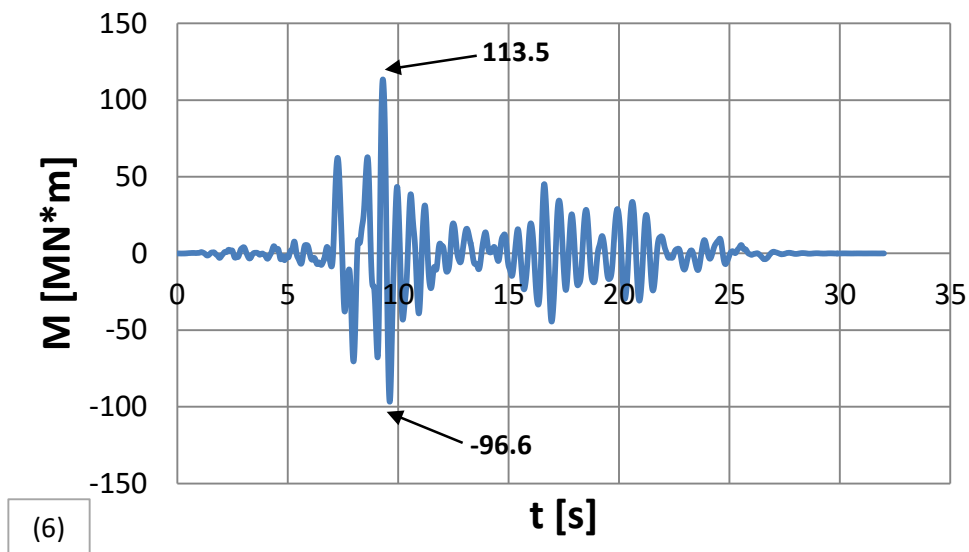
Figure 129: Time history of the base moment, M, for Tank I ($\lambda = 0.5$), under unanchored conditions for shape (6).

133

(7)
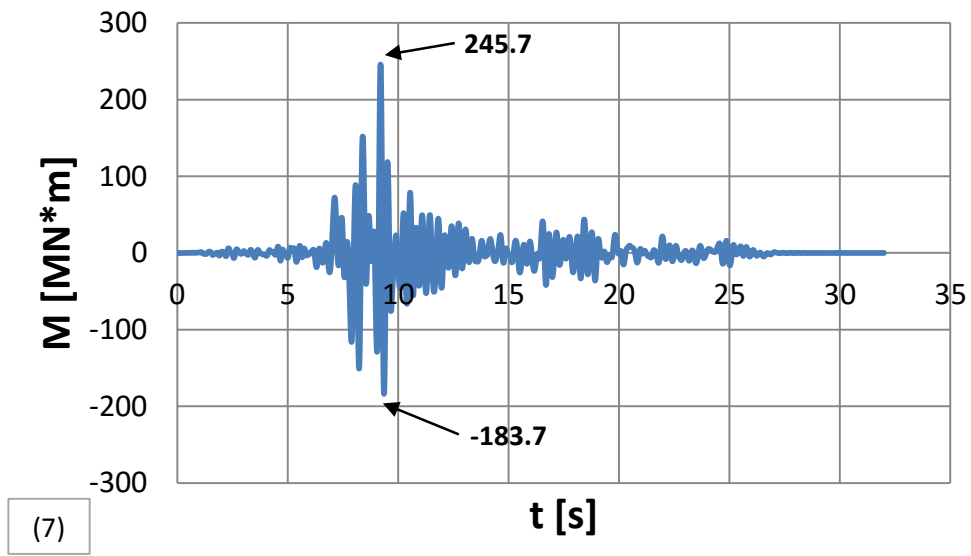
Figure 130: Time history of the base moment, M , for Tank I ($\lambda = 0.5$), under unanchored conditions for shape (7).

(8)
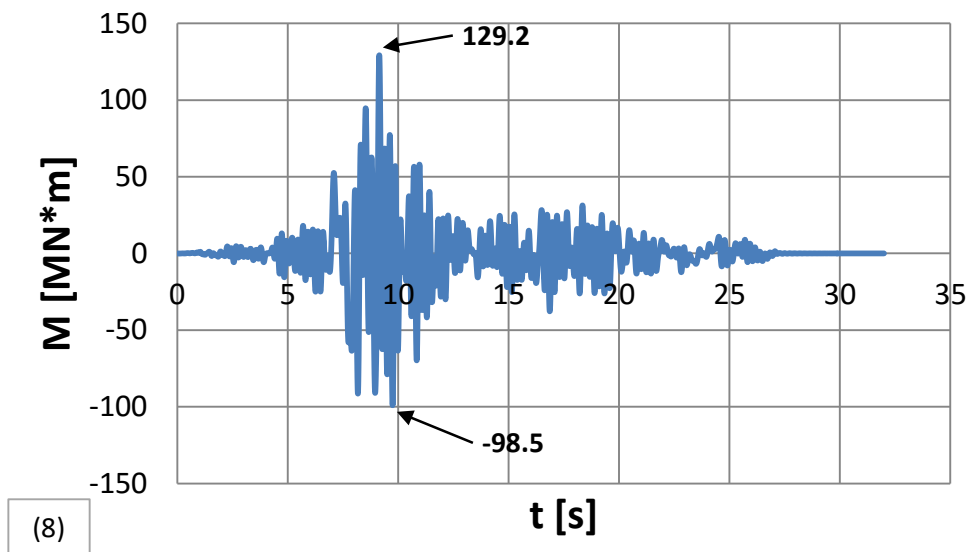
Figure 131: Time history of the base moment, M , for Tank I ($\lambda = 0.5$), under unanchored conditions for shape (8).

Table 7: Range of values of the base moment for each of the shapes of the rotational spring for case (a).

	M_{max} Right [MN]	M_{max} Left [MN]
(1)	183.6	143.3
(2)	115.1	91.5
(3)	107.5	79.3
(4)	96.7	77.2
(5)	70.6	76.5

Table 8: Range of values of the base moment for each of the shapes of the rotational spring for case (b).

	M_{max} Right [MN]	M_{max} Left [MN]
anchored	126.6	95.8
(6)	113.5	96.6
(7)	245.7	183.7
(8)	129.2	98.5

4.6.2 Rocking Seismic Action

Using the simplified dynamic model described in the previous section, Tank I and Tank II have been analyzed dynamically using the accelerogram of the Duzce earthquake shown in Figure 111. The tanks have been analyzed under both anchored and unanchored conditions.

Figure 132 and Figure 133 and refer to the time history of the base moment, M, for Tank I ($\lambda = 0.5$) and Tank II ($\lambda = 0.4$) respectively, under anchored conditions, while Figure 134 and Figure 135 refer to the time history of the vertical uplift, w, of the two tanks. The time history of the base moment for the two tanks under unanchored conditions is also shown in Figure 136 and Figure 137.
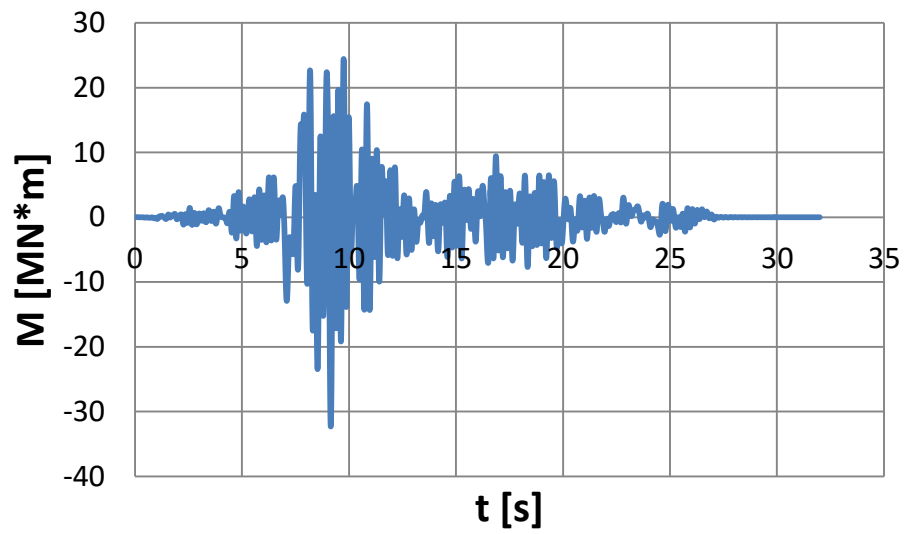
Figure 132: Time history of the base moment, M, for Tank I ($\lambda = 0.5$) under anchored conditions.
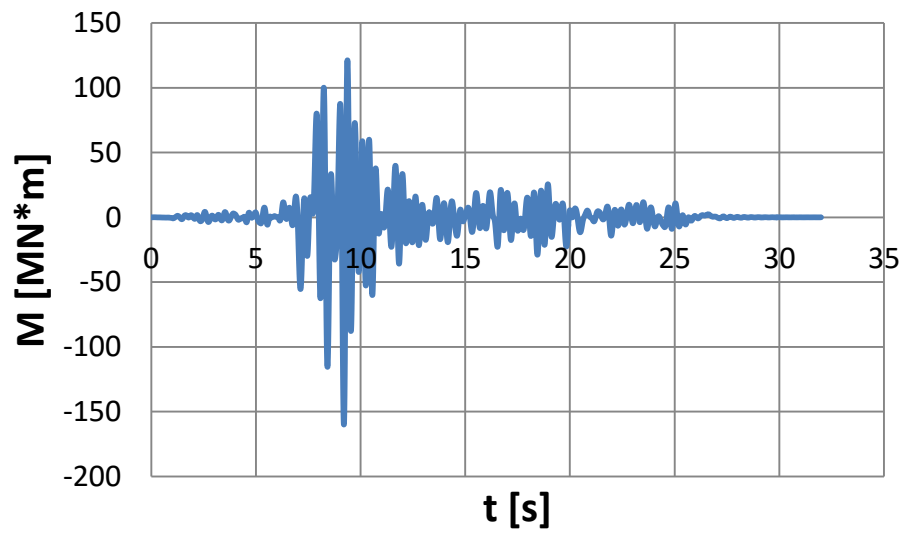
Figure 133: Time history of the base moment, M, for Tank II ($\lambda = 0.4$) under anchored conditions.

136
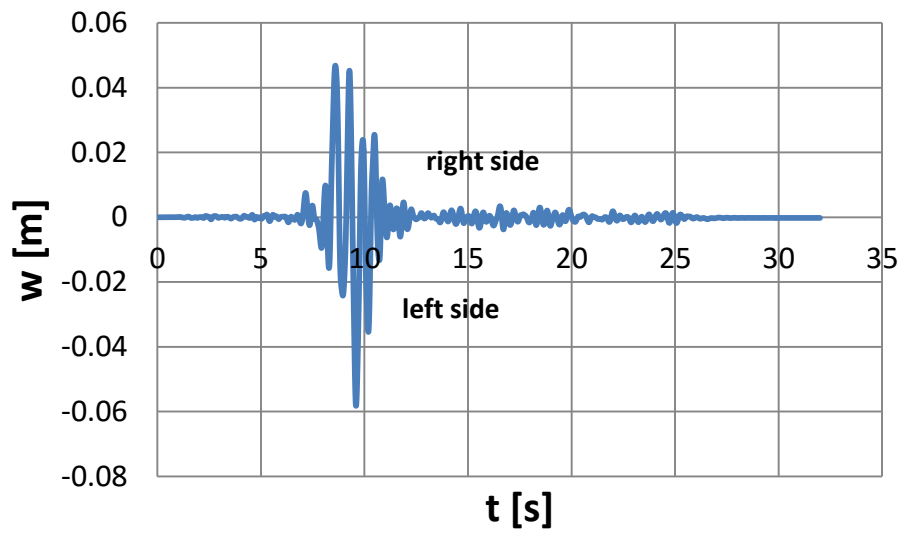
Figure 134: Time history of the vertical uplift, w, for Tank I ($\lambda = 0.5$) under unanchored conditions.
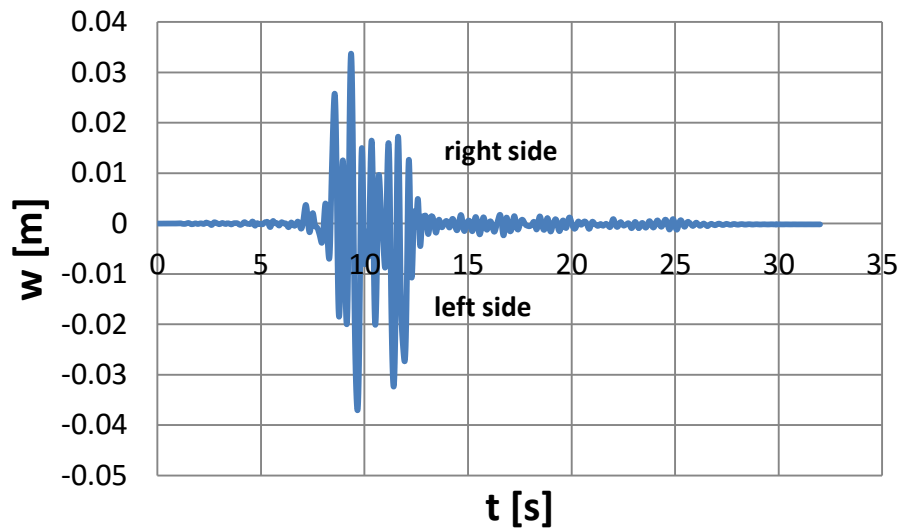
Figure 135: Time history of the vertical uplift, w, for Tank II ($\lambda = 0.4$) under unanchored conditions.

137
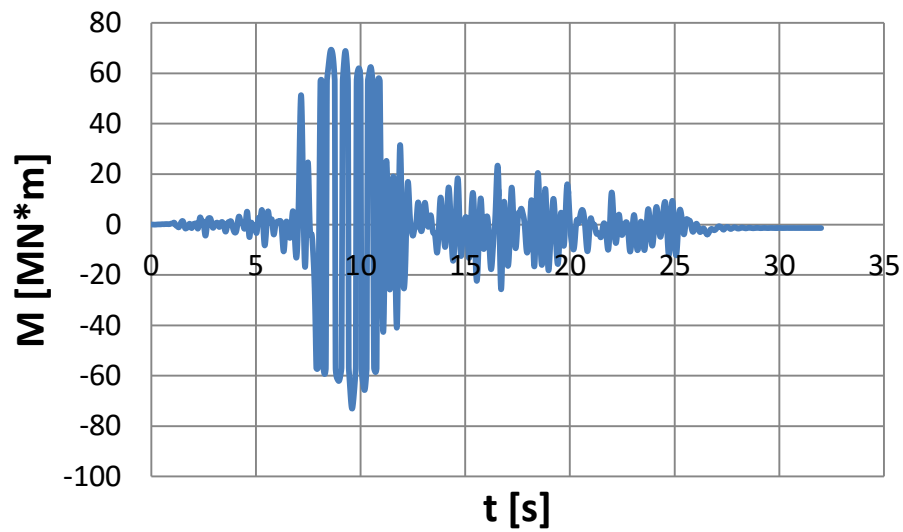
Figure 136: Time history of the base moment, M, for Tank I ($\lambda = 0.5$) under unanchored conditions.
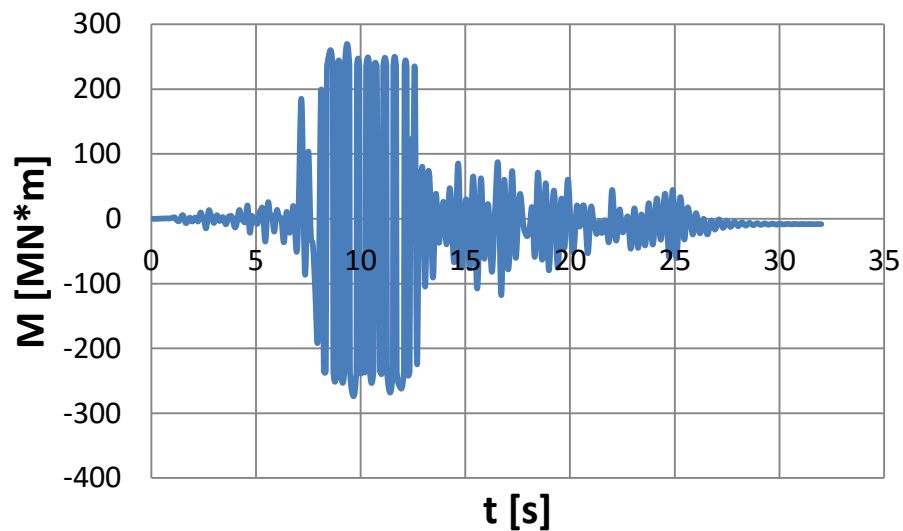
Figure 137: Time history of the base moment, M, for Tank II ($\lambda = 0.4$) under unanchored conditions.

Using the relation between the uplifting length L and the uplifting displacement w in Eq. (127), with β equal to 0.238 m^{-3} for Tank I and 0.231 m^{-3} for Tank II, the strain histories at the right and left side of the tank are computed for the earthquake under consideration, as shown in Figure 138, Figure 140, Figure 139 and Figure 141. The *SNCF* values for Tank I and Tank II are 8.55 and 7.72, respectively.

138

The strain ranges $\Delta\varepsilon_i$, the corresponding number of acting cycles n_i as obtained from the rainflow counting method, the number of cycles to failure N_i obtained from the fatigue curve of Figure 102 and the results for the fatigue damage factor, as obtained from Miner's rule, are shown in Table 9 and Table 10, for the two tanks under consideration. For the level of seismic input considered, the connections appear to be safe against fatigue fracture. On the other hand, repeating the above analysis for seismic level $\lambda = 1$, it can be shown that both tanks are not safe against fracture of the shell-bottom plate connection, because the value of damage parameter exceeds unity.
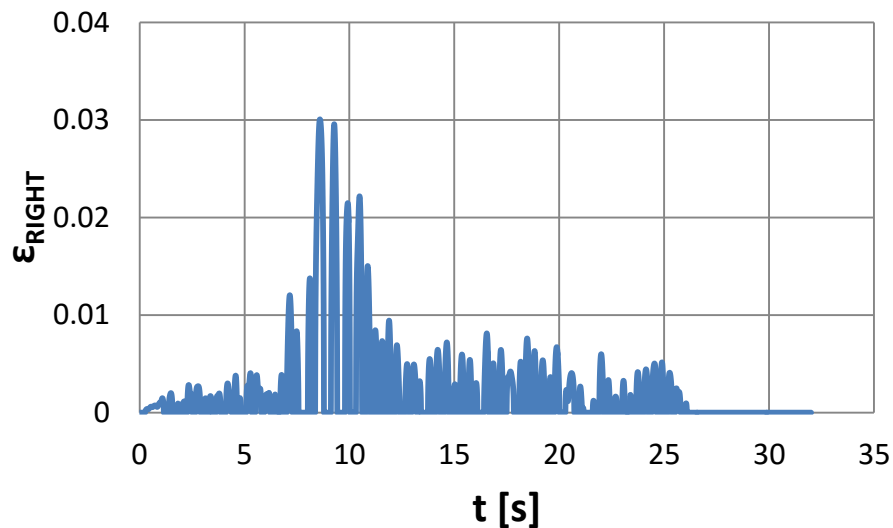
Figure 138: Time history of the local bending strains at the plate-shell connection at the right side of Tank I for the seismic input of Figure 111 ($\lambda = 0.5$).

139
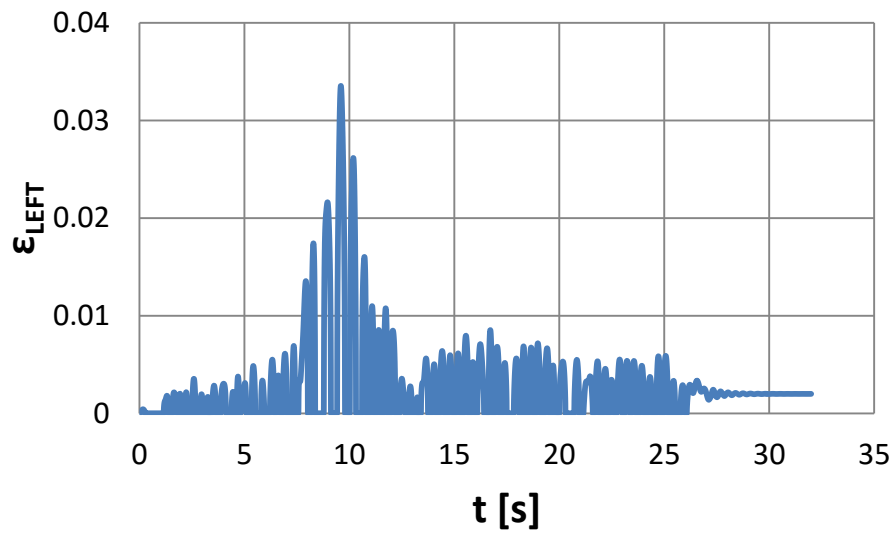
Figure 139: Time history of the local bending strains at the plate-shell connection at the left side of Tank I for the seismic input of Figure 111 ($\lambda = 0.5$).
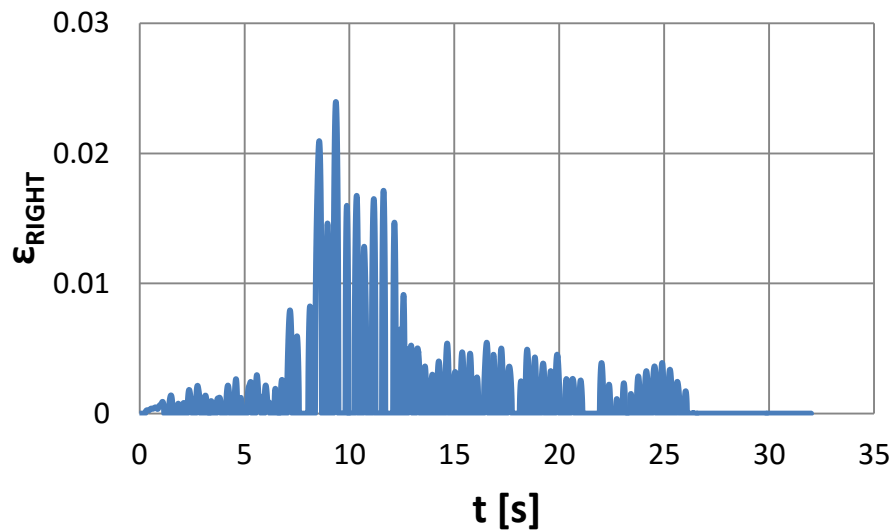
Figure 140: Time history of the local bending strains at the plate-shell connection at the right side of Tank II for the seismic input of Figure 111 ($\lambda = 0.4$).

140
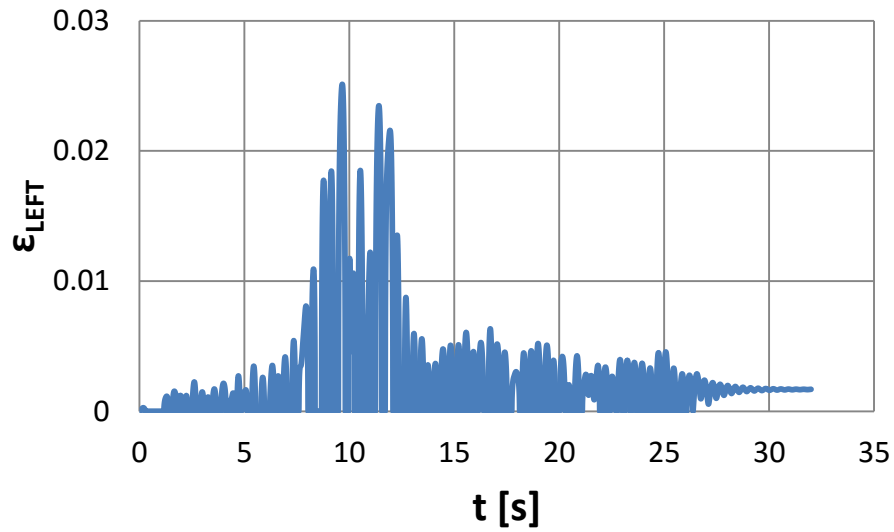
Figure 141: Time history of the local bending strains at the plate-shell connection at the left side of Tank II for the seismic input of Figure 111 ($\lambda = 0.4$).

Table 9: Fatigue analysis of Tank I using rainflow cycle counting method ($\lambda = 0.5$).

Right Side of Tank I				Left Side of Tank I			
$\Delta\varepsilon$	$\Delta\bar{\varepsilon}$	n_I	N_I	$\Delta\varepsilon$	$\Delta\bar{\varepsilon}$	n_I	N_I
0.0002	0.0013	26	62649	0.0002	0.0014	31	48338
0.0004	0.0038	21	2400	0.0005	0.0042	28	1764
0.0007	0.0063	16	520	0.0008	0.0070	16	379
0.0010	0.0088	5	190	0.0011	0.0098	5	138
0.0013	0.0113	1	89	0.0015	0.0126	1	65
0.0016	0.0138	2	49	0.0018	0.0154	1	36
0.0019	0.0163	0	30	0.0021	0.0182	1	22
0.0022	0.0188	0	20	0.0025	0.0210	1	14
0.0025	0.0213	2	14	0.0028	0.0238	0	10
0.0028	0.0238	0	10	0.0031	0.0265	1	7
0.0031	0.0263	0	7	0.0034	0.0293	0	5
0.0034	0.0288	2	6	0.0038	0.0322	1	4
$D = 0.594$				$D = 0.648$			

141

Table 10: Fatigue analysis of Tank II using rainflow cycle counting method (λ =0.4).

Right Side of Tank I				Left Side of Tank I			
$\Delta\varepsilon$	$\Delta\bar{\varepsilon}$	n_I	N_I	$\Delta\varepsilon$	$\Delta\bar{\varepsilon}$	n_I	N_I
0.0001	0.0010	20	122659	0.0001	0.0011	29	109304
0.0004	0.0030	28	4742	0.0004	0.0032	25	4146
0.0006	0.0050	12	1029	0.0007	0.0052	20	896
0.0009	0.0070	2	375	0.0010	0.0073	2	326
0.0012	0.0090	2	177	0.0012	0.0094	1	153
0.0014	0.0110	0	97	0.0015	0.0115	3	84
0.0017	0.0130	1	59	0.0018	0.0136	1	51
0.0019	0.0150	3	38	0.0020	0.0157	0	33
0.0022	0.0170	3	26	0.0023	0.0178	3	23
0.0025	0.0190	0	19	0.0026	0.0199	0	17
0.0027	0.0210	1	14	0.0028	0.0220	1	12
0.0030	0.0230	1	11	0.0031	0.0241	2	10
$D = 0.408$				$D = 0.906$			

4.7 Effect of roof stiffness on uplifting

An interesting issue on the uplifting mechanics is the effect of the roof on the uplift size. For this purpose, a parametric study of eight tanks has been performed using finite elements. These tanks are unanchored and have been modeled with and without a roof. All have a total height of 12 m and a filling height of 10 m and aspect ratios ranging from 0.625 to 2. Their shell thickness has been designed according to the provisions of API 650. The characteristics of the tanks are shown in Table 11. The results of this parametric study are shown in Figure 142.

The results in Figure 142 show that the stiffness of the roof affects the uplifting of the tanks and particularly it leads to a decrease of the vertical uplift of the tanks. This behavior can be also observed in Figure 143, Figure 144, Figure 145 and Figure 146 which show representative finite element models of the tanks under consideration. The same behavior can be concluded from Figure 148 for the two case studies.

Table 11: Characteristics of the tanks used in the parametric study.

	D [m]	H [m]	H_T [m]	$\gamma = H / R$	t_1 [mm]	t_2 [mm]	t_3 [mm]	t_b [mm]
Tank 1	10	10	12	2	6	5	5	6
Tank 2	11	10	12	1.818	6	5	5	6
Tank 3	12.4	10	12	1.613	6	5	5	6
Tank 4	13	10	12	1.538	6	5	5	6
Tank 5	14	10	12	1.43	6	5	5	6
Tank 6	20	10	12	1	7.5	6	6	7
Tank 7	26	10	12	0.77	9.6	7	6	9
Tank 8	32	10	12	0.625	12	8	6	11
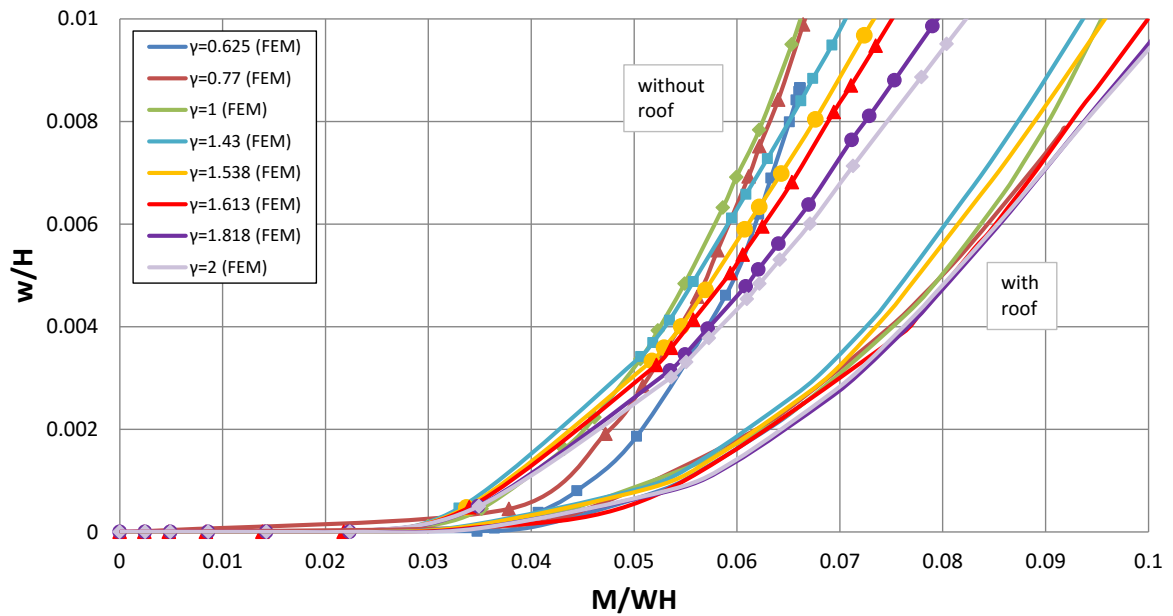
Figure 142: Parametric study of eight unanchored tanks with different aspect ratios, modeled with and without a roof.
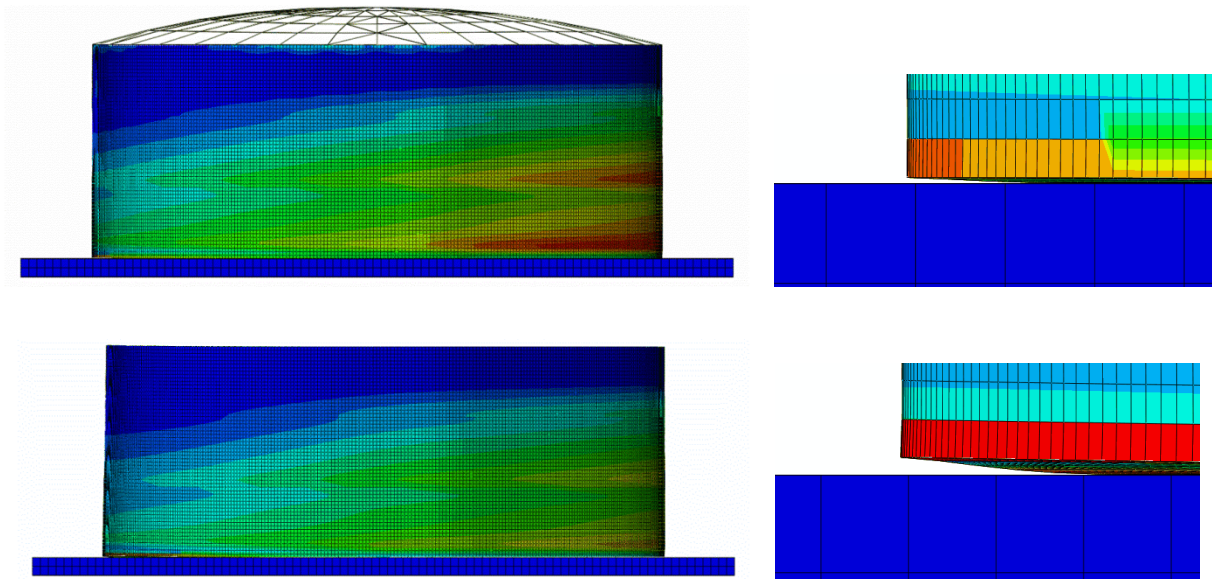
Figure 143: Finite element modelling of the tank with aspect ratio equal to 0.625; (a) with roof, (b) without roof.
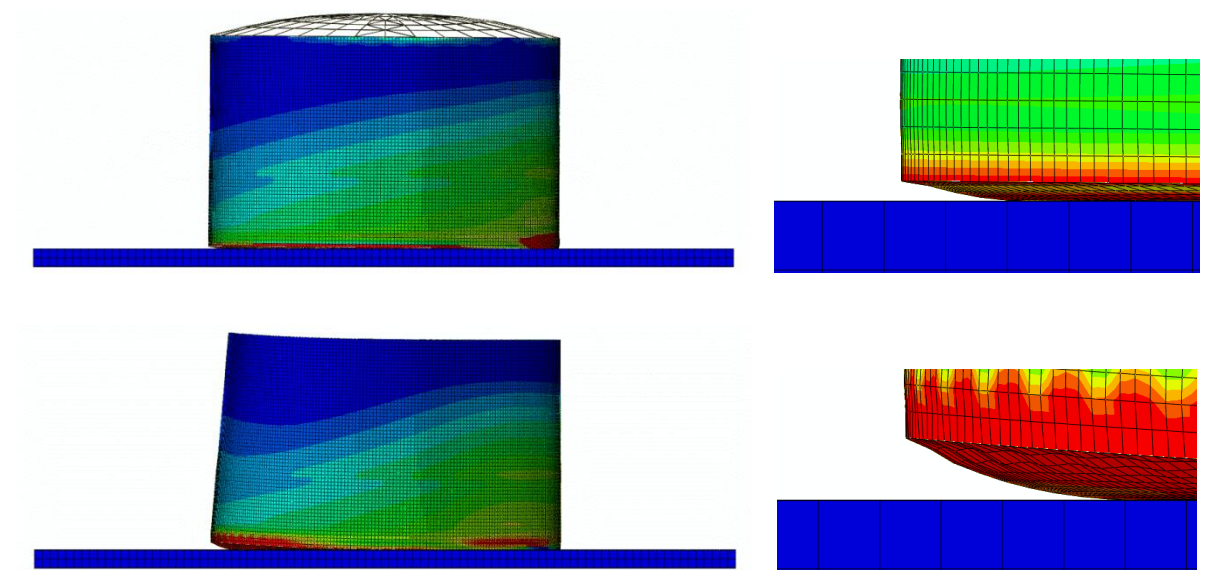
Figure 144: Finite element modelling of the tank with aspect ratio equal to 1; (a) with roof, (b) without roof.

144
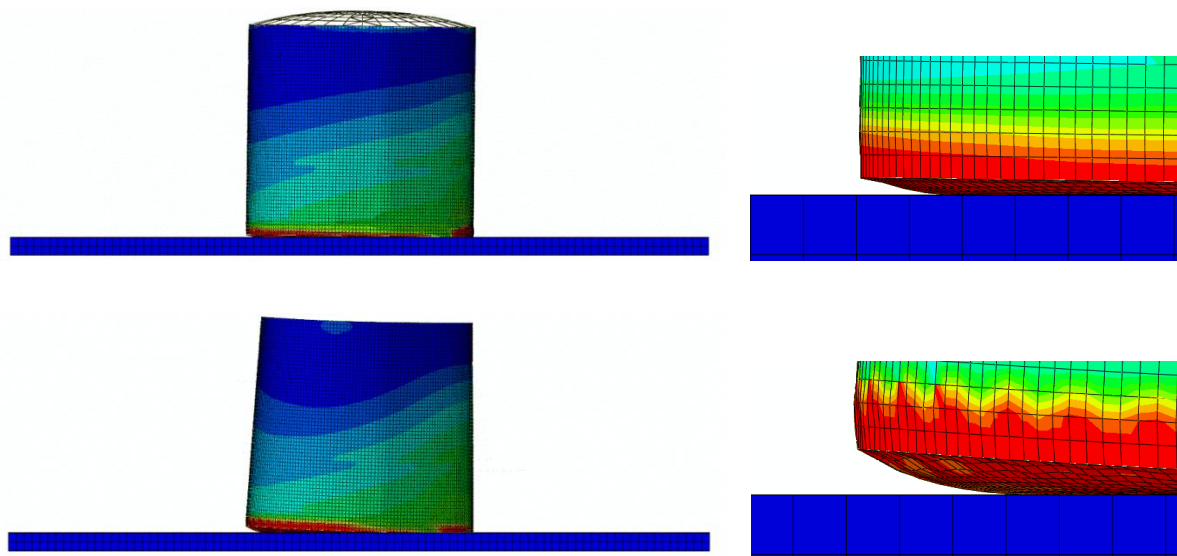
Figure 145: Finite element modelling of the tank with aspect ratio equal to 1.538; (a) with roof, (b) without roof.
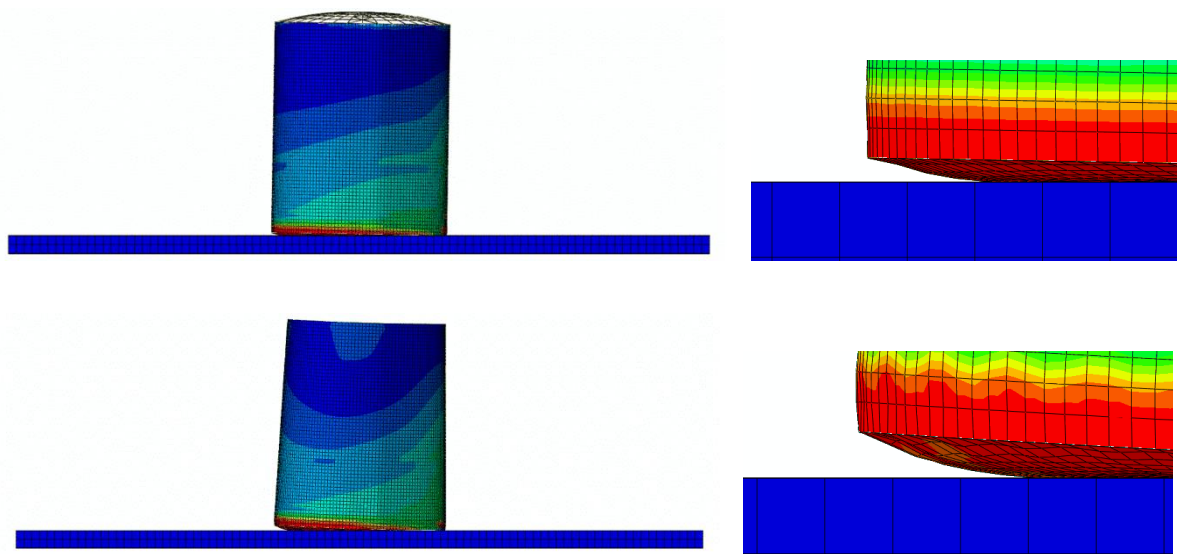
Figure 146: Finite element modelling of the tank with aspect ratio equal to 2; (a) with roof, (b) without roof.

145
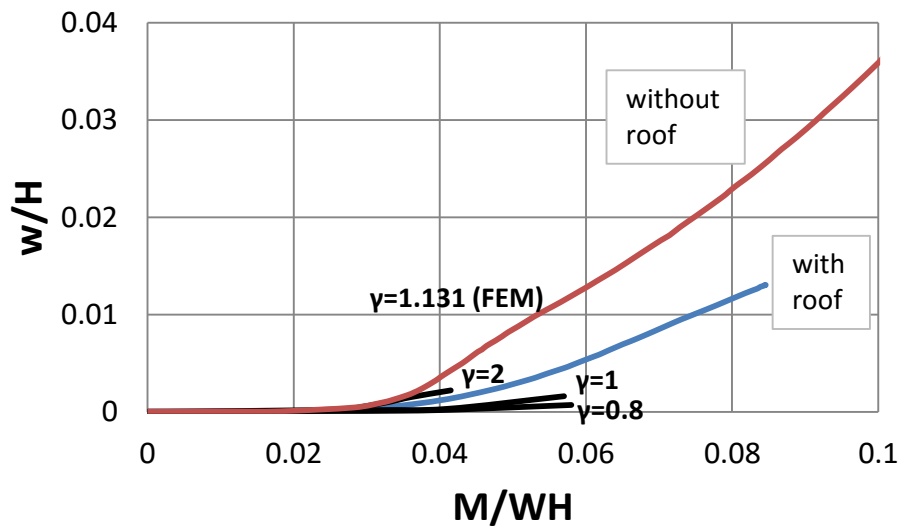
Figure 147: Maximum vertical uplift of the tank *w* versus overturning moment *M*; present finite element results for Tank I, with and without roof.
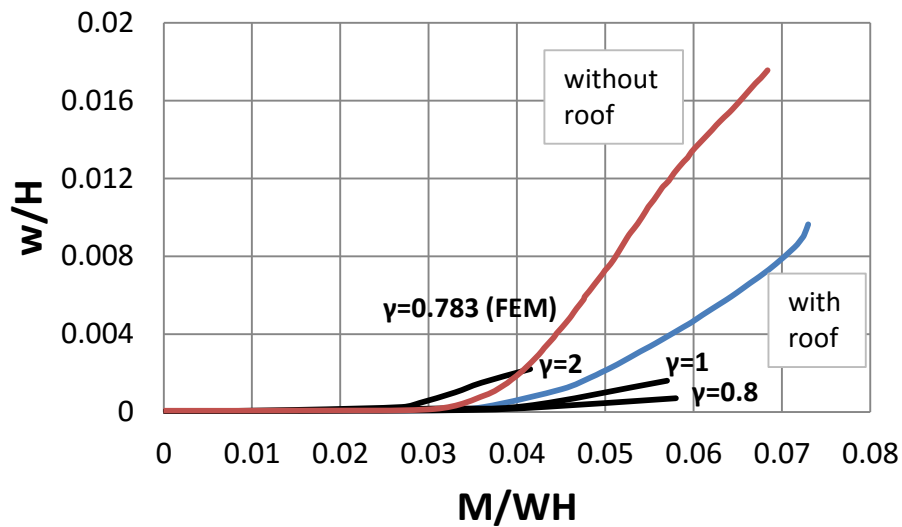
Figure 148: Maximum vertical uplift of the tank *w* versus overturning moment *M*; present finite element results for Tank II, with and without roof.

146

5. Performance-Based Design Framework for the Seismic Design of Liquid Storage Tanks

In this chapter, performance criteria for the seismic design of industrial liquid storage tanks are proposed, aimed at defining a performance-based design framework. This framework is suitable for the reliable development of fragility curves and assessment of seismic risk. Considering "loss of containment" as the ultimate damage state, the proposed performance limits are quantified in terms of local quantities obtained from a simple and efficient earthquake analysis. Liquid storage tanks and the corresponding principal failure modes (elephant's foot buckling, roof damage, base plate failure, anchorage failure and nozzle damage) are examined thoroughly. Lastly, using the numerical models described in Chapter 4, for seismic analysis of liquid storage tanks, the proposed performance limits are applied in two liquid storage tanks, located in areas of high seismicity.

5.1 Introduction

Industrial facilities (e.g. power/chemical/petrochemical plants, terminals) and their components, under seismic loading, may exhibit significant damage, which may threaten their structural integrity with severe consequences on the population, the environment and the economy. Liquid storage tanks are considered as critical components of those industrial facilities.

The structural response of liquid storage tanks under strong seismic loading constitutes an important issue for safeguarding the structural integrity of industrial facilities, especially in refineries and power plants. The dominant mode of tank failure is in the form of elephant's foot buckling at the tank base (Manos 1986). Other types of earthquake damages include base plate failure due to uplifting (Peek 1988, Natsiavas and Babcock 1988), roof damage due to excessive sloshing (ASCE 2000), or shell damage at nozzle areas due to non-flexible connections with piping (Vasilescu and Ilinca 2014). Current practice for the seismic design of tanks is based mainly on the application of Appendix E of API 650 standard. EN 1998-4 standard also contains design provisions for the seismic design of liquid storage tanks.

The seismic behavior of liquid storage tanks is quite unique and significant research is currently underway to understand better their mechanical behavior under strong earthquake-

147

induced cyclic loading. European research program INDUSE program 2009-2012 (Pappa et al. 2012) has been an important contribution towards this purpose; combining large-scale experimental work with extensive numerical simulations, design guidelines and recommendations have been developed for the structural integrity of industrial tanks, pressure vessels and piping under strong seismic action (Varelis et al. 2013a, Varelis et al. 2013b, Wieschollek et al. 2013, Papatheocharis et al. 2013, Ferino et al. 2013, Reza et al. 2013).

In addition to understanding mechanical behavior under strong seismic loading, several attempts to apply performance-based design (PBD) methodologies in the seismic design of industrial facilities have been reported (Reza et al. 2014, Bursi et al. 2015b, Bursi et al. 2016) and to the development of seismic fragility curves (O' Rourke et al. 2000, Salzano et al. 2003, Fabbrocino et al. 2005). Within this PBD framework, it is necessary to quantify all possible failure modes in terms of seismic response parameters, also referred to as Engineering Demand Parameters (EDPs) and to define appropriate performance levels, which classify the severity of damage. It is important to realize that liquid storage tanks may not be similar to civil engineering structural systems (e.g. buildings, bridges), because of important particularities (Pappa et al. 2011, Pappa et al. 2012). Furthermore, it is expected that under severe seismic loading, liquid storage tanks may exhibit severe deformations in the plastic range, so that the existing design tools for pressure containment may not be adequate.

The contents of the present chapter are part of the national project RASOR (Papadopoulos et al. 2015), aimed at developing efficient methodologies for assessing seismic vulnerability and risk of industrial facilities. The work reported herein is aimed at defining a PBD framework for the seismic analysis and design of liquid storage tanks (anchored and unanchored), through appropriate quantification of the failure modes and definition of seismic performance levels. The proposed methodology is supported by available test data on industrial components, numerical simulation results and engineering judgment, and is being currently employed in the European research program INDUSE-2-SAFETY (2014-2017) towards developing methodologies for seismic risk assessment of industrial facilities.

5.2 Failure modes (limit states) for liquid storage tanks

The main criterion for safeguarding structural integrity of a liquid storage tank subjected to strong seismic loading is to "maintain its containment". Towards this purpose, the failure modes, described in Chapter 2, likely to occur in the course of a seismic event, should be considered. Those limit states are described briefly below for the sake of completeness.

5.2.1 Elephant's foot buckling

Elephant's foot buckling occurs when the meridional compressive stress σ_x, in conjunction with hoop tension due to internal pressure, reaches shell resistance σ_b, and results in local buckling of the tank wall at the tank bottom, in the form of bulging and folding. The latter can be expressed in terms of the yield stress σ_Y and an appropriate reduction factor that depends on shell slenderness (EN 1993-1-6). Similar provisions for shell resistance against elephant's foot buckling exist in other shell design standards (API 650, EN 1998-4). Previous investigations have shown that the occurrence of elephant's foot buckling is usually associated with tank failure: post-buckling is quite unstable, local deformations are significant and non-repairable, and shell folding at the vicinity of a nozzle may result in immediate loss of containment.

5.2.2 Roof damage

In fixed roof tanks, if the maximum sloshing wave height d_{max} due to liquid free surface motion, exceeds tank freeboard δ, the tank roof may be damaged due to sloshing wave impact. The value of d_{max} (Figure 149) may be computed from potential flow theory as follows (EN 1998-4, Ibrahim 2005):

$$d_{max} = 0.84 R \ddot{u}_{max} / g \tag{146}$$
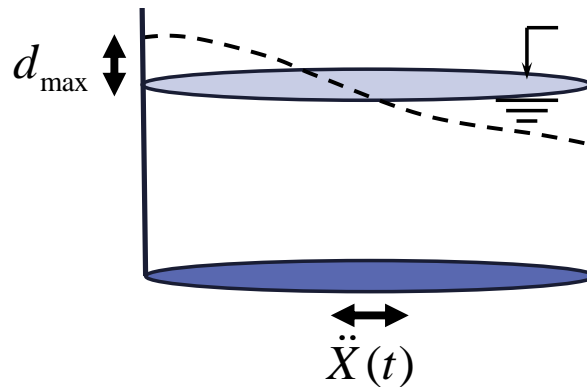
Figure 149: Sloshing wave height.

where $\ddot{u}_{max}$ is the maximum value of convective acceleration calculated from an appropriate linear oscillator equation that describes sloshing motion (Malhotra 2000, Ibrahim 2005) and R is the tank radius. Sloshing wave damage can be serious but not catastrophic; usually it does not result in loss of containment.

5.2.3 Failure of base plate

To identify failure due to excessive tensile strain, the maximum local tensile strain ε_T at the welded connection should be compared with the tensile resistance ε_{Tu} of the welded connection.

For a fatigue analysis of the welded connection, it is necessary to calculate the history of local strain $\varepsilon(t)$ at the weld toe induced by the seismic loading, and combine with an appropriate fatigue curve, representing the fatigue resistance of the connection. Note that strain history at the critical location is an irregular (non-constant amplitude) loading pattern, so that the loading spectrum of the strain action should be calculated through a "rainflow" analysis to perform variable-amplitude fatigue analysis; the strain ranges $\Delta\varepsilon_i$ and the corresponding numbers of cycles for each strain range, n_i are calculated. To determine whether fatigue failure may occur, this spectrum should be combined with an appropriate fatigue curve, so that the number of cycles to failure N_i for each strain range $\Delta\varepsilon_i$ is obtained. Finally, using Miner's rule, a fatigue damage parameter D is calculated, where fatigue failure corresponds to a unit value (Prinz and Nussbaumer 2012, Vathi and Karamanos 2015).

150

In both failure modes, the local strain should account for geometric effects of the connection, in terms of an appropriate strain concentration factor ($SNCF$) (Vathi and Karamanos 2015). The definition of the ε_{Tu} value and the choice of an appropriate low-cycle fatigue curve, together with the determination of local strain at the weld toe, may not be a trivial task. Towards this purpose, a dedicated research effort on this subject, which combines experimental and numerical work, is planned within the INDUSE-2-SAFETY project (Bursi et al. 2015a).

5.2.4 Anchor bolt failure

Bolt yielding or fracture may occur when the maximum tensile bolt force F induced by the seismic event exceeds a corresponding limit value:

• anchor bolt yielding:

$$F_Y = f_1 \sigma_Y A_s \qquad (147)$$

• anchor bolt fracture

$$F_U = f_2 \sigma_U A_s \qquad (148)$$

where σ_Y and σ_U are the yield and ultimate stress of the bolt material, A_s is the tensile stress area of the bolt, whereas f_1 and f_2 are safety factors (API 650, EN 1993-1-8). The severity of anchor bolt failure may depend on the existence of rigidly connected or flexible pipe attachments. In the case of rigidly connected pipes, fracture of anchor bolts is associated with tank uplifting, resulting in fracture of the attached pipes and loss of containment.

In addition, failure of the steel plates of the anchor chair can be identified when the maximum bolt seismic force F exceeds the prying resistance of the horizontal steel plate or the shear resistance of the vertical plates welded to the steel tank (API 650). Prying failure of the plate may not be catastrophic, but shear failure may result in fracture at its bottom, and immediate loss of containment. The latter failure mode can be quantified in terms of the shear stress developed at the welded connection compared with the yield and the ultimate shear strength of the steel material.

151

5.2.5 **Other failure modes**

Current design practice (API 650 and EN 1998-4) adopts an empirical procedure for determining actions on nozzles, whereas flexibility of the attached piping is suggested. In general, local loads on the tank nozzle depend primarily on the seismic response of the attached piping system, rather than the response of the liquid storage tank. Therefore, this failure mode can be examined with the help of the analysis of the attached piping system.

Buckling at the top of the tank and failures of floating roofs are difficult to be modeled and they were not considered in the present analysis.

5.3 **Performance levels for liquid storage tanks**

Based on the severity of damage associated with the failure modes stated in the previous paragraph, it is possible to define different levels of performance. Four performance levels are considered for liquid storage tanks, as shown in Table 12, and are quite similar to the ones suggested in the papers by O' Rourke et al. (2000), HAZUS (1997) and ALA Part 1 (2001).

Table 12: Performance levels for liquid storage tanks under seismic loading.

Level	Description
0	No damage
I	Minor (non-severe) damage
II	Major damage, but no loss of containment
III	Major damage with loss of containment

5.4 **Correlation of performance levels with failure modes**

The performance levels are quantified in terms of the Engineering Demand Parameters (EDPs), which correspond to the failure modes, as shown in Table 13, and can be used for the evaluation of appropriate seismic fragility curves and risk analysis (Fabbrocino et al. 2005, Salzano et al. 2003). Particularly:

152

- For elephant's foot buckling, the meridional compressive stress σ_x, should be less than the shell resistance σ_b in order this type of failure. If σ_x becomes larger than σ_b then there is a significant threat for immediate loss of containment, therefore in this case the performance level is "III".

- Roof damage usually does not result in loss of containment. In fixed roof tanks, if the maximum sloshing wave height d_{max} is smaller than the tank freeboard δ, If d_{max} exceeds δ, the tank roof may be damaged due to sloshing wave impact, especially if it exceeds 1.4δ. The value of 1.4 is taken from API 650 provisions.

- The failure of base plate could be either because of fracture of fatigue. To identify failure due to excessive tensile strain, the maximum local tensile strain ε_T should be compared with the tensile resistance ε_{Tu} of the welded connection. In lieu of a detailed investigation, a value between 2% and 5% is suggested for the ultimate tensile resistance ε_{Tu}, depending on the steel material and the weld defect tolerance. In addition, ε_T should be compared with the nominal yield strain of the material, ε_Y (where $\varepsilon_Y = \sigma_Y / E$) and with the limit ε_P at which severe plastification of the welded connection occurs. A strain level of 0.5% is proposed for this limit, but one may propose another value based on specific tests.

  To avoid fracture due to low-cycle fatigue, the damage factor, D, calculated from the "rainflow" analysis, should be less than unity. Values of $D > 1$ lead to loss of containment (performance level "III"). Intermediate limit values (D_1 and D_2) corresponding to minor or major damage with no loss of containment are defined according to the industrial plant operator. Possible values for D_1 and D_2 can be 0.50 and 0.80 respectively; those values are adopted in the present study.

- Anchor bolt failure can be identified when the maximum bolt seismic force F exceeds the prying resistance of the horizontal steel plate or the shear resistance of the vertical plates welded to the steel tank (API 650). In the first case, the yielding resistance and ultimate resistance of anchor bolt should be taken into account and it is not a catastrophic failure. On the other hand, shear failure may result in fracture at the tank bottom, and immediate loss of containment. The latter failure mode can be quantified in terms of the shear stress developed at the welded connection compared with the yield, τ_Y, and the ultimate shear strength, τ_U, of the steel material.

153

Reliable numerical models should be employed for the computation of the EDPs. Towards this purpose, the simple and efficient models described in Chapter 4, for seismic analysis of liquid storage tanks, are used here in a later section for the calculation of EDPs and definition of the corresponding performance levels for two design examples.

Table 13: Performance criteria for liquid storage tanks under seismic loading.

Failure mode	Engineering Demand Parameter	Performance level and corresponding range	
elephant's foot buckling	Meridional compressive stress σ_x	$\sigma_x \leq \sigma_b$	0
		$\sigma_x > \sigma_b$	III
roof sloshing damage	Sloshing wave height d_{max}	$d_{max} < \delta$	0
		$\delta \leq d_{max} \leq 1.4\delta$	I
		$d_{max} > 1.4\delta$	II
anchor bolt failure	Bolt force F	$F_Y \leq F \leq F_U$	I
		$F > F_U$	II
bolt plate failure	Shear stress τ	$\tau_Y \leq \tau \leq \tau_U$	II
		$\tau > \tau_U$	III
base plate fracture	Maximum tensile local strain ε_T	$\varepsilon_T \leq \varepsilon_Y$	0
		$\varepsilon_Y < \varepsilon_T \leq \varepsilon_P$	I
		$\varepsilon_P < \varepsilon_T \leq \varepsilon_{Tu}$	II
		$\varepsilon_T \geq \varepsilon_{Tu}$	III
base plate fatigue	Damage factor $D = \sum_i \dfrac{n_i}{N_i}$	$D \leq D_1$	0
		$D_1 < D \leq D_2$	I
		$D_2 < D \leq 1$	II
		$D > 1$	III

5.5 Design Examples

The seismic behavior of liquid storage tanks is quite complex, characterized primarily by the dynamic interaction of the deformable steel tank with the moving liquid containment. Instead of detailed modeling of tank-liquid interaction considering liquid free surface and shell-liquid interface, the simplified model described in Chapter 4 can be developed that accounts for the principal response features in a simple and efficient manner. The model used herein, refers

154

to lateral (horizontal) excitation, but this approach can be modified to include rocking excitation and vertical excitation (Veletsos and Tang 1987).

The above criteria are applied in two liquid storage tanks that are typical parts of petrochemical facilities, located in areas of significant seismicity. The present analysis is indicative, for the purpose of demonstrating the capabilities of the proposed methodology. The accelerogram from the 1999 Düzce earthquake with peak ground acceleration $PGA = 0.36g$ is employed as the seismic input of the seismic analysis (Figure 111).

Tank I and Tank II, described in paragraph 4.3, are utilized for the numerical analysis, simulated as both anchored and unanchored. Tank I is a 27.8-meter-diameter tank with a total height of 16.5 meters. The filling height of the tank H is equal to 15.7, which corresponds to an aspect ratio of the tank, $\gamma (= H / R)$, equal to 1.131. The tank thickness varies from 6.4 mm at its top course to 17.7 mm at its bottom course and the bottom plate is 6 mm thick with an 8-mm-thick annular plate. On the other hand, Tank II, is a broad 46.9-meter-diameter tank with a total height of 19.95 meters. The filling height of the tank H is equal to 18.37 resulting to an aspect ratio, $\gamma (= H / R)$, equal to 0.783. The tank thickness varies from 8 mm at its top course to 22.23 mm at its bottom course.

In the anchored case, M42 class 10.9 anchor bolts are considered, with yield and ultimate tensile strength, σ_{Yb} and σ_{Ub}, equal to 900 and 1000 MPa respectively. The effective tensile stress area of the anchor bolt A_s is equal to 1120 mm^2 and bolt spacing around the tanks is equal to 1.8 m. The Strain Concentration Factors ($SNCF$) value for the tanks have been calculated equal to 8.55 and 7.72, using a finite element procedure. Furthermore, the linear $\log \Delta\varepsilon - \log N$ fatigue curve of Figure 102 is used.

The tanks are analyzed for a series of seismic events of increasing amplitude; considering the Düzce earthquake as a basis, its ground acceleration values are multiplied by a factor, λ, to obtain an accelerogram with the desired value of PGA. At each value of PGA, a time history analysis is conducted, and the tanks are verified against all failure modes under consideration. Tank performance is presented in Table 14, Table 15, Table 16, Table 17 and Table 18 in terms of different performance criteria for the failure modes under consideration.

Table 14: Response of Tank I in terms of elephant's foot buckling for several PGA levels.

| PGA [g] | anchor | Engineering Demand Parameter | | Perf. Level |
		Action σ_x [MPa]	Resistance σ_b [MPa]	
0.25	yes	16.53		0
	no	9.04		0
0.36	yes	23.62		0
	no	11.57	30.7	0
0.50	yes	33.06		III
	no	20.90		0

Table 15: Response of Tank I in terms of roof sloshing damage for several PGA levels.

| PGA [g] | anchor | Engineering Demand Parameter | | Perf. Level |
		Action d_{max} [m]	Resistance (i) δ [m] (ii) 1.4δ [m]	
0.25	yes	0.852		I
	no	0.847	(i) 0.814	I
0.36	yes	1.217		II
	no	1.224	(ii) 1.14	II
0.50	yes	1.703		II
	no	1.723		II

Table 16: Response of Tank I in terms of anchor bolt failure for several PGA levels.

| PGA [g] | anchor | Engineering Demand Parameter | | Perf. Level |
		Action F [kN]	Resistance (i) F_Y [kN] (ii) F_U [kN]	
0.25		510.5	(i) 806.4	0
0.36	yes	729.3		0
0.50		1021.0	(ii) 1008	II

156

Table 17: Response of Tank I in terms of base plate fracture for different PGA levels, at the left (L) and right (R) side of the tank.

| PGA [g] | anchor | Engineering Demand Parameter | | Perf. Level |
		Action ε_T	Resistance i) ε_Y ii) ε_{Tu}	
0.25	no	0.032 (L)	i) 0.0011 ii) 0.02	III
		0.045 (R)		III
0.36		0.052 (L)		III
		0.062 (R)		III
0.50		0.080 (L)		III
		0.083 (R)		III

Table 18: Response of Tank I in terms of base plate fatigue for several PGA levels, at the two sides of the tank [left (L) and right (R)].

| PGA [g] | anchor | Engineering Demand Parameter | | Perf. Level |
		Action D	Resistance $D_{fatigue}$	
0.25	no	1.011 (L)	1	III
		1.956 (R)		III
0.36		2.935 (L)		III
		2.726 (R)		III
0.50		3.399 (L)		III
		2.392 (R)		III

Table 19: Response of Tank II in terms of elephant's foot buckling for several PGA levels.

| PGA [g] | anchor | Engineering Demand Parameter | | Perf. Level |
		Action σ_x [MPa]	Resistance σ_b [MPa]	
0.25	yes	20.42	19.58	III
	no	12.69		0
0.36	yes	29.17		III
	no	13.85		0
0.50	yes	40.84		III
	no	18.21		0

157

Table 20: Response of Tank I in terms of roof sloshing damage for several PGA levels.

PGA [g]	anchor	Engineering Demand Parameter		Perf. Level
		Action d_{max} [m]	Resistance (i) δ [m] (ii) 1.4δ [m]	
0.25	yes	0.544		0
	no	0.570	(i) 1.58	0
0.36	yes	0.777		0
	no	0.778		0
0.50	yes	1.088	(ii) 2.212	0
	no	1.121		0

Table 21: Response of Tank I in terms of anchor bolt failure for several PGA levels.

PGA [g]	anchor	Engineering Demand Parameter		Perf. Level
		Action F [kN]	Resistance (i) F_Y [kN] (ii) F_U [kN]	
0.25		1338.8	(i) 806.4	II
0.36	yes	1912.5		II
0.50		2677.6	(ii) 1008	II

Table 22: Response of Tank I in terms of base plate fracture for different PGA levels, at the left (L) and right (R) side of the tank.

PGA [g]	anchor	Engineering Demand Parameter		Perf. Level
		Action ε_T	Resistance i) ε_Y ii) ε_{Tu}	
0.25		0.045 (L)		III
		0.031 (R)		III
0.36	no	0.055 (L)	i) 0.0011	III
		0.064 (R)	ii) 0.02	III
0.50		0.077 (L)		III
		0.070 (R)		III

158

Table 23: Response of Tank I in terms of base plate fatigue for several PGA levels, at the two sides of the tank [left (L) and right (R)].

PGA [g]	anchor	Engineering Demand Parameter		Perf. Level
		Action D	Resistance $D_{fatigue}$	
0.25	no	1.503 (L)	1	III
		0.531 (R)		III
0.36		4.380 (L)		III
		3.014 (R)		III
0.50		6.832 (L)		III
		6.681 (R)		III

159

6. Summary and Conclusions

Significant damage observed in liquid storage tanks during past seismic events has motivated the investigation of the seismic response and integrity of liquid storage tanks. The present research focuses on two main failure modes: (a) elephant's foot buckling and (b) base uplifting of unanchored tanks. Following a brief literature review regarding tank seismic response and the scope of the present dissertation, some aspects of seismic analysis and design of tanks have been stated. Firstly, relevant standards and guidelines to seismic analysis of liquid storage tanks are summarized, with emphasis on EN 1998-4 Standard and API 650. Some important aspects of seismic loading of tanks are also described, and the failure modes of liquid storage tanks are presented in detail.

Elephant's foot buckling is the first major mode examined in the present thesis. It has been examined using three-dimensional and axisymmetric nonlinear finite element tools, in terms of buckling and post-buckling, considering material and geometric nonlinearities, accounting for initial imperfections for hydrostatic pressure, and for internal pressure levels up to 80% of yield pressure. Two types of imperfections are considered: (a) imperfections from real measurements in an existing tank, which are of random shape (Type SI1 imperfection) and (b) axisymmetric imperfections in the form of an initial bulge at the bottom of the cylinder around the circumference of the cylinder (Type SI2 imperfection). The results show that the tank is sensitive to these types of imperfections, but the sensitivity is rather moderate. Furthermore the height of lateral load may not be a critical factor for the value of maximum moment. Special emphasis has been given on the development of local stresses and strains at the buckled area, in the pre-buckling and the post-buckling configuration. The results show that the membrane stresses are quite low with respect to the stresses developed at the inner and outer surface of the shell, and the stresses and strains are larger on the outer surface of the buckled area.

The accuracy of simplified axisymmetric models in modelling this instability mode provided fairly good results. Special emphasis has been given on the development of local stresses and strains at the buckled area, in the pre-buckling and the post-buckling configuration. The numerical results have been compared with predictions from the relevant provisions of EN 1993-1-6 and EN 1998-4. The comparison showed that the EN 1993-1-6 specification for the cases under consideration appears to be conservative in predicting the bending moment

160

capacity. On the other hand, the empirical equation of EN 1998-4 may not provide reliable predictions of buckling strength for relatively large values of imperfection amplitude. Finally, some promising results have been obtained for the use of FRP in tank strengthening. It is shown that FRP wrapping may constitute a simple and economic way of improving tank strength against elephant's foot buckling.

The second issue examined in the present study refers to tank uplifting under severe dynamic (seismic) excitation. A systematic two-step methodology for analyzing the seismic lateral and rocking response of unanchored tanks that exhibit base uplifting has been developed, with emphasis on the failure of the welded connection between the base plate and the tank shell due to excessive local strain and fatigue. This methodology is applied on two typical liquid storage tanks.

For the tanks considered in the analysis, in the case of lateral loading, uplifting of the tank occurs at values of M/WH exceeding 0.03. Furthermore, this uplift is associated with inelastic deformation at the uplifted area of the base plate. It is also observed that the increase of the overturning moment leads to an increase of the top horizontal displacement, the uplift size and the length of the uplifted part of the tank. Moreover, it leads to an increase of the axial compressive stresses acting on the tank wall. The comparison of the membrane forces in the case of the unanchored and anchored tank shows that the simple analytical formula for calculating meridional stresses gives good results when there is no uplift of the tank. The equivalent plastic strain becomes maximum at the welded junction between the tank wall (primarily) and the base plate and at the inflection point (change of the slope of the base plate curve). These are the two locations where plastic yielding also begins to develop.

The first step of the present solution methodology consists of a lateral-load static analysis which determines the relationship between the overturning moment and the uplifting (rocking) angle, as well as the relationship between the uplifting size and length. Subsequently, based on those relationships, a nonlinear simplified model for the dynamic analysis of uplifted tanks is developed, calibrated and employed for the analysis of the tanks under seismic excitation. The results indicate a significant effect of uplifting in tank response, when compared with the case of anchored tanks. Those results are aimed at better understanding of uplifting phenomenon during dynamic excitation, and may be used for improvement of the current design practice.

161

Upon calculating the global tank seismic response, the maximum bending strain at the plate-shell connection is calculated, and a fatigue analysis of the connection can be carried out considering the corresponding fatigue loading spectrum, an appropriate curve for low-cycle fatigue and a fatigue damage accumulation factor. Key steps in this fatigue analysis methodology is the calculation of an appropriate value of local strain range $\Delta\bar{\varepsilon}$ and the definition of the corresponding fatigue curve for the welded connection under consideration. Towards this purpose a dedicated research effort, experimental and numerical has been planned within the INDUSE-2-SAFETY program 2014-2017 (Bursi et al. 2015a).

Subsequently, using a parametric study of eight tanks with different aspect ratios, it is found that the stiffness of tank roof may have a significant influence on the uplifting mechanism and size.

In the last part of the dissertation, a framework for performance-based design of liquid storage tanks under seismic loading conditions has been defined. The main failure modes have been identified and quantified in terms of appropriate engineering demand parameters (EDPs). In most of the cases, local strain has been considered as the principal EDP. Performance levels are defined for each mode of failure, considering an appropriate range of EDP values. The definition of performance level is based primarily on available experimental testing and numerical computations, as well as on engineering judgement. In addition, the simplified numerical models proposed in Chapter 4 for the seismic analysis of tanks are used, so that reliable estimates of EDP are obtained. The above concepts are applied in two typical tank case studies. The proposed performance-based framework is aimed at increasing the safety of industrial facilities against strong seismic events.

162

7. References

Ahari, M. N., Eshghi, S., and Ashtiany, M. G. (2009). "The tapered beam model for bottom plate uplift analysis of unanchored cylindrical steel storage tanks", *Engineering Structures*, Vol. 31, pp. 623-632.

American Lifelines Alliance (2001). Seismic Fragility Formulations for Water Systems, Part-1 – Guidelines, Report.

American Petroleum Institute (2003). Seismic Design of Storage Tanks - Appendix E, Welded Steel Tanks for Oil Storage, API 650, 10th Edition, Washington, D.C.

American Petroleum Institute (2007). Seismic Design of Storage Tanks - Appendix E, Welded Steel Tanks for Oil Storage, API 650, 11th Edition, Washington, D.C.

American Society of Civil Engineers (2000). "Izmit (Kocaeli) Turkey, earthquake of August 17, 1999", A. K. Teng (editor), Technical Council on Lifeline Earthq. Engrg., Reston, VA.

American Society of Civil Engineers (2006). Minimum Design Loads for Buildings and Other Structures, ASCE 7-05, Reston, VA.

Auli, W., Fischer, F. D., and Rammerstorfer, F. G. (1985). "Uplifting of earthquake-loaded liquid-filled tanks", *Proceedings, 1985 Pressure Vessels and Piping (PVP) Conference*, 98-7, pp. 71-85.

Bathe, K-J, (1996). "Finite Element Procedures", Prentice Hall Inc., New Jersey.

Batikha, M., Chen, J.F., Rotter, J.M. and Teng, J.G. (2009). "Strengthening metallic cylindrical shells against elephant's foot buckling with FRP", *Thin-Walled Structures*, Special Issue on FRP Strengthened Metallic Structures, Vol. 47, No. 10, October 2009, pp. 1078-1091.

Bendimerad, F., Coburn, A., Morrow, G., Johnson, L., and Rahnama, M. (1999). Kocaeli, Turkey Earthquake, Event Report.

British Standards Institution (1993). "Fatigue Design and Assessment of Steel Structures", BS 7608, UK.

Bursi, O. S., et al. (2015a). "Component Fragility Evaluation, Seismic Safety Assessment and Design of Petrochemical Plants Under Design-Basis and Beyond-Design-Basis Accident Conditions," Mid-Term Report, INDUSE-2-SAFETY project 2014-2017, RFCS program, European Commission, Brussels, Belgium, website: http://www.induse2safety.unitn.it/.

Bursi, O.S., Reza, M.S., Abbiati, G., Paolacci, F. (2015b). "Performance-based earthquake evaluation of a full-scale petrochemical piping system", *Journal of Loss Prevention in the Process Industries*, Vol. 33, pp. 10-22.

Bursi, O. S., Reza, Paolacci, F., Reza, M. S., Alessandri, S., Todini, N. (2016). "Seismic Assessment of Petrochemical Piping Systems Using a Performance-Based Approach," *Journal of Pressure Vessel Technology*, ASME, Vol. 138, No. 3, Article Number: 031801.

Cambra, F. J. (1982). "Earthquake response considerations of broad liquid storage tanks", Rep. UCB/EERC-82/25, Earthquake Engineering Research Center, Richmond, California.

Chen, J.F., Rotter, J.M., and Teng, J.G. (2005) "Strengthening silos and tanks against elephant's foot buckling", Proceedings of the Fourth International Conference on Advances in Steel Structures, ICASS'05, Shanghai, China, July 2005, pp. 459-466.

Chen, J.F., Rotter, J.M. and Teng, J.G. (2006) "A simple remedy for elephant's foot buckling in cylindrical silos and tanks", Advances in Structural Engineering, Vol. 9, No. 3, pp 409-420.

Clough, D. P. (1977), "Experimental Evaluation of Seismic Design Methods for Broad Cylindrical Tanks,"U.C. Berkeley, Report No. UCB/EERC-77/10

Clough, R. W., and Niwa, A. (1979), "Static Tilt Tests of a Tall Cylindrical Liquid Storage Tank," U.C. Berkeley, Report No. UCB/EERC-79/06

Cole, E., Santana, G., Singh, J., Ballantyne, D., Priestly, N., Jacob, K., Lavell, A., and Aguirre, B. (1991). Costa Rica Earthquake of April 22, 1991, Report.

De Angelis, M., Giannini, R., Paolacci, F. (2010). "Experimental investigation on the seismic response of a steel liquid storage tank equipped with floating roof by shaking table tests", *Earthquake Engineering and Structural Dynamics*, Vol. 39 (4), pp. 377-396.

Dowling, N. E, (1993). Mechanical Behavior of Materials, Engineering Methods for Deformation, Fracture, and Fatigue", Prentice Hall International Editions, New Jersey.

Eshghi, S., and Razzaghi, M. S. (2004). "The Behavior of Special Structures During the Bam Earthquake of 26 December 2003", JSEE: Special Issue on Bam Earthquake, pp. 197-207.

European Committee for Standardization (2004). General rules, seismic actions and rules for buildings, Eurocode 8, Part 1, CEN/TC 250, EN 1998-1, Brussels.

European Committee for Standardization (2004). "Specification for the design and manufacture of site built, vertical, cylindrical, flat-bottomed, above ground, welded, steel tanks for the storage of liquids at ambient temperature and above", EN 14015, Brussels.

European Committee for Standardization (2006). Design of Joints, Eurocode 3, Part 1-8, CEN/TC 250, EN 1993-1-8, Brussels.

European Committee for Standardization (2006). Tanks, Eurocode 3, Part 4-2, CEN/TC 250, EN 1993-4-2, Brussels.

European Committee for Standardization (2006), Silos, tanks and pipelines, Eurocode 8, part 4, CEN/TC 250, EN 1998-4, Brussels.

European Committee for Standardization (2007). Strength and Stability of Shell Structures, Eurocode 3, Part 1-6, CEN/TC 250, EN 1993-1-6, Brussels.

Fabbrocino, G., Iervolino, I., Orlando, F., Salzano, E. (2005). "Quantitative Risk Analysis of Oil Storage Facilities in Seismic Areas", *Journal of Hazardous Materials*, Vol. 123, pp. 61-69.

Ferino, J., Lucci, A., Demofonti, G. (2013). "Pressurized Flanged Joints Subjected to Bending Cyclic Loading – Finite Element Analyses", *ASME 2013 PVP Conference*, July 14-18, 2013, Paris, France.

Fischer, F. D. (1979). "Dynamic Fluid Effects in Liquid-Filled Flexible Cylindrical Tanks", *Earthquake Engineering and Structural Dynamics*, Vol. 7, pp. 587-601.

Fischer, F. D., Rammerstorfer, F. G. and Scharf, K. (1991), "Earthquake Resistant Design of Anchored and Unanchored Liquid Storage Tanks Under Three-Dimensional Earthquake Excitation", Structural Dynamics – Recent Advances, editor: G.I. Schueller, Berlin, Springer, pp. 317-371.

Fischer, F.D., and Seeber, R. (1988). "Dynamic Response of Vertically Excited Liquid Storage Tanks considering Liquid-Soil Interaction", *Earthquake Engineering and Structural Dynamics*, 16, pp. 329-342.

Gazetas, G. et al. (2015). "Contemporary Evaluation Methodology of Seismic Vulnerability and Upgrade of Port Facilities", Final Technical Report, UPGRADE project, THALES, NTU Athens.

Haroun, M. A. (1983a). "Behavior of unanchored oil storage tanks: Imperial Valley, earthquake", *J. Tech. Topics in Civil Engrg*., ASCE, 109(1), pp. 23-40.

Haroun, M. A. (1983b). "Vibration Studies and Tests of Liquid Storage Tanks", *Earthquake Engineering and Structural Dynamics*, Vol. 11, pp. 179-206.

Haroun, M. A., Badawi, H. S., and Nanda, C. B. (1987). "Nonlinear uplift analysis of crescent-shaped plate", *Proceedings of the 1987 Pressure Vessels and Piping (PVP) Conference*, San Diego, California, pp. 317-324.

Haroun, M. A., and Badawi, H. S., (1988). "Seismic behavior of unanchored ground-based cylindrical tanks", Proceedings, *9th World Conference on Earthquake Engineering*, Tokyo- Kyoto, Japan, Vol. 6, pp. 643-648.

Haroun, M. A., and Housner, G. W. (1981a). "Earthquake Response of Deformable Liquid Storage Tanks", *Journal of Applied Mechanics*, ASME, Vol. 48, pp. 411-417.

Haroun, M. A. and Housner, G. W. (1981b), "Seismic Design of Liquid Storage Tanks", *ASCE Journal of the Technical Councils*, Vol. 107, No. 1, pp. 191-207.

Harris, L. A., Suer, H. S., Skene, W. T., Benjamin, R. J. (1957). "The Stability of Thin-Walled Un-stiffened Circular Cylinders under Axial Compression including the Effects of Internal Pressure", *Journal of the Aeronautical Sciences*, 24 (8), pp. 587–596.

HAZUS (1997). "Earthquake Loss Estimation Methodology", National Institute of Building Sciences, prepared by Risk Management Solutions, Menlo Park, CA, USA.

Housner, G. W. (1957). "Dynamic Pressures on Accelerated Fluid Containers", Bulletin Seismological Society of America, Vol. 47, pp. 15-35.

Housner, G. W. (1963). "The Dynamic Behavior of Water Tanks", Bulletin Seismological Society of America, Vol. 53, No. 2, pp. 381-387.

Hutchinson, J. W. (1965). "Axial Buckling of Pressurised Imperfect Cylindrical Shells", AIAA Journal, 3, pp. 1461–1466.

Ibrahim, R (2005). "Liquid Sloshing Dynamics: Theory and Applications", Cambridge University Press.

Ibrahim, R. A., Pilipchuk, V. N. and Ikeda, T. (2001). "Recent Advances in Liquid Sloshing Dynamics", Applied Mechanics Reviews, ASME, Vol. 54, No. 2, pp. 133-177.

Ishida, K., and Kobayashi, N. (1988). "An effective method of analyzing rocking motion for unanchored cylindrical tanks including uplift", *Journal of Pressure Vessel Technology*, Vol. 110, pp. 76-87.

Iwatsubo, T. (1998). "Damage to industrial equipment in the 1995 Hyogoken Nanbu Earthquake", *Nuclear Engineering and Design*, Vol. 181, pp. 41–53.

Jennings, P. C. (1971). "Engineering Features of the San Fernando Earthquake of February 9, 1971", California Institute of Technology, Earthquake Engineering Research Laboratory, EERL;71-02.

Johnson, G. (2000). "Refinery Damage and Emergency Response in the 1999 Izmit, Turkey Earthquake".

Karamanos, S. A., Romeijn, A., and Wardenier, J., (2000). "Stress concentrations in tubular gap K-joints: mechanics and fatigue design", *Engineering Structures*, Vol. 22, pp. 4-14.

Kaufmann, E. J., Metrovich, B., and Pense, A. W., (2001). "Characterization of Cyclic Inelastic Strain Behavior On Properties of A572 Gr. 50 and A913 Gr. 50 Rolled Sections", Final Report to American Institute of Steel Construction, ATLSS Report No. 01-13.

Lau, D. T., and Clough, R. W. (1989). "Static tilt behavior of unanchored cylindrical tanks", Rep. UCB/EERC-89/ll, Earthquake Engineering Research Center, University of California, Berkeley, California.

Leon, G. S., and Kausel, E. A. M. (1986). "Seismic analysis of fluid storage tanks", *Journal of Structural Engineering*, Vol. 112(1), pp. 1-18.

Malhotra, P. K., and Veletsos, A. S. (1994a). "Beam Model for Base-uplifting Analysis of Cylindrical Tanks", *Journal of Structural Engineering*, Vol. 120, No. 12, pp. 3471-3488.

Malhotra, P. K., and Veletsos, A. S., (1994b). "Uplifting Analysis of base plates in cylindrical tanks", *Journal of Structural Engineering*, Vol. 120, No. 12, pp. 3489-3505.

Malhotra, P.K., and Veletsos, A. S., (1994c). "Uplifting Response of Unanchored Liquid-Storage Tanks", *Journal of Structural Engineering*, Vol. 120, No. 12, pp. 3525-3547.

Malhotra, P. K. (1995). "Base Uplifting Analysis of Flexibly Supported Liquid-Storage Tanks", *Earthquake Engineering and Structural Dynamics*, Vol. 24, No. 12, pp. 1591-1607.

Malhotra. P. K., and Veletsos, A. S. (1995). "Seismic response of unanchored and partially anchored liquid-storage tanks", Rep. TR-J05809. Electric Power Res. Inst., Palo Alto. Calif.

Malhotra, P. K. (1997). "Seismic Response of Soil-Supported Unanchored Liquid-Storage Tanks", *Journal of Structural Engineering*, Vol. 123, No.4, pp. 440-450.

Malhotra, P. K. (2000). "Practical Nonlinear Seismic Analysis of Tanks," Earthquake Spectra, 16 (2), pp. 473-492.

Manos, G. C. (1986). "Earthquake tank-wall stability of unanchored tanks", *Journal of Structural Engineering*, ASCE 112, pp. 1863-1880.

Manos, G. C. and Clough, R. W. (1982). "Further Study of the Earthquake Response of a Broad Cylindrical Liquid-Storage Tank Model", Report No. UCB/EERC-82/7, University of California, Berkeley.

Manos, G. C., and Clough, R. W. (1985). "Tank Damage during the May 1983 Coalinga Earthquake", *Earthquake Engineering and Structural Dynamics*, Vol. 13, pp. 449-466.

Mathon, C., Limam, A. (2006). "Experimental collapse of thin cylindrical shells submitted to internal pressure and pure bending", *Thin-Walled Structures*, 44, 39-50.

Myers, P. E. (1997). "Aboveground Storage Tanks", McGraw-Hill, ISBN 0-07-044272-X.

Natsiavas, S., (1987). "Response and failure of fluid-filled tanks under base excitation", PhD thesis, California Institute of Technology, Pasadena, California.

Natsiavas, S. (1988). "An Analytical Model for Unanchored Fluid-Filled Tanks under Base Excitation", *Journal of Applied Mechanics*, ASME, Vol. 55, pp. 648-653.

Natsiavas, S. (1990). "Simplified Models for the Dynamic Response of Tall Unanchored Liquid Containers", *Journal of Pressure Vessel Technology*, ASME, Vol. 112, pp. 124-131.

Natsiavas, S. and Babcock, C. D. (1987), "Buckling at the Top of a Fluid-Filled Tank during Base Excitation", *ASME Journal of Pressure Vessel Technology*, Vol. 109, No. 4, pp. 374-380.

Natsiavas, S., and Babcock, C. D. (1988). "Behavior of Unanchored Fluid-Filled Tanks Subjected to Ground Excitation", *Journal of Applied Mechanics*, ASME, Vol. 55, pp. 654-659.

Nielsen, R., and Kiremidjian, A. S. (1986). "Damage to oil refineries from major earthquakes", *ASCE Journal of Structural Engineering*, Vol. 112, No. 6, pp.1481-1491.

Niwa, A. (1978), "Seismic Behavior of Tall Liquid Storage Tanks," U.C. Berkeley, Report No. UCB/EERC-78/04

Niwa, A. and Clough, R. W. (1982). "Buckling of Cylindrical Liquid-Storage Tanks under Earthquake Excitation", *Earthquake Engineering and Structural Dynamics*, Vol. 10, pp. 107-122.

NZS 2654, Specification for manufacture of vertical steel welded non-refrigerated storage tanks with butt-welded shells for the petroleum industry, Standards New Zealand, Wellington, New Zealand, 1989.

O'Rourke, M. J., and So, P. (2000). "Seismic Fragility Curves for On-Grade Steel Tanks", *Earthquake Spectra*, Vol. 16, No. 4, pp. 801-815.

Papadopoulos, V. et al. (2015). "Risk assessment for the seismic protection of industrial facilities", Final Technical Report, RASOR project, THALES, NTU Athens, website: http://excellence.minedu.gov.gr/thales/en/thalesprojects/379422

Papatheocharis, T., Diamanti, K., Varelis, G. E., Perdikaris, P. C. and Karamanos, S. A. (2013). "Experimental and numerical investigation of pipe Tee junctions under strong cyclic loading", *ASME 2013 PVP Conference*, Paris, France.

Pappa P., Vasilikis, P., Vazouras, P., and Karamanos, S. A. (2011). "On the seismic behaviour and design of liquid storage tanks", *III ECCOMAS Thematic Conference on Computational Methods in Structural Dynamics and Earthquake Engineering (COMPDYN)*, Corfu, Greece, 26–28 May 2011.

Pappa, P. et al. (2012). "Structural safety of industrial steel tanks, pressure vessels and piping systems under seismic loading (INDUSE)", RFCS Project Final Report, Brussels, website: www.mie.uth.gr/induse

Peek, R. (1986). "Analysis of Unanchored Liquid Storage Tanks", Rep. EERL 86-01, California Institute of Technology, Pasadena, California.

Peek, R. (1988). "Analysis of Unanchored Liquid Storage Tanks under Lateral Loads", *Journal of Earthquake Engineering and Structural Dynamics*, Vol. 16(7), pp. 1087-1100.

Peek, R., and El-Bkaily M. (1991). "Post-buckling Behavior of Unanchored Steel Tanks under Lateral Loads", *Journal of Pressure Vessel Technology*, Vol. 113, pp. 423-428.

Peek, R., and Jennings, P. C., (1988), "Simplified analysis of unanchored tanks", *Journal of Earthquake Engineering and Structural Dynamics*, Vol. 16(7), pp. 1073-1085.

Priestley, M. J. N. (Chairman & Editor), Davidson, B. J., Honey, G. D., Hopkins, D. C., Martin, R., J., Ramsey, G., Vessey, J. V. and Wood, J. H. (1986). Seismic Design of Storage Tanks, Recommendations of a Study Group of the New Zealand National Society for Earthquake Engineering, New Zealand.

Prinz, G. S., and Nussbaumer, A. (2012). "Fatigue analysis of liquid-storage tank shell-to-base connections under multi-axial loading", *Engineering Structures*, Vol. 40, pp. 77-82.

Rammerstorfer, F. G., Fisher, F. D. and Scharf, K. (1988). "A Proposal for the Earthquake Resistant Design of Tanks – Results from the Austrian Project", *Proceedings of the 9th World Conference on Earthquake Engineering*, Tokyo, Japan, Vol. VI, pp. 715-720.

Rammerstorfer, F. G., Fisher, F. D. and Scharf, K. (1990). "Storage Tanks Under Earthquake Loading", Applied Mechanics Reviews, ASME, Vol. 43, No. 11, pp. 261-283.

Reza, S., Bursi, O.S., Abbiati, G., Bonelli, A. (2013). "Pseudo-dynamic heterogeneous testing with dynamic substructuring of a piping system under earthquake loading", *ASME 2013 PVP Conference*, Paris, France.

Reza, M.S., Bursi, O.S., Paolacci, F., Kumar, A. (2014). "Enhanced seismic performance of non-standard bolted flange joints for petrochemical piping systems", *Journal of Loss Prevention in the Process Industries*, Vol. 30 (1), pp. 124-136.

Rotter, J. M. (1990). "Local Inelastic Collapse of Pressurised Thin Cylindrical Steel Shells under Axial Compression", *ASCE Journal of Structural Engineering*, ASCE, 116 (7), pp. 1955–1970.

Rotter, J. M. (2006). "Elephant's Foot Buckling in Pressurised Cylindrical Shells", Stahlbau, Vol 75, Heft 9, Special Edition in honour of Profs Schmidt, Greiner and Wunderlich, Sept 2006, pp 742-747.

Rotter, J. M. (2009), "Silos and tanks in research and practice: state of the art and current challenges", *Proceedings of the International Association for Shell and Spatial Structures (IASS) Symposium*, Valencia.

Salzano, E., Iervolino, I., Fabbrocino, G. (2003). "Seismic Risk of Atmospheric Storage Tanks in the Framework of Quantitative Risk Analysis", *Journal of Loss Prevention in the Process Industry*, Vol. 16, pp. 403-409.

Scharf, K., (1990). "Beiträge zur Erfassung des Verhaltens von erdbebenerregten, oberirdischen Tankbauwerken," Fortschritt-Berichte VDI, Reihe 4. Bauingenieurwesen, Nr. 97, VDI Verlag, Düsseldorf.

Shih, C. F. (1981). "Failure of Liquid Storage Tanks Due to Earthquake Excitation", PhD thesis, Report No. EERL 81-04, Caltech, Pasadena, CA.

Steinberg, L. J., Cruz, A., Vardar-Sukan, F., and Ersoz, Y. (1999). "Risk Management Practices at Industrial Facilities during the Turkey Earthquake of August 17", Case Study Report.

Suzuki K. (2006). "Earthquake Damage to Industrial Facilities and Development of Seismic and Vibration Control Technology", *Journal of Disaster Research*, Vol.1, No. 2.

Varelis, G. E., Karamanos, S. A., and Gresnigt, A. M. (2013a). "Steel Elbow Response under Strong Cyclic Loading", *Journal of Pressure Vessel Technology*, ASME, Vol. 135, No.1, Article Number: 011207.

Varelis, G.E., Ferino J., Karamanos, S.A., Lucci A., Demofonti G. (2013b). "Experimental and Numerical Investigation of Pressurized Pipe Elbows under Strong Cyclic Loading Conditions", *ASME 2013 PVP Conference*, Paris, France.

Vasilescu, S. and Ilinca, C. (2014). "A strength calculation of a nozzle using comparative methods", *Key Engineering Materials*, 601, pp. 84-87.

Vathi, M., and Karamanos, S. A. (2013). "Seismic Response of Unanchored Liquid Storage Tanks", *ASME 2013 PVP Conference*, Paris, France.

Vathi, M., and Karamanos, S. A. (2014a). "Modeling of Uplifting Mechanism in Unanchored Liquid Storage Tanks Subjected to Seismic Loading", *2nd European Conference on Earthquake Engineering and Seismology (2ECEES)*, 24-29 August 2014, Istanbul, Turkey.

Vathi, M., and Karamanos, S. A. (2014b). "Liquid Storage Tanks: Seismic Analysis," Encyclopedia of Earthquake Engineering, Article: 368990, Chapter: 144, Springer.

Vathi, M., and Karamanos, S. A. (2015). "Simplified Model for the Seismic Response of Unanchored Liquid Storage Tanks," *Proceedings of the ASME 2015 Pressure Vessels & Piping Division Conference, PVP2015*, July 19-23, 2013, Boston, Massachusetts, USA.

Veletsos, A. S. (1974). "Seismic Effects in Flexible Liquid Storage Tanks", *Proceedings of the 5th World Conference in Earthquake Engineering*, Rome, Italy, Vol. 1, pp. 630-639.

Veletsos, A. S., and Tang, Y. (1987). "Rocking Response of Liquid Storage Tanks", *Journal of Engineering Mechanics*, 113 (11), pp. 1774-1792.

Veletsos, A. S. and Tang, Y. (1990). "Soil-Structure Interaction Effects for Laterally Excited Liquid Storage Tanks", *Earthquake Engineering and Structural Dynamics*, Vol. 19, pp. 473-496.

Veletsos, A. S., and Yang, J. Y. (1977). "Earthquake Response of Liquid Storage Tanks", *2nd Engineering Mechanics Conference*, ASCE, Raleigh, NC, pp. 1-24.

Weingarten, V. I., Morgan, E. J., Seide, P. (1965). "Elastic Stability of Thin-Walled Cylindrical and Conical Shells under Combined Internal Pressure and Axial Compression", AIAA Journal, 3 (6), pp. 1118–1125.

Whittaker, D., and Saunders, D.(2008). Revised NZSEE Recommendations for Seismic Design of Storage Tanks, *2008 NZSEE Conference*.

Wieschollek M., Hoffmeister B., Feldmann M., (2013). "Experimental and Numerical Investigation on Nozzle Reinforcements", *ASME 2013 PVP Conference*, Paris, France.

Wozniak, R. S., and Mitchell, W. W. (1978). "Basis of seismic design provisions for welded steel oil storage tanks", Session on Advances in Storage Tank Design, API 43rd mid-year meeting, Toronto, Canada.

Annex A: Method of solution for anchored and unanchored tanks

A.1 Anchored Tanks

The tank-liquid system is simulated with a simplified model that accounts for the geometry of the vertical cylindrical liquid storage tank of radius R and filling height H and the hydrodynamic response of the liquid. The tank is assumed to be excited by a horizontal base-ground seismic acceleration motion, $\ddot{X}_g$.

In the case of anchored tanks, the container is anchored to the foundation. The tank wall-liquid system can be modelled as a spring-mass system, as seen in Figure 97. The impulsive and convective motion of the liquid are modelled by assuming two linear oscillators with masses m_I and m_C at heights h_I and h_C respectively. The general equation has the form:

$$\ddot{a}_{I,C}(t) + 2\xi_{I,C}\omega_{I,C}\dot{a}_{I,C}(t) + \omega_{I,C}^2 a_{I,C}(t) = -\ddot{X}_g(t) \tag{A.1}$$

The method of solution consists of the following steps:

A. Initial Calculations

1. The $\omega_{I,C}$, $\xi_{I,C}$ and $\ddot{X}_g(t)$ are known for a specific tank geometry and accelerogram. For $t = 0$ assume that:

$$a_{I,C}(0) = \dot{a}_{I,C}(0) = 0 \tag{A.2}$$

so that:

$$\ddot{a}_{I,C}(0) = -\ddot{X}_g(0) \tag{A.3}$$

2. Select time step Δt which is taken equal to the time increment of the accelerogram.

3. Calculate the following helpful expression:

$$a_{I,C}(-\Delta t) = a_{I,C}(0) - \Delta t \dot{a}_{I,C}(0) + \frac{\Delta t^2}{2}\ddot{a}(0) \Leftrightarrow a_{I,C}(-\Delta t) = \frac{\Delta t^2}{2}\ddot{a}(0) \tag{A.4}$$

B. For each time step: $(t = 0, \Delta t, 2\Delta t, ...)$

171

4. The displacement can be calculated as follows:

$$a_{I,C}(t+\Delta t) = \left(\dfrac{1}{\dfrac{1}{\Delta t^2} + \dfrac{\xi\omega}{\Delta t}} \right) \left[-\ddot{X}_g(t) - \left(\omega^2 - \dfrac{2}{\Delta t^2} \right) a_{I,C}(t) - \left(\dfrac{1}{\Delta t^2} - \dfrac{\xi\omega}{\Delta t} \right) a_{I,C}(t-\Delta t) \right] \quad \text{(A.5)}$$

5. The velocity and acceleration can be calculated as follows:

$$\dot{a}_{I,C}(t) = \dfrac{1}{2\Delta t} \left(a_{I,C}(t+\Delta t) - a_{I,C}(t-\Delta t) \right) \quad \text{(A.6)}$$

$$\ddot{a}_{I,C}(t) = \dfrac{1}{\Delta t^2} \left(a_{I,C}(t-\Delta t) - 2a_{I,C}(t) + a_{I,C}(t+\Delta t) \right) \quad \text{(A.7)}$$

A.2 Method of solution for unanchored tanks

The method of solution for unanchored tanks that is used is based on the Newmark method (Bathe 1996) as it is a more stable and reliable method.

A.2.1 The Newmark Method

The Newmark integration scheme is an extension of the linear acceleration method. The following assumptions are used:

$$^{t+\Delta t}\dot{\mathbf{U}} = {}^{t}\dot{\mathbf{U}} + \left[(1-\delta)\,{}^{t}\ddot{\mathbf{U}} + \delta\,{}^{t+\Delta t}\ddot{\mathbf{U}} \right]\Delta t \quad \text{(A.8)}$$

$$^{t+\Delta t}\mathbf{U} = {}^{t}\mathbf{U} + {}^{t}\dot{\mathbf{U}}\Delta t + \left[\left(\dfrac{1}{2} - \alpha \right){}^{t}\ddot{\mathbf{U}} + \alpha\,{}^{t+\Delta t}\ddot{\mathbf{U}} \right]\Delta t^2 \quad \text{(A.9)}$$

where U, $\dot{U}$, and $\ddot{U}$ are the displacement, velocity and acceleration vectors of the finite element assemblage and α and δ are parameters that can be determined to obtain integration accuracy and stability. Parameters α and δ should be chosen such that $\delta \geq 0.50$ and $\alpha \geq 0.25(0.5+\delta)^2$.

172

When $\delta = \frac{1}{2}$ and $\alpha = \frac{1}{6}$, relations (A.8) and (A.9) correspond to the linear acceleration method. Newmark originally proposed as an unconditionally stable scheme the constant-average-acceleration method (also called trapezoidal rule), in which case $\delta = \frac{1}{2}$ and $\alpha = \frac{1}{6}$.

In addition to (A.8) and (A.9), for solution of the displacements, velocities, and accelerations at time $t + \Delta t$, the equilibrium equations at time $t + \Delta t$ governing the linear dynamic response of a system of finite elements are also considered:

$$\mathbf{M}\,{}^{t+\Delta t}\ddot{\mathbf{U}} + \mathbf{C}\,{}^{t+\Delta t}\dot{\mathbf{U}} + \mathbf{K}\,{}^{t+\Delta t}\mathbf{U} = {}^{t+\Delta t}\mathbf{R} \tag{A.10}$$

where $\mathbf{M}$, $\mathbf{C}$, and $\mathbf{K}$ are the mass, damping and stiffness matrices; $\mathbf{R}$ is the vector of externally applied loads.

For simplicity, we assume the following integration constants:

$$a_0 = \frac{1}{\alpha \Delta t^2}; \quad a_1 = \frac{\delta}{\alpha \Delta t}; \quad a_2 = \frac{1}{\alpha \Delta t}; \quad a_3 = \frac{1}{2\alpha} - 1$$

$$a_4 = \frac{\delta}{\alpha} - 1; \quad a_5 = \frac{\Delta t}{2}\left(\frac{\delta}{\alpha} - 2\right); \quad a_6 = \Delta t\left(1 - \delta\right); \quad a_7 = \delta \Delta t \tag{A.11}$$

Solving from (A.9) for ${}^{t+\Delta t}\ddot{\mathbf{U}}$ in terms of ${}^{t+\Delta t}\mathbf{U}$ and then substituting for ${}^{t+\Delta t}\ddot{\mathbf{U}}$ into (A.8), we obtain equations for ${}^{t+\Delta t}\ddot{\mathbf{U}}$ and ${}^{t+\Delta t}\dot{\mathbf{U}}$, each in terms of the unknown displacements ${}^{t+\Delta t}\mathbf{U}$ only. These two relations for ${}^{t+\Delta t}\dot{\mathbf{U}}$ and ${}^{t+\Delta t}\ddot{\mathbf{U}}$ are substituted into (A.10) to solve for ${}^{t+\Delta t}\mathbf{U}$, after which, using (A.8) and (A.9), ${}^{t+\Delta t}\ddot{\mathbf{U}}$ and ${}^{t+\Delta t}\dot{\mathbf{U}}$ can be calculated:

$$^{t+\Delta t}\dot{\mathbf{U}} = {}^{t}\mathbf{U} + a_6\,{}^{t}\ddot{\mathbf{U}} + a_7\,{}^{t+\Delta t}\ddot{\mathbf{U}} \tag{A.12}$$

$$^{t+\Delta t}\ddot{\mathbf{U}} = a_0\left({}^{t+\Delta t}\mathbf{U} - {}^{t}\mathbf{U}\right) - a_2\,{}^{t}\dot{\mathbf{U}} - a_3\,{}^{t}\ddot{\mathbf{U}} \tag{A.13}$$

A.2.2 Equations of motion for unanchored tanks

For unanchored tanks without uplifting, the equilibrium of forces (Figure A-1) gives:

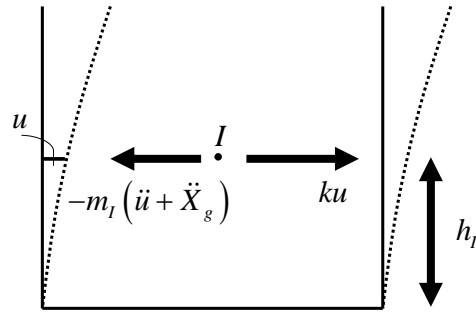$$m_I\left(\ddot{u} + \ddot{X}_g\right) + ku = 0 \tag{A.14}$$

173

Figure A-1: Equilibrium of forces for unanchored tanks without uplifting.

And for $k = \omega_I^2 m_I$, we have:

$$m_I \ddot{u} + \omega_I^2 m_I u = -m_I \ddot{X}_g \Leftrightarrow \ddot{u} + \omega_I^2 u = -\ddot{X}_g \tag{A.15}$$

If we have damping:

$$\ddot{u} + 2\xi_I \omega_I \dot{u} + \omega_I^2 u = -\ddot{X}_g \tag{A.16}$$

And the total horizontal force is:

$$F = -m_I \left(\ddot{u} + \ddot{X}_g \right) \tag{A.17}$$

For unanchored tanks with uplifting, the equilibrium of forces (Figure A-2) gives:

$$F_a + ku = 0 \Leftrightarrow m_I \left(\ddot{u} + \ddot{X}_g + \ddot{\psi} h_I \right) + ku = 0 \tag{A.18}$$
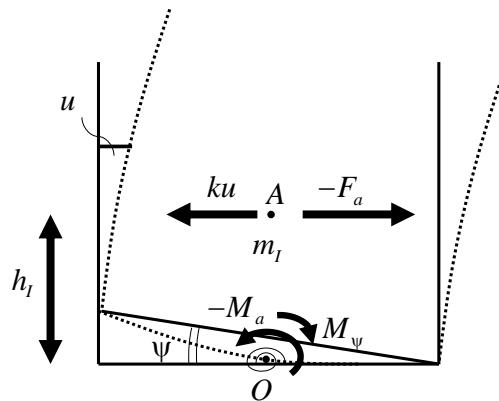

Figure A-2: Equilibrium of forces and moments for unanchored tanks with uplifting, where O is the center of the base and I is the "impulsive" center.

174

And for $k = \omega_I^2 m_I$, we have:

$$m_I \ddot{u} + m_I h_I \ddot{\psi} + m_I \omega_I^2 u = -m_I \ddot{X}_g \tag{A.19}$$

The equilibrium of moments gives:

$$M_a + M_\psi + m_I h_I \left(\ddot{u} + \ddot{X}_g \right) = 0 \tag{A.20}$$

And for $M_a = I_O \ddot{\psi}$, we have:

$$m_I h_I \ddot{u} + I_O \ddot{\psi} + M_\psi \left(\psi \right) = -m_I h_I \ddot{X}_g \tag{A.21}$$

For $\delta = h_I \psi$, the above equations become:

$$m_I \ddot{u} + m_I \ddot{\delta} + m_I \omega_I^2 u = -m_I \ddot{X}_g \tag{A.22}$$

$$m_I \ddot{u} + \left(\frac{I_O}{h_I^2} \right) \ddot{\delta} + \frac{1}{h_I} M_\psi \left(\psi \right) = -m_I \ddot{X}_g \tag{A.23}$$

Or in incremental form:

$$m_I \Delta \ddot{u} + m_I \Delta \ddot{\delta} + m_I \omega_I^2 \Delta u = -m_I \Delta \ddot{X}_g \tag{A.24}$$

$$m_I \Delta \ddot{u} + \left(\frac{I_O}{h_I^2} \right) \Delta \ddot{\delta} + \frac{1}{h_I^2} K_\psi \Delta \delta = -m_I \Delta \ddot{X}_g \tag{A.25}$$

And matrix form:

$$\begin{bmatrix} m_I & m_I \\ m_I & \dfrac{I_O}{h_I^2} \end{bmatrix} \begin{bmatrix} \Delta \ddot{u} \\ \Delta \ddot{\delta} \end{bmatrix} + \begin{bmatrix} k & 0 \\ 0 & \dfrac{1}{h_I^2} K_\psi \end{bmatrix} \begin{bmatrix} \Delta u \\ \Delta \delta \end{bmatrix} = - \begin{bmatrix} m_I \\ m_I \end{bmatrix} \Delta \ddot{X}_g \tag{A.26}$$

With damping:

$$\begin{bmatrix} m_I & m_I \\ m_I & \dfrac{I_O}{h_I^2} \end{bmatrix} \begin{bmatrix} \Delta \ddot{u} \\ \Delta \ddot{\delta} \end{bmatrix} + \begin{bmatrix} c_1 & 0 \\ 0 & c_2 \end{bmatrix} \begin{bmatrix} \Delta \dot{u} \\ \Delta \dot{\delta} \end{bmatrix} + \begin{bmatrix} k & 0 \\ 0 & \dfrac{1}{h_I^2} K_\psi \end{bmatrix} \begin{bmatrix} \Delta u \\ \Delta \delta \end{bmatrix} = - \begin{bmatrix} m_I \\ m_I \end{bmatrix} \Delta \ddot{X}_g \tag{A.27}$$

175

A.2.3 Method of solution

Eq. (A.27) has the form $\mathbf{M}\,{}^{t+\Delta t}\ddot{\mathbf{U}} + \mathbf{C}\,{}^{t+\Delta t}\dot{\mathbf{U}} + \mathbf{K}\,{}^{t+\Delta t}\mathbf{U} = {}^{t+\Delta t}\mathbf{R}$ or for simplicity:

$$[M]\cdot\Delta\ddot{\underset{\sim}{y}} + [C]\cdot\Delta\dot{\underset{\sim}{y}} + [K]\cdot\Delta\underset{\sim}{y} = [R] \tag{A.28}$$

where:

$$[M] = \begin{bmatrix} m_I & m_I \\ m_I & \dfrac{I_O}{h_I^2} \end{bmatrix},\ [C] = \begin{bmatrix} c_1 & 0 \\ 0 & c_2 \end{bmatrix},\ [K] = \begin{bmatrix} k & 0 \\ 0 & \dfrac{1}{h_I^2}K_\psi \end{bmatrix},\ [R] = -\begin{bmatrix} m_I \\ m_I \end{bmatrix}\Delta\ddot{X}_g(t)\ \text{and}\ \Delta\underset{\sim}{y} = \begin{bmatrix} \Delta u \\ \Delta\delta \end{bmatrix}$$

.

The velocities and accelerations of Eq. (A.12) and (A.13) can be adjusted and rewritten as follows:

$${}^{t+\Delta t}\dot{\mathbf{U}} = {}^{t}\dot{\mathbf{U}} + a_6\,{}^{t}\ddot{\mathbf{U}} + a_7\,{}^{t+\Delta t}\ddot{\mathbf{U}} \Leftrightarrow {}^{t+\Delta t}\dot{\mathbf{U}} - {}^{t}\dot{\mathbf{U}} = a_6\,{}^{t}\ddot{\mathbf{U}} + a_7\,{}^{t+\Delta t}\ddot{\mathbf{U}} \Leftrightarrow$$

$$\Leftrightarrow \Delta\dot{\mathbf{U}} = a_6\,{}^{t}\ddot{\mathbf{U}} + a_7\left({}^{t}\ddot{\mathbf{U}} + \Delta\ddot{\mathbf{U}}\right) \Leftrightarrow \boxed{\Delta\dot{\mathbf{U}} = (a_6 + a_7)\,{}^{t}\ddot{\mathbf{U}} + a_7\Delta\ddot{\mathbf{U}}} \tag{A.29}$$

$${}^{t+\Delta t}\ddot{\mathbf{U}} = a_0\left({}^{t+\Delta t}\mathbf{U} - {}^{t}\mathbf{U}\right) - a_2\,{}^{t}\dot{\mathbf{U}} - a_3\,{}^{t}\ddot{\mathbf{U}} \Leftrightarrow {}^{t}\ddot{\mathbf{U}} + \Delta\ddot{\mathbf{U}} = a_0\Delta\mathbf{U} - a_2\,{}^{t}\dot{\mathbf{U}} - a_3\,{}^{t}\ddot{\mathbf{U}} \Leftrightarrow$$

$$\Leftrightarrow a_0\Delta\mathbf{U} = {}^{t}\ddot{\mathbf{U}} + \Delta\ddot{\mathbf{U}} + a_2\,{}^{t}\dot{\mathbf{U}} + a_3\,{}^{t}\ddot{\mathbf{U}} \Leftrightarrow \boxed{\Delta\mathbf{U} = \dfrac{1+a_3}{a_0}\,{}^{t}\ddot{\mathbf{U}} + \dfrac{1}{a_0}\Delta\ddot{\mathbf{U}} + \dfrac{a_2}{a_0}\,{}^{t}\dot{\mathbf{U}}} \tag{A.30}$$

and for the specific system:

$$\Delta\dot{\underset{\sim}{y}} = (a_6 + a_7)\,{}^{t}\ddot{\underset{\sim}{y}} + a_7\Delta\ddot{\underset{\sim}{y}} \tag{A.31}$$

$$\Delta\underset{\sim}{y} = \dfrac{1+a_3}{a_0}\,{}^{t}\ddot{\underset{\sim}{y}} + \dfrac{1}{a_0}\Delta\ddot{\underset{\sim}{y}} + \dfrac{a_2}{a_0}\,{}^{t}\dot{\underset{\sim}{y}} \tag{A.32}$$

Substituting Eq. (A.31) and (A.32) into (A.28), we obtain the following equation for $\Delta\ddot{\underset{\sim}{y}}$:

$$\left([M] + a_7[C] + \dfrac{1}{a_0}[K]\right)\Delta\ddot{\underset{\sim}{y}} = [R] - (a_6 + a_7)[C]\ddot{\underset{\sim}{y}}(t_n) - [K]\left(\dfrac{a_2}{a_0}\dot{\underset{\sim}{y}}(t_n) + \dfrac{1+a_3}{a_0}\ddot{\underset{\sim}{y}}(t_n)\right) \tag{A.33}$$

which has the form of $[A]\Delta\ddot{\underset{\sim}{y}} = [F]$, where:

$$[A] = [M] + a_7[C] + \dfrac{1}{a_0}[K] \tag{A.34}$$

176

and

$$[F] = [R] - (a_6 + a_7)[C]\ddot{\underset{\sim}{y}}(t_n) - [K]\left(\frac{a_2}{a_0}\dot{\underset{\sim}{y}}(t_n) + \frac{1+a_3}{a_0}\ddot{\underset{\sim}{y}}(t_n)\right) \tag{A.35}$$

$\Delta\ddot{\underset{\sim}{y}}$ can be calculated as follows:

$$\Delta\ddot{\underset{\sim}{y}} = \frac{1}{DET}\begin{bmatrix} A_{22} & -A_{12} \\ -A_{21} & A_{11} \end{bmatrix}\begin{bmatrix} F_1 \\ F_2 \end{bmatrix} \tag{A.36}$$

where $DET = det[A] = A_{11} \cdot A_{22} - A_{21} \cdot A_{12}$ \hfill (A.37)

So:

$$\Delta\ddot{u}_0 = \frac{1}{DET}\left(A_{22}F_1 - A_{12}F_2\right) \tag{A.38}$$

$$\Delta\ddot{\psi}h = \frac{1}{DET}\left(-A_{21}F_1 + A_{11}F_2\right) \tag{A.39}$$

Here, we have:

$$[A] = [M] + a_7[C] + \frac{1}{a_0}[K] = \begin{bmatrix} m_I & m_I \\ m_I & \dfrac{I_O}{h_I^2} \end{bmatrix} + a_7\begin{bmatrix} c_1 & 0 \\ 0 & c_2 \end{bmatrix} + \frac{1}{a_0}\begin{bmatrix} k & 0 \\ 0 & \dfrac{K_\psi}{h_I^2} \end{bmatrix} =$$

$$= \begin{bmatrix} m_I + a_7 c_1 + \dfrac{1}{a_0}k & m_I \\ m_I & \dfrac{I_O}{h_I^2} + a_7 c_2 + \dfrac{1}{a_0}\dfrac{K_\psi}{h_I^2} \end{bmatrix} = \begin{bmatrix} A_{11} & A_{12} \\ A_{21} & A_{22} \end{bmatrix} \tag{A.40}$$

$$[F] = [R] - (a_6 + a_7)[C]\ddot{\underset{\sim}{y}}(t_n) - [K]\left(\frac{a_2}{a_0}\dot{\underset{\sim}{y}}(t_n) + \frac{1+a_3}{a_0}\ddot{\underset{\sim}{y}}(t_n)\right) =$$

$$= -\begin{bmatrix} m_I \\ m_I \end{bmatrix}\Delta\ddot{X}_g - (a_6 + a_7)\begin{bmatrix} c_1 & 0 \\ 0 & c_2 \end{bmatrix}\begin{bmatrix} \ddot{u} \\ \ddot{\delta} \end{bmatrix} - \begin{bmatrix} k & 0 \\ 0 & \dfrac{K_\psi}{h_I^2} \end{bmatrix}\left\{\frac{a_2}{a_0}\begin{bmatrix} \dot{u} \\ \dot{\delta} \end{bmatrix} + \frac{1+a_3}{a_0}\begin{bmatrix} \ddot{u} \\ \ddot{\delta} \end{bmatrix}\right\} =$$

$$= \begin{bmatrix} -m_I\Delta\ddot{X}_g - c_1(a_6 + a_7)\ddot{u} - \dfrac{a_2}{a_0}k\dot{u} - \dfrac{1+a_3}{a_0}k\ddot{u} \\ -m_I\Delta\ddot{X}_g - c_2(a_6 + a_7)\ddot{\delta} - \dfrac{a_2}{a_0}\dfrac{K_\psi}{h_I^2}\dot{\delta} - \dfrac{1+a_3}{a_0}\dfrac{K_\psi}{h_I^2}\ddot{\delta} \end{bmatrix} = \begin{bmatrix} F_1 \\ F_2 \end{bmatrix} \tag{A.41}$$

177

A.2.4 Algorithm

A. Initial calculations

(i) Assume a formula for $\psi(t_n) = f\left(M(\psi(t_n))\right)$ using the results from ABAQUS.

(ii) Assume an initial value for u, $\dot{u}$, $\ddot{u}$, ψ, $\dot{\psi}$, $\ddot{\psi}$.

Here $u(t_0) = \dot{u}(t_0) = \psi(t_0) = \dot{\psi}(t_0) = \ddot{\psi}(t_0) = 0$ and $\ddot{u}(t_0) = -\ddot{X}_g(t_0)$.

B. For each time step:

(iii) Calculate $K_\psi(t_n) = dM(t_n)/d\psi(t_n)$

(iv) Calculate $\Delta\ddot{v}(t_n)$, $\Delta\dot{v}(t_n)$ and $\Delta v(t_n)$ from (A.31), (A.32) and (A.36).

(v) Using the values of $\Delta\ddot{v}(t_n)$, $\Delta\dot{v}(t_n)$ and $\Delta v(t_n)$ determined from (iv), the accelerations, velocities and displacements are obtained from:

$$\ddot{v}(t_{n+1}) = \ddot{v}(t_n) + \Delta\ddot{v}(t_n) \tag{A.42}$$

$$\dot{v}(t_{n+1}) = \dot{v}(t_n) + \Delta\dot{v}(t_n) \tag{A.43}$$

$$v(t_{n+1}) = v(t_n) + \Delta v(t_n) \tag{A.44}$$